Oxidation of Soot with Modified Silver Catalysts

By

Aaron Lau

366792

University College

A dissertation submitted for the degree of Doctor of Philosophy at the Inorganic Chemistry Laboratory, Department of Chemistry,

University of Oxford

2015

Oxidation of Soot with Modified Silver Catalysts

By

Aaron Lau

366792

University College

Supervisor

Professor S. C. E. Tsang

Industrial Supervisor

Professor A. York

Internal Assessor

Professor L. L. Wong

A dissertation submitted for the degree of Doctor of Philosophy at the Inorganic Chemistry Laboratory, Department of Chemistry,

University of Oxford

2015

Table of Contents

Declaration

I confirm that this is my own work and the use of all material from sources has been properly and fully acknowledged.

Aaron Lau

Dedication

To my parents.

Acknowledgement

First of all I would like to say a big thank you to my supervisor, Prof. Edman Tsang for giving me the opportunity for this DPhil, also for his guidance and insight throughout my time in the group. His ideas are truly inspired, and without his advice during these past few years, it would have been nearly impossible to reach this stage I am at now.

Equally important is my industrial supervisor, Prof. Andy York, who offers a different perspective to a problem often overseen from an academic point of view. I would also like to thank Johnson Matthey for funding for this studentship. Moreover, a huge thank you to the research staff at Johnson Matthey Technology Centre who has taken an interest in this project, and offered insightful discussions to further it.

Many thanks to everyone in the Tsang group, both academically and socially, to make my time at Oxford so enjoyable. A special thank you to Dr. Amy Kolpin, Bin Yu and Hanif Mahadi for helping me perform TEM, even with their very busy schedule; to Dr. Kerry Yu, Dr. Aaron Chan, Dr. Terry Wu, Dr. Simon Jones, and Dr. Clive Eley for training on various equipment within the lab. To David Wen, the Part 2 student I co-supervised, for his assistant in my project. To Dr. Enna Ha for her assistance in the TGA. To Ben Lo for his assistance for XRD peak fitting using TOPAS. To Dr. Simon Fairclough for his impeccable safety standards. To the rest of the Tsang group, Linda, Adam, Joe, Ieuan, Hannah, Ivo, Will, Kevin, Louis, Chris, Lizzie, Elisabeth, Canna, Molly, Jin, Qin, Keizo, Feng, Leo, Shaffer, Yusuke for never failing to brighten up the lab with a good laugh.

A massive thank you to Dr. Phil Wiseman of the Inorganic Chemistry Laboratories for training on the XRD and In-situ High Temperature XRD. Thank you to Dr. David Morgan of Cardiff University for helping me perform XPS. Without these vital techniques my project would not have been possible.

A special thank you to Ms. Terri Adams, the glassblower, for all the custom made glassware that enabled me to carry out my project so smoothly; to Mr. Levi Dash, the stores manager, for bending over backwards to cater for all my whims; to Ms. Hazel Osborne, the receptionist, for dealing with my chemical orders and room bookings so promptly.

Thanks to all members and staff of University College, which makes my life outside the lab bearable. To Prof. Martin Smith, my college adviser, for his guidance on all and any matters concerning life in Oxford, whether academic or not. To Bob and his team of porters, who deal with any problems I may have in college.

A thank you to Dr. Phil Wiseman and Dr. Fabrice Birembaut for giving me an opportunity for lab demonstration in the undergraduate teaching lab. This has developed my skills in the research lab further, and made me concentrate on any shortcomings I may otherwise not have realised. To Fred Dunn, the teaching lab technician, for his willingness to offer assistance on matters even outside the teaching lab.

Last but most definitely not least, thanks to my parents who provide unconditional love and support throughout my DPhil, as they have been since I was born.

Abstract

As the demand for motor vehicles has soared dramatically with the emergence of rapidly developing countries, the need for regulating vehicle emissions and pollutants is increasingly more important. With the newest regulations for diesel particulate emissions soon to be enforced, there is a great need to catalytically convert soot particles from the exhaust into relatively less polluting carbon dioxide.

Here a supported silver catalyst is reported for the soot oxidation reaction. The silver catalyst is protected and supported using various capping agents and metal oxides, and modified using various synthetic methods. The catalysts are then tested with soot using thermogravimetric analysis (TGA) at a reaction temperature up to 700 ^{o}C.

In order for a better design and modification of the silver catalyst, an improved understanding of the interaction between silver nanoclusters and the metal oxide support must be established.

XPS and UV/VIS spectroscopy are amongst the techniques used to probe the metal/metal oxide interaction. It is shown that the surface plasmon resonance of silver can be perturbed by the metal oxide support, modifying its band structure.

It is also extremely important for the catalyst to be thermally stable up to 600oC for it to be employable in an exhaust system. In-situ XRD can be used to investigate the thermal stability of both the silver and metal oxide species in an oxidising environment. The phase changes, if any, of either species under heating can also provide a better understanding of the metal/metal oxide interaction and ultimately the soot combustion mechanism.

It has been demonstrated that different catalyst surfaces can have different catalytic performances. By altering the morphology of the support, preferential growth of one surface can be achieved, thereby modifying the catalytic performance for soot combustion.

Keywords: Heterogeneous catalyst, Soot combustion, Morphology modification, Size Effect, Metal – Support Interaction

List of Abbreviations

[ ]	Oxygen Vacancy
$[O]^*$	Energetic Oxygen
Ag/MO	Silver supported on metal oxide (see MO)
Ag-MO/Al_2O_3	Ag and metal oxide co-supported on Al_2O_3
ATR	Attenuated Total Reflectance
c.f.	*confer*
ca.	*circa.*
CRT	Continuously. Regenerating Technology
DEG	Diethylene Glycol
DoS	Density of State
DSC	Differential Scanning Calorimetry
DTG	Differential Thermogravimetric
E_c	Conduction Band
E_f	Fermi Level
E_v (or VB)	Valence Band
EDX	Energy Dispersion Spectroscopy
EG	Ethylene Glycol

EMSI	Electronic Metal – Support Interaction
EU	European Union
FT-IR	Fuorier – Transform Infrared Spectroscopy
GWP	Global Warming Potential
IR	Infrared
JM	Johnson Matthey
Ln	Lanthanide
Ln_2O_3	Lanthanide Oxide (see Ln)
LSPR	Localised Surface Plasmon Resonance
MO	Metal Oxide
MS	Mass Spectrometry
$NADP^+$	Nicotinamide Adenine Dinucleotide Phosphate
NO_x	Nitrous Oxides
OA	Oleic Acid
O_α	Alpha (surface) Oxygen
O_β	Beta (interstitial) Oxygen
O_γ	Gamma (lattice) Oxygen
PGM	Platinum Group Metal

PM	Particulate Matter
PTFE	Poly(tetrafluoroethylene)
SDT	Simultaneous DSC – TGA (See DSC, TGA)
SMSI	Strong Metal – Support Interaction
SO_x	Sulphur Oxides
SPR	Surface Plasmon Resonance
T_{50}	Temperature of 50% combustion
T_m	Temperature of peak combustion rate
TEG	Triethylene Glycol
TEM	Transmission Electron Microscopy
TGA	Thermogravimetric Analysis
TMO	Transition Metal Oxide
TOA	Trioctylamine
TPR/O	Temperature Programmed Reduction/Oxidation
USA	United States of America
UV-Vis	Ultraviolet – Visble spectroscopy
ν_{as}	Asymmetric Stretch
ν_s	Symmetric Stretch

wt	Weight
XPS	X-Ray Photoelectronic Spectroscopy
XRD	X-Ray Diffraction

List of Figures

List of Tables

Contents

Chapter 1. Introduction

1.1 Overview

The increasing industrialisation of countries means that an increasing amount of energy is needed to keep up with this rate of development. Until renewable energies can fully fulfil this ever growing energy demand, fossil fuels will have to be heavily relied on as the backbone of this energy source. Amongst the different types of non-renewable energies, diesel is one of the most widely used in both heavy duty industrial engines and, increasingly, vehicle engines. Diesel, due to its lower combustion temperature, results in a range of pollutants such as particulate matter, NO_x, and CO[1].

Particulate matter (PM), or soot, is in particular a major contributor to different pollutions, such as global warming and photochemical smog[2,3]. Although various methods have already been developed in the past decade to cut down on PM emission levels, stricter levels are going to be in place as part of the Euro 6 regulations, and even more stringent regulations over the coming decade[4,5]. However, as the exhaust from a diesel engine differs greatly from that of a petrol engine[6], the three–way catalyst currently in place with the petrol engine cannot be applied to a diesel engine[7]. Therefore, there is an urgent need to come up with an effective catalyst for PM abatement in order to meet these requirements.

The leaner combustion environment of a diesel engine means that there is going to be oxygen left over after the combustion process, which can be used to oxidise soot in the exhaust. Therefore an oxidation catalyst is needed for soot abatement. The current technology, the Continuously Regenerating Trap (CRT), can only combust soot at a temperature higher than that in the diesel exhaust[8], so an injection of diesel fuel is required in order to raise the temperature for effective soot combustion. The development of an oxidation catalyst that can function at low temperature (< 300 ^{o}C) is thus required for a more efficient soot combustion process.

Various metal oxide supported Ag nanocatalysts have been successfully demonstrated to be effective soot combustion catalysts[9–39]. As different supports are employed, a more detailed mechanistic study can be elucidated. Various additive effects have also been investigated in an attempt to find a more effective catalyst[9,20–22,26,29,34,37,40–49].

1.2 Petrol vs. Diesel Engine

Petrol and diesel are two of the most commonly used fuels for vehicles, powering anything from a motorcycle to a truck. Diesel is also used widely in heavy duty engines in industries, including ships and other heavy transportation vehicles.

Petrol and diesel engines rely on different operating mechanisms, leading to different advantages, and more importantly, different problems[6]. A petrol engine operates on four basic steps: induction, compression, ignition, and exhaust. Induction is where fuel is either mixed with air at a pre-determined ratio in a carburettor before arriving at the engine, or the fuel is directly injected as a fine mist with air into the engine cylinder. In the following step, the fuel/air mixture is compressed by a rising piston. Then the fuel/air mixture is ignited by a spark from the spark plug, creating an explosion driving the pistol downwards. Finally the pistol rises uses the residue energy from the ignition, driving spent gases out through the exhaust valve. This process is illustrated below in Figure 1-1[50].

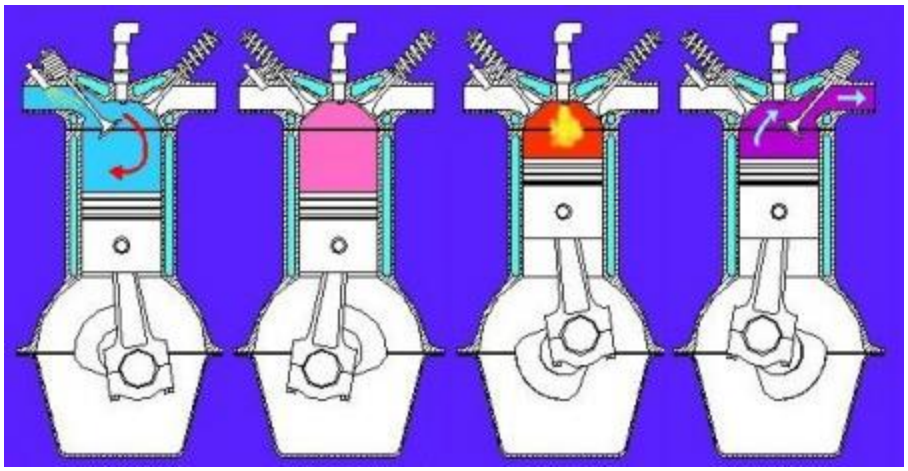

Figure 1-1 Operation mechanism of a petrol engine. The four steps correspond to induction, compression, ignition, and exhaust respectively. Image reproduced from source[51].

In order for a petrol engine to function efficiently, the fuel chosen must not self-ignite during the compression process, as energy would be wasted in trying to counteract this process. This is known as knocking, and anti-knocking fuels have been developed in order to minimise the effects of knocking[50].

Diesel engines, on the other hand, rely on the self-ignition of fuels to operate. Developed by Rudolf Diesel at the turn of the 20th century[52], he theorised that a high compression ratio would lead to higher efficiency and more power. He argued that a higher compression ratio would mean more tightly packed air molecules upon compression, leading to a more readily available oxygen source for combustion. This higher efficiency also means that the diesel engine can operate at much leaner conditions, with an air/fuel ratio of over 15:1 compared to 8:1 in conventional petrol

engines. As the fuel is auto-ignited, the spark plug within the engine is not required, but instead a glow plug is used for cold starting a diesel engine as there is not enough heat in the engine to auto-ignite the diesel effectively.

As previously mentioned, an anti-knocking fuel is vital in the operation of a diesel engine. The level of knocking from a molecule can be measured with an octane rating, where 2,2,4-trimethylpentane (iso-octane) has an octane number of 100; and n-heptane has an octane number of 0[50]. A higher octane number means that it is a more knocking-resistant fuel. Conversely, as diesel relies on auto-ignition, its fuel rating is measured by the time between injection of fuel and its combustion, known as the cetane number. Like petrol, a higher cetane number fuel is more desirable as it means the delay between injection and ignition is less, leading to a smoother running engine. In Europe, the current minimum cetane number is 51; whereas the average cetane number in the USA is typically 45[53]. This difference in fuel will lead to a difference in their exhaust composition, and also the effectiveness of a soot abatement catalyst in dealing with the exhaust, as discussed in future sections.

Due to the different combustion environments of a petrol and diesel engine, the exhausts of the two types of engines are remarkably different. Figure 1-2 shows the typical composition of petrol and diesel exhausts.

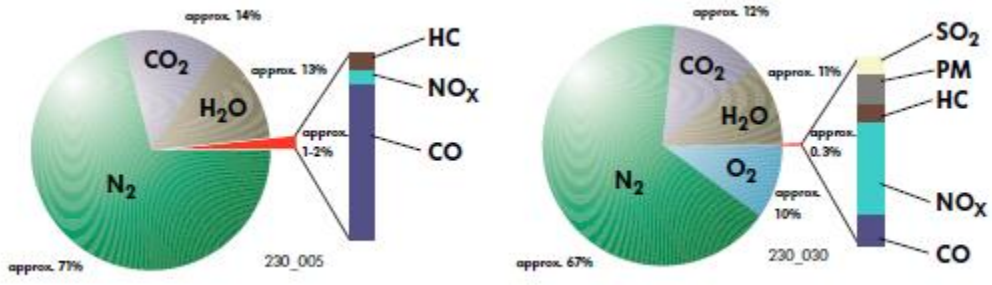

Figure 1-2 Composition of petrol (left) and diesel (right) exhausts[6].

As previously discussed, diesel engines work at a higher compression in the absence of a spark plug, the combustion temperature is lower than petrol engines with a more lean combustion environment[50]. This leads to a significant increase in the production of NO_x, and also contributes to the incomplete combustion of fuel, producing particulate matters (PM), or soot. The leaner combustion environment, however, means there is around 10% oxygen remaining after combustion, leading to a reduction in CO production. Residue oxygen is often found in the exhaust. The sulphur containing compounds often found in diesel can combust to form SO_x, although the introduction of ultra-low sulphur diesel in the EU and USA has almost eradicated this problem in these parts of the world[5,50,54].

1.3 Diesel Soot – Implications to the Environment and Health

Although NO_x and CO are both major pollutants which contribute to a variety of environmental problems, PM is by far the most significant contributor to pollution, leading to extremely damaging environmental and health impacts.

Soot causes photochemical smog, where soot, when mixed with other pollutants such as SO_2, reacts with sunlight to give a thick fog like atmosphere. This smog is highly reactive and oxidising, and causes damage to both health and buildings[3].

Figure 1-3 City polluted by photochemical smog[55].

Soot is also a major contributor to global warming, and it is claimed to be the second biggest contributor to the greenhouse effect, after only CO_2[56].

Global warming is caused by the release of greenhouse gases that were previously "locked" in fossil fuels. The combustion of these fossil fuels releases CO_2, amongst other greenhouse gases, which absorbs infrared (IR) radiation released from the earth. This absorption of IR radiation converts this energy into heat, warming up the atmosphere.

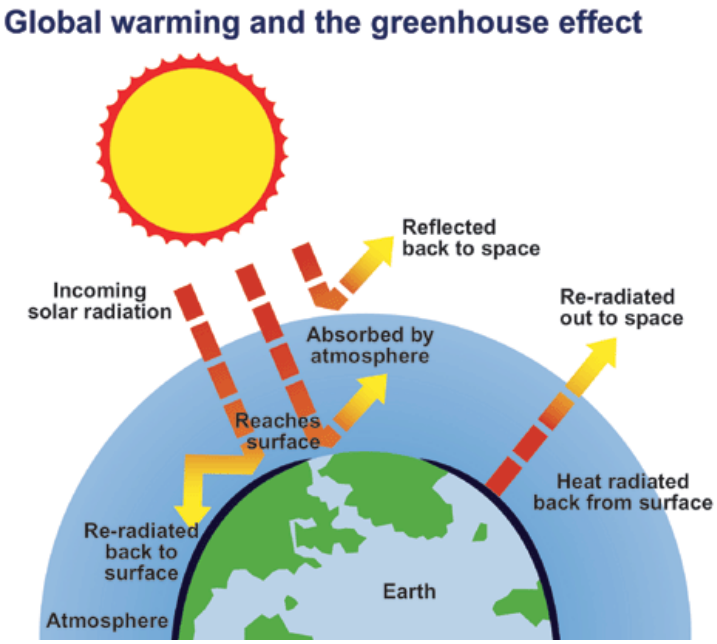

Figure 1-4 Illustration of the cause of the Greenhouse Effect[57].

Although soot is released into the atmosphere in relatively small quantities compared to CO_2, a well-known greenhouse gas, its effects are much more severe than its better known counterpart.

Table 1-1 Greenhouse Gas Potential (GWP) of Selected Greenhouse Gases[56]

Greenhouse Gas	20 Year Greenhouse Gas Potential (GWP)
CO_2	1
CH_4	85
Soot	4500
N_2O	270

GWP is used to evaluate how much heat a certain gas is able to trap within the atmosphere. The GWP is standardised as 1 ton of CO_2 has a GWP of 1, and its value is the equivalent of releasing that amount of CO_2 into the atmosphere. For example, releasing 1 ton of CH_4 would have an equivalent of releasing 85 ton of CO_2 over a 20 year period. So with soot, its effects on the atmosphere are equivalent to 4.5 kiloton of CO_2 being emitted. If soot is assumed to be pure carbon, then 1 ton of soot will combust to form 3.7 ton of CO_2. This means the GWP of soot can potentially be reduced from 4500 to 3.7 by full combustion of soot, again indicating the severity of the environmental problems caused by soot.

With the increasing environmental impact caused by soot, its implication on health is getting increasingly stark. It has been known for over 20 years that PM causes a range of diseases, from a shortness of breath to lung cancer. More recent studies have shown that eyes, nose, and throat irritation is a common symptom of PM exposure. It can also raise blood pressure, and cause hardening of blood vessels, leading to heart attacks,

strokes, and aneurysms. PM is a trigger for asthma, which can lead on to further deterioration and complications of other respiratory diseases[5].

With such great impact on the environment and people's health, it is imperative that an effective catalyst be developed in order to convert PM into less harmful substances, such as CO_2.

1.4 Regulations into Diesel Soot Emission

Particulate matter is produced by the incomplete combustion of diesel fuel, and its main components are carbon and volatile organic compounds. These VOCs include a wide range of molecules, from polycyclic aromatic hydrocarbons, to cyclic aliphatic hydrocarbons, to long chain hydrocarbons[58].

PM is normally in a form of agglomerate chains with typical lengths from 0.1 μm to 10 μm, and a diameter of 10 – 50 nm. The classification of PM is normally with this length of agglomerate chain length, where a chain length of 10 μm is known as PM_{10}; and a chain length of 2.5 μm is known as $PM_{2.5}$.

A schematic diagram of soot formation is shown in Figure 1-5, where the VOCs are first adsorbed onto graphitic carbon, which then undergoes nucleation to form larger

aggregations of graphite sheets. These sheets then coagulate and grow to form spherical soot particulates, and finally agglomerate to form chains of particulate matter.

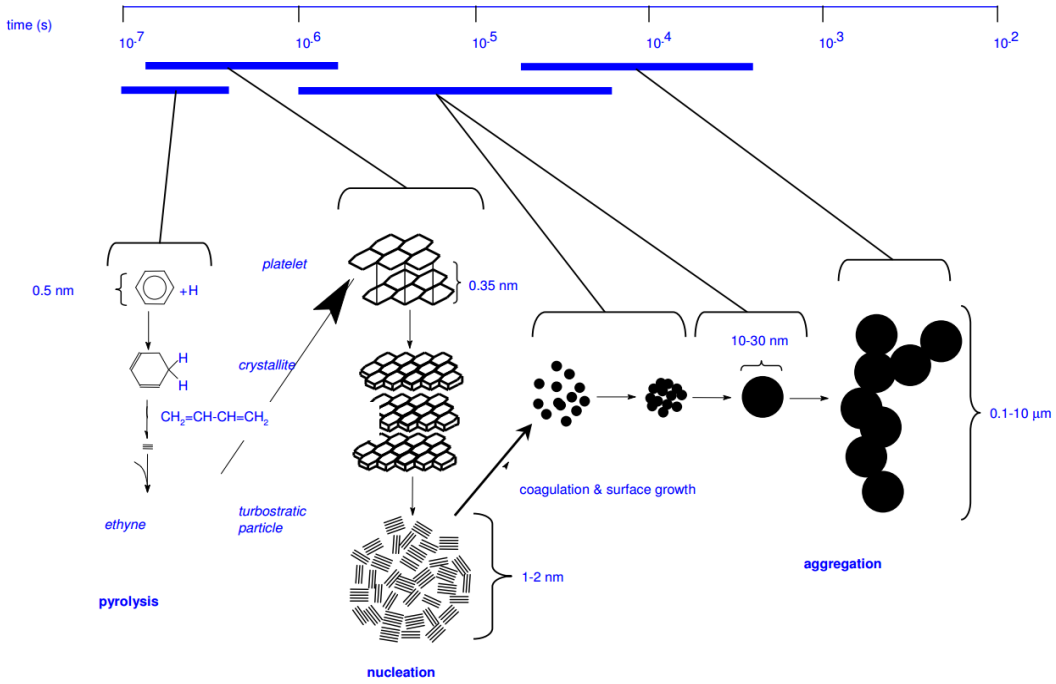

Figure 1-5 Schematic diagram of PM formation[46].

The EU has come up with a string of regulations concerning PM emissions, from the Euro I directive in 1993, to Euro VI in 2014. Table 1-2 gives a summary of the PM regulations of the different EU regulations[54].

Table 1-2 PM Regulations of EU directives, values in bracket correspond to emission values for heavy duty engines[54].

Regulation	Date	PM Emission Limits (g km^{-1})
Euro 1	July 1992	0.14 (0.612 g kWh^{-1})
Euro 2	January 1996	0.08 (0.25 g kWh^{-1})
Euro 3	January 2000	0.05 (0.13 g kWh^{-1})
Euro 4	January 2005	0.025 (0.12 g kWh^{-1})
Euro 5	September 2009	0.005 (0.02 g kWh^{-1})
Euro 6	September 2014	0.005 (0.01 g kWh^{-1})

The amount of PM emission of heavy duty engines is measured in g kWh^{-1} instead of g km^{-1} since it is based on the static testing of these engines. It can be seen that the regulation is getting increasingly stringent on PM emission limits, with even stricter limits coming into force with the EU 7 directive, expected to be enforced in 2016. Table 1-3 shows the PM emission limits as of 2014.

Table 1-3 PM emission limits of various countries in 2014[56].

Country	PM Emission Limit (g km^{-1})	$PM_{2.5}$ Limit (μg m^{-3})
EU	0.005	N/A (25)
USA	0.01	35 (12)
Japan	0.01	35 (15)
China	0.03	75 (35)
India	0.05 (Euro 3)	
South Africa	0.08 (Euro 2)	
Russia	0.025 (Euro 4)	

The $PM_{2.5}$ limits are normally quoted as two values, the 24 hour limit, and the annual limit, given in brackets in the table above. Most developed, and developing, countries

employ the Euro directive as their standard emission standards, though most developing countries are still currently on Euro 5, with Euro 6 coming into force from 2015. Other developed countries not adopting the Euro directive have less strict regulations, with both the USA and Japan limiting PM emission to 0.01 g km^{-1}. Emerging countries such as India and China are both adopting increasingly stricter regulations in order to combat pollution problems faced by these countries.

$PM_{2.5}$ is a much greater threat to health as it is small enough to penetrate much deeper into the lung, causing much more damage than PM_{10}. They are also too small to be trapped by conventional filter systems, which mean they cannot be treated in the exhaust system. Most countries, including developing countries, are beginning to realise the damages caused by $PM_{2.5}$, and have very strict limits for both 24 and annual limits. However, in reality, most countries are over the set limit, with China at >100 μg m^{-3} at present. These limits are realistically not going to be met until 2020, and with increasingly more stringent emission controls to be put in place over the next few years, the race is on to develop a new and effective catalyst for soot abatement, especially for $PM_{2.5}$.

1.5 Continuously Regenerating Trap (CRT)

In a conventional petrol engine, a three-way catalyst (TWC) is used to convert pollutants such as NO_x, CO, and hydrocarbons into CO_2, H_2O, and N_2. It works by reducing NO_x, and oxidising CO and hydrocarbons respectively[59], as shown in the equations below.

$$NO + CO \rightarrow {}^{1}/_{2}N_2 + CO_2$$ **Equation 1-1**[59]

$$2CO + O_2 \rightarrow 2CO_2$$ **Equation 1-2**[59]

$$C_xH_{2x+2} + [{}^{(3x+1)}/_{2}]O_2 \rightarrow xCO_2 + (x+1)H_2O$$ **Equation 1-3**[59]

However, this Pt/Rh on CeO_2 support catalyst system suffers from poisoning if employed in a diesel system, as PM builds up on the catalyst and leads to deactivation of the catalyst. Therefore, a different exhaust system is required for the diesel engine. Furthermore the lean environment means that the NO reduction does not proceed effectively.

Currently, Johnson Matthey (JM) is utilising a PM trapping and abatement device, called the Continuously Regenerating Trap (CRT)[60]. There are many other soot trapping devices in use, which are effective against soot emission, however, that leaves the problem of burning off the soot once it has been trapped in the filter system. JM has developed two main types of CRT's, namely the Passive CRT and the Active CRT. The Passive CRT system traps PM in its filter system, and removes the PM by either combustion with NO_2 or O_2.

NO_2 is the result of NO oxidation in the exhaust with oxygen, as shown in the equations below. It is known as a passive system because no external input is required for catalyst regeneration.

$2NO + O_2 \rightarrow 2NO_2$ **Equation 1-4**[60]

$2NO_2 + [C] \rightarrow CO_2 + 2NO$ **Equation 1-5**[60]

$[C] + O_2 \rightarrow CO_2$ **Equation 1-6**[60]

The NO_2 is produced upstream of the diesel particulate filter, which can then be used to oxidise PM and regenerate NO. Soot combustion with oxygen only occurs at 600 ^{o}C, whereas soot reaction with NO_2 can occur at 250 ^{o}C, as long as there is a constant supply of NO_2. Therefore a passive system relies heavily on the process of NO oxidation.

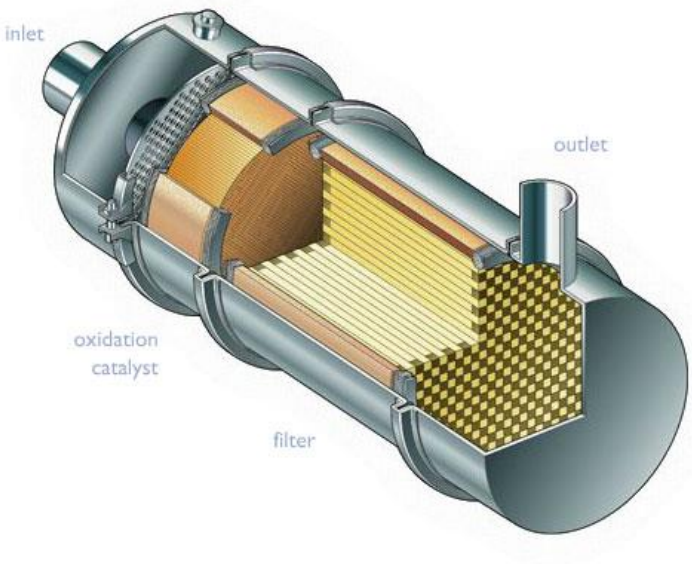

Figure 1-6 A cut-away section of the Passive CRT Exhaust System[60].

On the other hand, the active system is where an external energy input is required to raise the temperature of the filter to around 600 ^{o}C, which is the optimum operating temperature of the catalyst for soot combustion with oxygen. The energy input is typically either electric power, or fuel injection.

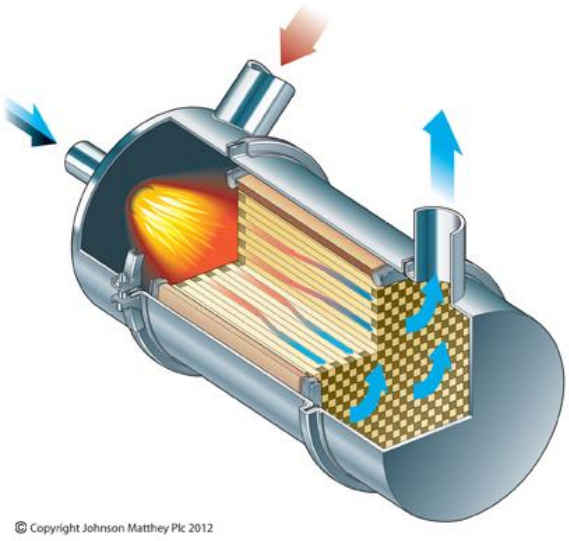

Figure 1-7 An Active CRT system using a diesel burner, where the diesel is injected at the red arrow[60].

The active system has a few disadvantages, regardless of the method of regeneration. Chief of which is energy, or fuel, is required for the regeneration, which can be costly, and ultimately unsustainable.

1.6 Catalysis

The word “catalysis” is derived from the Greek “καταλύω”, *katalyein*, from *kata-* + *lyein*, meaning “to annual”, “to untie”, or “to pick up”. The word “catalysis” was first used by Jöns Jakob Berzelius in science and chemistry in 1835. He used the term to describe reactions that were accelerated by certain substances, but at the same time the substances were left unchanged after the reaction. Examples of catalytic reactions are numerous, including the decomposition reaction of hydrogen peroxide with a metal oxide, or the Haber – Bosch Process for the synthesis of ammonia using an iron-based catalyst.

Berzelius originally proposed that “although still too little known to be accurately explained, [catalysis] must play a far more important part throughout nature than we have hitherto been led to suppose”. The development of catalysis in the past 180 years helps to develop insights into catalysis. A more contemporary definition of a catalyst is “a substance that increases the rate of a chemical reaction without itself undergoing any permanent chemical change”. Catalysis plays a major role in nature, and other processes, and also bringing in billions of pounds of revenue in industrial processes. For example, the Haber – Bosch Process for the synthesis of ammonia accounts for 80% of the nitrogen eventually found in the human body, and has led to quadruple crop yield within the past century. It is fair to say that it is one of the most important catalysed processes in the development of catalysis. The move from its use of an osmium based

compound to a much cheaper, and less environmentally harmful iron catalyst highlights the continuous need for development and advancement in the field of catalysis.

Another important catalytic reaction is the Fischer-Tropsch process, where CO and H_2 are converted to hydrocarbons. This process is used to produce low sulphur fuels, or to convert gaseous fractions into liquid fractions which are more plausible fuel sources. It was initially developed by Franz Fischer and Hans Tropsch in Germany during the inter-war years. This method of producing synthetic fuels was an attempt to overcome her limited supply of crude oil. The Fischer-Tropsch reaction typically involves a transition metal catalyst, such as iron, for the conversion of synthesis gas ("syngas", CO + H_2) to hydrocarbons, and the water–gas shift reaction to control the CO:H_2 ratio using steam. By controlling the ratio of CO and H_2 in the syngas feed, and the composition of catalyst, different desired products with different carbon chain lengths can be produced.

Catalysis forms the cornerstone of modern industrial processes, with global catalyst industry revenue forecasted at nearly $100 billion by the end of this decade, and growth is expected to continue. The continuous development of existing catalysts and reactions, and the discovery of new catalysts for new processes, is highly demanded in both academia and industry. The study of catalytic reaction mechanism, catalytic testing and characterisation, its incorporation into industrial reactors, and its optimisation at an

industrial scale requires further improvement from the fields of chemistry, material science, and engineering.

More recent developments of catalysis have led to rapid progresses on prototypes of fuel cells employed in motor vehicles. The Honda FCX Clarity in the US stores hydrogen under high pressure, much like light petroleum gas, and oxidises it using a hydrogen fuel cell. This technique shows the high possibility of generating power at a much higher efficiency than an internal combustion engine.

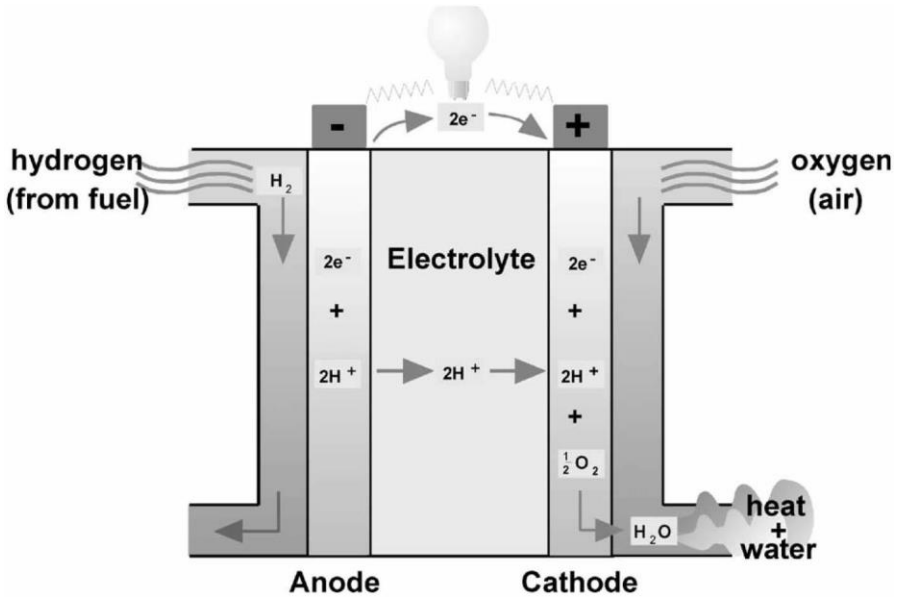

Figure 1-8 Diagram of a Polymer Exchange Membrane Hydrogen Fuel Cell.

1.7 Types of Catalysis

All catalytic reactions can be divided into three general categories: Biocatalysis, Homogeneous Catalysis, and Heterogeneous Catalysis.

Biocatalysis is the use of natural catalysts, such as enzymes and micro-organisms, to perfom bio-involved catalytic reactions. As nature has already developed and optimised its catalysts to be the most active and selective for specific reactions over millions of years, much interest is in the field of biocatalysis to mimic the catalysts used in nature for a wider range of catalytic reactions. For example, ferredoxin found in $NADP^+$ reductase has been isolated, and tailored for other synthetic reactions.

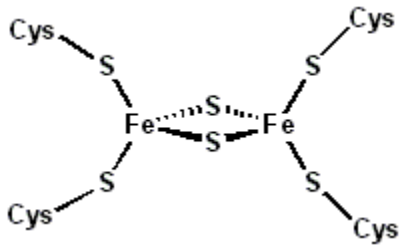

Figure 1-9 Fe_2S_2 cluster centre of Ferredoxin found in a number of natural enzymes.

Homogeneous catalysis is a reaction between catalyst and reactants in the same phase, typically the liquid phase. The catalyst may be an organometallic compound, or a simple acid/base solution that are dissolved in the same medium as the reactants and products. Homogeneous catalysis can be found in a very wide range of reactions, from the acid

catalysed esterification reactions, where the proton activates the carbonyl group of the carboxylic acid, to complex organometallic catalysts for a wide range of reactions.

The Grubbs' catalyst, for example, is a Ru based organometallic catalyst used for ring metathesis reactions[61]. From its development in complexity of ligands, and the tailoring of functional groups, the stereoselectivity and selectivity of the catalyst can be dramatically improved. This can either be due to the electronic or steric modifications of the ligands present on the metal centre which can radically alter the chemical properties of the catalyst.

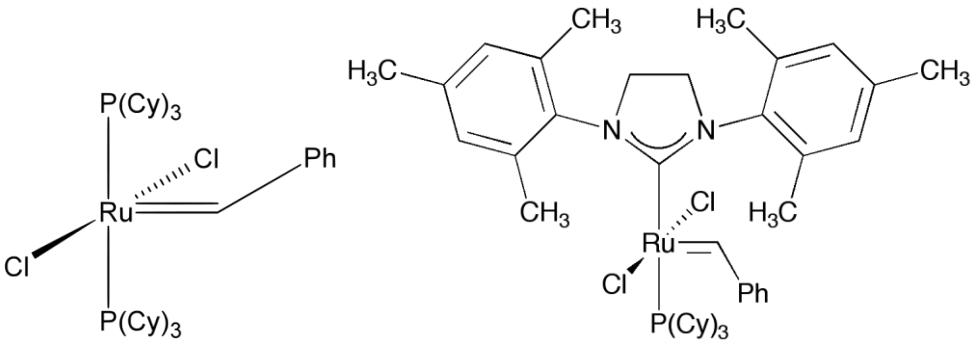

Figure 1-10 1st Generation Grubbs' Catalyst (Left)[61], and 2nd Generation Grubbs' Catalyst (Right)[61].

Heterogeneous catalysis happens when the catalyst and reactants are in different phases, typically the catalyst is in the solid phase, and the reactant(s) in either the gas or liquid phase. Heterogeneous catalysis is widely used in industrial processes, and is often

preferred over homogeneous catalysis since the catalyst can be easily recovered by physical means, and large scale reactor systems, such as fixed bed flow reactors, can be designed with relative ease. Heterogenous catalysts are generally more stable than homogeneous catalysts, resulting in less catalyst replenishment, and thus a further saving in cost.

Catalysis works by providing an alternative reaction pathway for reactants, through interaction with reactants, intermediates, or products, facilitating a reaction pathway that has a lower activation energy than the un-catalysed reaction. The catalyst must not undergo any permanent change after the reaction has taken place. The catalyst often undergoes change during the reaction process in order to provide a lower energy pathway for the reactants, but is always reverted back to its original form at the end of the reaction.

For homogeneous catalysis this is often drawn as a reaction cycle, where the catalyst is depicted to go through its different states, before going back to its original form which is shown at the end of the cycle.

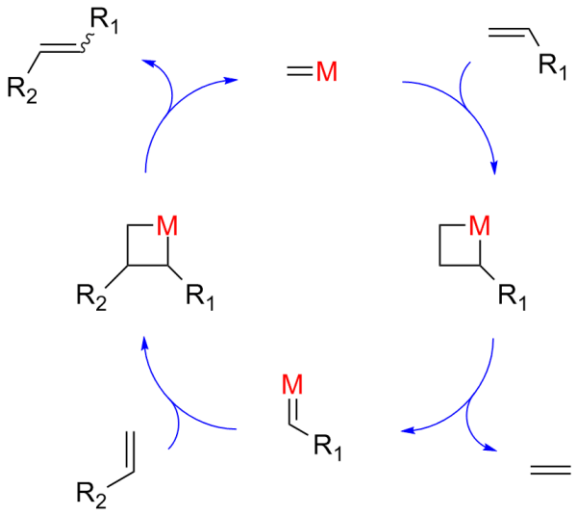

Figure 1-11 Reaction cycle of an olefin metathesis cycle.

Figure 1-11 shows a typical homogeneous reaction cycle, where the catalyst, =M, is depicted at the centre of the reaction cycle, and reacts with various reactants to produce different products, returning to its original structure at the end of the reaction.

For a heterogeneous catalyst, the catalyst typically does not change significantly during the reaction process, but provides active surface sites for reactant molecules, either a liquid or gas, to react on. It is often impractical to draw reaction cycles for heterogeneous catalysis since the intermediates are much less well defined than homogeneous catalysis, but the general idea can still be applied to determine the energies of each of the intermediates involved in the reaction.

The synthesis of ammonia with an iron catalyst described above is a well known example of heterogeneous catalysis. In the first step of all heterogeneous catalysis, the reactant species are adsorbed onto the catalyst surface, either strongly through chemisorption; or weakly through physisorption. A physisorbed species is able to move on the catalyst surface, changing its configuration on the surface, in order to achieve an energy minimum. This then becomes a strongly binding species, which can undergo further reaction. The energy diagram for a typical Haber – Bosch reaction is shown below in Figure 1-12.

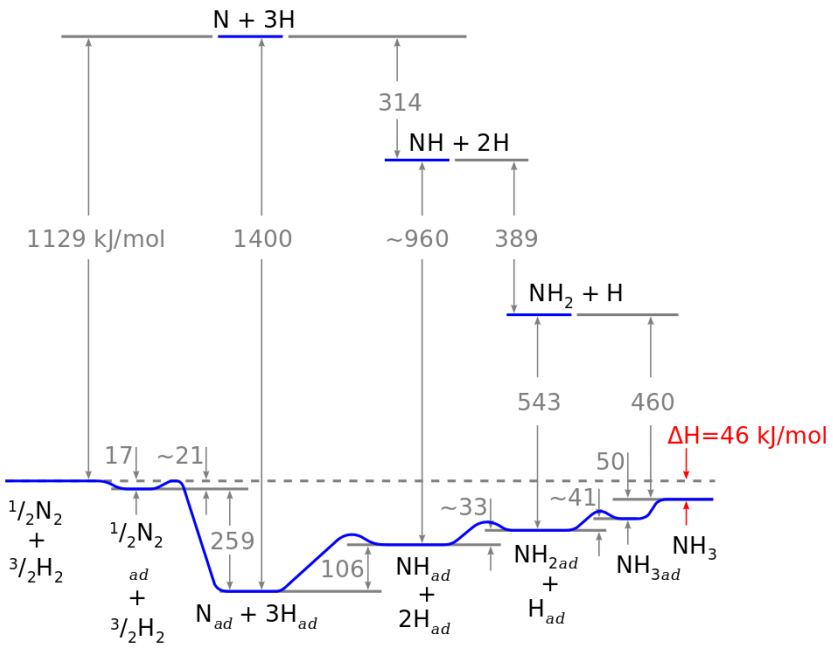

Figure 1-12 Energy diagram of catalysed and un-catalysed reaction for the synthesis of ammonia from elemental nitrogen and hydrogen[62].

Figure 1-12 demonstrates the importance of using a catalyst in the reaction for the synthesis of ammonia. The un-catalysed reaction of elemental nitrogen and hydrogen has a theoretical activation energy of over 1100 kJ mol^{-1}, which would suggest that it is impossible to perform unless under extreme reaction conditions. For the catalysed reaction, however, the energy barrier, which is the maximum amount of energy required in order to make the reaction proceed, is much lower owing to the stepwise adsorption and dissociation of nitrogen and hydrogen, making the reaction much more plausible. The huge energy barrier in the un-catalysed reaction arises from the energy required in order to break the triple bond in gasous nitrogen.

The Maxwell – Boltzmann distribution suggests that only a certain number of molecules with sufficient energy over the activation barrier can react. This means that with such a high activation barrier, few molecules can react in the un-catalysed reaction.

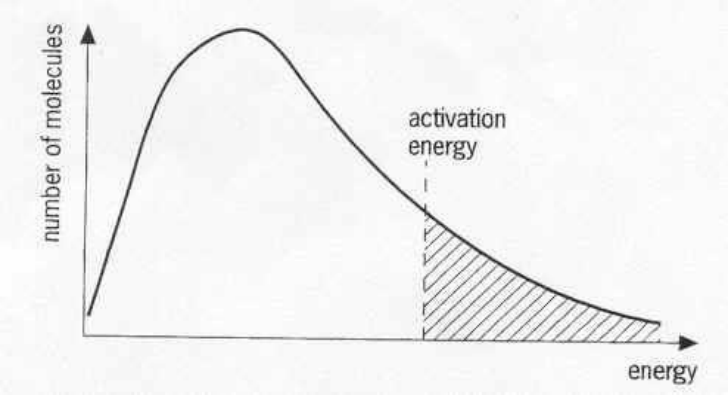

Figure 1-13 Maxwell – Boltzmann Distribution[63].

On the other hand, the catalysed reaction has a much lower activation energy, meaning that a much greater proportion of the molecules are able to react on the catalyst surface, and so the rate of the catalysed reaction would be much greater than that of its un-catalysed counterpart. This in turn means that less energy input is required for the catalysed reaction to take place, and therefore cost can be saved in industrial processes.

This adsorption process has been proposed by Sabatier, which is of vital importance in the activity of the catalyst. He suggested that the adsorption strength had to be "just right" in order for the optimal reaction conditions[64].

If a molecule is adsorbed too weakly, then it would simply desorb, resulting in a low possibility for the surface reaction; contraily, if a molecule adsorbs too strongly, however, it would bind to the catalyst surface too strongly, and becomes inert for catalytic reaction. At that point such a species has become a poison to the catalyst, where the molecule is unable to desorb and causes blockage of the catalyst surface, resulting in a loss of activity.

Sabatier's Principle is used to explain the volcano plot, where the activity of a catalyst is correlated to the binding strength between the intermediate and catalyst surfaces.

Figure 1-14 shows the volcano plot, where it depicts the temperature of formic acid conversion against the enthalpy of metal formate species formation.

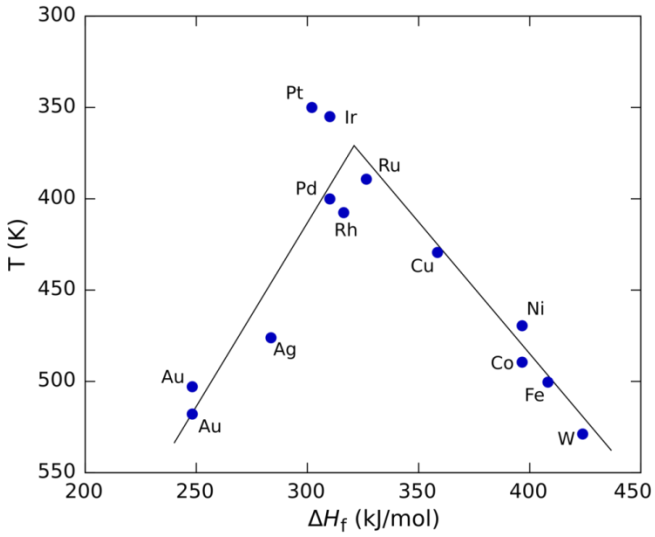

Figure 1-14 Volcano plot of temperature of formic acid conversion against enthalpy of formation of metal formates[65].

Formic acid decomposition firstly requires the dissociation of the proton to form a formate species, then the C – H bond can be cleaved in order to form CO_2 and H_2. Side reactions can also occur where CO and H_2O is produced instead. Regardless of which reaction pathway the formate undergoes, the first step of the process requires the formation of a metal formate species. Sabatier's Principle suggests that if the enthalpy of formation is too low, there is not sufficient energy to carry out the subsequent steps of the decomposition reaction; whereas if the enthalpy of formation is too high, the formate binds too strongly to the metal catalyst, making it difficult to desorb and

decompose. Therefore the formation enthalpy of the metal formate species has to be "just right" in order to obtain the lowest decomposition temperature. For different reactions, there are going to be different catalysts that interacts the most favourably with the reactants for the optimum reaction conditions, therefore it is important to understand the characteristics and behaviour of each catalyst for their role in the catalytic reaction.

1.8 Reaction Kinetics

Reaction kinetics is the study of the rates of processes in each step of a reaction pathway. This can be derived from the observable changes in the rate by altering the temperature or pressure of the reaction system, to the calculated changes of the interactions of adsorbed species on the catalyst surface. The empirical observations can be expressed in terms of rate constants and activation energies. The activation energy is defined as the energy required to initiate a chemical reaction.

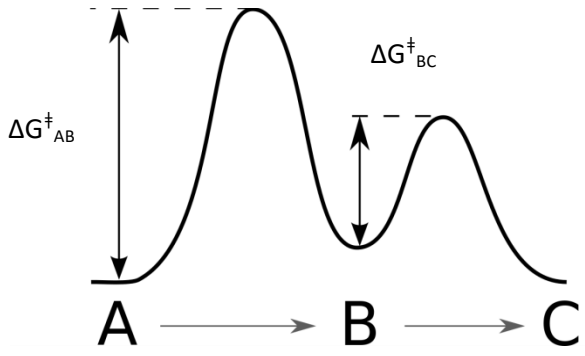

Figure 1-15 Energy profile diagram of a typical reaction.

Figure 1-15 depicts a typical reaction from A, *via* intermediate B, to product C. $\Delta G^{\ddagger}_{AB}$ and $\Delta G^{\ddagger}_{AB}$ are the activation energies for the individual steps A → B and B → C respectively. The overall activation energy $\Delta G^{\ddagger}$ is defined as the energy required to get over the highest energy barrier, which is $\Delta G^{\ddagger}_{AB}$ in this case. As the step A → B requires more energy than B → C, it will also be the slowest step in the whole reaction, making it the rate determining step. The rate of reaction will increase by increasing the rate of the RDS; whereas altering the rates of any other steps will have no effect in the overall rate of reaction, as long as they do not become the rate determining step themselves. As the rate of reaction depends on the activation energy, which in turn is temperature dependent, this relationship can be described by the Arrhenius Equation, shown in Equation 1-7 below.

$$\boldsymbol{k = Ae^{-\frac{E_a}{RT}}} \qquad \textbf{Equation 1-7}$$

Where k is the rate constant; A is the pre-exponential factor, determined empirically; E_a is the activation energy; R is the gas constant; and T is the temperature of reaction. As the rate of reaction is the same as the rate of the RDS, this equation can be used to determine the relationship between the rate of reaction and the activation energy.

Consider a typical gas phase bi-molecular reaction A + B → C with no intermediate steps, the rate determining step often involves the collision of A and B, and its rate equation can be written as follows:

$$r = k [A] [B] \qquad \text{Equation 1-8}$$

Where r is the rate of reaction; k is the rate constant; [A] and [B] are the concentrations of A and B respectively. However, in a catalysed reaction involving a heterogeneous catalyst, a solid surface is often involved, where the desorption of the molecular species is fast compared to the reaction step that follows. In which case, the rate of reaction is dependent on the surface coverage of the reactant species A, θ_A.

Many different models can describe a gaseous species on a solid surface, and the Langmuir adsorption isotherm is one of the most used isotherm models. For a unimolecular reaction shown in Equation 1-9, the rate of formation of the adsorbed species is considerably higher than the reaction step, making the reaction step the RDS ($k_2 >> k_1$). K_A is defined as the equilibrium k_1/k_{-1}, C_S is the number of surface sites (whether occupied or not), and p_A is the pressure of A.

$$\boldsymbol{A_{(g)}} \underset{k_{-1}}{\overset{k_1}{\rightleftharpoons}} \boldsymbol{A_{(ads)}} \xrightarrow{k_2} \boldsymbol{Product} \qquad \text{Equation 1-9}$$

$$r = k_2\theta_A C_S = \frac{k_2 K_A p_A}{(1 + K_A p_A)}$$ Equation 1-10[66]

The Langmuir adsorption isotherm can be used to describe the rate of reaction at the two extreme conditions: (i) at low pressure of A, or (ii) at high pressure of A. At low pressures of A, $(1 + K_A p_A)$ is close to 1, which means the rate is dependent on the pressure of A; whereas at high pressure, θ_A tends towards 1, making the reaction independent of A.

As most reactions are not monomolecular reactions, the above Languir adsorption isotherm cannot be used to adequately describe more complex surface reactions. Therefore, an improved model has to be implemented for bimolecular reactions. The Languir – Hinshelwood mechanism can thus be used to describe a bimolecular reaction.

$$A_{(g)} \underset{k_{-1}}{\overset{k_1}{\rightleftharpoons}} A_{(ads)}$$ Equation 1-11

$$B_{(g)} \underset{k_{-2}}{\overset{k_2}{\rightleftharpoons}} B_{(ads)}$$ Equation 1-12

$$A_{(ads)} + B_{(ads)} \xrightarrow{k} Products$$ Equation1-13

$$r = k\theta_A\theta_B C_S^2$$ Equation 1-14[67]

Equation 1-14 is an extension from Equation 1-10, where the rate depends on the surface adsorption coverages of A and B. As *per* Equation 1-10, the surface coverage of A, and indeed B, can be modelled as follows:

$$\boldsymbol{\theta_A = \frac{k_1 C_A \theta_E}{k_{-1} + kC_S \theta_B}} \qquad \textbf{Equation 1-15}$$

$$\boldsymbol{r = kC_S^2 \frac{K_1 K_2 C_A C_B}{(1 + K_1 C_A + K_2 C_B)^2}} \qquad \textbf{Equation 1-16}^{67}$$

Where C_A is the surface concentration of sites occupied by A; and θ_E is the fraction of empty sites ($\theta_A + \theta_B + \theta_E = 1$). It is assumed that the rate limiting step is the reaction of the adsorbed molecules, and the probability of two adsorbed molecules colliding is low. Thus Equation 1-15 can be reduced and substituted back into Equation 1-14 to yield Equation 1-16. This means that there are more possible scenarios than the monomolecular case. If both molecules have low adsorption, then $1 >> K_1C_A + K_2C_B$; $r = kC_S^2 K_1 K_2 C_A C_B$, and the order of reaction is one with respect to both reactants.

If one molecule (say B) has much lower adsorption compared to the other, then $K_1 C_A + 1 \gg K_2 C_B; r = kC_S^2 \frac{K_1 K_2 C_A C_B}{(1 + K_1 C_A)^2}$, and this can lead to two further possibilities. At low concentrations of A, then $r = kC_S^2 K_1 K_2 C_A C_B$, and the order of reaction is one with respect to each molecule; at high concentrations of A, then $r = kC_S^2 \frac{K_2 C_B}{K_1 C_A}$, and the order

of reaction is one with respect to B, and -1 with respect to A, which is to say A inhibits the reaction.

On the other hand, if one molecule (say A) has a much higher adsorption than the other, then $K_1C_A \gg 1 + K_2C_B; r = kC_S^2 \frac{K_2C_B}{K_1C_A}$, which is the same as the latter case mentioned above. The Langmuir – Hinshelwood can be used to describe reactions such as CO oxidation to form CO_2, CO hydrogenation to form methanol, or ethylene hydrogenation to form ethane.

There are also cases where the second reactant species does not necessarily adsorb on the catalyst surface in order for a reaction to occur. This leads to the Eley – Rideal mechanism, where only one of the reactant species adsorbs on the catalyst surface, and the other reactant species does not. The reaction pathway is then modified from Equation 1-11, Equation 1-12, and Equation 1-13 to Equation 1-17 below.

$$\boldsymbol{A_{(g)} \underset{k_{-1}}{\overset{k_1}{\rightleftharpoons}} A_{(ads)} + B_{(g)} \xrightarrow{k} Product} \qquad \textbf{Equation 1-17}$$

$$\boldsymbol{r = kC_S \frac{K_1C_AC_B}{1+K_1C_A}} \qquad \textbf{Equation 1-18}^{67}$$

The rate equation above suggests that the reaction will always be first order with respect to B, the unadsorbed species, but the order of reaction with respect to A depends on its concentration. At low concentration, $r = kC_S K_1 C_A C_B$, so the order of reaction is one with respect to A as well; at high concentration, $r = kC_s C_B$, making the rate of reaction independent of A. This can be understood as the the catalyst surface is saturated with excess adsorbed reactant species, the RDS then becomes the rate at which it can be reacted and desorbed from the surface. The Eley – Rideal mechanism can be used to describe a series of reactions such as the partial oxidation of ethylene to form ethylene oxide, the water – gas shift reaction of CO_2 and H_2 to form H_2O and CO, and the partial hydrogenation of acetylene to form ethylene.

The above models assume that different surface sites would adsorb different molecules with equal probability, and with the same affinity. For a real catalyst this is of course not true, but this model can lead to a better understanding of the real catalyst system.

1.9 Nanoparticle Synthesis

Particles on the nanoscale (1-100 nm) have interesting properties that deviate from their bulk counterparts. Nanoparticles exhibit modified electronic structures and high surface area to volume ratio. Their physical and electronic properties can easily be tuned, making them ideal candidates for catalysis. Fundamentally, the synthesis of nanoparticles can be divided into two categories: top down, and bottom up synthesis.

Top down synthesis of nanoparticles is where the nanoparticle is formed from a bulk material *via* different synthetic methods, such as milling, exfoliation, and etching. The top down technique often starts off with a solid reagent, and is broken down into nanoparticles. These techniques have been widely employed in the semiconductor industry for the production of silicon nanoparticles, or using electron beam lithography to utilise pattern formations. Graphene was also first isolated using a top down synthesis method, where graphite was cleaved with a micromechanical method, and stabilised using a silica wafer, famously known as the "Scotch tape" technique[68].

On the other hand, bottom up syntheses are usually in either the liquid or gas phase. The main methods include wet-impregnation, sol-gel synthesis, and spray pyrolysis. These methods rely on the initial nucleation of nanoparticle seeds, then the seeds grow and aggregate into nanoparticles of particular sizes.

In a bottom up colloidal synthesis pathway, the first step of nanoparticle synthesis is the nucleation of nanoparticle seeds, or the introduction of seeds from an external source. As the surface particles are less well bound than the particles in the bulk, they have a higher free energy compared to the bulk. This is known as the interfacial free energy of a particle, which will always destabilise the particle with respect to the bulk material. A smaller particle with a higher proportion of surface atoms will therefore have a higher interfacial free energy than a larger particle, and therefore more unstable. In theory,

adding more particles to an existing particle will increase the number of surface atoms, thus further destabilising the particle. This would mean that a particle should dissociate instead of aggregate. However, the decrease in the bulk's energy can overcome the increase in interfacial free energy, making larger particles more stable. The total change in Gibb's free energy, ΔG, can be described as:

$$\Delta \boldsymbol{G} = \frac{\boldsymbol{4}}{\boldsymbol{3}}\boldsymbol{\pi r^3 \Delta G_v} + \boldsymbol{4\pi r^2 \gamma} = -\frac{\boldsymbol{4\pi r^3 kT}}{\boldsymbol{3V}}\ln(\boldsymbol{\sigma}) + \boldsymbol{4\pi r^2 \gamma} \qquad \textbf{Equation 1-19}^{69}$$

Where ΔG_v is the Gibb's energy change per unit volume in the solute, T is the temperature, V is the atomic volume, σ is the saturation ratio, r is the radius of the particle, and γ is the surface energy change per unit area.

Under supersaturation conditions, where σ>1, ΔG will always be negative, meaning particle nucleation and aggregation is always favourable. There is a balance of whether a particle will dissociate or aggregate, known as the critical size, r_c. r_c can be obtained by differentiating Equation 1-19 above to obtain $\frac{d\Delta G}{dr} = 0$:

$$\boldsymbol{r_c} = \frac{\boldsymbol{2\gamma}}{|\boldsymbol{\Delta G_v}|} \qquad \textbf{Equation 1-20}^{69}$$

The Gibb's free energy change can be affected by several factors, including reaction temperature, precursor concentration and surfactant effects. Strongly binding ligands will have a greater effect in stabilising the Gibb's free energy change, and resulting in smaller particles.

Another method of stabilising nanoparticles is to employ a solid support, usually a metal oxide. In this case the nanoparticle is considered to be nucleating on a foreign surface. This can lead to more favourable nanoparticle formation conditions as the interfacial energy between a nanoparticle and the solid support is often lower than that of a nanoparticle and the solvent, thus forming stronger bonds between the nanoparticle and the support.

Consider a nanoparticle with radius r, the change in Gibb's free energy depends on the change in Gibb's free energy of both the bulk (i.e. the support) and the surface atoms (i.e. the nanoparticles), hence:

$$\Delta g = \Delta g_b + \Delta g_s = -\frac{\left(\frac{4}{3}\right)\pi r^3}{\Omega}\Delta\mu + 4\pi r^2\alpha \qquad \text{Equation 1-21}^{69}$$

Where Δg_b and Δg_s are the changes in Gibb's free energy of the bulk and the surface atoms, respectively, Ω is the volume per molecule, Δμ is the change in chemical

potential, α is the interfacial free energy. The two terms counteract each other, creating a free energy barrier as the terms cross-over, shown in Figure 1-16.

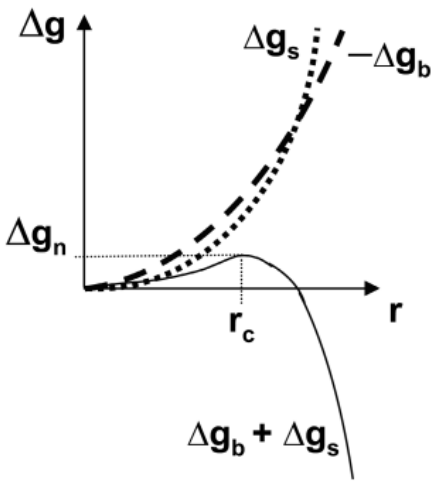

Figure 1-16 The cross-over of Δgb and Δgs to create a free energy barrier[69].

In the case of a supported nanoparticle, the critical radius can be expressed as:

$$r_c = \frac{2\Omega\alpha}{\Delta\mu} = \frac{2\Omega\alpha}{kT\sigma}$$ **Equation 1-22[69]**

Like homogeneous nucleation, heterogeneous nucleation also depends on the supersaturation ratio, where a more supersaturated solution would yield smaller nanoparticles.

1.10 Metal – Support Interaction

As previously discussed, nanoparticles are inherently unstable unless they are attached to a support or a capping agent which is employed in order to lower the surface energy of the nanoparticle. Nanoparticles attached onto the support is immobilised and difficult to aggregate.

Typically, support with a high surface area is employed so that the metal nanoparticles can achieve a higher dispersion. However, for catalysts operating under harsh conditions (i.e. high temperature or high pressure), a more stable support is preferred to ensure minimal catalyst deactivation.

The activity of the catalyst can be greatly enhanced through the interactions between the nanoparticles and the support, whereby the support provides a synergic promotion effect to the nanoparticles. This is known as Strong Metal–Support Interaction (SMSI).

Wu *et al.* demonstrated the potential of SMSI by showing the stabilisation of single Pd atoms adsorbed on a sudo-Fe_2O_3 support for the effective production of methanol[70]. These single Pd adatoms are stable at temperatures up to 200 ^{o}C due to the effects of SMSI.

A second kind of Metal–Support Interaction is known as the Electronic Metal–Support Interaction, where the electron from the metal is able to interact strongly with the support resulting in a modification of the band structure.

Campbell demonstrated that the electronic properties of the metal and the support, particularly the different facets of the metal nanoparticle, have a dramatic effect on the the adsorption of reactants, such as CO, and thus have a dramatic effect on the rate of reaction[71]. Similarly, Acerbi *et al.* demonstrated that different PGM's have different work functions, and therefore their ceria supported catalysts were able to reduce at different temperatures[72].

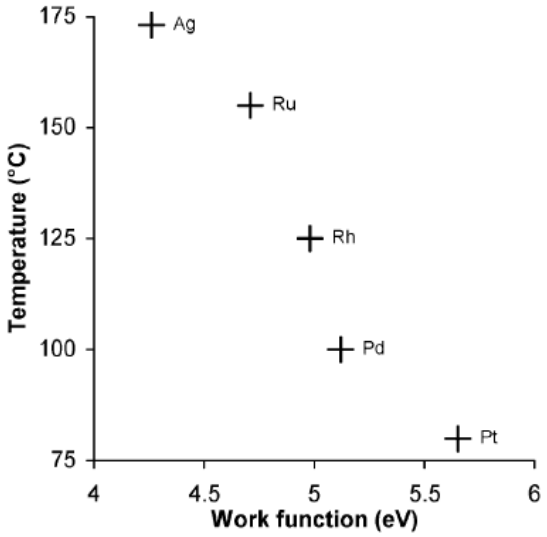

Figure 1-17 Work function of PGM's vs. promoted ceria reduction temperature for silica supported catalysts[72].

By utilising the different metal–support interactions, an effective catalyst with a good control of physical, chemical and electronic properties can be developed.

1.11 Morphology Control of Nanoparticles

As previously discussed, different facets of a nanoparticle show different affinities to reactant particles, thus it is important to control the selective growth of the most reactive face over other faces. Many studies were performed on morphology control of nanoparticles, both the metal, and the support. Various techniques can be employed to achieve effective morphology control, which can be categorised as the control using capping agents, or altering reaction conditions.

For example, Andelman *et al.* showed that the solvent, trioctylamine (TOA), also acted as a ligand which strongly bound to the atoms on the face of the {1 1 -2 0} plane, thus encouraged the preferential growth of the {0 0 2} face to form nanorods. When the solvent was switched to octadecene, only nanospheres were formed[73]. On the other hand, Qian *et al.* exploited the different chemical potentials of the different faces in order to achieve selective growth of $Ln(OH)_3$ nanorods. As OH^- ions are stacked up on the {1 0 0} plane compared to the {1 1 0} plane, it has a higher chemical potential. This enabled the selective growth of nanorods in the {1 0 0} direction by precipitation using NaOH without the use of any surfactants[74].

Similarly, morphology control of PGM nanoparticles can be achieved by the use of surfactants. Yu and Yam showed the use of HTAB for the synthesis of Ag nanocubes with a preferential growth of the {2 0 0} plane. The growth mechanism was similar to those already described above, whereby Br^- selectively bound to the {1 1 0} plane of the Ag nanoparticles, thereby hindering growth in that direction.

1.12 Surface Plasmon Resonance

Surface Plasmon Resonance (SPR) is "a photon-driven coherent oscillation of the surface conduction electrons in a material with negative real and near-zero imaginary dielectric constant"[75]. The surface electron is excited by electromagnetic radiation of specific wavelengths.

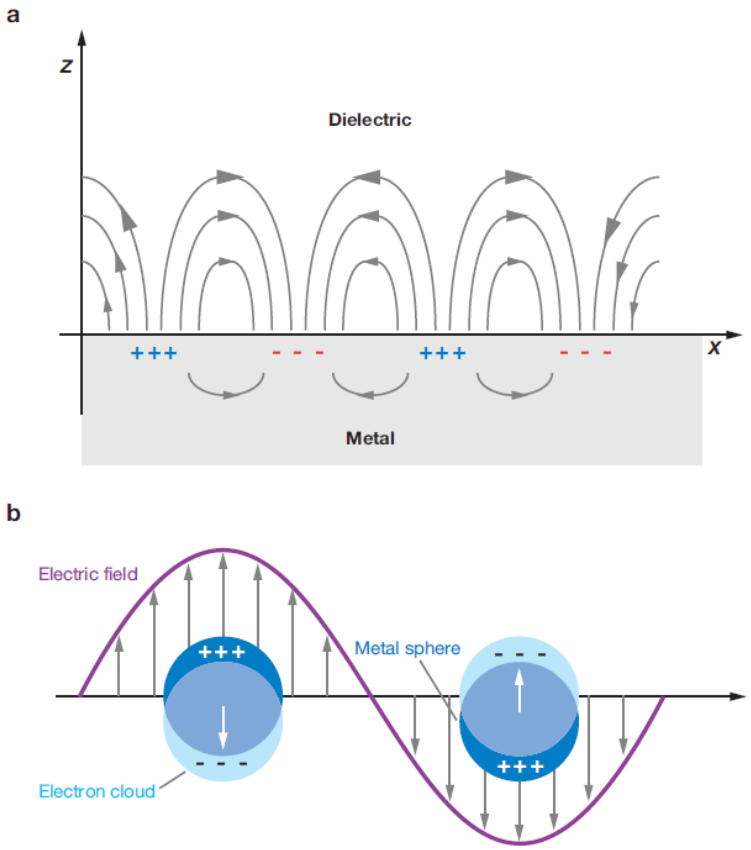

Figure 1-18 Schematic diagrams illustrating a) a surface plasmon polariton, and b) a localised surface plasmon[75].

When the light interacts with particles much smaller than the incident wavelength, the plasmon oscillates locally around the nanoparticles with a frequency known as the localised surface plasmon resonance (LSPR). The electron cloud of the metal counteracts the effects of the polarised electric field to create a localised resonance. Consider a spherical nanoparticle of radius α irradiated by z-polarised light of wavelength λ, and α to be much smaller than λ, then the Maxwell's equations can be solved to give an EM field outside the particle to be:

$$\boldsymbol{E_{out}}\,(\boldsymbol{x},\boldsymbol{y},\boldsymbol{z}) = \boldsymbol{E_0}\hat{\boldsymbol{z}} - \left[\frac{\boldsymbol{\varepsilon_{in}} - \boldsymbol{\varepsilon_{out}}}{\boldsymbol{\varepsilon_{in}} + 2\boldsymbol{\varepsilon_{out}}}\right]\boldsymbol{\alpha^3 E_0}\left[\frac{\hat{\boldsymbol{z}}}{\boldsymbol{r^3}} - \frac{3\boldsymbol{z}}{\boldsymbol{r^5}}(\boldsymbol{x}\hat{\boldsymbol{x}} + \boldsymbol{y}\hat{\boldsymbol{y}} + \boldsymbol{z}\hat{\boldsymbol{z}})\right] \qquad \textbf{Equation 1-23}^{75}$$

Where E_{out} is the extinction coefficient of the external environment, E_0 is the extinction of the metal nanoparticle, ε_{in} is the dielectric constant of the metal nanoparticle, ε_{out} is dielectric constant of the external environment, $\hat{\boldsymbol{x}}$, $\hat{\boldsymbol{y}}$, and $\hat{\boldsymbol{z}}$ are EM radiation polarised in the x, y, and z directions with magnitude x, y, and z, respectively.

ε_{in} is strongly dependent on the incident wavelength, and where ε_{in} is roughly equal to -$2\varepsilon_{out}$, the EM field is enhanced relative to the polarised incident field. The Mie solution to the Maxwell's Equations gives the wavelength of the extinction spectrum of the metal sphere as :

$$\boldsymbol{E(\lambda)} = \frac{\boldsymbol{24\pi^2 N\alpha^3 \varepsilon_{out}^{3/2}}}{\boldsymbol{\lambda \ln(10)}}\left[\frac{\boldsymbol{\varepsilon_i(\lambda)}}{\{\boldsymbol{\varepsilon_r(\lambda)} + \boldsymbol{\chi\varepsilon_{out}}\}^2 + \boldsymbol{\varepsilon_i(\lambda)^2}}\right] \qquad \textbf{Equation 1-24}^{75,76}$$

Where ε_r and ε_i are the real and imaginary components of the metal dielectric function respectively. χ is a factor that is shape dependent, where χ is 2 for a spherical particle, but can be as high as 20 for particles with higher aspect ratios[77]. However, only the χ

values can be measured accurately for a spherical particle, with χ values of other geometries an approximate.

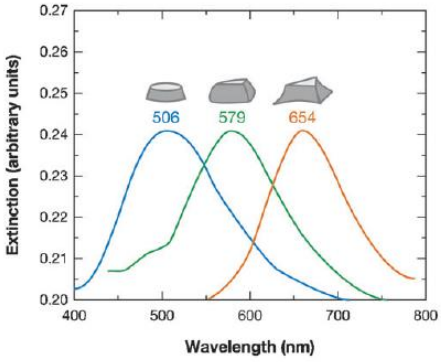

Figure 1-19 LSPR λ_{max} of Ag nanoparticles shifts as the aspect ratio of the particle[75].

Apart from the morphology dependence of SPR, it is also size dependent. The SPR bandwidth increases with decreasing particle size.

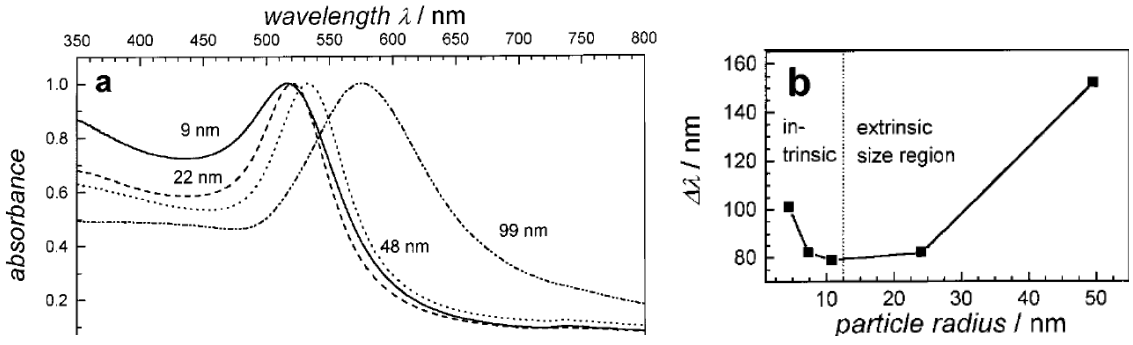

Figure 1-20 a) LSPR λ_{max} of Au nanoparticles of different sizes, where a larger particle size has a higher λ_{max}; b) the bandwidth either increases with decreasing particle size due to intrinsic size regions, or with increasing particle size due to extrinsic size regions[77].

Under irradiation, the electrons of the noble metal oscillate. When combined with a metal oxide support, the electrons accumulate at the interface between the metal and the support, leading to the downward bending of the metal oxide conduction band. The electrons from the metal Fermi level can be depicted as a promotion into a "virtual state" as LSPR, and SPR is the "spillover" of the excited electrons into the metal oxide conduction band. This results in an overall lowering in energy of the metal Fermi Level, and population of the oxide conduction band, as demonstrated in Figure 1-21 below.

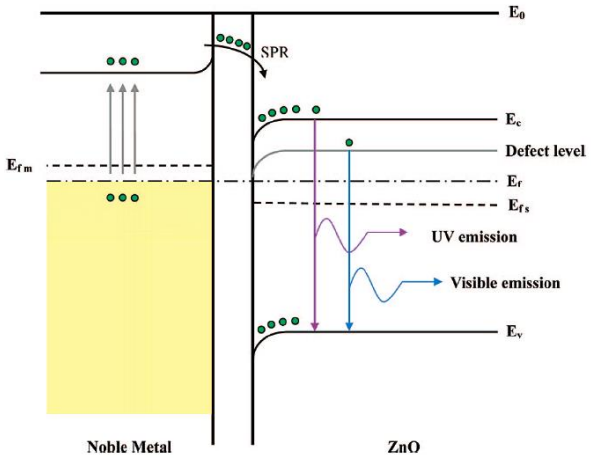

Figure 1-21 Band Structure of plasmonic metal on metal oxide, in this case Au/ZnO[78].

1.13 Metal Oxide Supported Silver Nanoparticles as Soot Combustion Catalyst

Previous studies have shown Ag to be an effective soot combustion catalyst. Various metal oxide supported Ag catalysts have been employed as a soot combustion catalyst, with varying degrees of success. For example, Villani *et al.* have demonstrated the use of a Ag/Al_2O_3 catalyst to lower the combustion temperature of carbon black from 570 ^{o}C to

475 ^{o}C[37]. Guilhaume *et al.* used a Ag/MnO_x catalyst to combust soot at 440 ^{o}C[14]; Aneggi *et al.* employed a variety of Ag/CeO_2 and Ag/ZrO_2 catalysts which burnt soot at temperatures as low as 340 ^{o}C[16]. There are also much research on further additive effects on soot combustion, such as the addition of K and Co to a Ag catalyst for enhanced catalytic activities. Halawy explored the role of K in an oxidation reaction to provide both acid and basic sites on the catalyst surface[79]. It was argued that at high temperature, K exhibits both acidic and basic character, thus creating two new phases on the catalyst surface for reaction.

Apart from soot combustion, Ag has also been widely studied for the partial oxidation of organic compounds, most notably ethylene and propylene. Studies as early as the 1970's have demonstrated the feasibility of Ag as a selective oxidation catalyst, where ethylene oxide has been found to be formed selectively from ethylene[80,81]. It was argued that atmospheric oxygen is able to dissociate to form energetic surface oxygen species, which is weakly bound to the silver surface, and is thus able to selectively form epoxide species over total combustion[80–85]. This mobile active oxygen has also been shown to be an active species in the soot combustion reaction[86]. Pisarello *et al.* combined the ideas of surface oxygen on the silver surface, and the influence of metal–support interaction to propose the interface of the metal and support to be a source of mobile oxygen sites. The nature of the lattice oxygen changes at the interface to

become more energetic, and behaves like electrophilic oxygen species, which can contribute to the soot combustion reaction.

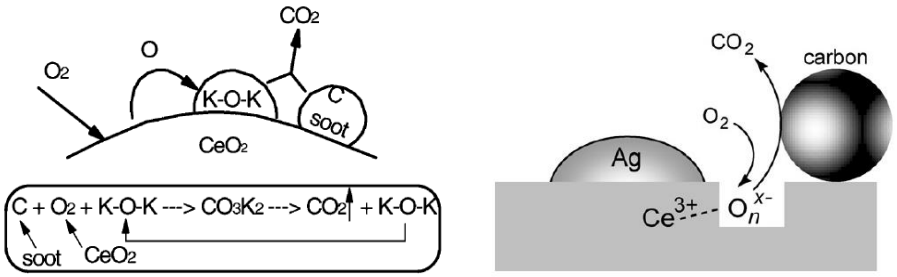

Figure 1-22 Examples of schematic diagrams of oxygen dissociation and migration on a metal oxide support[22,32].

Both Guilhaume *et al.* and Bueno-Lopez *et al.* used labelled oxygen, $^{18}O_2$, for soot combustion. Mass spectrometry was used to identify the species of CO and CO_2 produced. It was found that $C^{16}O_2$ and $C^{16}O$ were the only two species produced with no labelled oxygen incorporated in the carbon oxides[14,87]. This suggests that the oxygen is from the metal oxide support, and atmospheric oxygen is not involved in the initial oxidation of soot.

Goncharova *et al.* also demonstrated the importance of the size of Ag for oxidation reactions. A contrary result has been found comparing with conventional studies, where a small nanoparticle with a higher surface area is more reactive, a larger nanoparticle of 100 nm had a greater turnover frequency than a small particle at 15 nm[88].

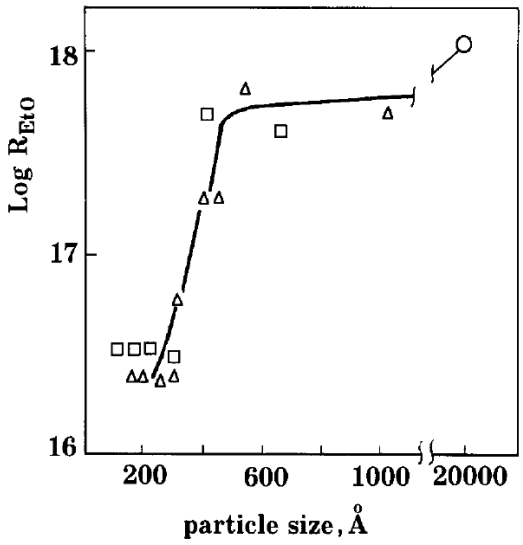

Figure 1-23 Size effect on ethylene oxidation, where triangle is Ag/α-Al_2O_3; square is Ag/SiO_2, and circle is Ag powder[88].

It was argued that the existence of "covalent" or electrophilic oxygen species that are much more active than the ionic oxide of Ag_2O at the surface defect sites are able to form π-complexes with ethylene for selective oxidation of ethylene. This is only possible with larger Ag particles where the interfacial energy is lower, which makes it possible to stabilise such energetic oxygen species. The change in Ag sizes also has an effect on the equilibrium between the bulk and surface metal properties. These effects were shown to be most pronounced in the range of 20 – 100 nm, with diminishing effects at larger sizes[88].

Mills *et al.* has demonstrated the possibility of decomposition of soot *via* a photocatalytic method, albeit extremely slow[89]. A P25 TiO_2 catalyst has been used, with a UV radiation of 365 nm, to completely oxidise soot over a 45 day period. However, little work has been done on catalytic systems utilising SPR excitation of plasmonic metals.

1.14 Aim and Objectives

In this thesis some novel metal supports will be used in conjunction with Ag for the soot combustion reaction. A series of modifications on the catalyst will be carried out in order to investigate each individual effect on soot combustion.

Two main effects that affect soot combustion have been identified, and will be the focus of research in this thesis: size effect of Ag nanoparticles, and metal – support interaction between Ag and the metal oxide support. The influence of the two effects on soot combustion are not well studied, and more importantly, few have reported on the influence of the two effects on each other. This project aims to look into more detail how size effect and metal – support interaction influence soot combustion, and also on each other.

The main objective of this thesis is to identify the main factors that influence and promote the soot combustion reaction. Having a better understanding of these factors, a reaction mechanism and electronic structure of the system can be devised.

1.15 Thesis Overview

This thesis consists of eleven chapters. Chapters four to ten inclusive, detail the research performed during my study for this D.Phil. degree.

Chapter One – introduces the problem caused by soot pollution, the existing technology for soot trapping, and regulations into soot emission. Also the basic theory of catalysis, and details of nanoparticle modification.

Chapter Two – Gives a detailed description of the experimental methods used for the synthesis of the catalysts discussed in this thesis.

Chapter Three – The background and theory of the analytical techniques used to characterise the catalysts used throughout this thesis are given.

Chapter Four – Background characterisation of soot, preliminary testing of industrial catalysts, and optimisation of reaction conditions.

Chapter Five – Screening tests and characterisation of Ag/Ln_2O_3 catalysts, and the factors that affect soot combustion are explored.

Chapter Six – Screening tests and characterisation of Ag/TMO catalysts, and a comparison in activity with lanthanide oxide supported catalysts.

Chapter Seven – Looking in more detail at the effects of Ag particle size and metal – support interaction on soot combustion. The influence of the two effects on each other is also investigated.

Chapter Eight – Looking into the effects of selective growth of nanoparticle facets on soot combustion.

Chapter Nine – Investigating promotional effects of novel doped metal oxides, in particular modification of existing industrial catalysts for enhanced soot combustion performance.

Chapter Ten – Other oxidation reactions, such as photochemical decomposition of soot, and propylene epoxidation, to look at the role of Ag in other reactions than soot combustion.

Chapter Eleven – Conclusions and the future outlook of the work is presented.

1.16 References

1 P. Zelenka, W. Cartellieri and P. Herzog, *Appl. Catal. B-Environmental*, 1996, **10**, 3–28.

2 T. C. Bond, S. J. Doherty, D. W. Fahey, P. M. Forster, T. Berntsen, B. J. DeAngelo, M. G. Flanner, S. Ghan, B. Kärcher, D. Koch, S. Kinne, Y. Kondo, P. K. Quinn, M. C. Sarofim, M. G. Schultz, M. Schulz, C. Venkataraman, H. Zhang, S. Zhang, N. Bellouin, S. K. Guttikunda, P. K. Hopke, M. Z. Jacobson, J. W. Kaiser, Z. Klimont, U. Lohmann, J. P. Schwarz, D. Shindell, T. Storelvmo, S. G. Warren and C. S. Zender, *J. Geophys. Res. Atmos.*, 2013, **118**, 5380–5552.

3 Air Quality Expert Group, *http://uk-air.defra.gov.uk/assets/documents/reports/cat11/1212141150_AQEG_Fine_Particulate_Matter_in_the_UK.pdf*, 2012, 1–191.

4 Official Journal of the European Union, *http://eur-lex.europa.eu/LexUriServ/LexUriServ.do?uri=OJ:L:2007:171:0001:0016:EN:PDF*, 2007.

5 *http://delphi.com/pdf/emissions/delphi-worldwide-emissions-standards-hd-ohv-2014-15.pdf*.

6 Volkswagen, *http://www.volkspage.net/technik/ssp/ssp/SSP_230.pdf*, .

7 R. J. Farrauto and R. M. Heck, *Catal. Today*, 1999, **51**, 351–360.

8 Johnson Matthey, *http://www.dieselnet.com/jm/sec_crt.pdf*.

9 G. A. Stratakis and A. M. Stamatelos, *Combust. Flame*, 2003, **132**, 157–169.

10 A. Raj, S. Y. Yang, D. Cha, R. Tayouo and S. H. Chung, *Combust. Flame*, **160**, 1812–1826.

11 G. Neri, L. Bonaccorsi, A. Donato, C. Milone, M. G. Musolino, A. M. Visco, M. Grazia and A. Maria, *Appl. Catal. B-Environmental*, 1997, **11**, 217–231.

12 S. Vaccaro, P. Ciambelli, P. Corbo, M. Gambino and V. Palma, *Catal. Today*, 1996, **27**, 99–106.

13 J. P. A. Neeft, M. Makkee and J. A. Moulijn, *Appl. Catal. B-Environmental*, 1996, **8**, 57–78.

14 N. Guilhaume, B. Bassou, G. Bergeret, D. Bianchi, F. Bosselet, B. Jouguet, C. Mirodatos and A. Desmartin-Chomel, *Appl. Catal. B Environ.*, 2012, **119-120**, 287–296.

15 E. Aneggi, C. de Leitenburg, G. Dolcetti and A. Trovarelli, *Catal. Today*, 2006, **114**, 40–47.

16 E. Aneggi, J. Llorca, C. de Leitenburg, G. Dolcetti, A. Trovarelli, C. De Leitenburg and O. Ag, *Appl. Catal. B-Environmental*, 2009, **91**, 489–498.

17 M. Dhakad, T. Mitshuhashi, S. Rayalu, P. Doggali, S. Bakardjiva, J. Subrt, D. Fino, H. Haneda and N. Labhsetwar, *Catal. Today*, 2008, **132**, 188–193.

18 C. Badini, V. Serra, G. Saracco and M. Montorsi, *Catal. Letters*, 1996, **37**, 247–254.

19 N. Gungor, S. Isci, E. Gunister, W. Mista, H. Teterycz, R. Klimkiewicz, N. Güngör, I. Sevim and E. Günister, *Appl. Clay Sci.*, 2006, **32**, 291–296.

20 X. D. Wu, D. X. Liu, K. Li, J. Li, D. Weng, F. Lin and H. B. Xu, *Appl. Catal. B-Environmental*, 2007, **8**, 1274–1278.

21 M. A. Peralta, M. S. Zanuttini, M. A. Ulla and C. A. Querini, *Appl. Catal. a-General*, 2011, **399**, 161–171.

22 M. L. Pisarello, V. Milt, M. A. Peralta, C. A. Querini and E. E. Miro, *Catal. Today*, 2002, **75**, 465–470.

23 D. Fino, N. Russo, C. Badini, G. Saracco and V. Specchia, *Aiche J.*, 2003, **49**, 2173–2180.

24 C. Badini, G. Saracco, N. Russo and V. Specchia, *Catal. Letters*, 2000, **69**, 207–215.

25 D. Uner, M. K. Demirkol and B. Dernaika, *Appl. Catal. B-Environmental*, 2005, **61**, 334–345.

26 H. Shimokawa, Y. Kurihara, H. Kusaba, H. Einaga and Y. Teraoka, *Catal. Today*, 2012, **185**, 99–103.

27 B. Bassou, N. Guilhaume, E. E. Iojoiu, D. Farrusseng, K. Lombaert, D. Bianchi and C. Mirodatos, *Catal. Today*, 2011, **159**, 138–143.

28 E. E. Miro, F. Ravelli, M. A. Ulla, L. M. Cornaglia, C. A. Querini and E. E. Miró, *Catal. Today*, 1999, **53**, 631–638.

29 B. Bialobok, J. Trawczynski, T. Rzadki, W. Mista and M. Zawadzki, *Catal. Today*, 2007, **119**, 278–285.

30 P. G. Harrison, I. K. Ball, W. Daniell, P. Lukinskas, M. Cespedes, E. E. Miro and M. A. Ulla, *Chem. Eng. J.*, 2003, **95**, 47–55.

31 K. Shimizu, A. Satsuma and T. Hattori, *Appl. Catal. B-Environmental*, 2000, **25**, 239–247.

32 K. Shimizu, H. Kawachi and A. Satsuma, *Appl. Catal. B-Environmental*, 2010, **96**, 169–175.

33 B. A. A. L. van Setten, J. M. Schouten, M. Makkee, J. A. Moulijn and B. A. A. L. Van Setten, *Appl. Catal. B-Environmental*, 2000, **28**, 253–257.

34 C. B. Lim, H. Kusaba, H. Einaga and Y. Teraoka, *Catal. Today*, 2011, **175**, 106–111.

35 V. G. Milt, C. A. Querini and E. E. Miro, *Thermochim. Acta*, 2003, **404**, 177–186.

36 J. P. A. Neeft, T. X. Nijhuis, E. Smakman, M. Makkee and J. A. Moulijn, *Fuel*, 1997, **76**, 1129–1136.

37 K. Villani, R. Brosius and J. A. Martens, *J. Catal.*, 2005, **236**, 172–175.

38 P. Ciambelli, P. Corbo, P. Parrella, M. Scialo and S. Vaccaro, *Thermochim. Acta*, 1990, **162**, 83–89.

39 W. Choi, *Catal. Surv. from Asia*, 2006, **10**, 16–28.

40 J. C. Summers, S. VanHoutte and D. Psaras, *Appl. Catal. B-Environmental*, 1996, **10**, 139–156.

41 P. W. Park and C. L. Boyer, *Appl. Catal. B-Environmental*, 2005, **59**, 27–34.

42 L. E. Lindfors, K. Eranen, F. Klingstedt and D. Y. Murzin, *Top. Catal.*, 2004, **28**, 185–189.

43 I. Atribak, I. Such-Basaniez, A. Bueno-Lopez and A. Garcia-Garcia, *J. Catal.*, 2007, **250**, 75–84.

44 V. G. Milt, M. L. Pissarello, E. E. Miro and C. A. Querini, *Appl. Catal. B-Environmental*, 2003, **41**, 397–414.

45 I. Atribak, A. Bueno-Lopez and A. Garcia-Garcia, *J. Catal.*, 2008, **259**, 123–132.

46 B. A. A. L. van Setten, M. Makkee and J. A. Moulijn, *Catal. Rev. Eng.*, 2001, **43**, 489–564.

47 K. Masuda, K. Tsujimura, K. Shinoda and T. Kato, *Appl. Catal. B-Environmental*, 1996, **8**, 33–40.

48 L. Zhu, J. J. Yu and X. Z. Wang, *J. Hazard. Mater.*, 2007, **140**, 205–210.

49 J. P. A. Neeft, M. Makkee and J. A. Moulijn, *Chem. Eng. J.*, 1996, **64**, 295–302.

50 W. Dabelstein, A. Reglitzky, A. Schutze and K. Reders, *Ullmann's Encyclopedia of Industrial Chemistry*, Wiley-VCH Verlag GmbH & Co. KGaA, Weinheim, Germany, 2007.

51 *http://www.ict4us.com/r.kuijt/en_strokeengine.htm*.

52 542846, *United States Pat.*, 1895.

53 European Committee for Standardisation, *EN 590*, 2003.

54 *Off. J. Eur. Union*, 2007.

55 Swedish Environmental Research Institute, 2014.

56 *http://www.ipcc.ch/pdf/assessment-report/ar4/wg1/ar4-wg1-chapter2.pdf*.

57 *http://www.elements-srm.com.au/what-is-climate-change-and-global-warming/*.

58 Volkswagen, *Motor Vehicle Exhaust Emissions*, .

59 J. Kaspar, P. Fornasiero, N. Hickey and J. Kašpar, *Catal. Today*, 2003, **77**, 419–449.

60 Johnson Matthey, *Johnson Matthey CRT Particulate Filter System*, .

61 R. H. Grubbs, *Handbook of Metathesis*, 2003.

62 G. Ertl, *J. Vac. Sci. Technol. A Vacuum, Surfaces, Film.*, 1983, **1**, 1247–1253.

63 *http://driverlayer.com/showimg?v=g&img=https://lh3.googleusercontent.com/-2G6QrkJZwXw/TW1IOhY34PI/AAAAAAAAADU/sSV2_e7ag8o/s1600/maxwel2.gif.jpg&org=http://driverlayer.com/img/boltzmann%20distribution/20/image?tab=1*.

64 J. M. Thomas and W. J. Thomas, *Principles and Practice of Heterogeneous Catalysis*, 1996.

65 W. J. M. Rootsaert and W. M. H. Sachtler, *Zeitschrift für Phys. Chemie*, 1960, **26**, 16–26.

66 I. Langmuir, *J. Am. Chem. Soc.*, 1916, **11**, 2221–2295.

67 G. W. Roberts and C. N. Satterfield, *Ind. Eng. Chem. Fundam.*, 1965, **3**, 288–293.

68 7071258, 2006, 1.

69 J. J. De Yoreo and P. G. Vekilov, in *Principles of Crystal Nucleation and Growth*, 2003, pp. 57–93.

70 C.-T. Wu, K. M. K. Yu, F. Liao, N. Young, P. Nellist, A. Dent, A. Kroner and S. C. E. Tsang, *Nat. Commun.*, 2012, **3**, 1050.

71 C. T. Campbell, *Nat. Chem.*, 2012, **4**, 597–8.

72 N. Acerbi, S. C. Tsang, S. Golunski and P. Collier, *Chem. Commun.*, 2008, 1578–80.

73 T. Andelman, Y. Y. Gong, M. Polking, M. Yin, I. Kuskovsky, G. Neumark and S. O'Brien, *J. Phys. Chem. B*, 2005, **109**, 14314–14318.

74 L. W. Qian, Y. C. Gui, S. A. Guo, G. Qiang, X. F. Qian and Q. Gong, *J. Phys. Chem. Solids*, 2009, **70**, 688–693.

75 K. A. Willets and R. P. Van Duyne, *Annu. Rev. Phys. Chem.*, 2007, **58**, 267–297.

76 G. Mie, *Annu. Phys.*, 1908, **25**, 377–445.

77 S. Link and M. A. El-Sayed, *J. Phys. Chem.*, 1999, **103**, 8410–8426.

78 M. K. Lee, T. G. Kim, W. Kim and Y. M. Sung, *J. Phys. Chem. C*, 2008, **112**, 10079–10082.

79 S. A. Halawy, *Monatshefte fur Chemie / Chem. Mon.*, 2003, **134**, 371–380.

80 R. E. Kenson and M. Lapkin, *J. Phys. Chem. B*, 1970, **74**, 1493–1502.

81 E. L. Force and A. T. Bell, *J. Catal.*, 1975, **371**, 356–371.

82 X. E. Verykios, F. P. Stein and R. W. Coughlin, *Catal. Rev.*, 2006, **22**, 197–234.

83 P. a. Kilty and W. M. H. Sachtler, *Catal. Rev.*, 2006, **10**, 1–16.

84 R. A. van Santen and C. P. M. de Groot, *J. Catal.*, 1986, **539**, 530–539.

85 R. B. Grant and R. M. Lambert, *J. Catal.*, 1985, **375**, 364–375.

86 E. Aneggi, C. de Leitenburg and A. Trovarelli, *Catal. Today*, 2012, **181**, 108–115.

87 A. Bueno-Lopez, K. Krishna, M. Makkee and J. A. Moulijn, *J. Catal.*, 2005, **230**, 237–248.

88 S. N. Goncharova, E. A. Paukshtis and B. S. Bal'zhinimaev, *Appl. Catal. a-General*, 1995, 67–84.

89 A. Mills, J. S. Wang and M. Crow, *Chemosphere*, 2006, **64**, 1032–1035.

Contents

Chapter 2. Synthetic Method

2.1 Materials

$AgNO_3$ (99+%), La_2O_3 (99.99%), CeO_2 (99.9%), Pr_6O_{11} (99.9%), Nd_2O_3 (99.9%), Sm_2O_3 (99.9%), Eu_2O_3 (99.9%), Gd_2O_3 (99.9%), Ho_2O_3 (99.9%), Tm_2O_3 (99.9%), Yb_2O_3 (99.9%), Lu_2O_3 (99.9%), TiO_2 (99%), Cr_2O_3 (99%), Fe_3O_4 (99%), CoO(99%), NiO (99%), CuO (99%), ZnO (99%), Al_2O_3 (acidic), Al_2O_3 (neutral), Al_2O_3 (basic), SiO_2 (99.5%), $La(NO_3)_3$ (99.99%), $Ce(NO_3)_3$ (99.99%), $Nd(NO_3)_3$ (99.99%), $Eu(NO_3)_3$ (99.99%), $Gd(NO_3)_3$ (99.99%), $Ho(NO_3)_3$ (99.99%), $Yb(NO_3)_3$ (99.99%), ethylene glycol (EG, 99.8%), ethanol (EtOH, 99.5%), diethylene glycol (99%), triethylene glycol (99%), Na_2CO_3 (99%), Polyvinylpyrrolidone (PVP, MW=40k), NaOH (98%), $Zn(OAc)_2$ (98%), oleic acid (OA, 99%), trioctylamine (TOA, 70%), C_{60} (99.5%) were obtained from Sigma-Alrich, and used without modifications.

$AuCl_3$ (99.99%) was obtained from Alfa Aesar, and used without modifications.

ex-CRT Soot, *ex*-ET Soot, 2% Ag/Al_2O_3, 8% Ag/Al_2O_3 were obtained from Johnson Matthey, and used without further modifications.

Norit Carbon and Carbon Black were obtained from members of the Tsang Group, and used without further modifications.

2.2 Ag/MO Nanoparticle Synthesis

The wet-impregnation of Ag nanoparticles on metal oxide supports was based on that described by Sun *et al.*[1], where 500 mg of metal oxide was dispersed in 50 mL ethylene glycol, and 78.75 mg (10% wt) $AgNO_3$ was dissolved in the suspension. The suspension was heated to 160 ^{o}C for 1 hr under stirring. The colour of the suspension turned black, indicating the formation of Ag nanoparticles. The suspension was cooled after 1 hr, then filtered, washed with H_2O and EtOH, and dried at 100 ^{o}C overnight. Samples were calcined at 600 ^{o}C for 2 hr to simulate aging.

The production of Au nanoparticles was the same, except $AuCl_3$ was used in place of $AgNO_3$. The colour of the suspension turned purple indicating the formation of Au nanoparticles.

2.3 Modified Ag/MO Nanoparticle Synthesis

The modified Ag/MO nanoparticle synthesis was also based on that described by Zhao *et al.*[2], where an appropriate amount of PVP was dissolved in 10 mL ethylene glycol, and heated to 160 ^{o}C under stirring to give a light yellow solution. 170 mg of $AgNO_3$ dissolved in 10 mL EG was then added into the PVP solution at 3.75 mL min^{-1} using a syringe pump. The reaction was allowed to proceed for a further 4 hr at 160 ^{o}C, where a brown colloidal suspension was formed. The resulting colloidal dispersion was cooled to room temperature and precipitated by adding 10 times excess EtOH. The precipitate

was collected by centrifugation at 8000 rpm for 30 min, and washed 4 more times using EtOH, then finally dispersed in 30 mL of H_2O.

300 mg of metal oxide was then heated to 90 ^oC in a 10 mL beaker, and 5.3 mL of the pre-made Ag colloidal solution was added dropwise on to the oxide whilst under stirring. The mixture was heated for a further 3 hr, then dried in the oven at 120 ^oC for 24 hr.

2.4 Sol-gel Synthesis of Metal Oxide

The sol-gel method has been proposed in several journals[3-5], where $M(NO_3)_x$ (x = 2, 3) was dissolved in 500 mL H_2O, and Na_2CO_3 was added at a rate of 10 mL min^{-1} using a syringe pump until the pH of the solution reached 10. The metal nitrate would precipitate upon addition of Na_2CO_3, and the precipitate was allowed to age under stirring for 24 hr, then filtered, washed and dried in the oven as described above.

$AgNO_3$ could be dissolved in H_2O with $M(NO_3)_x$ as a co-sol-gel product, or it could be loaded on using the wet-impregnation method as described in Chapter 2.2 above.

2.5 ZnO Nanorod and Nanoplate Synthesis

The synthesis of ZnO nanorods and nanoplates was based on that described by Mclaren *et al.*[6], where $Zn(OAc)_2$ was capped by oleic acid (OA) with trioctylamine (TOA) as a solvent. The mixture in their appropriate quantities were heated to 290 ^{o}C for up to 4 hr, where a white suspension was formed. The suspension was isolated by centrifugation at 9000 rpm for 10 min, then washed with 20 mL of EtOH 5 times.

2.6 Nd_2O_3 Nanorod Synthesis

The synthesis of Nd_2O_3 nanorods was based on a modified method that described by Zhang *et al.*[7], where $Nd(NO_3)_3$ and NaOH were dissolved in 150 ml and 10 ml H_2O respectively, then the NaOH solution was added to the $Nd(NO_3)_3$ solution rapidly whilst under stirring. The resultant precipitate was stirred and aged for 24 hr, and isolated by centrifugation as described above.

2.7 References

1. J. M. Sun, D. Ma, H. Zhang, X. M. Liu, X. W. Han, X. H. Bao, G. Weinberg, N. Pfander and D. S. Su, *Journal of the American Chemical Society*, 2006, **128**, 15756-15764.
2. T. Zhao, R. Sun, S. H. Yu, Z. J. Zhang, L. M. Zhou, H. T. Huang and R. X. Du, *Colloids and Surfaces a-Physicochemical and Engineering Aspects*, 2010, **366**, 197-202.
3. X. G. Wang, M. L. Wang, H. Song and B. J. Ding, *Materials Letters*, 2006, **60**, 2261-2265.
4. Y. S. Chang, Y. H. Chang, I. G. Chen, G. J. Chen and Y. L. Chai, *Journal of Crystal Growth*, 2002, **243**, 319-326.
5. A. Garcia-Murillo, C. Le Luyer, C. Pedrini and J. Mugnier, *Journal of Alloys and Compounds*, 2001, **323**, 74-77.
6. A. Mclaren, T. Valdes-Solis, G. Q. Li and S. C. Tsang, *Journal of the American Chemical Society*, 2009, **131**, 12540-+.
7. N. Zhang, R. Yi, L. B. Zhou, G. H. Gao, R. R. Shi, G. Z. Qiu and X. H. Liu, *Materials Chemistry and Physics*, 2009, **114**, 160-167.

Contents

Chapter 3. Experimental Techniques

3.1 Powder X-Ray Diffraction (XRD)

XRD is a simple and accurate technique to investigate the structure of a material at the atomic level. When X-ray is irradiated onto the sample, the radiation is scattered by individual layers of atoms to form scattering waves.

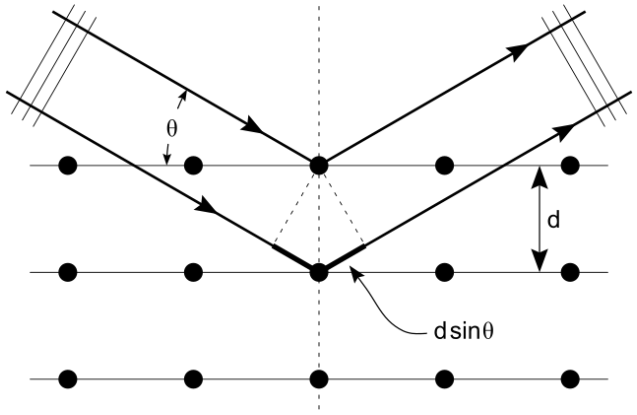

Figure 3-1 X-ray diffracted by layers of atoms. Only X-rays that are in phase after diffraction will add constructively to give a peak in the XRD profile[1].

Typically, a Cu cathode is used in the XRD for X-ray generation. The X-ray is generated by the relaxation of higher–shell electrons to the K-shell (1s). If the electron is from the 2p orbital, then the X-ray generated is known as K_α radiation; K_β from the 3p orbital, etc. K_α and K_β radiations can be separated easily as they have a large difference in energy.

However, due to spin-orbit coupling, K_α radiation is further split into $K_{\alpha1}$ an $K_{\alpha2}$ radiations from $2p_{3/2}$ and $2p_{1/2}$ shells respectively. These two admissions cannot be

effectively separated with an energy filter, and could only be separated using computer algorithms.

The diffracted X-rays would interfere with each other, either constructively or destructively depending on the phase difference of the scattered X-ray. Constructive interference would add to build up a stronger X-ray signal, whereas destructive interference would lead to cancellation of the X-rays. These interferences in turn produce a pattern according to Bragg's law,

$$n\lambda = 2d \sin\theta \qquad \text{Equation 3-1}$$

Where n is any positive integer (normally taken as 1), λ is the wavelength of the monochromatic X-ray beam, d the inter-planar spacing between crystal planes, and θ the monochromatic incident angle of the X-ray beam.

As nanoparticles are not perfectly crystalline, the grain boundaries of the nanoparticles would cause the X-ray to scatter, leading to line broadening of the diffraction pattern. This phenomenon can be described by the Scherrer Equation,

$$\tau = \frac{K\lambda}{\beta cos\theta}$$ Equation 3-2[2]

Where τ is the mean crystal domain, K is the form factor (typically 0.9 for a cubic system), λ is the wavelength of the monochromatic X-ray beam, β is the line broadening at full width half maximum, and θ is the Bragg angle as described above. This equation typically applies to nanoparticles under 100 nm, and it describes the lower boundary of the nanoparticle size distribution.

XRD data was obtained using a Phillips PW 1710 diffractometer, using $Cu_{K\alpha}$ radiation (λ = 1.5406 Å). The sample was placed on an aluminium plate with a depression for the sample, and compressed with a glass slide to ensure a tight packing and smooth surface. The sample was scanned from 10^{o} to 70^{o} at a scan rate of about 2^{o} min^{-1}.

3.2 *In situ* High Temperature X-Ray Diffraction (*In situ* XRD)

Like XRD, *in situ* XRD operates using the same principle where an XRD profile is obtained by the constructive interference of scattered X-rays by the layers of atoms in the crystal structure. *In situ* XRD differs with conventional XRD in that the sample could be heated in a sealed compartment whilst an XRD profile is being obtained, recreating conditions much more similar to actual reaction conditions. It can also provide a much clearer picture to how a material behaves upon heating, and when potential phase changes may occur.

In situ XRD was obtained using a Siemens D5000 diffractometer *in situ* X-ray diffractometer. The sample was placed onto a circular PTFE sample holder, and packed using a glass slide. The sample was scanned from 10^{o} to 90^{o} at a scan rate of about 1.5^{o} min^{-1}, up to 600 ^{o}C at a heating rate of about 1 K min^{-1}.

3.3 Thermogravimetric Analysis (TGA)

TGA is an extremely useful technique where the weight of a sample is measured against temperature, or time, which shows the material's characteristics such as oxidation, reduction, or decomposition which would lead to any weight change.

TGA was performed on the TA Instruments TGA Q50. The sample was placed in a Pt sample pan, which was then loaded onto the TGA via a hang down wire. The sample was then heated to 700 ^{o}C at a heating rate of 10 K min^{-1}. Either air or N_2 was used for TGA, with a flow rate at 60 mL min^{-1}. The derivative thermogravimetric (DTG) profile of weight loss against temperature was used for analysis.

The exhaust gases of the TGA could be further analysed by couplingwith a Mass Spectrometer.

3.4 Simultaneous Differential Scanning Calorimetry – Thermogravimetric Analysis (SDT)

SDT is a technique where Differential Scanning Calorimetry (DSC) and TGA could be performed simultaneously. DSC is a thermoanalytical technique where the amount of energy required to increase the temperature of a material is measured against a known reference. As the heat flow is calibrated against the reference, and it has a defined heat capacity in the given temperature range, any heat flow discrepancy between the sample and the reference can be easily recorded.

DSC is especially useful for materials that undergo phase changes without any weight changes, such as melting or glass temperature transitions.

SDT was performed on the TA Instruments SDT Q600. The sample was placed in an alumina ceramic crucible, and placed onto one of the sample arms of the SDT. An empty alumina ceramic crucible was placed on the other sample arm as a reference. The sample was heated to 700 ^{o}C at a heating rate of 10 K min^{-1}. Either air or N_2 was used for SDT, with a flow rate of 100 mL min^{-1}. Similar to the TGA, a DTG profile was obtained for further analysis. A heat flow profile was also obtained for analysis.

3.5 Temperature Controlled Reduction/Oxidation (TPR/O)

TPR/O is a technique which investigates the most efficient reduction or oxidation conditions of a material. It measures the electrical conductivity of either hydrogen or oxygen against temperature, and if either hydrogen or oxygen is consumed in the reduction/oxidation process, a change in electrical conductivity would be registered.

TPR/O was performed on the CE Instruments TPDRO 1100. About 20 mg of sample was placed in a quartz inner tube with quartz wool holding the sample in place. The inner tube was then placed in a quartz outer tube, where a thermocouple was inserted into the inner tube for more accurate temperature readings. The tubes were then placed in a temperature programmed oven, where it was heated to 150 ^{o}C in He to purge any air or volatile organic compounds from the system. The sample was then placed into a different temperature controlled oven, where it was heated to 600 ^{o}C in either 5% H_2/He or 5% O_2/He at a heating rate of 5 K min^{-1}.

3.6 X-Ray Photoelectron Spectroscopy (XPS)

XPS is a surface technique that gives a wide range of information, such as chemical state, empirical formula, elemental composition and electronic state of individual elements within the sample. The X-ray beam ionises the top few layers of the sample, and the resultant kinetic energy of the electron given off is measured. The binding energy of an electron within an atom can be calculated using the equation below,

$$E_{binding} = E_{photon} - (E_{kinetic} + \phi)$$ **Equation 3-3**

Where $E_{binding}$ is the binding energy (BE) of the electron in an atom of the sample, E_{photon} is the incident energy of the X-ray beam, $E_{kinetic}$ is the resultant kinetic energy of the electron ionised by the X-ray, and ϕ is an arbitrary correction factor unique to the instrument.

As the orbital energies of each element are unique to their electronic configuration, the BE recorded by XPS will be specific to individual elements by an excitation from a specific energy level. The difference in chemical environments in the sample, such as changes in adjacent atomic environments, or electronic interactions with neighbouring atoms, can cause subtle changes to the binding energy of an electron. Therefore, by studying the energy shift of one spectral line with respect to others, a detailed surface chemical environment can be elucidated.

The oxidation state of an element also plays a vital part in determining the BE of the electrons. As the amount of shielding decreases or increases upon oxidation or reduction, an upshift or downshift in BE can be observed respectively. Therefore the spectral shifts not only provide an indication of the electronic environments of an element, but the oxidation state as well. The same is true for elements in an electron withdrawing or donating environment, where it is effectively being partially oxidised or

reduced, changing the BE of its electrons. Coupling the electronic and chemical information obtained from XPS gives a much more complete picture of the nature of the nanoparticle surface.

XPS data were obtained by Dr. David Morgan of Cardiff University. BE's were calibrated using C 1s orbital energy at 284.8 eV as charge reference.

3.7 Transmission Electron Microscopy (TEM)

TEM works on a similar principle as conventional optical microscopy. Compared to the wavelength of visible light, electrons have a much smaller deBroglie wavelength, which means electron microscopy is able to achieve a much higher resolution than conventional optical microscopy, down to the scale of 0.1 nm.

A focused beam of electrons is accelerated and transmitted through a very thin layer of sample. The collisions between the electrons and the sample atoms change the direction of the beam, resulting in a solid angle scattering. This scattering can be captured as an image on a fluorescent screen and recorded by a charged-coupled device camera.

The intensity of electron beam interaction with the sample depends on the atomic number of the sample, where an atom with a higher atomic number interacts with the electron beam more strongly, creating a darker area in the image. The areas where no sample is present is left unchanged, and appears bright. Hence this technique is known as light field TEM.

The limit to the resolution of any form of microscopy is the wavelength of light used, therefore there is no theoretical limit to the resolution of TEM, as the wavelength of an electron can be reduced indefinitely, creating higher resolution images. However, according to the Planck equation,

$$E = hv \qquad \textbf{Equation 3-4}$$

Where E is the energy of the photon, h is Planck's constant, and v is the frequency of the photon. A lower wavelength, therefore a higher frequency electron beam would result in a higher energy, potentially leading to degradation of the TEM sample. Therefore whilst there is no theoretical limit to the resolution of TEM, there is a practical limitation where the electron beam becomes too powerful to be used.

TEM images were obtained using a TEM JOEL 2010 operating at 200 kV. Samples were prepared by first dispersing and sonicating in EtOH for 30 min, then a drop of the suspension added onto a holey carbon-coated 400 mesh nickel TEM grid.

3.8 Energy Dispersive X-Ray Spectroscopy (EDX)

EDX is a powerful tool for elemental analysis used in tandem with TEM. A high energy X-ray beam is used to bombard and ionise an electron from the core shell of the sample, creating a hole. The hole is then filled by an electron from one of the outer shells. The energy is released in the form of a photon. By measuring the number of these photons, the elemental information and composition of the sample can be determined.

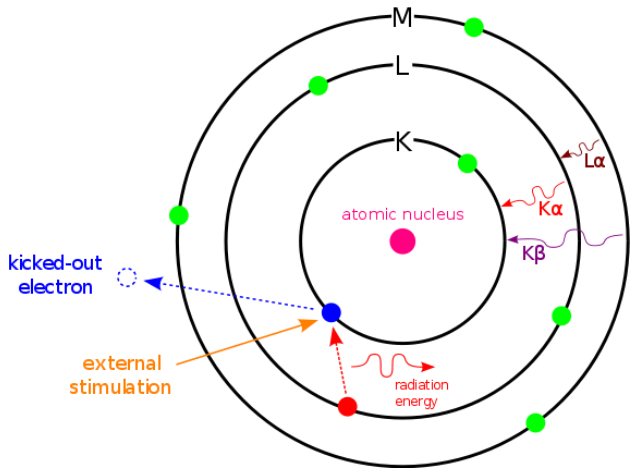

Figure 3-2 Principles of EDX, where an outer shell electron fills a hole created by an ionised core electron, releasing a photon[3].

Elemental compositions and elemental mapping of the sample were performed by EDX attached to the TEM.

3.9 Ultraviolet/Visible (UV-VIS) Spectroscopy

UV-VIS Spectroscopy is a powerful technique that gives vital information about a sample's optical properties. A range of electromagnetic radiation from the UV to near-infrared (NIR) is used to scan the sample. As the sample is excited electronically from its ground state, it absorbs light at a certain wavelength. This absorption results in a peak in the absorption spectrum.

This technique is especially useful in determining the surface plasmon resonance (SPR) of a material, where electrons on a plasmonic metal line up when irradiated with a photon of specific wavelength.

US-VIS spectra were obtained using the Perkin Elmer Lambda 750S spectrometer. 4 mg sample was mixed and milled with 500 mg KBr, which was then pressed into a pellet at a pressure of up to 10 ton. The pellet was placed in a custom made sample holder, which was placed in the integrating sphere of the spectrometer in order to obtain a spectrum. A spectrum from 800 nm to 200 nm with a scanning interval of 0.5 nm was obtained. Pure KBr was used as a reference.

3.10 Attenuated Total Reflectance Fourier Transform Infrared Spectroscopy (ATR FT-IR)

Infrared (IR) spectroscopy is a useful technique in knowing the functional groups present in an organic molecule. As certain band excitation modes are IR active, they absorb IR radiation at a certain frequency to give absorption peaks in the spectrum.

IR active molecule possesses a dipole moment. This means that the selection rule for IR spectroscopy is $\Delta v = \pm 1$. For an asymmetric molecule, such as H_2O, which possess a dipole moment, all vibration modes are IR active; for a symmetric molecule, such as CO_2, the irreducible representation of the stretching modes have to correspond to the x, y, or z axes in order for that mode to be IR active.

Attenuated Total Reflectance (ATR) is a technique that uses total internal reflectance to increase the contact surface of the IR beam and the sample.

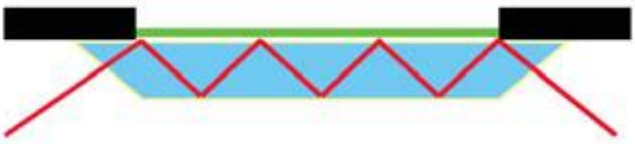

Figure 3-3 Principles of ATR, where the IR beam is reflected internally within a diamond cell, increasing the contact surface with the sample, and therefore giving a better signal[4].

Liquid nitrogen is used to cool the detector of the IR spectrometer, which minimises vibrations from the detector and the ambient environment, further enhancing the signal-to-noise ratio.

IR spectrum was obtained using the Thermo Scientific Nicolet 6700 FT-IR spectrometer. Liquid nitrogen was added to cool the detector compartment for 30 min before the IR beam was aligned for the best signal.

Formic acid was used as a probe molecule for IR spectroscopy, where formic acid was added to the sample, and left overnight for complete adsorption of formic acid onto the sample. The sample was then filtered, and placed on the diamond cell window of the IR spectrometer. It was then dried using an atmosphere of nitrogen to ensure all unadsorbed formic acid was evaporated. A spectrum between 3500 cm^{-1} to 800 cm^{-1} was obtained at a sampling interval of 1 cm^{-1}. The cell window was then cleaned with isopropyl alcohol (IPA) and fully dried before the next spectrum was taken.

3.11 Mass Spectrometry (MS)

MS is an analytical technique that measures the mass-to-charge ratio of gas phase ions. A sample is first ionised by bombardment with electrons, then it is accelerated across an electric potential. As different fractions of the sample has different masses, they require

a different amount of time to travel across the column to the detector according to its mass. This is known as time-of-flight mass spectrometry, and the amount of time a certain molecule takes to travel to the detector can be summarised with the following equation,

$$t = \frac{d}{\sqrt{2U}}\sqrt{\frac{m}{z}} \qquad \text{Equation 3-5}$$

Where t is the time of fight, d is the distance travelled, U is the potential difference, m is the mass of the molecule, and z is the charge of the molecule. This can be simplified, as the distance and potential difference of the MS is constant, to,

$$t = k\sqrt{\frac{m}{z}} \qquad \text{Equation 3-6}$$

Where k is a constant. This means that a molecule will take longer to reach the detector if it is either heavier, or has a smaller charge. As the charge of the fractions in the sample should all be the same, the time of flight will therefore be solely dependent on the mass of the fractions.

MS was used in conjunction with TGA, where the exhaust gas of the TGA was connected to the ionisation and acceleration chamber of the MS. Different m/z ratios were monitored as a function of time, which could then be correlated with TGA data in order to obtain the temperature in which a molecule was observed.

3.12 Photoreactor

A photoreactor was used in order to investigate the photocatalytic performance of the different catalysts. The sample was attached onto a glass slide using vacuum grease, then placed 5 cm from the photoreactor. A 500 W Hg lamp with peak output wavelength at 250 nm was used to irradiate the sample. The sample was measured for weight loss at certain intervals of time.

3.13 Catalyst Testing

The catalysts were tested using a variety of carbon sources. This testing method was based on that devised by the Cardiff Catalysis Institute. In a typical catalyst test, 10 mg of catalyst was mixed with 3 mg of ex-CRT soot, unless otherwise stated. In a loose contact test, the mixture was mixed with a spatula in a sample vial for 5 min until a homogeneous mixture was achieved. In a tight contact test, the mixture was mixed and ground with a pestle and mortar for 5 min. A loose contact test would be able to recreate a more realistic real life environment which the catalyst would operate; whereas a tight contact test would give a better understanding in the reaction mechanism for soot combustion.

3.14 References

1 *http://commons.wikimedia.org/wiki/File%3ABragg_XRD.svg*.

2 a. L. Patterson, *Phys. Rev.*, 1939, **56**, 978–982.

3 *http://commons.wikimedia.org/wiki/File:EDX-scheme.svg*.

4 *http://sites.temple.edu/strongingroup/laboratories/atr/*.

Contents

Chapter 4. Soot Characterisation and Screening Tests

4.1 Introduction

Particulate matter is a major source of pollution and also a precursor to atmospheric sulphates[1], leading to a series of problems such as global warming and photochemical smog. A new study has identified soot and black carbon matter as the second largest contributor to global warming[2]. Its health implications have also been widely studied, and its carcinogenic potential have been discovered[3]. Therefore, having a clear understanding of the composition of soot, and also its reactivity is going to provide an invaluable platform to a better design of soot combustion catalyst.

A series of preliminary screening tests using Al_2O_3 as the metal oxide support gives a basic understanding to the reaction mechanism of the soot combustion reaction. A better appreciation of the soot combustion mechanism could be achieved by tuning the size of the Ag nanoparticles, and also the support effect of Al_2O_3. A series of different parameters, such as temperature ramping rate, catalyst-to-soot ratio, oxygen content were investigated in order to optimise reaction conditions, which would in turn give insights into the reaction mechanism of the soot combustion reaction.

4.2 Soot Characterisation

In this project several types of soot were used for the testing of different Ag catalysts, their physical and chemical properties must be clearly understood in order for a more complete understanding of the reaction mechanism. 2 different types of soot, and C_{60}, were used as the real soot and a model soot for the soot combustion reaction respectively.

The two types of soot were ex-CRT Soot from the USA, and ET Soot from Sweden, both provided by Johnson Matthey. The ex-CRT soot had been filtered by a JM CRT filter, whereas the ET soot went through a normal particulate filter. Both types of soot were used as received without any further processing.

4.2.1 TGA/SDT Characterisation

TGA was performed on the soot to determine the composition of the soot. When performed in N_2, only volatile hydrocarbons would desorb, whereas in air both hydrocarbons and graphitic carbon would oxidise. Any inorganics from engine oil and lubricants would remain unburnt at 1000 ^{o}C. Figure 4-1below shows the TGA profiles of heating ex-CRT soot in N_2 and in air.

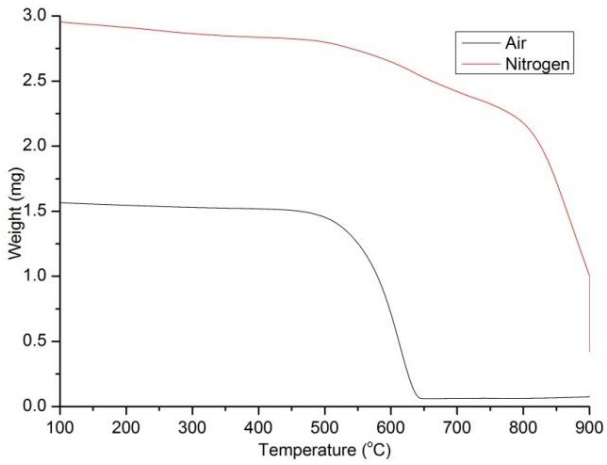

Figure 4-1 TGA profiles of heating ex-CRT soot in air (black), and in N_2 (red).

Table 4-1 Summary of compositions of the two different types of soot.

	Total Hydrocarbons (%)	Graphitic Carbon (%)	Inorganics (%)
Ex-CRT Soot	68 ± 2	28 ± 2	4 ± 2
ET Soot	67 ± 2	30 ± 2	3 ± 2

Table 4-1 summarises the compositions of the two different types of soot, where both types of soot are mainly comprised of volatile hydrocarbons at over 65%, and comparable amounts of incombustible inorganics in both. The resultant unburnt components after heating to 1000 ^{o}C would be the incombustible inorganics.

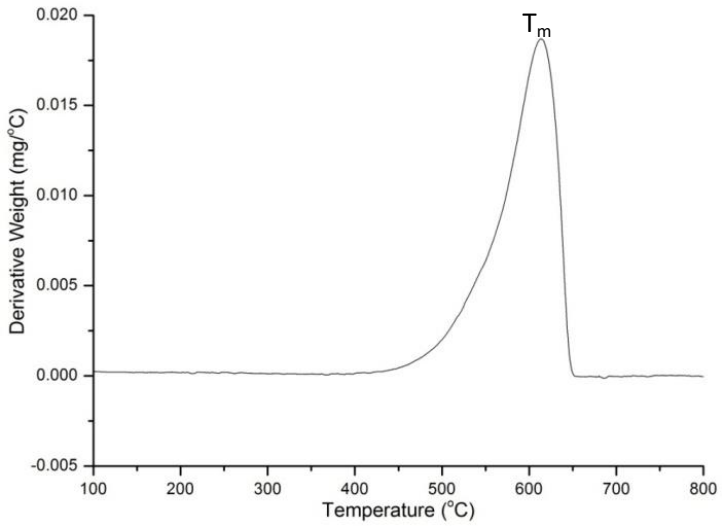

Figure 4-2 DTG profile of ex-CRT soot in air. T_m is defined as the temperature of maximum peak height.

Figure 4-2 is a DTG profile of ex-CRT soot in air. The combustion temperature is defined as the temperature at which the highest rate of oxidation, i.e. weight loss, is reached. This is known as T_m[4,5]. Another temperature, where 50% of the soot is burnt, known as T_{50}, was also used extensively in reporting soot combustion activities[6,7].

Table 4-2 T_m and T_{50} of ex-CRT and ET Soot.

	T_m (^oC)	T_{50} (^oC)
Ex-CRT Soot	610 ± 1	595 ± 1
ET Soot	617 ± 1	601 ± 1

For both ex-CRT and ET soot, T_{50} is slightly lower than T_m, which suggested that the graphitic carbon present in the soot was more difficult to combust than the hydrocarbons, therefore skewing the profile towards a higher temperature. In order to remain consistent, all future values for soot combustion will be quoted as T_m unless otherwise stated.

As the proportion of graphitic carbon was found to be higher in ET soot, its T_m was also found to be higher than that of ex-CRT Soot. However, the difference was not significant. Therefore, the two types of soot could effectively be treated as the same.

SDT study was performed on the soot to understand their reactivity. As the soot was burnt, it gave off heat, which could be recognised as an exothermic peak in a DSC profile.

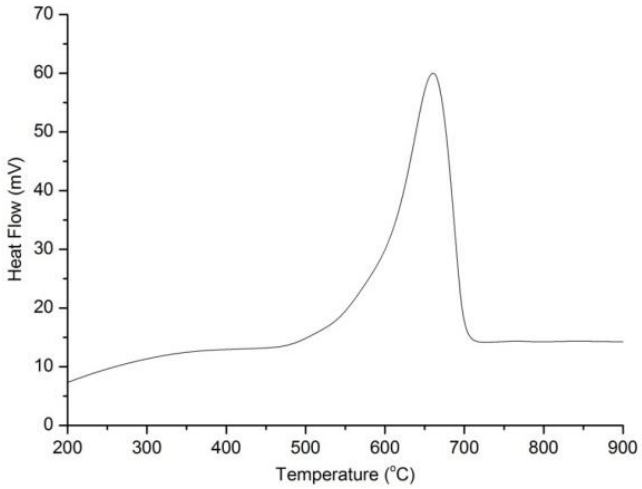

Figure 4-3 DSC profile of ex-CRT Soot, where a positive peak represent exothermic.

The enthalpy of combustion was found to be 13.8 and 7.3 kJ g^{-1} for ex-CRT Soot and ET Soot respectively. This meant the reaction for ET Soot was considerably less energetic than ex-CRT Soot. Various other types of carbons have also been tested as comparison.

Table 4-3 T_m and ΔH_{comb} of various carbon sources.

	T_m (°C)	ΔH_{comb} (kJ g^{-1})	ΔH_{comb} Standard Deviation ((kJ g^{-1})
Ex-CRT Soot	610 ± 1	13.8	0.058
ET Soot	617 ± 1	7.3	0.058
Carbon Black	681 ± 1	10.2	0.060
Norit Carbon	601 ± 1	15.4	0.057

Table 4-3 shows the enthalpy of combustion of some other carbon sources. It could be seen that whereas ex-CRT soot had a comparable enthalpy of combustion to the other two "pure" carbons of Carbon Black and Norit Carbon, ET soot was significantly lower. This suggested that ET soot contained much more graphitic soot in its composition than ex-CRT soot, which

would in fact be a lot more graphitic than previous measured in the TGA as hydrocarbons have a higher enthalpy of combustion compared to pure carbon.

4.2.2 Kinetic Studies

The kinetics of soot combustion can be studied by systematically oxidising soot at different temperatures and calculating different rates of oxidation. For ex-CRT soot, isothermal studies between 400 and 500 ^{o}C have been carried out. The weight loss of each sample was recorded at a set temperature in the TGA for 30 min isothermally, as shown in Figure 4-4.

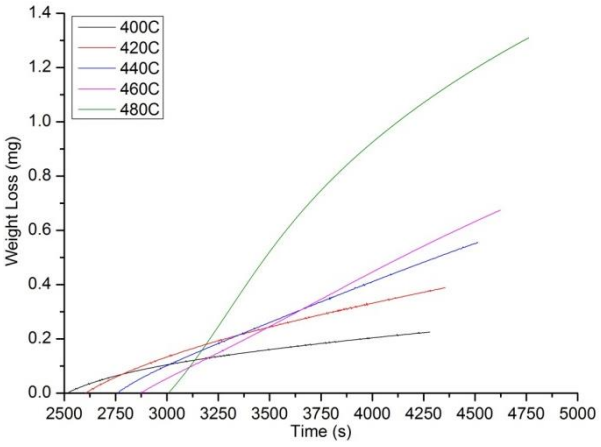

Figure 4-4 Weight loss of ex-CRT soot at different temperatures.

Firstly, the rate of oxidation decreased steadily at a certain temperature. This was not to be expected if it were a pure sample. Instead, as soot was made up of different fractions of hydrocarbons and graphitic soot, the different fractions would oxidise at different rates. As the lighter hydrocarbons were oxidised, the heavier hydrocarbons would become more difficult to be oxidised, therefore decreasing the rate of oxidation.

Secondly, decomposition of soot tended towards the same rate for the higher temperatures, most notably at 460 and 480 ^{o}C as seen in Figure 4-4 above. This could be attributed to the complete oxidation of hydrocarbons, and graphitic soot which was beginning to be oxidised.

As the rate of oxidation was different at different stages of the isothermal treatment, the initial rate was used as the rate of oxidation as it was a better representation of the species present at the beginning of the reaction. From these data, an activation energy for ex-CRT soot could be estimated using the Arrhenius plot, as it is shown in Figure 4-5.

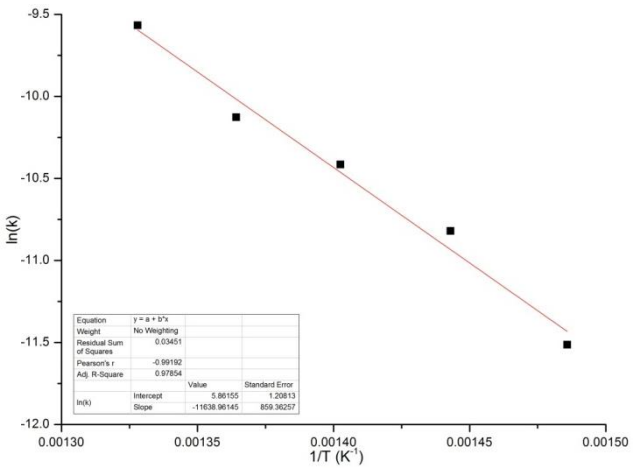

Figure 4-5 Arrhenius Plot of ex-CRT Soot Oxidation.

The activation energy of ex-CRT soot was therefore found to be 96.7 kJ g^{-1}; whereas the activation energy of ET soot was found to be 142 kJ g^{-1} using the same method. However, as the soot were not pure compounds, and there was no way of determining the chemical composition of the soot, it would be impossible to convert the units to kJ mol^{-1}.The

activation energy of ET soot was much higher than that of ex-CRT soot, which suggested certain species in ET soot was much more difficult to oxidise than ex-CRT soot.

4.2.3 Other Characterisations

TEM and XPS were performed on the ex-CRT soot in order to further understand its structure, and its relationship to its combustion characteristics.

TEM was performed at Johnson Matthey Technology Centre (JMTC) in Reading, where the sample was coated onto a holey carbon coated Cu TEM grid. The instrument used was the Tecnai F20 Transmission Electron Microscope using the following instrumental conditions: 200 kV, C2 aperture 30 and 50 µm.

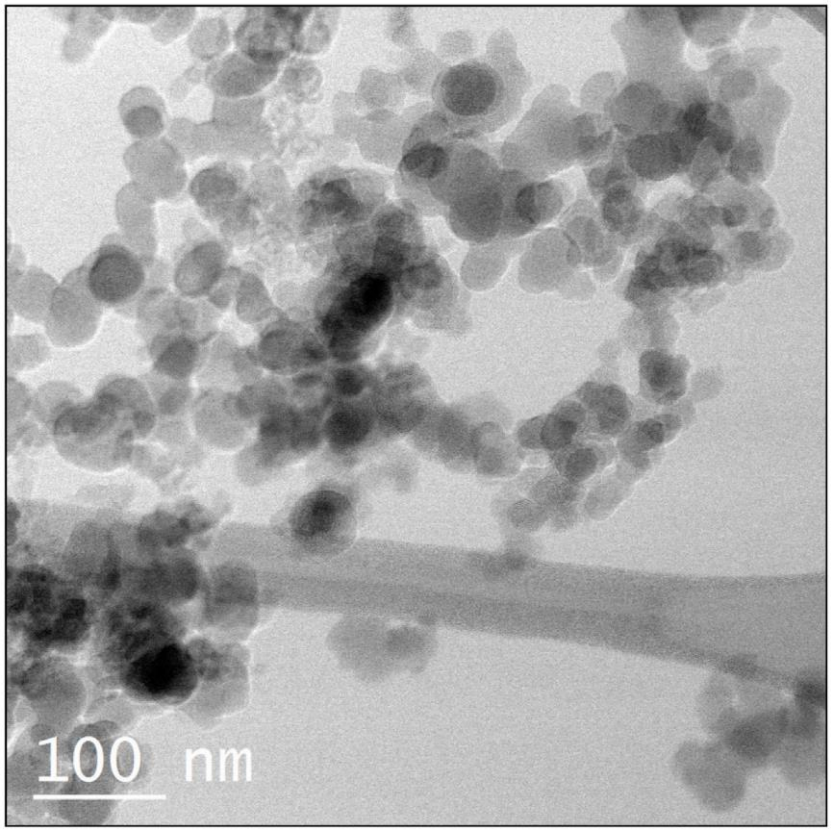

Figure 4-6 TEM Image of ex-CRT Soot.

Figure 4-6 shows a typical TEM image of the ex-CRT soot. It could be seen that most of the soot particulates were spherical in shape, and they were agglomerated to form a larger cluster of particulate.

Each soot particulate was found to be fairly monodispersed with a mean size of 31 nm, and a standard deviation of 8.3 nm. The size range of the particulates were found to be between 15 to 55 nm, with the vast majority of the particulates between 20 and 30 nm.

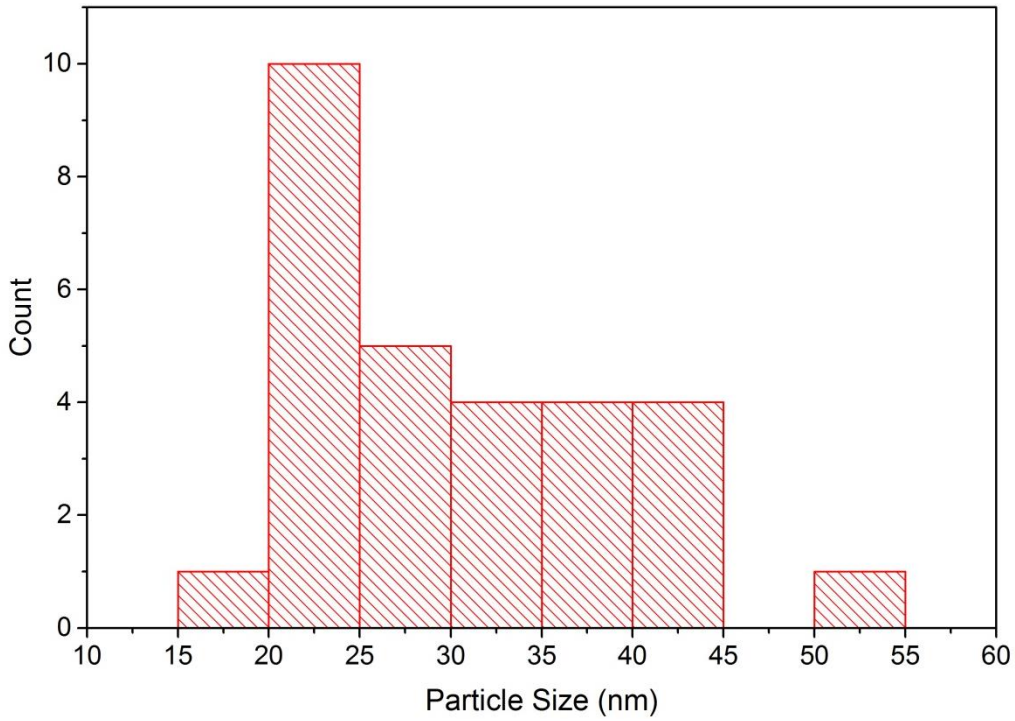

Figure 4-7 Histogram showing the size distribustion of ex-CRT soot particulates.

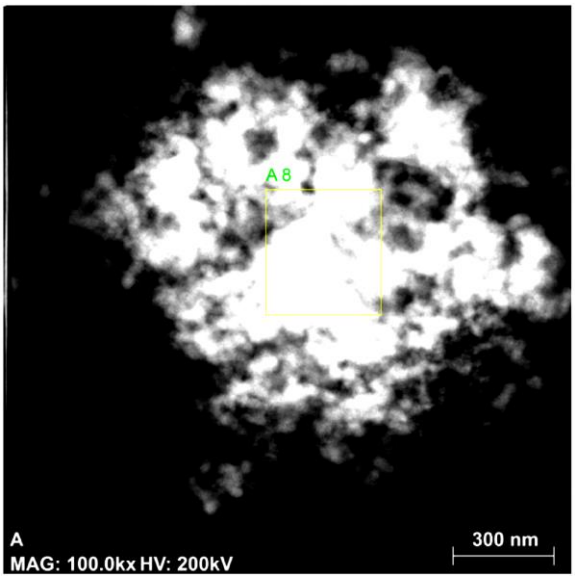

Element	Count (%)
C	99.61
O	1.24
Al	2.15
S	0

Figure 4-8 Yellow box showing area scanned by EDX spectroscopy (left); analysis of EDX spectroscopy (right).

Figure 4-8 shows the EDX spectroscopy analysis of a specific area of the ex-CRT soot. It shows that the majority of the soot particulate was made up of carbon. A large proportion

was also present in the soot, most probably from different compartments of the engine. A small percentage of oxygen was also detected, but no sulphur was found in this particular area of soot. This suggested that the soot came from a low sulphur diesel, and the lack of sulphur could mean that catalyst poisoning by sulphur was not significant with this particular sample of soot.

4.3 Screening Tests

4.3.1 JM Catalysts

A series of screening tests were performed to give a better understanding to the factors that could affect soot combustion. Two catalysts provided by Johnson Matthey (JM), were initially tested. Both were Ag/Al_2O_3 catalysts, with different loadings of 2% and 8%. Neither catalyst was found to be active enough for soot combustion, with T_m of 596 and 498 ^oC respectively, as shown in Figure 4-9.

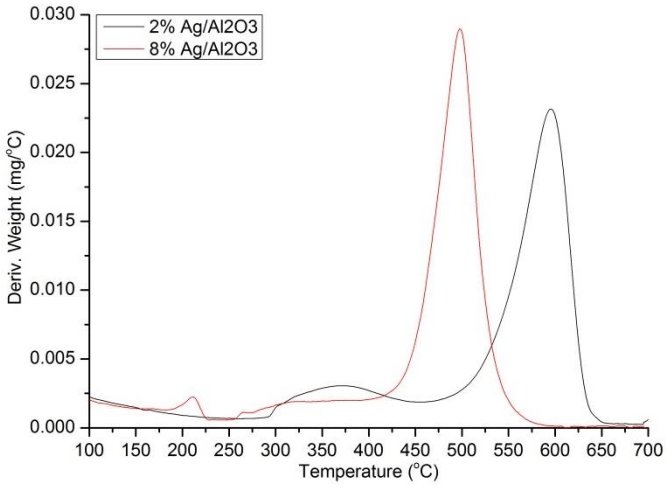

Figure 4-9 DTG plots of soot combustion for JM catalysts.

XRD revealed more details on the properties of the two catalysts, which could explain the inactivity. Figure 4-10 below shows the XRD profiles of the two catalysts, and both catalysts contain Al_2O_3 in the bauxite structure. However, neither catalyst appeared to show peaks of Ag, which suggested that the Ag particles in the catalyst were too small to be detected by XRD.

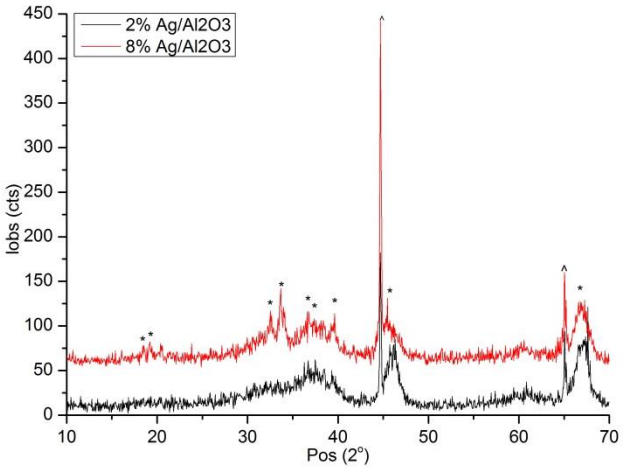

Figure 4-10 XRD profiles of JM catalysts. (*) = Bauxite; (^) = Al sample holder. The broad peaks are due to the small particle sizes of bauxite. No Ag observed in either XRD profiles.

In-situ XRD was then performed, which showed the emergence of Ag crystalline peaks from 150 ^{o}C. However, these peaks disappeared at 600 ^{o}C, which suggested the crystalline Ag became mobile and amorphous again at that temperature.

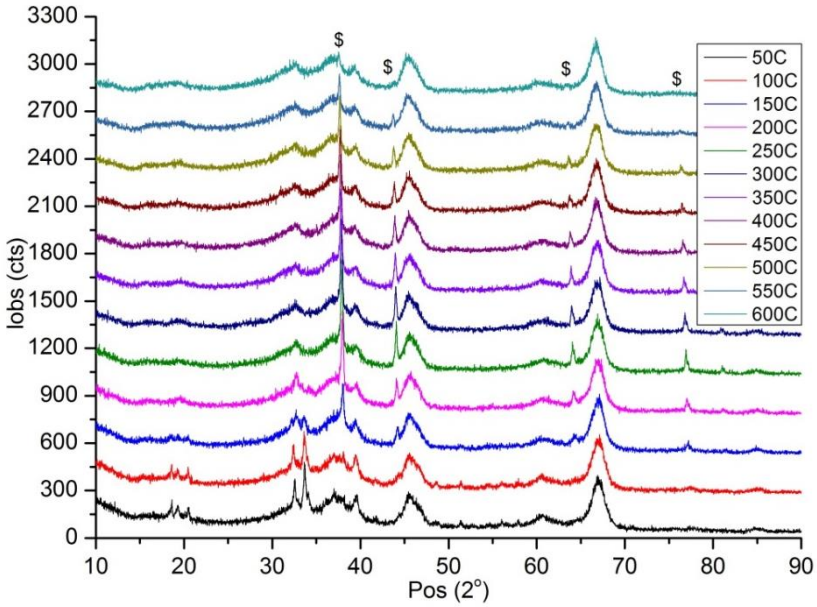

Figure 4-11 In-situ XRD profile of 8% Ag/Al_2O_3. ($) = Ag. The phase change from bauxite to gibbsite can be observed at 150 °C.

Another feature observed in the *in situ* XRD profile was the disappearance of the low angle bauxite peaks at 150 °C. This suggested a phase change from bauxite to gibbsite. A possible explanation was that at higher temperatures, the catalyst gained enough kinetic energy for atoms to become mobile. The migration of mobile atoms then led to the loss of crystallinity. It should be noted that bauxite and gibbsite are $Al(OH)_3$, not Al_2O_3 species, and none of the peaks in the in-situ XRD profile matched the alumina phase.

4.3.2 Al_2O_3 Catalysts

Other than JM catalysts, a series of Ag/Al_2O_3 catalysts were synthesized in order to test their soot combustion capability. The main difference in the Al_2O_3 supports were their surface functional groups, which were either acidic, neutral, or basic.

Table 4-4 T_m of various Ag/Al_2O_3 catalysts, and the average Ag (111) particle size obtained from XRD. N/A = Not available.

Support	**Surface Functionalisation**	**T_m (^oC)**	**Ag (111) Particle Size (nm)**
Acidic Al_2O_3	Carboxylic Acid	563	6.55
Neutral Al_2O_3	Epoxide	545	4.86
Basic Al_2O_3	Hydroxide	352	13.03
γ-Al_2O_3	None	610	N/A

Table 4-4 summarises the catalytic performance of the Ag/Al_2O_3 with various surface functionality. The basic functionalisation had a dramatically lower T_m than either the neutral or acidic supports, which suggested that soot combustion could be affected by the presence of surface functional groups. Ag/γ-Al_2O_3, on the other hand, was completely ineffective as a soot combustion catalyst, with its T_m exactly the same as pure ex-CRT soot. No Ag peaks were identified from XRD for the γ-Al_2O_3 support, which suggested there is no metal – support interaction between Ag and the alumina support.

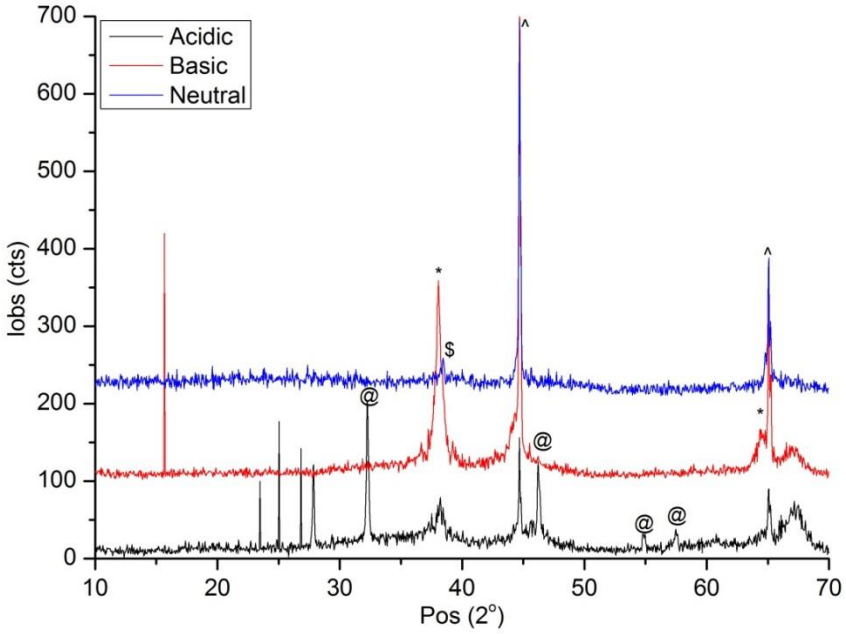

Figure 4-12 RD profiles of Ag/Al_2O_3 catalysts. (^) = Al support; ($) = Boehmite; (@) = Gibbsite; (*) = Ag. Black: Neutral Al_2O_3 support; Red: Basic Al_2O_3 support; Blue: Acidic Al_2O_3 support. The sharp peaks on neutral and basic Al_2O_3 supports are unidentified.

As shown in Figure 4-12, the main phase of γ-Al_2O_3 was boehmite, which had a formula of γ-AlOOH. The acidic Al_2O_3 appeared to be amorphous, whilst the main phase of the basic Al_2O_3 was gibbsite, γ-$Al(OH)_3$. The sharp peak at 15° for basic Al_2O_3 is adsorbed H_2O, whereas any un-indexed peaks on acidic Al_2O_3 could not be identified to any Al containing species.

When the catalysts were heated in the TGA without any soot, it was found that all 3 supports had the same percentage weight loss upon heating. This suggested that all 3 catalysts had retained some water or other volatile organic species from the synthetic process, as shown in Figure 4-13. The initial weight loss before 200 °C could be attributed to water desorption from the catalyst. At temperatures above 250 °C a phase change was

observed, where the boehmite of the neutral Al_2O_3 was observed to lose the highest proportion of weight. This suggested that boehmite was not as thermally stable as gibbsite found in acidic Al_2O_3.

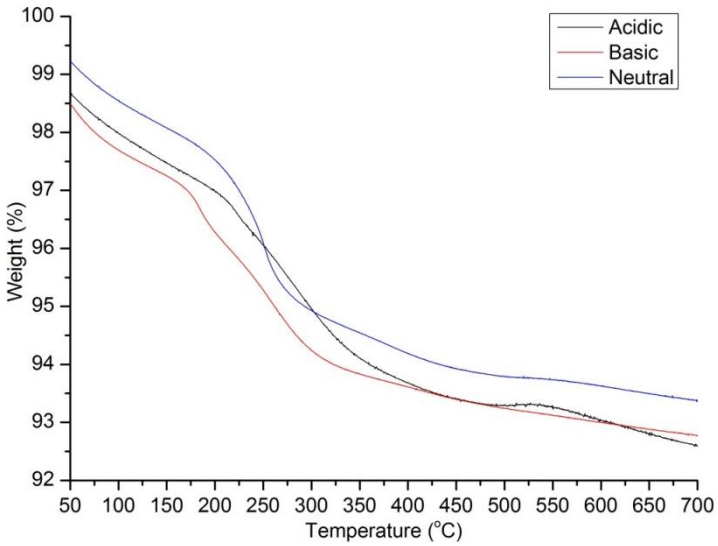

Figure 4-13 TGA profiles of Ag/Al_2O_3 in air from 50 to 700 °C.

4.4 Size Effect of Ag Nanocrystals

It has been found that larger Ag nanoparticles were more active in oxidation compared to smaller Ag particles, where particles with an average size of 100 nm had a turnover frequency of an order of magnitude greater than that of Ag particles with a size of 15 nm[8]. The extent of metal particle size on the soot combustion capability of Ag were tested.

In order to prepare Ag particles of different sizes, the reaction temperature was altered in order to achieve different rates of nucleation. At higher temperatures, the rate of growth of the Ag nanoparticles was faster, making them larger. Neutral Al_2O_3 was used as a model support for the investigation of size effect as it could be considered as a non-interacting

support with little SMSI. A range of Ag particle sizes from under 2.5 nm to 5.5 nm was achieved by changing the reaction temperature from 100 ^{o}C to 200 ^{o}C.

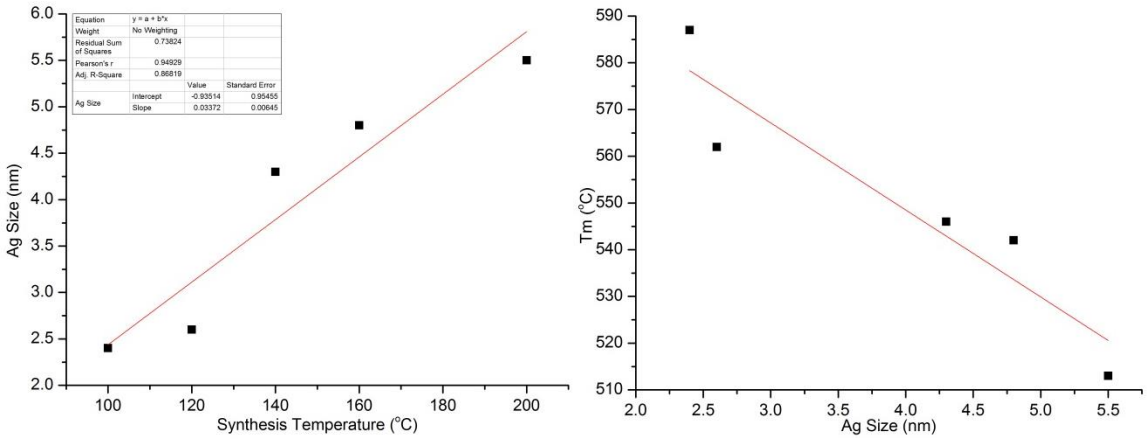

Figure 4-14 Ag particle sizes at different synthesis temperatures as calculated from XRD pattern (left); T_m of soot combustion with different Ag particles sizes (right).

Figure 4-14 shows that as the reaction temperature increased, the rate of nucleation increased, and the size of Ag particle increased almost linearly from 2.5 nm to 5.5 nm. As Ag particle size increased, the ex-CRT soot combustion temperature decreased accordingly. This was in good agreement with Goncharova *et al.*[8] This could be due to the more intimate contact that was achieved by larger Ag nanoparticles and soot, which was relatively large in size compared to the nanoparticles.

UV-Vis spectroscopy was used to investigate the surface plasmon resonance peaks of the various Ag nanoparticle on the Al_2O_3 support. It has been widely demonstrated that larger Ag nanoparticles would cause a red-shift in the surface plasmon resonance peak[9].

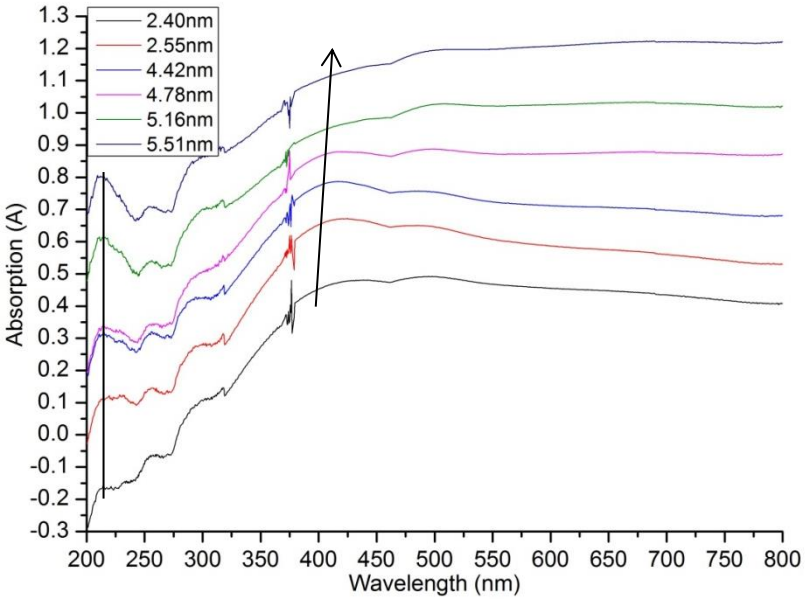

Figure 4-15 UV/Vis spectrum of Ag/Al_2O_3 of different Ag particle sizes.

Figure 4-15 shows the UV/Vis spectrum of Ag/Al_2O_3 with different Ag particle sizes. The peak at 260 and 420 nm represented the dipolar and quadrupolar surface plasmon resonance peaks of Ag nanoparticles respectively. The peak at 320 nm was attributed to the lamp change, and the peak at 280 nm was due to water desorption from the KBr pellets. Whereas there was little change to the 260 nm peak position, there was an observable redshifting of the surface plasmon peak at 420 nm. This meant that the Ag nanoparticles behaved like free particles, with little interaction with the Al_2O_3 support. This suggested that the position of the quadrupolar SPR of Ag was highly size dependent in a free Ag particle.

On the other hand, the dipolar SPR of Ag at 260nm had little change in its peak position, suggesting that the position of the dipolar resonance was not size dependent. However, it could be observed that the intensity of the peak increased as the size of Ag increased, which

suggested that the intensity of the dipolar resonance of Ag was size dependent. By coupling these two pieces of information, the size of an Ag nanoparticle could therefore be estimated by looking at the intensity of the dipolar SPR peak, and also the position of the quadrupolar SPR peak.

As there was little SMSI between Ag and Al_2O_3, the enhancement in activity was therefore due to the increased size of Ag, and its ability to attain a better contact with the soot particulates.

4.5 Altering Reaction Conditions

In a commercial exhaust system, the conditions that the catalyst experience are constantly changing. However, in a laboratory, these conditions could be controlled and changed in a precise manner in order to investigate how each factor affects the soot combustion ability of the catalyst. These studies provide invaluable insight into the way catalyst behave in a real exhaust system, and how the reaction conditions may be optimised for the lower soot combustion temperature to be achieved.

4.5.1 Heating Rate

Different heating rates were used to look at the differences it may have on the profiles of the soot combustion. A slower heating rate would allow for greater extent of thermal equilibrium between the reactants and the furnace, and also giving more details in the oxidation profiles as different fractions of the soot was oxidised at different rates; whereas a higher heating rate would give more accurate real life conditions in the exhaust. The JM 8%

Ag/Al_2O_3 catalyst was used for all the test conditions in order to avoid any discrepancies that may occur in the synthesis process.

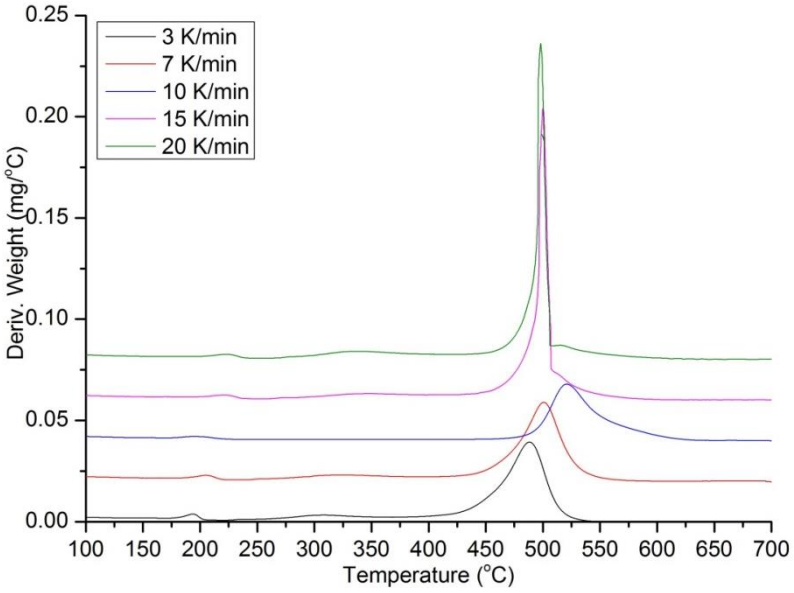

Figure 4-16 DTG profiles of ex-CRT soot combustion with 8% Ag/Al_2O_3 at different heating rates. Soot:Catalyst = 3:10 w/w.

Figure 4-16 shows DTG profiles of ex-CRT soot combustion with 8% Ag/Al_2O_3 at different heating rates. It could be seen that as the heating rate increased, the T_m increased accordingly, even thermal equilibrium was not established between the furnace and reactants. No further details on the DTG could be observed at a lower heating rate, however, which suggested that the different fractions of soot burnt at the much faster rate and much more homogenously than previously thought. However, at the higher heating rates of 15 and 20 K min^{-1}, T_m became lower than that of 10 K min^{-1}. They also had a peculiar looking profile, where the tail of the DTG profile was almost flat. This was due to the overheating of

the mixture to react an uncontrollable exothermic reaction of soot combustion. Figure 4-17 shows the temperature profile against time for the soot combustion at 20 K min^{-1}.

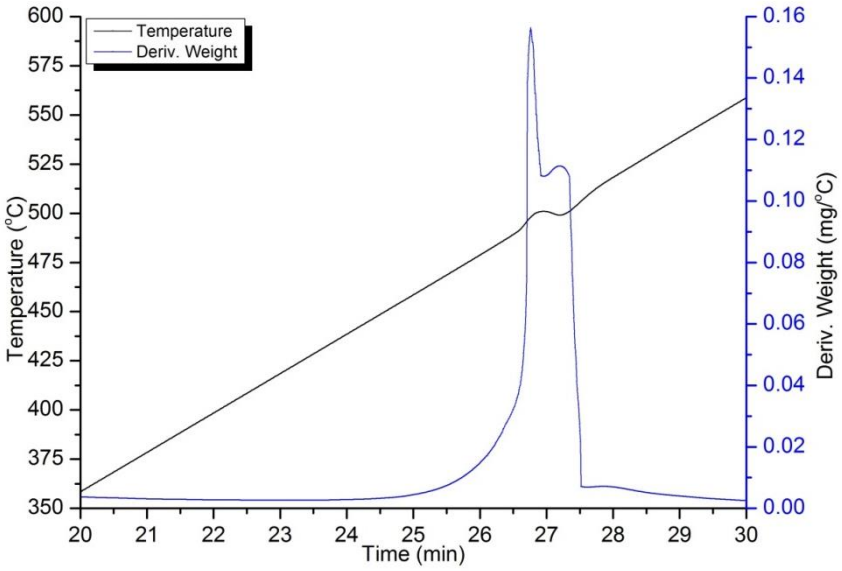

Figure 4-17 Temperature profile against time for soot combustion at 20 K min^{-1} (black); derivative weight change profile against time (blue).

It could be seen that the temperature rise was not linear against time, but a small rise in temperature due to the exothermic combustion of soot was observed, which correlated to the time at which the highest rate of soot combustion was occurring. This uncontrolled exothermic "runaway" reaction would give inaccurate results, and therefore should be avoided. Therefore, a heating rate of 10 K min^{-1} should be used for the best balance between avoiding an uncontrolled reaction, and the reaction taking too long to run.

4.5.2 Soot: Catalyst Ratio

A conventional vehicle diesel trap operates by trapping soot in a honeycomb structure within the exhaust, then raising the temperature by various means to burn the soot at

regular intervals. It is therefore important to know the performance of the catalyst at different loadings of soot in order for optimal conditions when employed in a commercial exhaust system. Thus, various ratios of soot and catalyst were tested in order to investigate the effects of increasing soot loading on the performance of the catalyst.

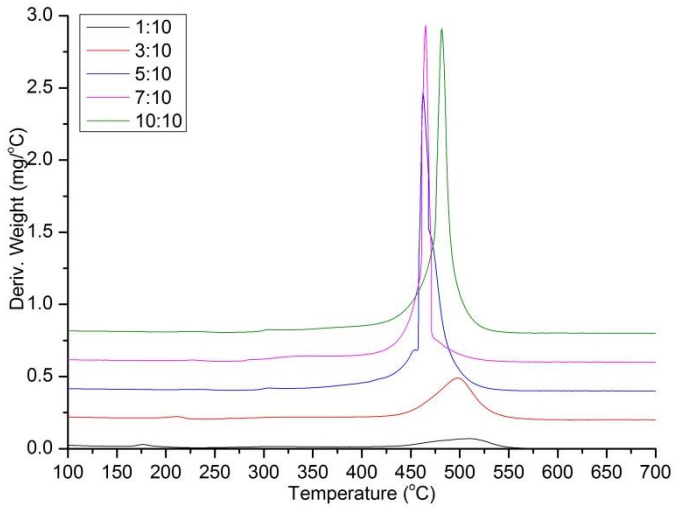

Figure 4-18 DTG profiles of ex-CRT soot at different soot:catalyst ratios (w/w).

As shown in Figure 4-18, there was little difference in the shape of the DTG profile between 1:10 and 3:10 soot: catalyst ratios, except for the area, which represented the amount of soot burnt. However, at higher loadings of 5:10 and 7:10, the profile shapes were both characteristic of an uncontrolled exothermic reaction, where the heat generated by the combustion of a large quantity of soot generated a sharp peak in the DTG profile. The profile of the 10:10 appeared to be a more "normal" shape with little evidence of the uncontrolled exothermic reaction, most probably due to the large amount of soot that required to be burnt, and the uneven contact of the catalyst with the soot, as the soot had a lower density than the catalyst.

The ratio of soot to catalyst used for further testing should therefore be kept at a maximum of 3:10 in order to avoid the uncontrolled exothermic combustion of soot. Whereas the ratio was shown to be unimportant to the soot combustion temperature of the catalyst, the ratio should be kept at 3:10 for this project in order to provide consistency throughout.

4.5.3 Oxygen Content

In a typical unturbocharged diesel exhaust, there can be up to 17% O_2 remaining after diesel combustion[10], which means there is plenty of oxygen for the complete removal of diesel soot in the exhaust system. However, oxygen content differs from engine to engine, and in particular those with turbocharged engines. Therefore, the catalyst must be able to operate at lower oxygen content than air, and retain its catalytic performance.

In order to change the proportion of O_2 in the reaction feed, compress air, assumed to be 21% O_2, and N_2, are mixed in the appropriate quantities in order to achieve the correct percentage of O_2. Table 4-5 summarises the T_m of soot combustion at different O_2 contents.

Table 4-5 T_m of ex-CRT soot with 8% Ag/Al_2O_3 at different O_2 contents. Heating rate = 10 K min^{-1}, soot: catalyst ratio = 3:10 (w/w).

O_2 Content	**T_m (^oC)**
5%	501
10%	502
15%	500
Air (21%)	498

It can be seen that the O_2 content above 5% made almost no difference to the soot combustion temperature. This suggested that the reaction at O_2 content above 5% was not diffusion limited. Since realistically, the O_2 content in a commercial vehicle exhaust should not be below 10%, air could be used as a reliable model for the soot combustion reaction under laboratory conditions.

4.6 Summary

Two types of soot were characterised, which were both found to have hydrocarbons as the main composition. Combustion temperature of soot was found to be in excess of 600 ^{o}C, which was higher than the temperature of a diesel exhaust.

Existing industrial catalysts were tested, and found to decrease the soot combustion temperature, and Ag/Al_2O_3 with different surface functionalization were found to have different effects on soot combustion, where the basic functionalization was more active in soot combustion than either the neutral or acidic functionalizations.

Screening tests with different reaction parameters were also carried out to find the optimal reaction conditions. It was found that soot combustion appeared to be independent of catalyst ratio or oxygen content.

4.7 References

1 W. H. Su, Q. P. Zhang, W. Z. Song, C. Luo and Y. F. Siu, *Aerosol Sci. Technol.*, 1989, **10**, 231–235.

2 T. C. Bond, S. J. Doherty, D. W. Fahey, P. M. Forster, T. Berntsen, B. J. DeAngelo, M. G. Flanner, S. Ghan, B. Kärcher, D. Koch, S. Kinne, Y. Kondo, P. K. Quinn, M. C. Sarofim, M. G. Schultz, M. Schulz, C. Venkataraman, H. Zhang, S. Zhang, N. Bellouin, S. K. Guttikunda, P. K. Hopke, M. Z. Jacobson, J. W. Kaiser, Z. Klimont, U. Lohmann, J. P. Schwarz, D. Shindell, T. Storelvmo, S. G. Warren and C. S. Zender, *J. Geophys. Res. Atmos.*, 2013, **118**, 5380–5552.

3 *http://www.ipcc.ch/pdf/assessment-report/ar4/wg1/ar4-wg1-chapter2.pdf*.

4 E. Aneggi, C. de Leitenburg, G. Dolcetti and A. Trovarelli, *Catal. Today*, 2006, **114**, 40–47.

5 C. Badini, G. Saracco, N. Russo and V. Specchia, *Catal. Letters*, 2000, **69**, 207–215.

6 E. Aneggi, J. Llorca, C. de Leitenburg, G. Dolcetti, A. Trovarelli, C. De Leitenburg and O. Ag, *Appl. Catal. B-Environmental*, 2009, **91**, 489–498.

7 E. Aneggi, C. de Leitenburg, G. Dolcetti and A. Trovarelli, *Catal. Today*, 2008, **136**, 3–10.

8 S. N. Goncharova, E. A. Paukshtis and B. S. Bal'zhinimaev, *Appl. Catal. a-General*, 1995, 67–84.

9 K. Qian, B. C. Sweeny, A. C. Johnston-Peck, W. X. Niu, J. O. Graham, J. S. DuChene, J. J. Qiu, Y. C. Wang, M. H. Engelhard, D. Su, E. A. Stach and W. D. Wei, *J. Am. Chem. Soc.*, 2014, **136**, 9842–9845.

10 Volkswagen, *http://www.volkspage.net/technik/ssp/ssp/SSP_230.pdf*, .

Contents

Chapter 5. Lanthanide Oxide Supported Catalysts

5.1 Introduction

CeO_2 as a soot combustion catalyst support has been extensively studied in previous research[1–4]. Other metal oxides such as La_2O_3 and Co_3O_4 have also been used in conjunction with CeO_2 as a dopant [5–7]. Aneggi *et al.* reported a massively enhanced soot combustion performance using Ag/CeO_2, with a soot combustion temperature as low as 330 ℃[8]. La_2O_3 has also been employed as a support for soot combustion, albeit with K instead of Ag as the active metal[9]. It has been demonstrated that K/La_2O_3 was able to burn soot at temperatures under 400 ℃.

The +3 oxidation state across most of the Lanthanide Series (Ln) made them ideal for studying the effects of Ag on soot combustion, as the support would not change in oxidation state and get involved in any redox reaction.

A series of Ag/Ln_2O_3 catalysts were synthesised using the wet impregnation method, and their soot combustion performances have been investigated. The sol-gel method was also used in order to investigate the difference in soot combustion performance by different synthetic methods. Their thermal stability have been investigated using *in situ* XRD, and the electronic interactions between Ag and the support have been studied by various techniques such as FT-IR and XPS.

C_{60} can be used as a model carbon, as it has a well-known structure with clearly defined combustion properties. The surface interactions of carbon and the catalyst, and the oxygen mobility can both be investigated using C_{60}.

5.2 Lanthanide Oxide Supported Catalysts

Unlike transition metal oxides, lanthanide oxides have valence electrons in the f-shell, which can be considered as inner shell electrons. Therefore, little or no electronic interactions should be present between Ag and the lanthanide oxides.

Table 5-1 Electronic configuration of various lanthanide oxides, and the T_m of the correlating 10% Ag/MO with ex-CRT soot in tight contact. (*) represents oxides with no stable sesquioxide; (N/A) represents no data available. For brevity, all lanthanide oxides will be named as Ln_2O_3.

Metal Oxide	Electronic Configuration	ex-CRT Soot T_m (°C)	Standard Deviation (°C)	ET Soot T_m (°C)	Standard Deviation (°C)
La_2O_3	f^0	315	2.92	345	3.42
CeO_2*	f^0	335	2.08	373	2.31
Pr_6O_{11}*	f^1, f^2	438	0.77	N/A	N/A
Nd_2O_3	f^3	284	4.71	308	4.34
Sm_2O_3	f^5	333	3.68	350	3.79
Eu_2O_3	f^6	342	3.88	391	3.57
Gd_2O_3	f^7	347	1.24	423	1.50
Tb_4O_7*	f^8, f^9	444	0.42	N/A	N/A
Ho_2O_3	f^{10}	389	0.41	513	0.22
Tm_2O_3	f^{12}	442	0.26	484	0.16
Yb_2O_3	f^{13}	411	0.47	469	0.35
Lu_2O_3	f^{14}	410	0.17	N/A	N/A

From Table 5-1, if the non-sesquioxides were not taken into account, there was a general increase in T_m from Nd_2O_3 to Ho_2O_3, while decrease towards Lu_2O_3. Ag/Nd_2O_3 had an ex-CRT soot T_m of 284 °C, and ET soot T_m of 305 °C, the lowest soot combustion temperatures from any reported values. The same trend in T_m could be observed in the combustion of both ex-CRT soot and ET Soot, suggesting that although the composition of the two types of soot were different, they had a very similar interaction with the catalyst. As all sesquioxides have a +3 oxidation state, and lanthanide oxides were unlikely to have any redox activity, this trend could be attributed to the differences in metal – support interaction across the lanthanide series.

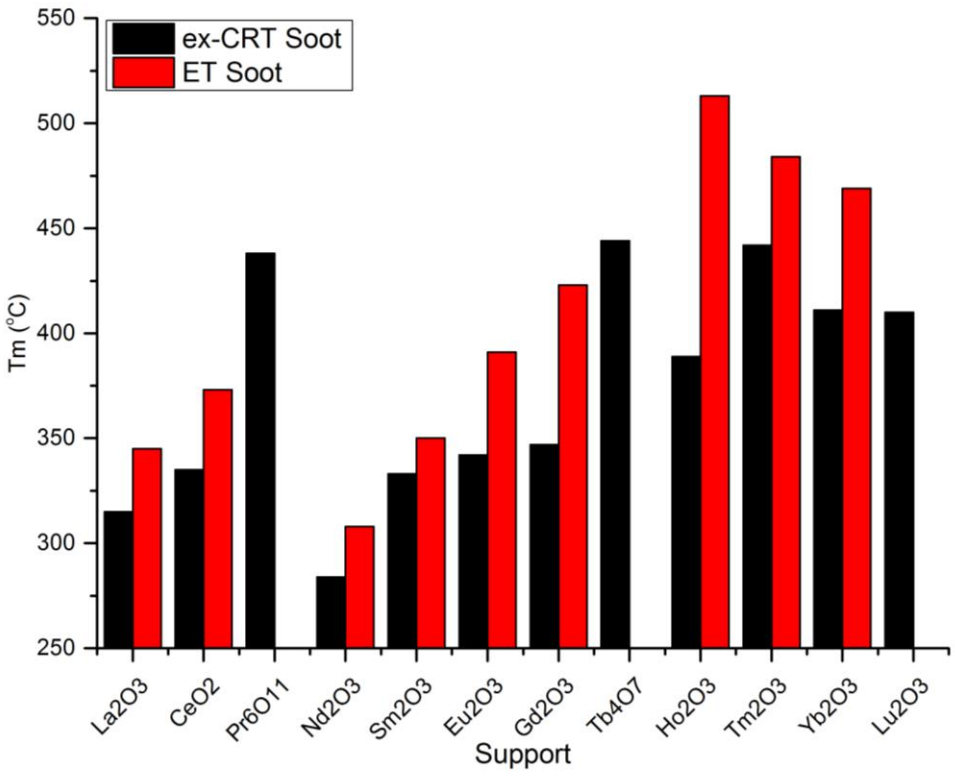

Figure 5-1 A graphical summary of the T_m of the two types of soot using different Ag/Ln_2O_3.

5.3 Metal – Support Interactions between Ag Nanoparticles and Ln_2O_3

It is important to understand the metal – support interactions between Ag nanoparticles and the metal oxide support in order to have a better understanding of the reaction mechanism.

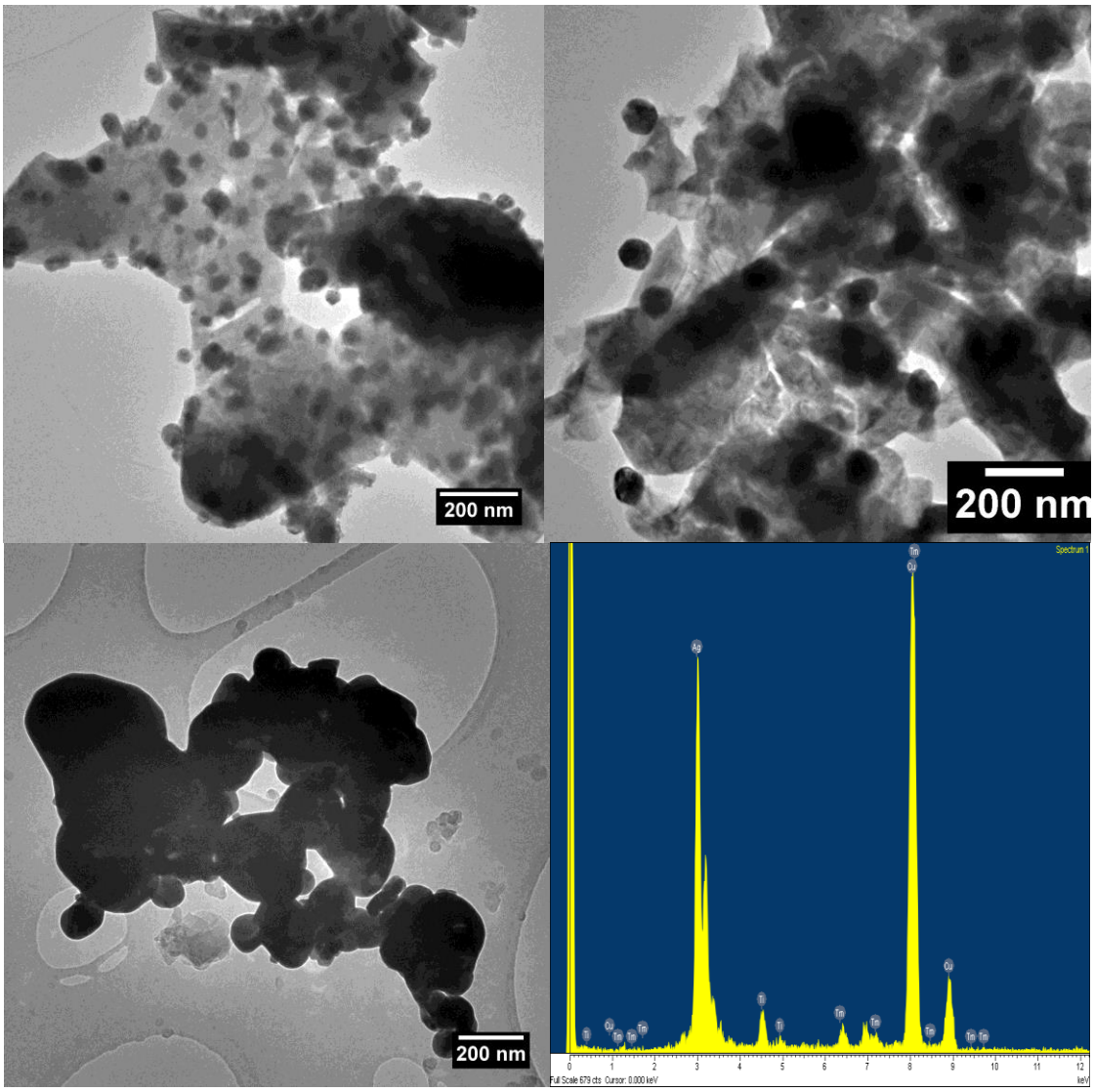

Figure 5-2 TEM images of Ag/La_2O_3 (top left); Ag/Nd_2O_3 (top right); Ag/Tm_2O_3 (bottom left); and EDX spectrum of the Ag/Tm_2O_3 (bottom right). All scale bars represent 200 nm.

Figure 5-2 shows the TEM images of the lanthanide series catalyst, where two distinctive types of Ag nanoparticle growth were observed. For the early lanthanides, such as La_2O_3, Nd_2O_3, and Sm_2O_3, Ag was found attached to the metal oxide support, observed in the TEM images as dark spheres on a lighter background. However, no Ag was found to be supported by the late lanthanide oxides. In the case of Ho_2O_3 and Tm_2O_3 in particular, Ag clusters were found to be detached from the support altogether. EDX confirmed that less than 3% of the atoms in the imaged cluster were Tm. Other images were also found to be either pure Ln_2O_3, or pure Ag clusters. This meant that the late Ag/Ln_2O_3 actually experienced no metal – support interactions, which could explain their poor activities.

Table 5-2 Summary of extent of SMSI and Ag particle sizes of Ag/Ln_2O_3

Metal Oxide	SMSI	Mean Ag Size (nm)	Standard Deviation (nm)
La_2O_3	Yes	131	72
Nd_2O_3	Yes	64	24
Sm_2O_3	Yes	94	23
Eu_2O_3	Yes	49	17
Gd_2O_3	Some	166	51
Ho_2O_3	No	N/A	N/A
Tm_2O_3	No	N/A	N/A
Yb_2O_3	No	N/A	N/A
Lu_2O_3	No	N/A	N/A

Table 5-2 gives a summary of the mean Ag particle sizes and extent of SMSI as seen from TEM. For the late Ag/Ln_2O_3, as the Ag nanoparticles were not found to be attached on the metal oxide surface, there were not enough for calculating the mean size of Ag particle. Gd_2O_3 was

found to be a borderline sample where Ag was found to be both attached to the oxide surface, and also in isolated clusters. This suggested that Gd_2O_3 was the point where metal – support interaction had reduced to an extent where the support could no longer stabilise Ag nanoparticles, and Ag clusters began to be formed.

5.4 Electronic Interactions between Ag Nanoparticles and Ln_2O_3

It was interesting to find that the order of T_m over the lanthanide series was the same for the two types of soot. It suggested a similar interaction between the soot and the catalyst that promoted the soot combustion.

Figure 5-3 shows the plot of T_m versus 4d binding energy of the Ln^{3+} ions as measured by XPS. There is a clear linear correlation that the higher 4d binding energy hinders soot combustion. It is widely accepted that the increase in nuclear change across the lanthanide series causes a reduction in ionic radius, and thus an increase in binding energy, known as lanthanide contraction. This contraction could result in a poorer overlap between Ag E_f and Ln_2O_3 E_c for soot combustion.

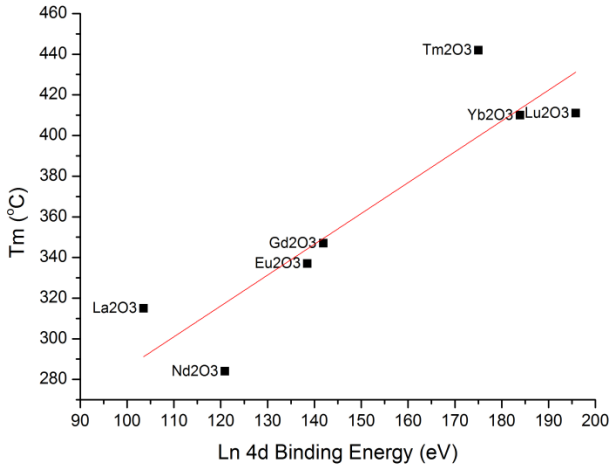

Figure 5-3 ex-CRT Soot T_m versus Ln^{3+} 4d binding energy.

Another indication of the poorer metal – support interaction was to measure the melting points of the Ln_2O_3.

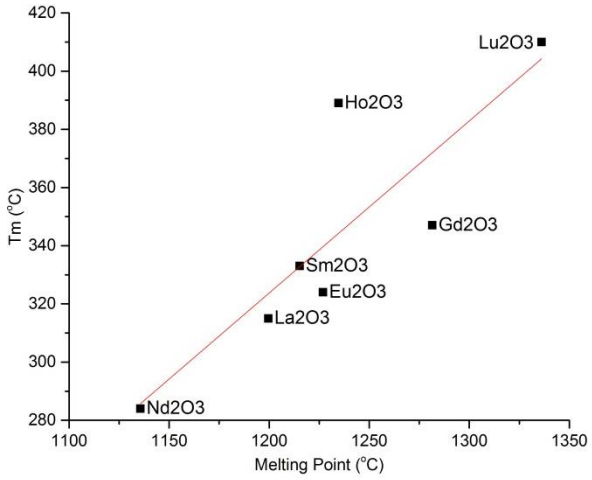

Figure 5-4 ex-CRT Soot T_m versus melting point of Ln_2O_3.

A linear relationship could be observed between the melting point of the Ln_2O_3 and its corresponding ex-CRT soot T_m. This appeared to be in good agreement with Neri *et al.* who observed a similar trend[10]. This was because the melting point of Ln_2O_3 could be related to its Hüttig temperature (~$^1/_3$ melting point), a measure at which surface atoms become mobile. This meant that the oxides with a lower melting point had more mobile surface atoms which were able to interact with either Ag, or the soot for combustion at the lower temperature.

5.4.1 Surface Oxygen Promotion

Although lanthanide oxides have been widely considered to be purely ionic with little covalency, O_{1s} XPS studies on Ln_2O_3 and Ag/Ln_2O_3 have shown the contrary. Figure 5-5 is a deconvaluted O_{1s} XPS spectrum of Ag/Nd_2O_3, where 2 types of oxygens could be observed. It can be see that although pure Nd_2O_3 contains a small proportion of O_β, the addition of Ag to Nd_2O_3 has significantly increased that proportion.

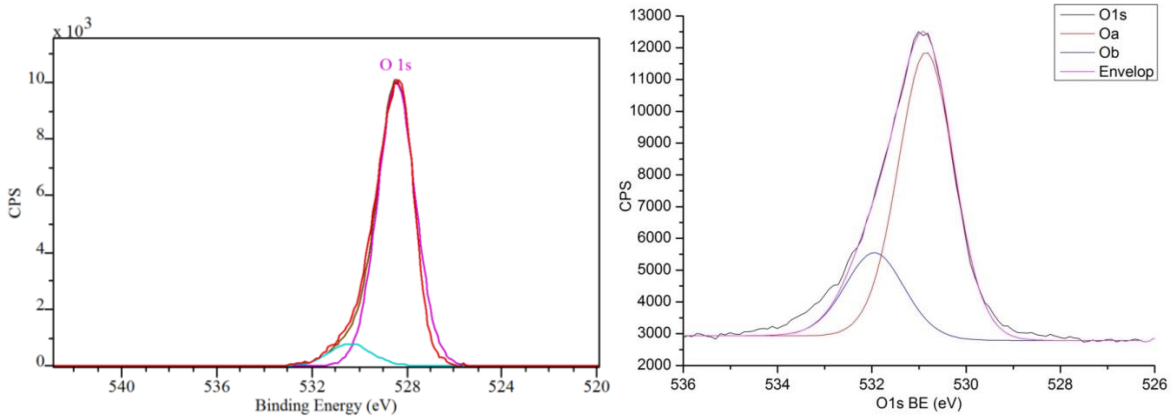

Figure 5-5 O_{1s} XPS spectrum of pure Nd_2O_3 (left), and Ag/Nd_2O_3 (right), where deconvaluted Oa represents O_γ and Ob represents O_β. O1s binding energy of pure Nd_2O_3 was found to be 529 eV, whereas the O1s binding energy of Ag_2O was 532 eV.

The increase in O1s binding energy for Ag/Nd_2O_3 suggested a withdrawal of valence electrons, resulting in an overall oxidation of the oxide to become an "electrophilic oxygen species". It is this oxygen species that is reactive towards soot combustion.

3 types of oxygen can normally be found on a metal oxide, O_α, O_β, and O_γ. These three types of oxygen represent surface oxygen, interstitial, or sub-surface oxygen, and lattice oxygen respectively. It could be seen from Figure 5-5 that both O_β and O_γ were present in Ag/Nd_2O_3. The lower lattice energy of O_β meant that it would be more mobile on the subsurface of the metal oxide, which could then be transported for soot combustion. O_α was not observed in XPS, as surface oxygens desorb readily under high vacuum conditions of the XPS.

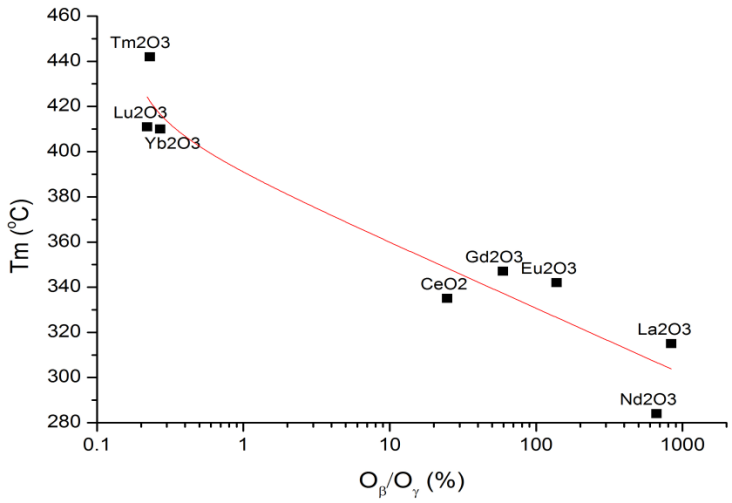

Figure 5-6 ex-CRT Soot T_m versus O_β/O_γ ratio.

Figure 5-6 shows the correlation between the proportions of O_β observed in XPS, and the T_m of ex-CRT soot. It could be seen that an exponential relationship between the proportions of O_β and T_m was observed. This meant that as the proportions of O_β increased with respect to O_γ, more active sub-surface oxygens were able to react with soot at the lower temperature. However, as the proportion of O_β continued to increase, its effects were distressingly stark, most probably due to the diffusion limit of oxygen transfer. Nonetheless, this has confirmed the role of active oxygen species in the soot combustion reaction, where they were vital in providing an oxygen source for the initial combustion of soot at low temperatures.

5.4.2 Valence Band Promotion

Valence Band XPS can be used as a tool to investigate the electron population within the metal oxide species. Figure 5-7 are typical valence band XPS of Nd_2O_3 and Tm_2O_3, with and without the loading of Ag.

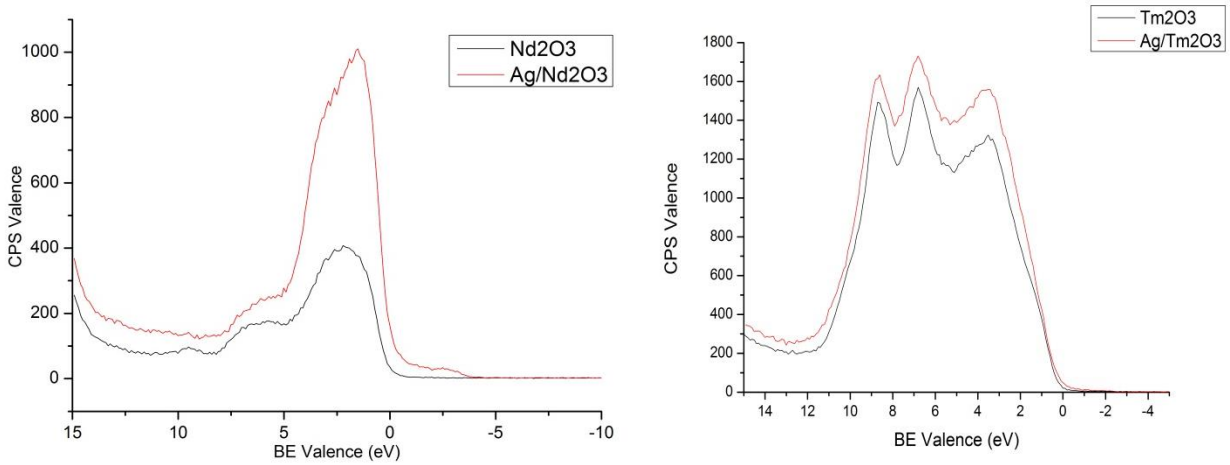

Figure 5-7 Valence Band (VB) XPS of Nd_2O_3 (left), and Tm_2O_3 (right), without Ag (black), and with Ag (red).

The density of state (DoS) of the VB XPS above gives an idea of the electron population in different states within the metal oxide species. It could be seen that there was a great promotion in the DoS of the VB of Nd_2O_3, whereas Ag had little influence in the DoS of the VB population of Tm_2O_3. This meant that there was a much stronger metal – support interaction between Ag and Nd_2O_3 than with Tm_2O_3, and the increase in DoS was due to the population of the metal oxide VB by electrons from the Ag E_f. The net effect was an overall electron withdrawing effect by the metal oxide on Ag. The Ag DoS promotion and the extent of electron

withdrawing ability by the metal oxide could be correlated to its soot combustion ability, as shown in Figure 5-8 below.

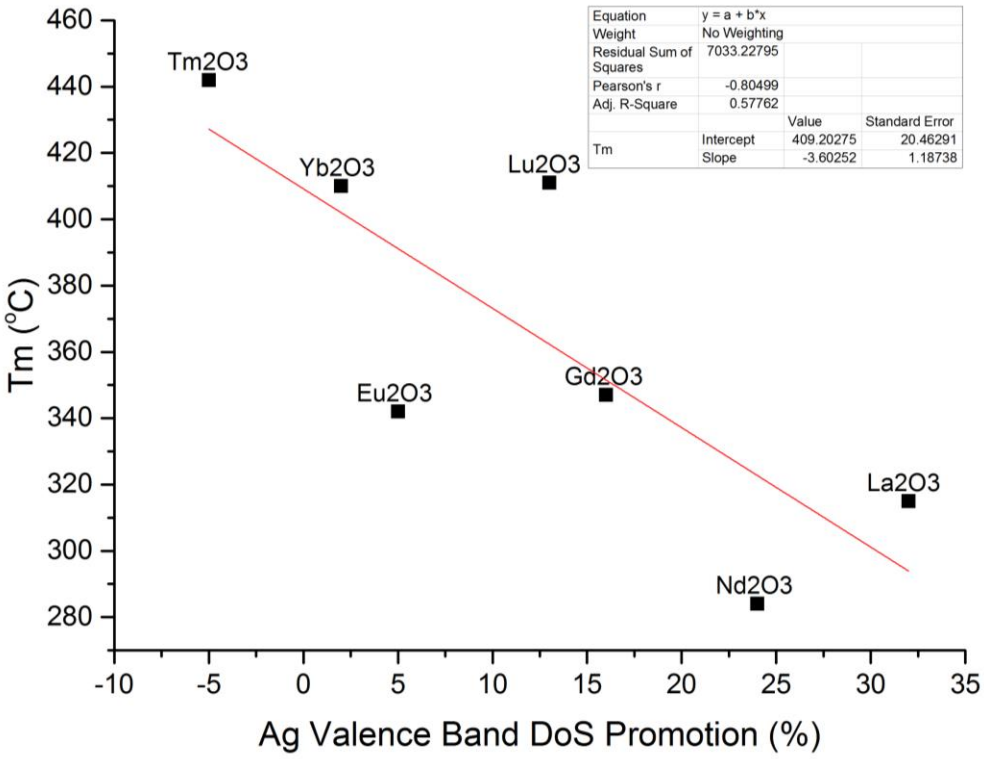

Figure 5-8 ex-CRT Soot T_m versus percentage of Ag VB DoS Promotion.

The population DoS were normalised using the transition at the highest energy, and the Ag promotion was to the lower energy transition. It could be seen that there was a linear relationship between the extent of Ag promotion of the VB DoS, and the soot combustion ability of the corresponding catalyst. With the exception of Tm_2O_3, which had a negative promotion (decrease in DoS), Ag promoted electrons into the VB of the other metal oxides to a certain extent. A general trend was that Ag promotion was much more effective to the early

Ln_2O_3 than the later Ln_2O_3, most probably due to the better electronic interactions between the uncontracted Ln_2O_3 and Ag.

5.4.3 Electron Withdrawing Ability

As discussed in the previous section, the promotion of the metal oxide VB DoS should lead to a positive polarisation of the Ag nanoparticles, resulting in an overall electron withdrawing environment experienced by Ag. Formic acid was used as a probe molecule, and the change in wavenumber of the vibrational modes of adsorbed formic acid would give an indication of the extent of electron withdrawing ability of the metal oxide.

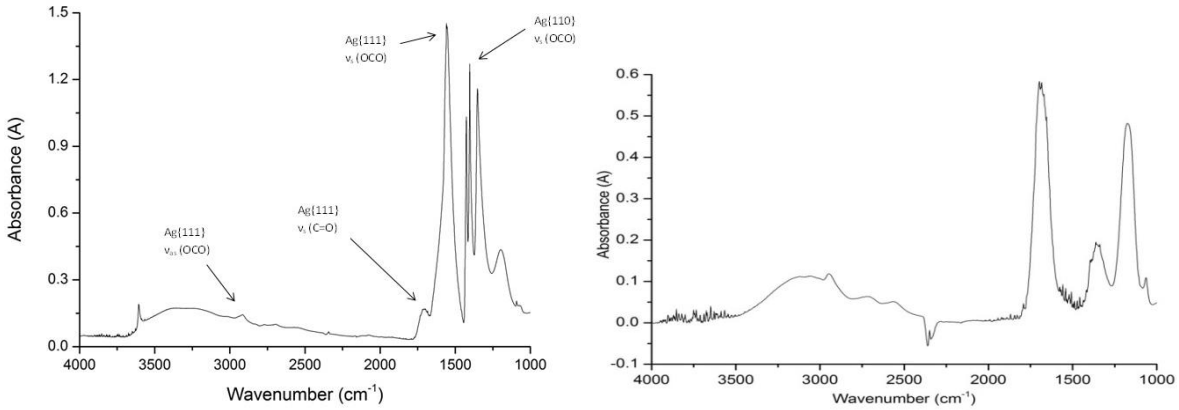

Figure 5-9 FT-IR spectrum of formic acid on Ag/Nd_2O_3, with the vibrational modes labelled (left), and FT-IR spectrum of pure formic acid.

4 vibrational modes could be observed for adsorbed formic acid in Figure 5-9, namely v_s(OCO) on Ag {110} surface at 1300 cm^{-1}; v_s(OCO) on Ag {111} surface at 1650 cm^{-1}; v_s(C=O) on Ag {111}

surface at 1700 cm^{-1}; and v_{as}(OCO) on Ag {111} surface at 2800 cm^{-1}. The symmetric stretch of the carbonyl group on Ag {111} was used as comparison as it offered a direct comparison with unadsorbed formic acid species.

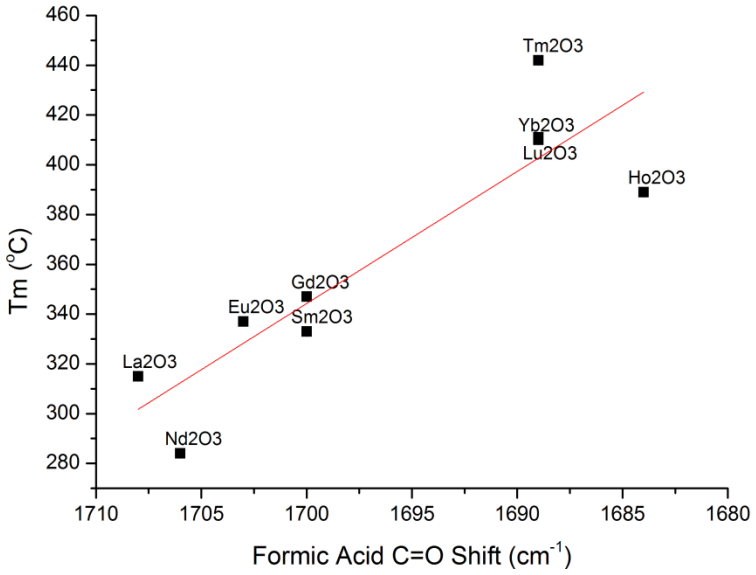

Figure 5-10 ex-CRT Soot T_m versus v_s(OCO). Pure formic acid has v_s(OCO) at 1694 cm^{-1}

From Figure 5-10, it could be seen that all the early Ln_2O_3 had a frequency higher than 1694 cm^{-1} of the unbound species, whereas the late Ln_2O_3 were lower. This meant the Ag on early Ln_2O_3 were electron withdrawing, and electron donating on late Ln_2O_3. This was in good agreement with the VB XPS data shown above, where Ag had a much greater promotion in the VB DoS in the early Ln_2O_3 than the later ones. There was also a clear linear correlation between the electron donating/withdrawing ability of Ag, and its soot combustion ability. It was thus suggested that the metal – support interaction between Ag and Ln_2O_3 were not necessarily

promoting soot combustion, as a "free" Ag with no electronic perturbation from a metal oxide would be expected to have a T_m of around 370 °C, though such an estimation would have been over-simplified. Nonetheless, the SMSI between Ag and Ln_2O_3 could be established, with a strong influence by EMSI, whereby the early Ln_2O_3 had a much more favourable electronic interaction than the late Ln_2O_3.

5.4.4 Oxygen Mobility

From previous sections, it has been established the existence of mobile oxygen species in the form of O_β in Ag/Ln_2O_3. In order to investigate the reactivity of these O_β species, TPR was used to see at what temperatures these active oxygen species could be reduced.

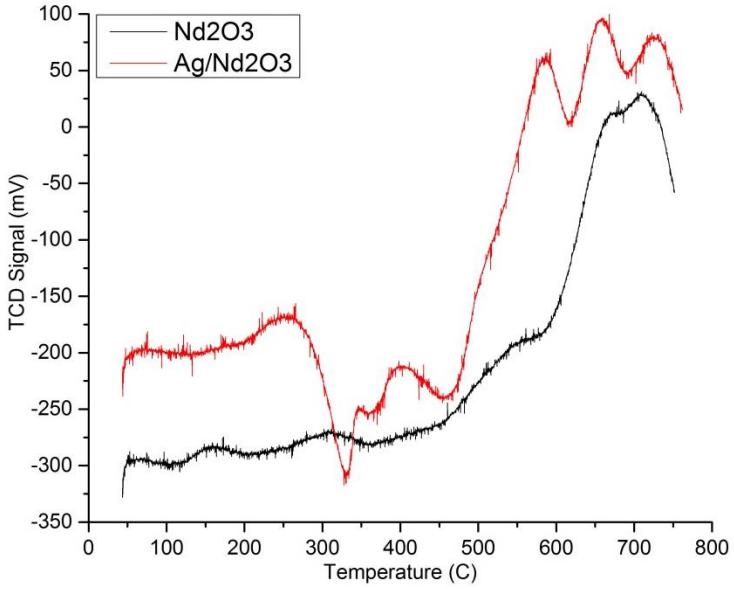

Figure 5-11 TPR profile of Nd_2O_3 (black), and Ag/Nd_2O_3 (red).

Figure 5-11 shows the TPR profile of Nd_2O_3 with and without Ag loading. It could be seen that without Ag loading, only one reduction peak was seen at over 700 °C, corresponding to the reduction of Nd_2O_3. More features on Ag/Nd_2O_3 could be observed, most notably two reduction peaks at 250 °C and 400 °C. These reduction peaks correspond to the reduction of mobile oxygen species induced by the addition of Ag on Nd_2O_3. All early Ln_2O_3 exhibited these reduction peaks, and their positions could be correlated to soot combustion T_m.

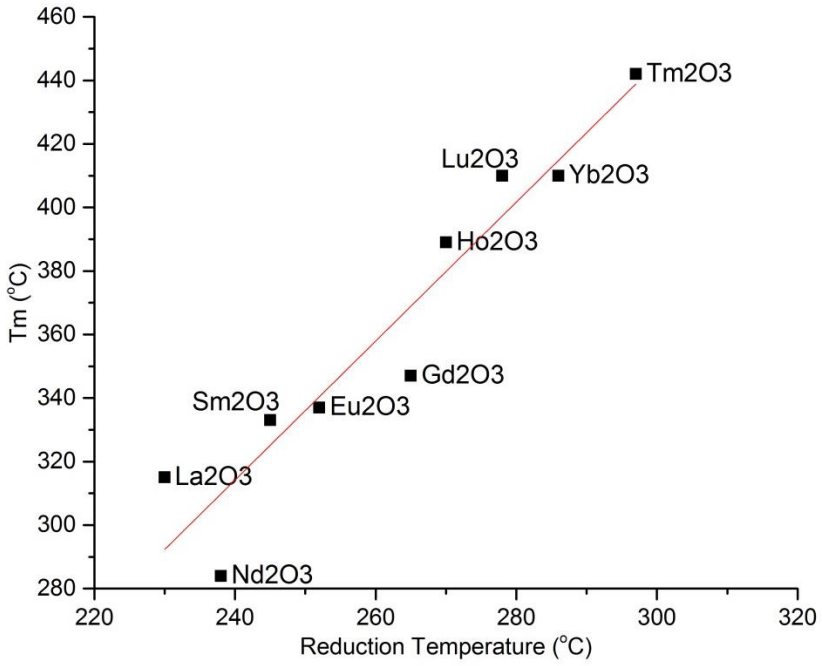

Figure 5-12 ex-CRT Soot T_m versus mobile oxygen reduction temperature as measured by TPR.

Figure 5-12 shows a clear linear correlation between the reduction temperature of the mobile oxygen species, and the ex-CRT T_m. This meant that as the reduction temperature of the mobile

oxygen species decreased, they were more readily available for reaction with soot. This proved that Ag/Ln_2O_3 provided an oxygen source for the soot combustion reaction.

5.5 Thermal Stability of Ag/Ln_2O_3

5.5.1 Ag Aggregation Study

The catalysts must be thermally stable over many heat cycles under the constant temperature flux of a diesel exhaust system before commercially viable. Therefore, *in situ* high temperature studies have been carried out to investigate their thermal stabilities.

The Ag/Ln_2O_3 catalysts were then synthesized with a modified method, where they were calcined in air at 500 °C for 24 hr before use to simulate the conditions experienced after prolonged heat exposure in a diesel exhaust.

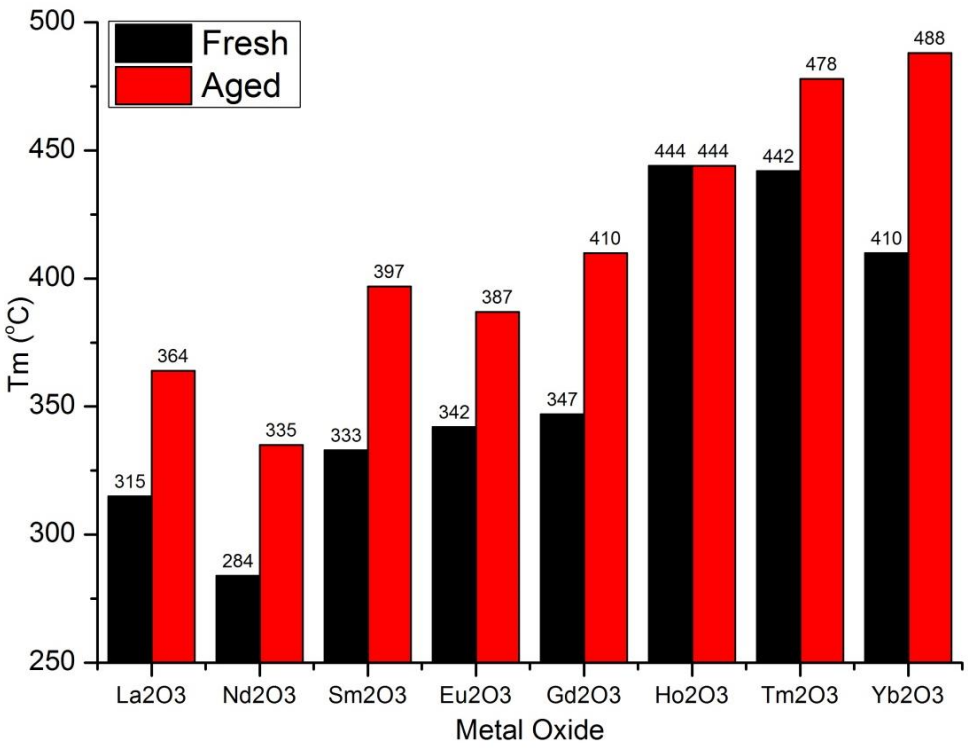

Figure 5-13 ex-CRT Soot T_m of fresh (black), and aged (red) samples of Ag/Ln_2O_3.

Figure 5-13 shows the ex-CRT T_m of fresh and aged samples of Ag/Ln_2O_3. With the exception of Ho_2O_3, all the other Ln_2O_3 had an increase in T_m by 50 K on average. This phenomenon could be better understood by looking at the TEM images of some of the Ag/Ln_2O_3 before and after calcination.

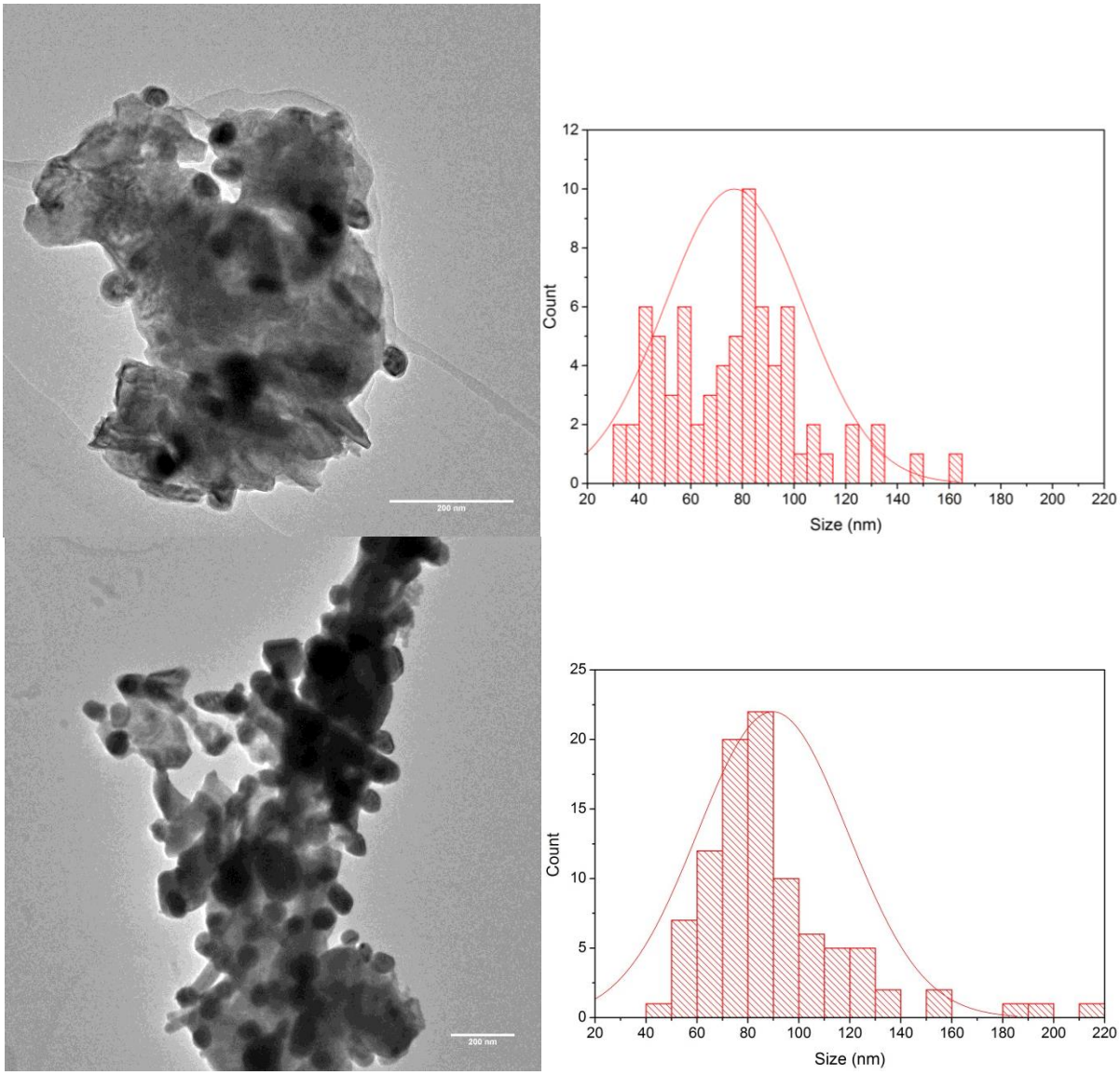

Figure 5-14 TEM images of fresh (top left) and calcined (bottom left) Ag/Nd_2O_3, and the size distribution histogram of fresh (top right) and calcined (bottom right) Ag/Nd_2O_3.

Upon calcination, it was widely expected that Ag aggregation would take place. TEM images confirmed that the size of Ag did increase. At the same time, the extent of aggregation depended on the metal oxide support the Ag was on.

Table 5-3 Ag particle sizes of selective Ln2O3 before and after calcination.

Metal Oxide	Ag Size before Calcination (nm)	Ag Size after Calcination (nm)	Size Increase (%)
La_2O_3	131	141	7.6
Nd_2O_3	64	85	33.8
Eu_2O_3	49	80	63.3

Table 5-3 shows all Ag nanoparticles experienced aggregation upon calcination. The percentage increase in size was different depending on the support. Ag aggregation was greater across the early lanthanide series, which suggested that there was a lower degree of metal – support interaction across the series, and so the Ag nanoparticles were not held on to the Ln_2O_3 support as strongly. As the late Ag/Ln_2O_3 had little metal – support interactions, the thermal aggregation of these Ag nanoparticles were also going to be much greater. However, as the support played almost no role in promoting the soot combustion reaction, the effects of the Ag agglomeration were not as significant as the early Ag/Ln_2O_3.

5.5.2 Repeated Testing

Instead of using calcined samples, fresh samples were used to investigate the stability of Ag/Ln_2O_3 for repeated reactions of soot. However, as some catalyst was lost in the grinding process when making a tight contact mixture with soot, it would be unfeasible to do multiple tight contact tests as the amount of catalyst lost would be substantial. Therefore, loose contact was used for repeated testing of the catalysts.

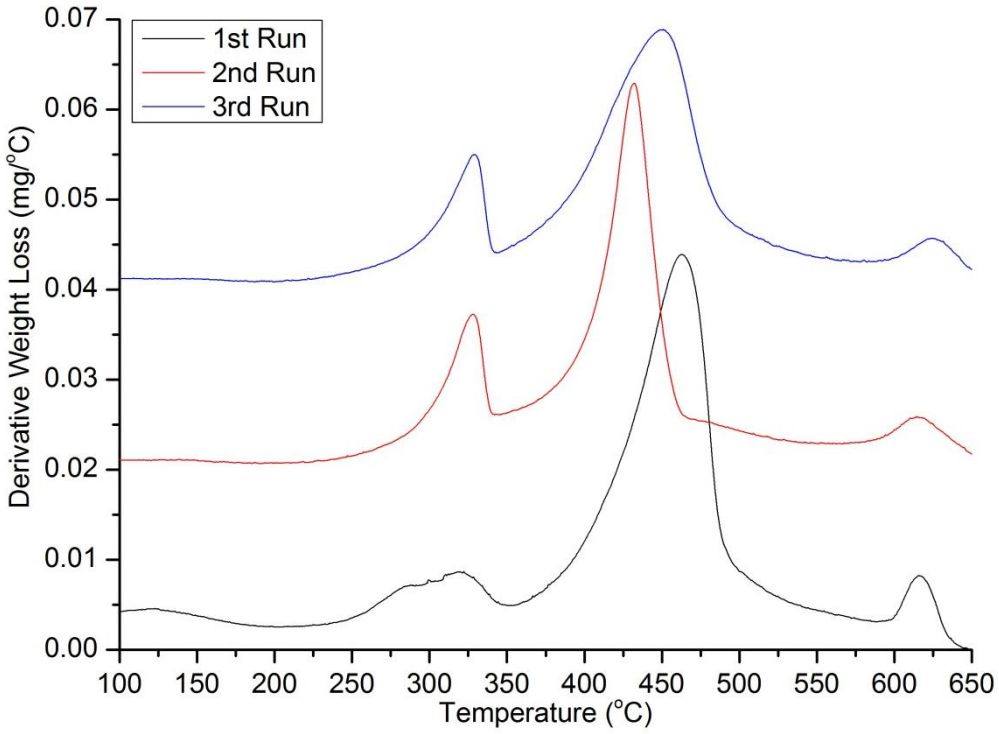

Figure 5-15 DTG profiles of successive ex-CRT Soot combustion with Ag/Nd_2O_3 in loose contact.

Figure 5-15 shows DTG profiles of successive ex-CRT soot combustion with Ag/Nd_2O_3 in loose contact. Some features could be seen in the DTG profiles that would not have been immediately obvious in a tight contact profile. Firstly, there appeared to be three peaks of weight loss at 300 ^{o}C, 450 ^{o}C, and 620 ^{o}C. These peaks corresponded to soot that had a more intimate contact with the catalyst through mixing, soot with little contact with the catalyst, and soot with no contact with the catalyst at all, respectively. There appeared to be little difference in T_m between successive runs. This suggested that Ag/Nd_2O_3 was able to withstand multiple heat cycles for repeated reaction of soot. A very similar profile could be observed with late Ag/Ln_2O_3, where there was little change in T_m over three reaction cycles with soot.

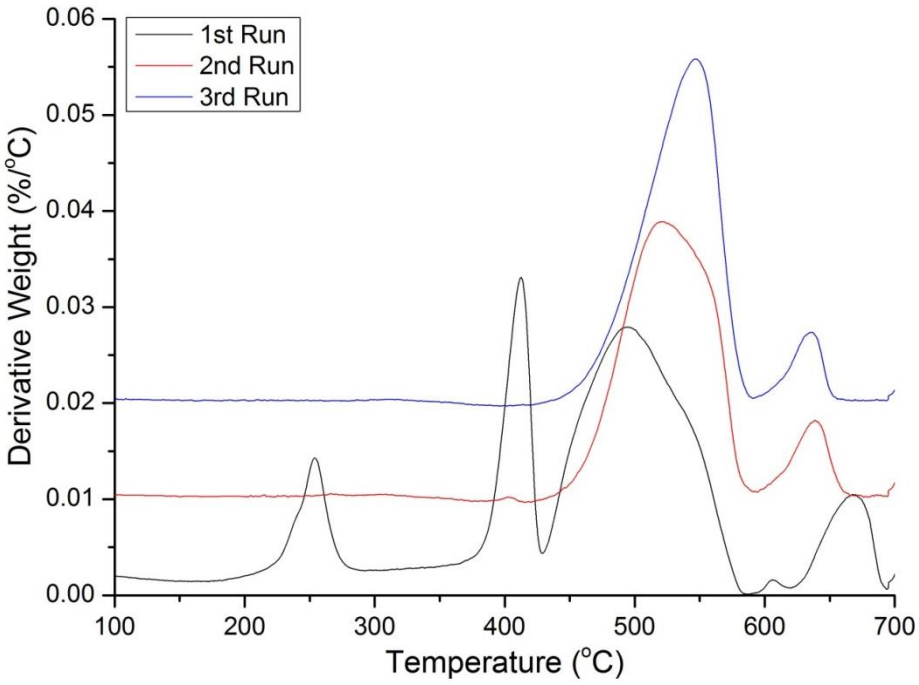

Figure 5-16 DTG profiles of successive ex-CRT Soot combustion with Ag/La_2O_3 in loose contact.

However, this was not the case for Ag/La_2O_3, where T_m was observed to increase steadily over three successive reaction cycles with soot. This suggested that Ag/La_2O_3 was not suitable for use for multiple reaction cycles. This loss in activity would be discussed in more detail in later sections.

5.5.3 *In Situ* XRD Study

Hu *et al.* proposed that heating Ag in air and vacuum would result in different extents of lattice expansion[11]. It was argued that atmospheric oxygen in air would adsorb into the Ag subsurface and form $Ag^{+}O^{-}_{2(ads)}$ species. As this was performed on standalone Ag nanoparticles, it would be interesting to observe the effects Ln_2O_3 had on the Ag lattice parameter on heating.

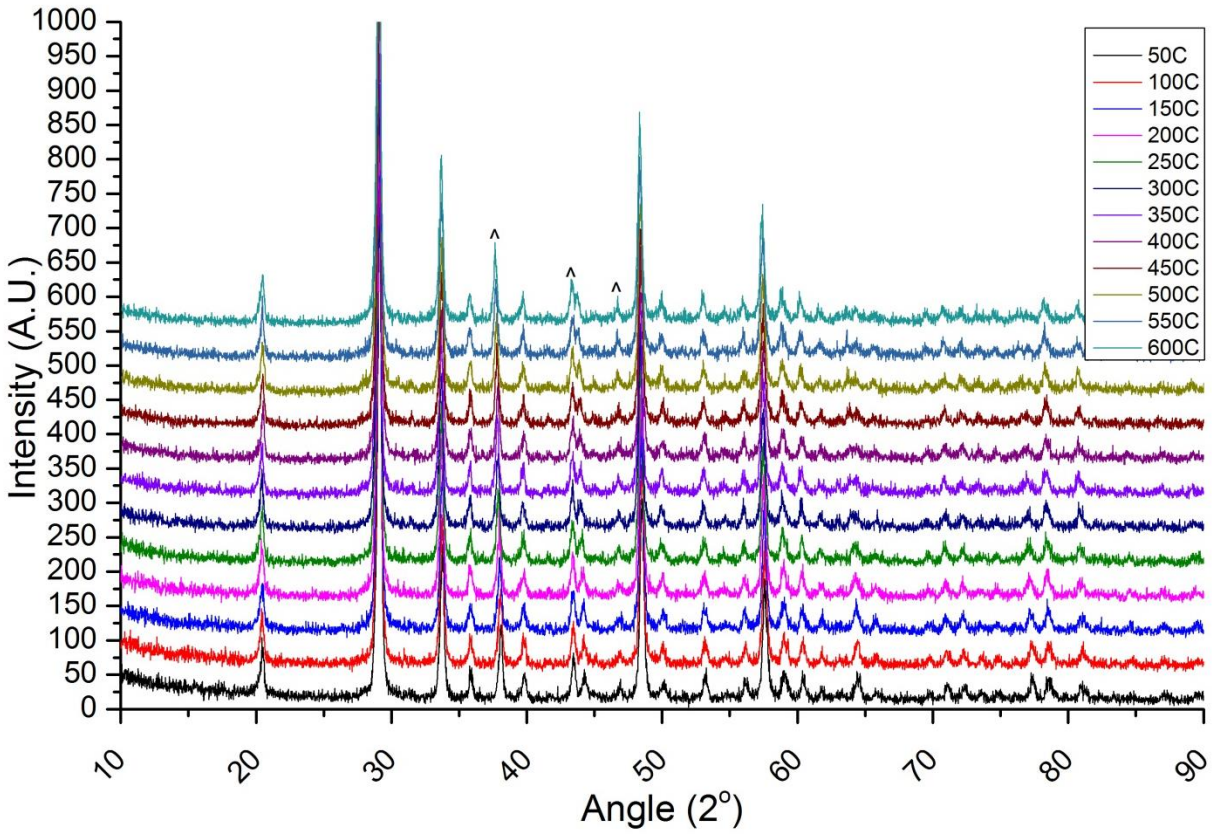

Figure 5-17 *In situ* XRD profile of 10% Ag/Ho_2O_3 in air. (^) represents Ag peaks, all other peaks are Ho_2O_3.

Figure 5-17 shows the *in situ* XRD profile of 10% Ag/Ho_2O_3 in air up to 600 ^{o}C. Very little could be seen as there were no phase changes observed in this temperature range. However, on closer inspection of the Ag (111) peak (*ca.* 38^{o}), it could be seen that there was indeed lattice expansion of Ag (111) upon heating.

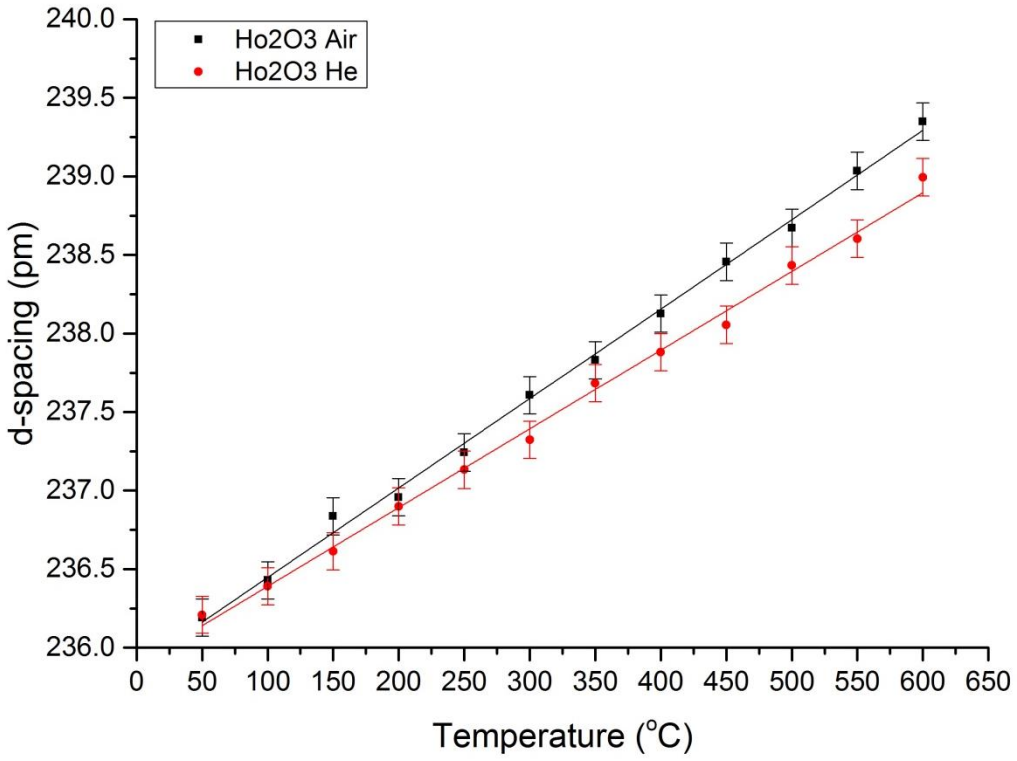

Figure 5-18 Ag (111) lattice parameter in air (black), and in He (red) versus temperature.

Figure 5-18 shows linear lattice expansion of Ag (111) in both air and He. It also conformed to what Hu *et al.* reported[11]. Ag expansion was greater in air (5.69 fm K^{-1}) compared to He (5.01 fm K^{-1}). This suggested that there was indeed oxygen adsorption into the Ag subsurface when supported on Ho_2O_3. However, it was not as straightforward for the early Ag/Ln_2O_3, as demonstrated in Figure 5-19 below.

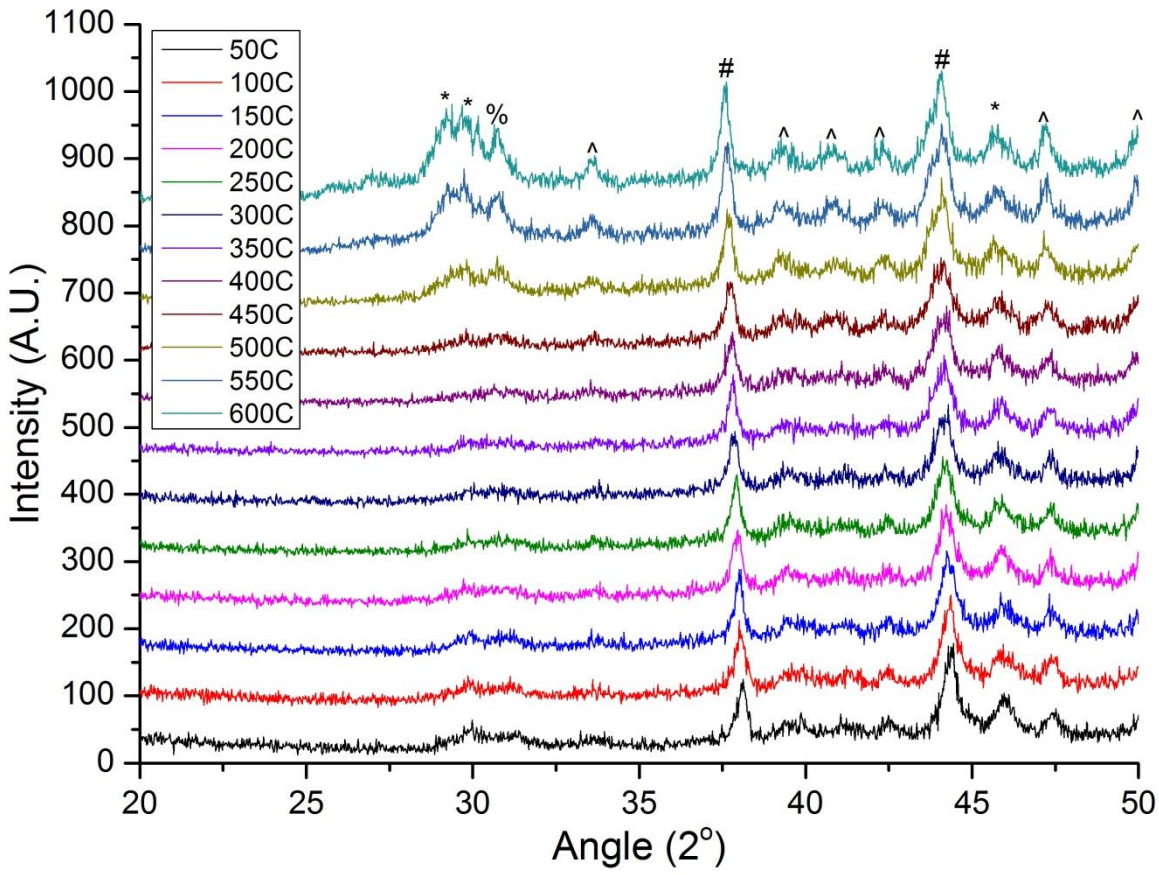

Figure 5-19 *In situ* XRD profile of 10% Ag/La_2O_3 in air. (*) = La2O3; (^) = LaOOH; (%) = La2O2CO3; (#) = Ag.

Figure 5-19 shows the *in situ* XRD profile of Ag/La_2O_3 in air. It showed a much different picture to that seen with Ag/Ho_2O_3. Firstly, the La_2O_3 had a small proportion of LaOOH present, even up to 600 ^{o}C. Secondly, CO_2 appeared to be adsorbed onto the La_2O_3 to form a $La_2O_2CO_3$ phase at 500 ^{o}C, becoming more prominent towards 600 ^{o}C. Thirdly, La_2O_3 appeared to be aggregating to become more crystalline at higher temperatures. This aggregation of La_2O_3 would explain the loss of activity of Ag/La_2O_3 over successive reactions with soot, since the active surface area of the La_2O_3 would have dramatically decreased, making contact with soot more difficult.

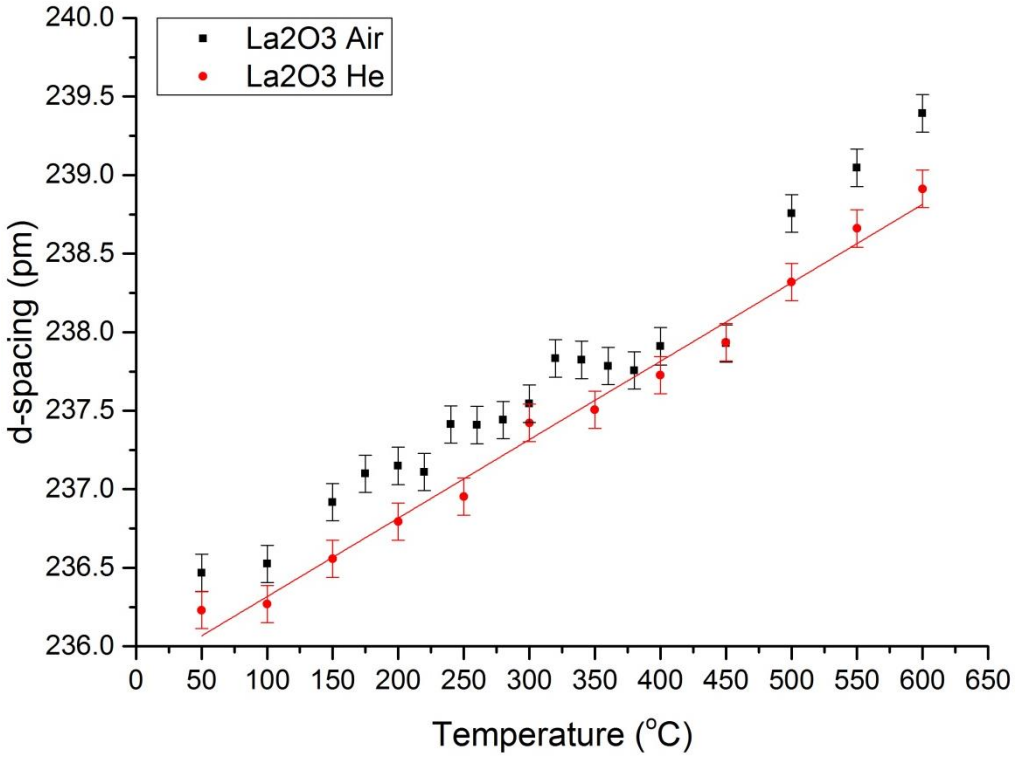

Figure 5-20 Ag (111) lattice parameter in air (black), and in He (red) versus temperature.

Figure 5-20 shows the Ag (111) lattice parameter of Ag/La_2O_3 when heated in air and He. Whereas the lattice expansion in He was the same as Ag/Ho_2O_3 (5 fm K^{-1}), interesting features could be observed when heated in air. "Steps", or temperature ranges with no thermal expansion, were observed. To the best of my knowledge, this has not been reported in open literature before. Looking at Ag/Nd_2O_3 and Ag/Eu_2O_3, a similar feature could be observed.

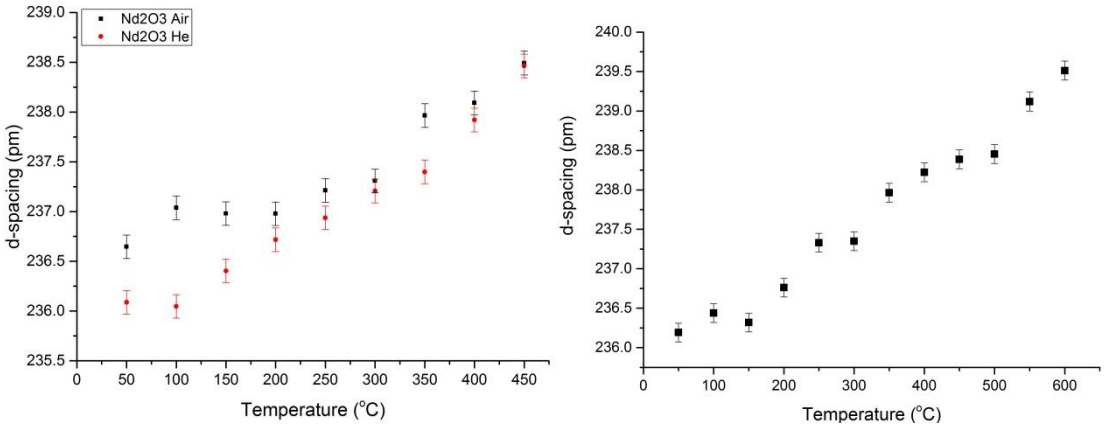

Figure 5-21 Ag (111) lattice parameter in air (black), and in He (red) of Ag/Nd_2O_3 (left), and Ag/Eu_2O_3 (right) versus temperature.

Since metallic Ag lattice expansion was linear in the temperature range that was tested, even with oxygen absorption, these steps observed must be due to species that were not metallic Ag. The Ag_2O (200) peak also occurred at 38^o, which overlapped with the metallic Ag (111) peak. Therefore the species observed at lower temperature would be Ag_2O from the reaction of adsorbed oxygen with Ag on the surface of the Ln_2O_3. As discussed in previous sections, the Ag on the early Ln_2O_3 was positively polarised, which made them more prone to reaction with oxygen to form Ag_2O. This meant that early Ag/Ln_2O_3 had a much greater ability to activate atmospheric oxygen to form adsorbed oxygen or even ionic oxide species, both of which could be used for low temperature activation of soot combustion.

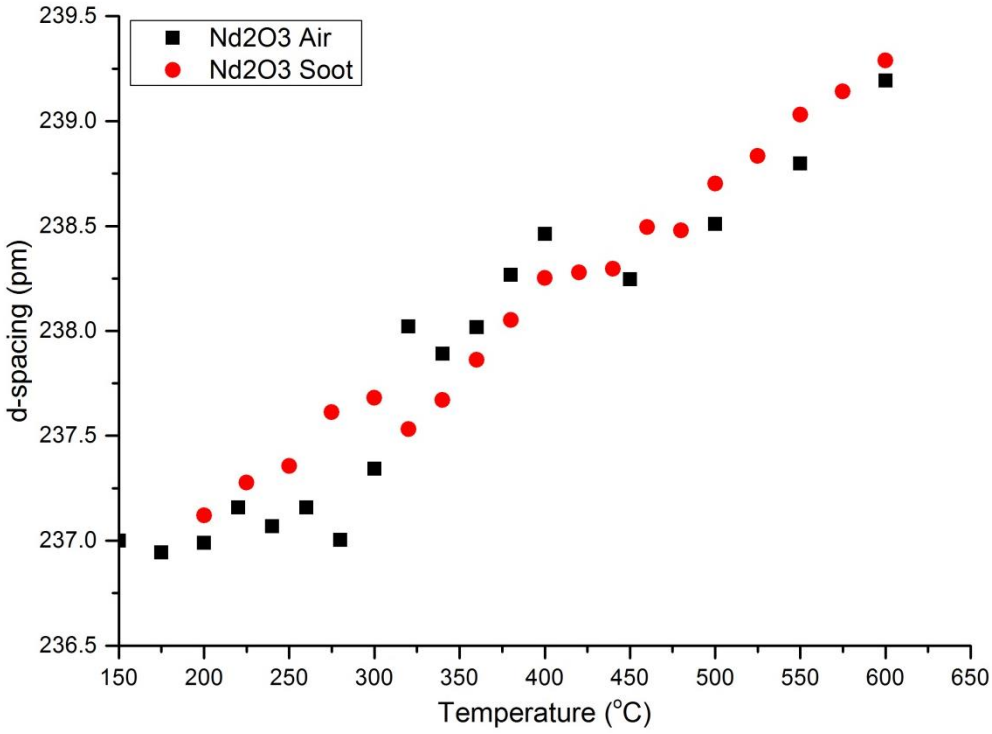

Figure 5-22 Ag (111) lattice expansion of Ag/Nd_2O_3 in air without soot (black), and with soot (red).

When soot was added to Ag/Nd_2O_3, these "steps" became much less pronounced, and a much more linear expansion was observed, in line with what was observed when Ag/Nd_2O_3 was heated in He. This suggested that the Ag_2O was no longer formed in the presence of soot. This confirmed that as the soot was being burnt at this temperature range (250 – 400 °C), the oxygen that was otherwise bound as Ag_2O was used as an oxygen source for soot combustion. The Ag_2O found in the early Ag/Ln_2O_3 was therefore an easily assessable oxygen source for the soot, and therefore early Ag/Ln_2O_3 had a much lower T_m than later Ag/Ln_2O_3.

Figure 5-22 shows that the Ag (111) lattice expansion became linear at 450 °C, which suggested the decomposition of Ag_2O to re-form Ag. On successive runs these "steps" were still found to be present in the expansion of early Ag/Ln_2O_3, which suggested the formation and decomposition of Ag_2O species were completely reversible.

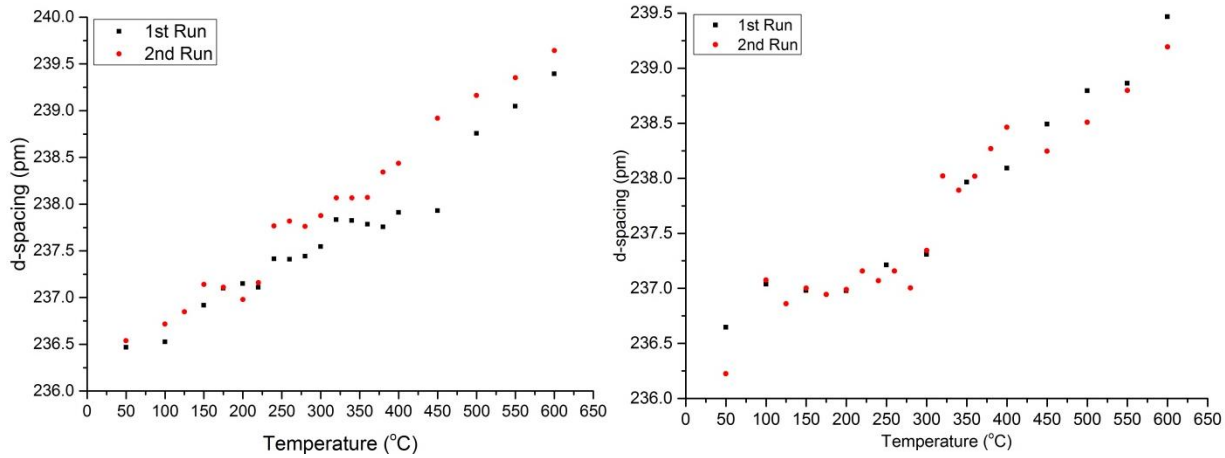

Figure 5-23 Ag (111) lattice parameter on 1st run (black), and 2nd run (red) of Ag/La_2O_3 (left), and Ag/Nd_2O_3 (right).

For Ag/La_2O_3, the "steps" on the re-run was not as clear as the first run, most probably due to La_2O_3 aggregation and the loss of surface area for Ag support. However, the formation of Ag_2O was still evident, which suggested there was still a large extent of SMSI between Ag and La_2O_3. However, the lattice parameters of Ag were nearly identical for the two runs on Ag/Nd_2O_3, which indicated the formation of Ag_2O to be facile and reversible.

5.6 Exhaust Gas studies

Having established a possible reaction mechanism, another important point is to investigate the gas output, and whether complete combustion has been achieved. For this, MS was attached after the TGA to analyse the exhaust gases.

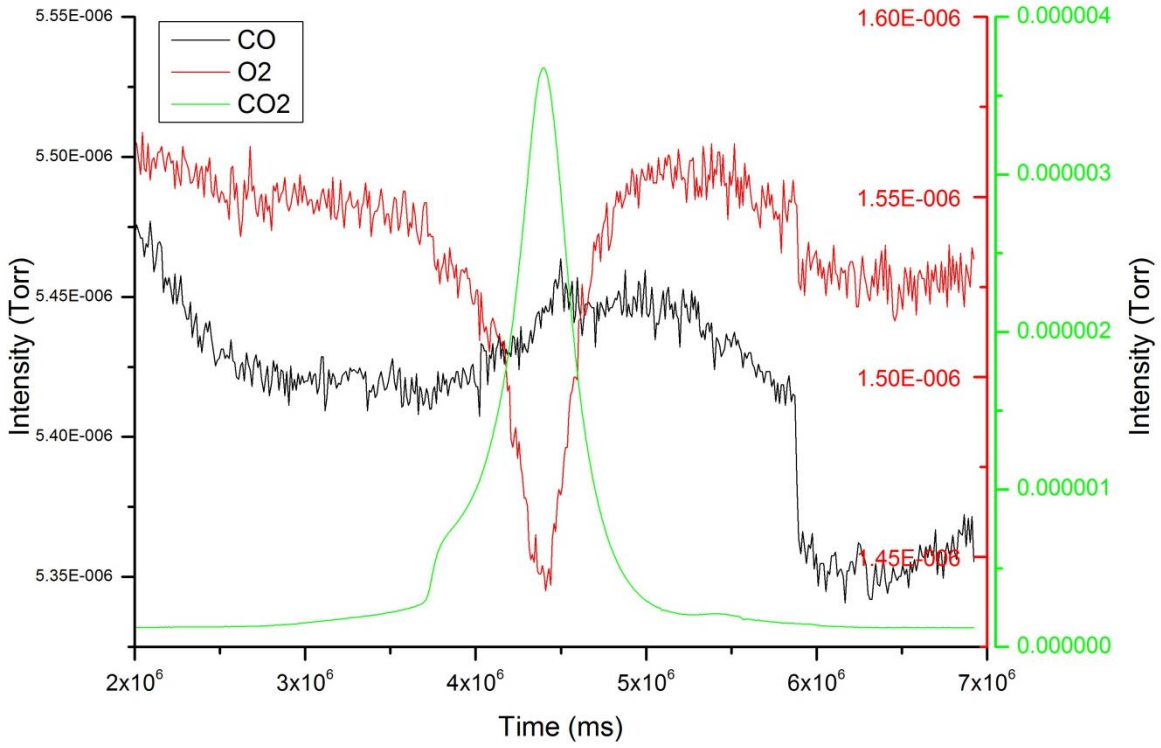

Figure 5-24 MS profile of ex-CRT soot with Ag/Nd_2O_3 in tight contact. CO (black), O_2 (red), and CO_2 (green) intensities were detected. *N.B.* CO and N_2 have the same m/z.

Figure 5-24 shows the MS profile of ex-CRT soot with Ag/Nd_2O_3 in tight contact. It appeared that only CO_2 was produced from the complete combustion of soot, and no CO was produced. There was a slight increase in CO signal intensity due to the fragmentation of CO_2, which was consistent with the ratios expected for CO_2.

However, when put on the same scale, it was found that the amount of O_2 consumed in the combustion process was much less than the amount of CO_2 produced.

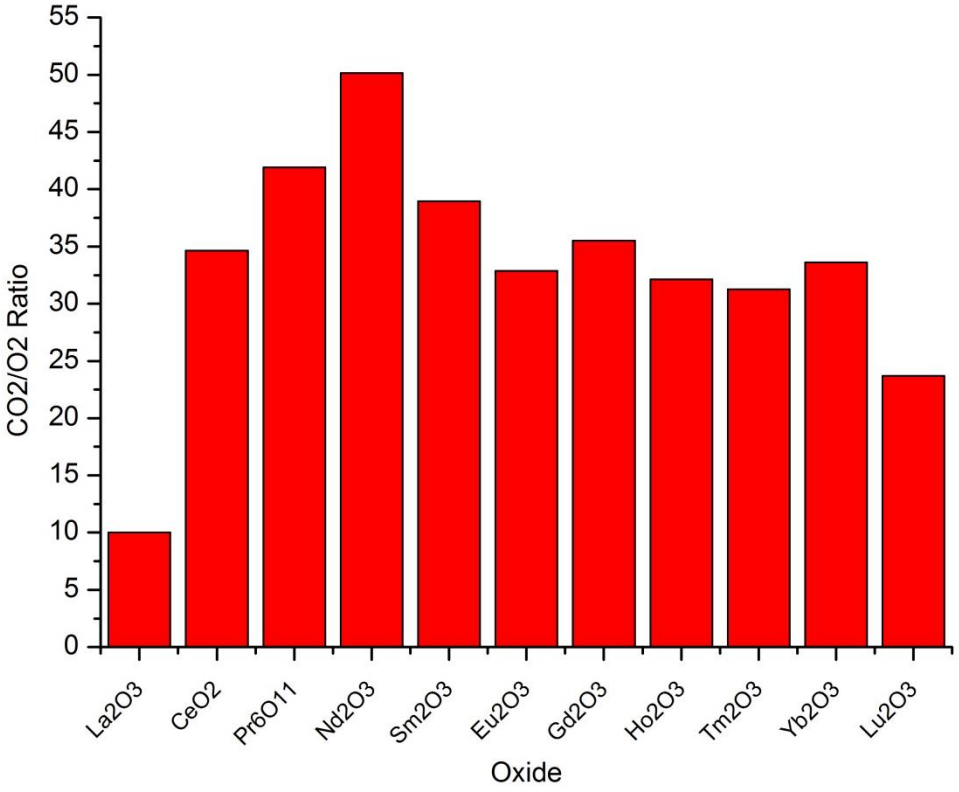

Figure 5-25 CO_2/O_2 ratio of integrated MS intensities for ex-CRT soot with Ag/Ln_2O_3.

As one molecule of oxygen would react to form one molecule of CO_2, the integral of the O_2 and CO_2 peaks would be expected to be the same. However, the CO_2 peak integral was found to be 10 to over 50 times greater than the O_2 signal. This suggested that the response factor for the two gases were different. Nonetheless, the ratio between the two gases could still give an indication of the soot combustion mechanism.

Figure 5-25 shows the integrated CO_2/O_2 peak ratios for ex-CRT soot combustion with Ag/Ln_2O_3. There was a huge variation in the ratio of CO_2/O_2 peak integrals, with Ag/Nd_2O_3 having the highest ratio of over 50. This meant that Ag/Nd_2O_3 consumed the least amount of O_2 in the soot combustion process relatively. On the other hand, Ag/La_2O_3 had the lowest ratio of 10, which suggested that a much greater amount of the oxygen consumed came from the gas feed. The CO_2/O_2 ratio could be correlated to the respective T_m, as shown in Figure 5-26.

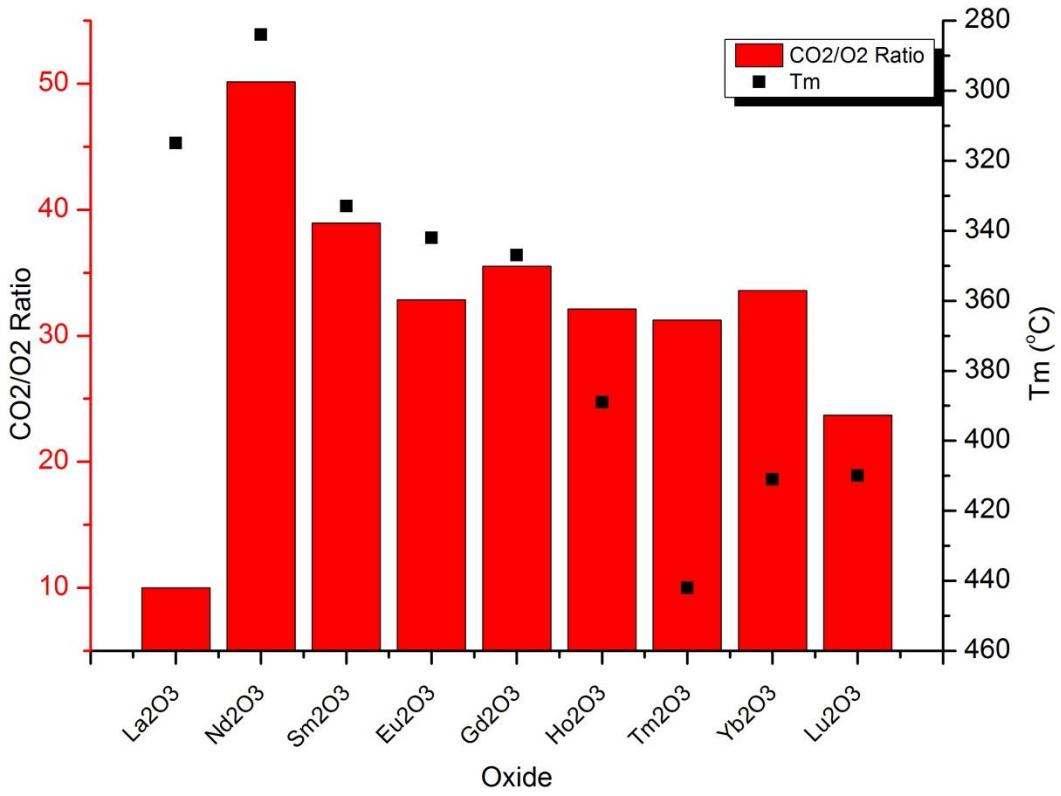

Figure 5-26 CO_2/O_2 ratio (red) and T_m (black) of ex-CRT Soot with Ag/Ln_2O_3. N.B. T_m scale reversed.

With the exception of Ag/La_2O_3, it was generally found that a higher CO_2/O_2 ratio would yield a lower T_m. This meant that the Ln_2O_3 support must be providing an oxygen source for the soot combustion. A reasonable soot combustion mechanism could thus be devised.

The electron withdrawing Ln_2O_3 firstly positively polarised Ag on its surface, which could activate O_γ in the oxide to become more mobile O_β. This O_β species were then responsible for the low temperature combustion of soot, with atmospheric oxygen activation at the metal – support interface for soot combustion as well. At high temperature the oxygen deficiency of the metal oxide could be replenished by atmospheric oxygen after soot combustion. This could suggest that Ag and Ln_2O_3 had an intimate EMSI, and Ln_2O_3 were not purely ionic as previously thought.

5.7 Industrial Testing

Having established that Ag/Ln_2O_3 was active soot combustion catalysts, and they were thermally stable for repeated testing, the reaction was scaled up to investigate the potential for further developments in a commercial system.

Tests were carried at Johnson Matthey Technology Centre (JMTC) using a Hiden Catlab. The reaction mixture was scaled up to 100 mg, and was placed in a quartz reactor tube for reaction.

12% O_2/He was used the reactor feed gas, and the exhaust gas output was monitored by MS. 4 catalysts were tested at JMTC, namely Ag/La_2O_3, Ag/Nd_2O_3, Ag/Pr_6O_{11}, and Ag/Lu_2O_3.

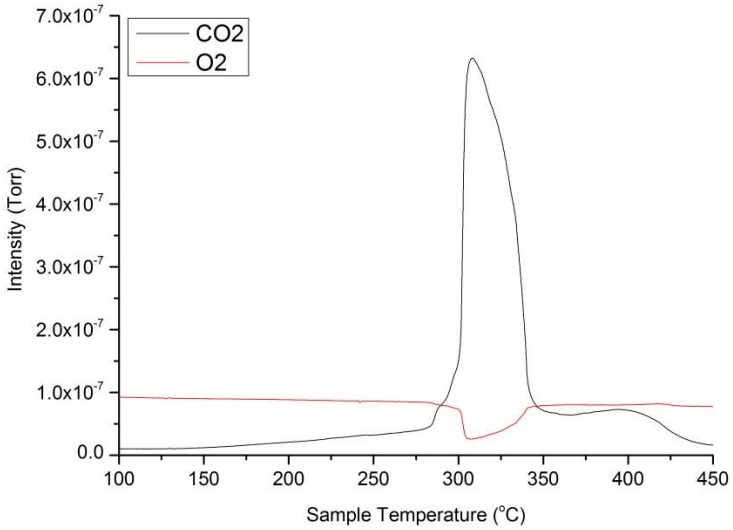

Figure 5-27 MS Profile of ex-CRT soot with Ag/Nd_2O_3 in tight contact. CO_2 (black) and O_2 (red) intensities were detected.

The scaled up reaction, like the lab-based testing, showed the evolution of CO_2 as the sole product, with no CO production detect. This suggested that the catalysts were suitable for soot combustion in a larger scale than the previous tests performed in the laboratory.

The catalysts were then aged at 500 ^oC to simulate prolonged exposure in high temperature. The results were striking as it did not conform to laboratory testing results, shown in Figure 5-28.

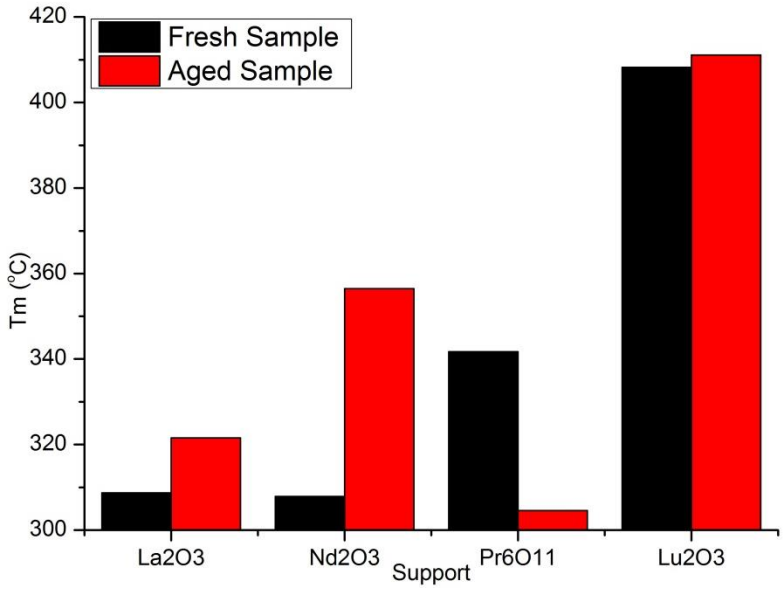

Figure 5-28 ex-CRT soot T_m with Ag/Ln_2O_3 of fresh samples (black), and samples aged at 500 °C (red).

Firstly, Ag/Pr_6O_{11} was found to be much more active in industrial testing than in laboratory testing, and Ag/Lu_2O_3 much less active. Secondly, the T_m increase for Ag/Nd_2O_3 was much more after aging in industrial testing. Thirdly, Ag/Pr_6O_{11} actually had a decrease in T_m after aging, which had never been observed in any of the previous laboratory testing, nor had there been any literature reports on activation by aging.

However, some general trends still conformed to laboratory findings. Firstly, the extent of deactivation was much greater for early Ag/Ln_2O_3 or La_2O_3 and Nd_2O_3 than Lu_2O_3, due to the diminishing extent of SMSI. Secondly, the general trend for T_m was the same for sesquioxide lanthanide oxides, where the most active soot combustion catalyst was Ag/Nd_2O_3, albeit by a smaller margin.

5.8 Au/Ln_2O_3 Catalysts

The activity of Ag/Ln_2O_3 was mainly due to the EMSI between Ag and Ln_2O_e, which led Ag to be positively polarised by early Ln_2O_3, which could then activate molecular oxygen to form O_β. Au also has a +1 oxidation state, which in theory perform the analogous reaction. Few papers have reported the use of Au as a soot combustion catalyst, and it would be interesting to look at the activity of Au for the soot combustion reaction.

5% Au/Ln_2O_3 were synthesised using the same method as Ag/Ln_2O_3, and the catalysts were tested using the same method under the same conditions as their Ag counterparts.

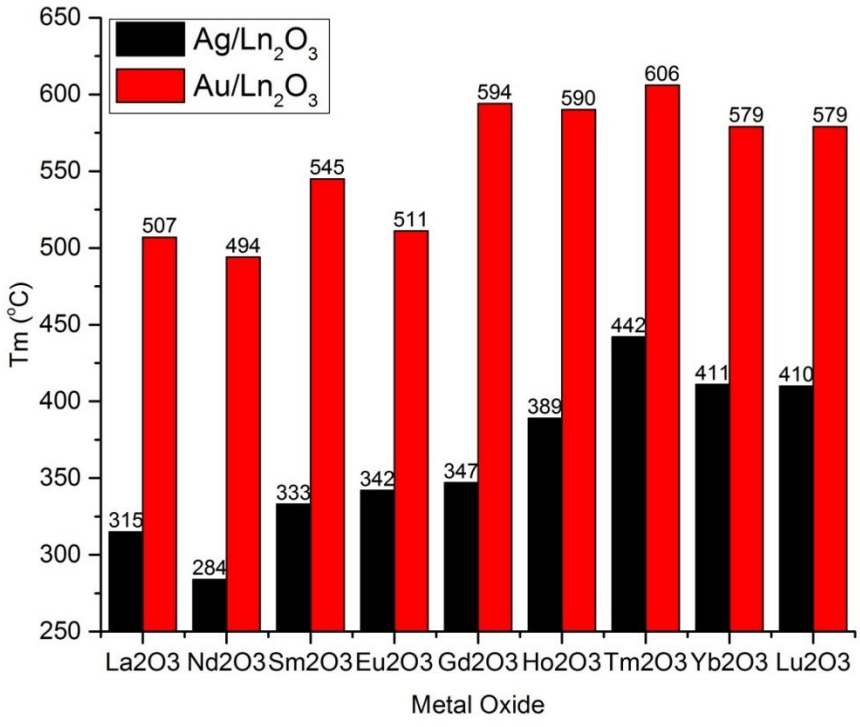

Figure 5-29 ex-CRT Soot T_m of Ag/Ln_2O_3 (black) and Au/Ln_2O_3 (red).

Figure 5-29 shows that whereas the general trend for both Ag and Au supported catalyst were the same, Au/Ln_2O_3 were much less active than their Ag counterpart to a point of nearly no activity at all (*cf.* ex-CRT T_m at 610 ^oC).

This lack of activity was mainly due to the lack of any active oxygen species present in Au/Ln_2O_3.

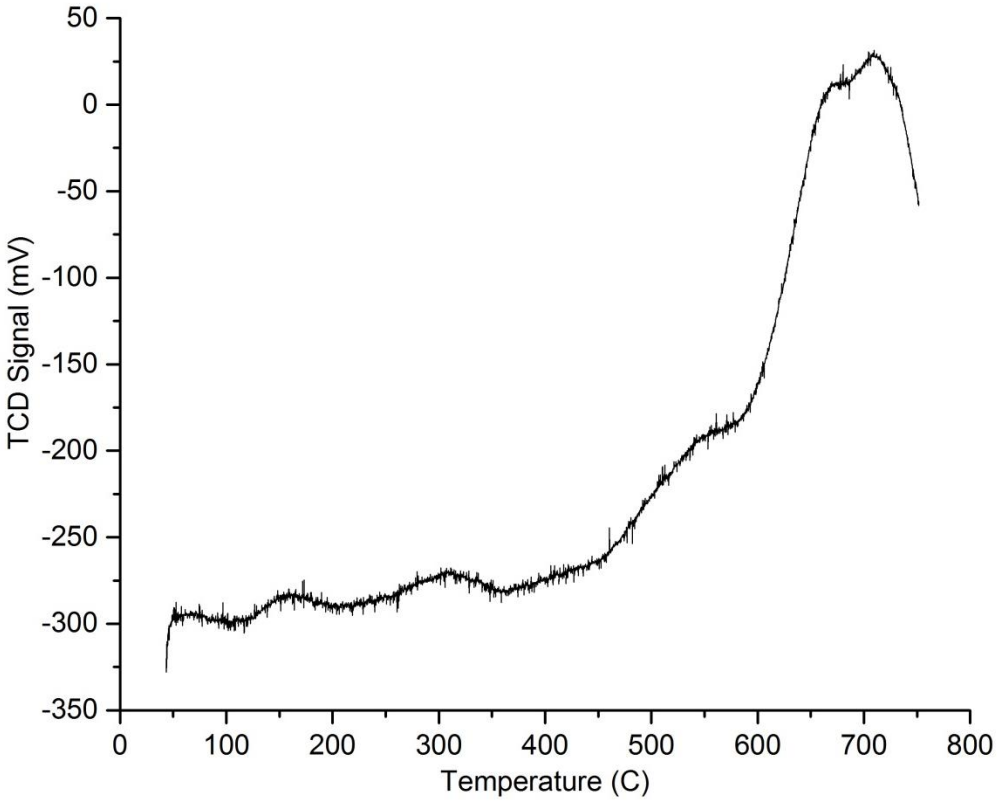

Figure 5-30 TPR profile of Au/Nd_2O_3.

Figure 5-30 shows the TPR profile of Au/Nd_2O_3, which showed a lack of any reduction peaks at low temperatures. The same observation was made across the entire lanthanide series, where no reduction peaks were seen at temperatures below 500 ^{o}C. This meant that the mobile oxygen species found in Ag/Ln_2O_3 were absent in Au/Ln_2O_3.

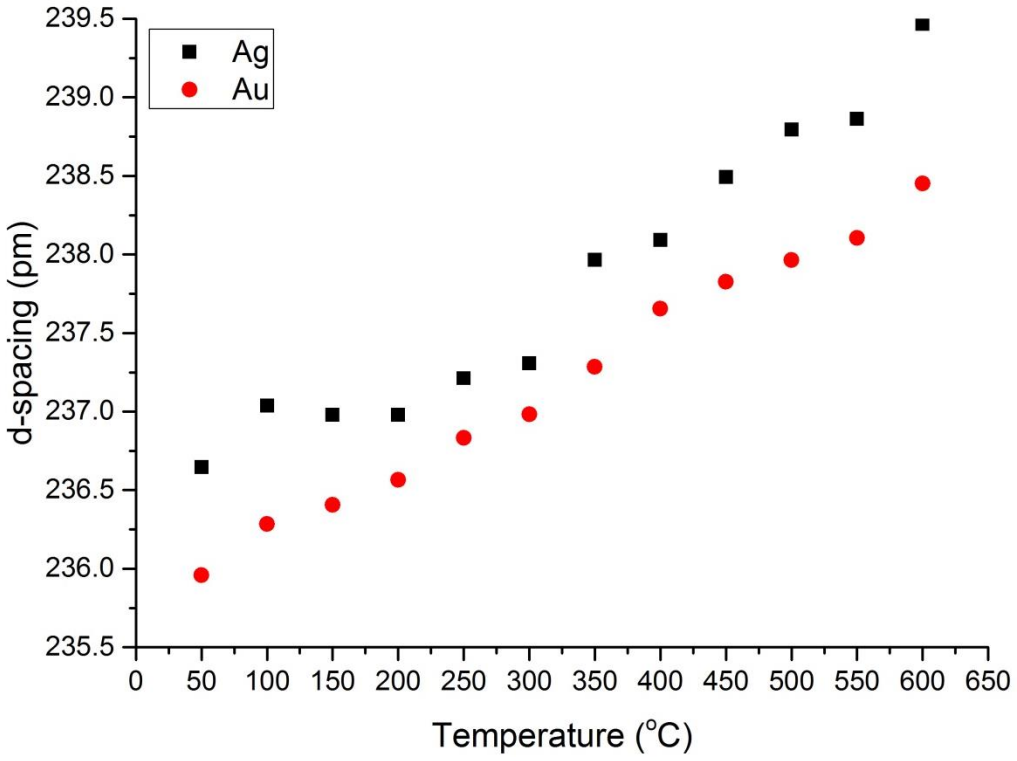

Figure 5-31 Lattice Parameter of Ag (111) and Au (111) loaded on Nd_2O_3 in air.

Figure 5-31 shows the lattice parameter of Ag (111) and Au (111) loaded on Nd_2O_3 when both were heated in air. Au (111) had a linear expansion of 4.46 fm K^{-1}, with no "steps" that were seen with Ag loaded on early Ln_2O_3. This also suggested the absence of adsorbed oxygen species that was able to form Au_2O.

From the TPR and *in situ* XRD results, it could be concluded that Au lacked the ability to activate molecular oxygen to form O_β, and therefore it was not suitable as a soot combustion catalyst.

5.9 C_{60} Combustion

C_{60} was chosen to be a model carbon as it was a pure carbon source with a defined structure. Pyrene was also chosen to be a model carbon as its ringed aromatic structure more closely resembled what would be emitted as diesel exhaust. However, pyrene had a boiling point that was below its ignition point, meaning it was unable to be burnt. C_{60} had a much higher boiling point, so although its structure was not as closely related to diesel soot, it still provided valuable information into the reaction mechanism of soot combustion.

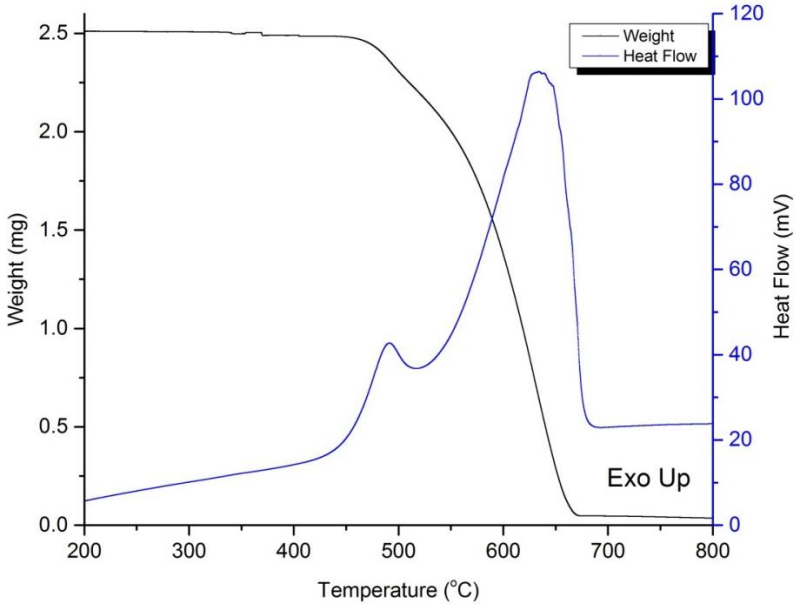

Figure 5-32 TGA (black) and DSC (blue) profiles of C_{60} combustion.

T_m of pure C_{60} was 635 ^oC, which was significantly higher than the two types of soot used for catalyst testing. This was because C_{60} was a pure carbon molecule, so there were no volatile hydrocarbons that could be burnt at a lower temperature. DSC showed the enthalpy of combustion was 16.3 MJ mol^{-1} (22.6 kJ g^{-1}), again significantly higher than that of the two types of soot. This suggested C_{60} would be much harder to burn than the soot previously tested.

Table 5-4 T_m of C_{60} with Ag/Ln_2O_3 under low or high O_2 flow.

Metal Oxide	**Low O_2 Flow T_m (^oC)**	**High O_2 Flow T_m (^oC)**
La_2O_3	489 ± 4	379 ± 2
Nd_2O_3	419 ± 4	376 ± 2
Sm_2O_3	454 ± 4	368 ± 3
Eu_2O_3	455 ± 4	366 ± 2
Gd_2O_3	526 ± 4	362 ± 2
Ho_2O_3	558 ± 4	425 ± 2
Tm_2O_3	557 ± 4	487 ± 2
Yb_2O_3	528 ± 4	408 ± 2

Unlike soot combustion, C_{60} combustion was affected by the concentration of O_2. At low O_2 concentration of *ca.* 5%, C_{60} combustion temperatures were significantly higher than when it was burnt in a high concentration of O_2 (20%).

The C_{60} T_m of late Ag/Ln_2O_3 in low O_2 concentration was indicative of an inactive catalyst, where it almost played no part in the combustion of C_{60}. This meant that at low O_2 concentration, there was not enough atmospheric oxygen to interact with the catalyst to form the O_β species for C_{60} combustion. Although the metal oxide was also able to some O_β in the form of O_γ activation, it was not enough to sustain the oxidation reaction with C_{60}. At high O_2 concentration, atmospheric oxygen activation was much quicker, and so the catalyst was able to provide high energy oxygen species to C_{60} for oxidation. Therefore the reaction was diffusion limited only at low O_2 concentration.

This was in stark contrast to soot combustion, where T_m appeared to be independent of O_2 concentration down to 5%. However, as C_{60} was much harder to burn, it could be possible that the process of oxygen activation was diffusion limited, volatile hydrocarbon fractions were still able to be burnt. It is therefore not unreasonable to postulate that at even lower oxygen concentrations an increase in T_m for soot combustion was observed.

5.10 Soot Combustion Mechanism

In previous sections, various factors that determined the soot combustion activity of Ag/Ln_2O_3 were discussed. In summary, an active support should be electron withdrawing, with Ag activating lattice O_γ to form active mobile O_β. Ag was also able to promote electrons into the metal oxide VB, increasing its DoS. Atmospheric oxygen was activated at the interface to replenish the O_β depleted in the combustion process. This can be summarised as a band structure diagram shown below.

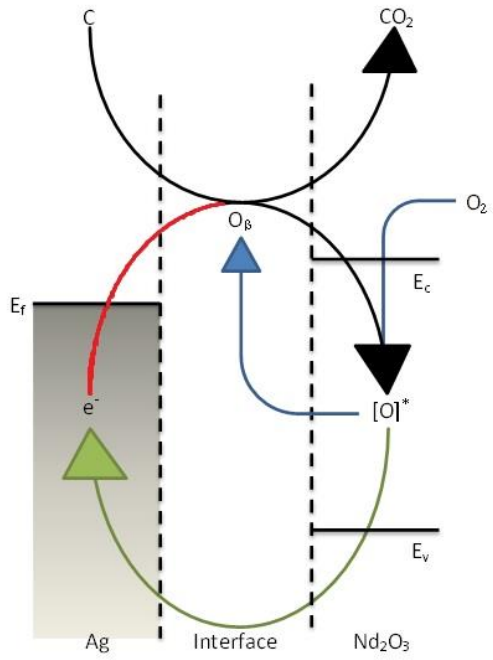

Figure 5-33 Schematic diagram of the band structure of Ag/Nd_2O_3, representative of the band structure of early Ag/Ln_2O_3. E_c, E_v, and E_f represent conduction band, valence band and Fermi Level, respectively. From XPS data, the E_v and E_c energies were found to be -7.57 and -2.87 eV respectively.

Unlike classical Schottky barriers formed between metal and semi-conductors, where the electron flows from the conduction band to the Fermi Level of the metal, this scheme suggests a "hot electron injection" from the Ag Fermi Level to the oxide conduction band. This excited electron could then activate atmospheric oxygen to form a mobile oxygen species, here known as $[O]^*$, which could be used for the oxidation of soot. This also has the effect of relaxing the excited electron to promote the metal oxide valence band density of state. After reaction with soot, these mobile oxygen species would create vacancies, [ ], which could migrate back to Ag to complete the cycle. Another way of representing this is to look at the overall mechanism of the soot combustion reaction, shown below in Figure 5-34.

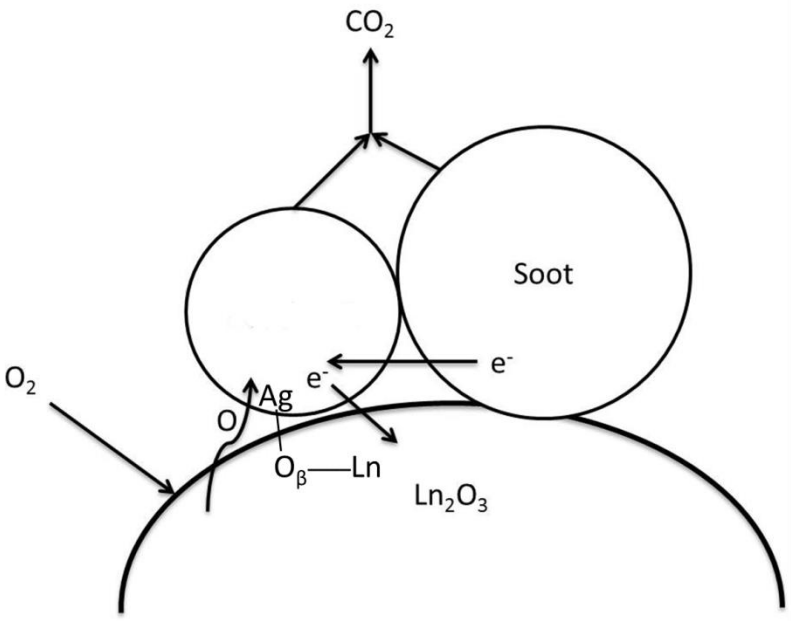

Figure 5-34 Schematic diagram of the reaction mechanism for the soot combustion reaction with Ag/Ln_2O_3.

Figure 5-34 shows that there is an overall electron withdrawing effect exerted on Ag by Ln_2O_3, which in turn polarises the soot for a more facile reaction. O_β formed by activation of lattice oxygen reacts with soot to form CO_2, leaving holes which could be replenished by atmospheric oxygen.

5.11 Summary

Ag/Ln_2O_3 had been successfully used as soot combustion catalysts, with Ag/Nd_2O_3 being the most active catalyst. The T_m of 284 ^oC was the lowest temperature for soot combustion of any open literature.

Early Ag/Ln_2O_3 were found to be much more active than late Ag/Ln_2O_3 due to stronger SMSI, where an intimate contact between Ag and the support was achieved. Late Ag/Ln_2O_3 were found to be in isolated clusters away from the support.

Early Ag/Ln_2O_3 were also found to have a much stronger EMSI, where Ag was much more effective in inducing the formation of O_β, and promoting electrons into the metal oxide valence band. It was also found that early Ln_2O_3 were electron withdrawing, resulting in Ag being more positively polarised.

These oxygen mobility properties appeared to be unique to Ag, as Au/Ln_2O_3 was inactive soot catalysts, with little promotion from Au to form O_β. Au appeared to be unable to form Au_2O, which could provide a source of energetic oxygen for soot combustion.

In aging studies, it was found that Ag aggregation occurred upon calcination of the sample, but repeated testing showed early Ag/Ln_2O_3 to be effective catalysts over three successive runs.

5.12 References

1 E. Aneggi, C. de Leitenburg, G. Dolcetti and A. Trovarelli, *Catal. Today*, 2006, **114**, 40–47.

2 E. Aneggi, C. de Leitenburg, G. Dolcetti and A. Trovarelli, *Catal. Today*, 2008, **136**, 3–10.

3 E. Aneggi, C. de Leitenburg and A. Trovarelli, *Catal. Today*, 2012, **181**, 108–115.

4 E. Aneggi, D. Wiater, C. de Leitenburg, J. Llorca and A. Trovarelli, *ACS Catal.*, 2014, **4**, 172–181.

5 A. Bueno-Lopez, K. Krishna, M. Makkee and J. A. Moulijn, *J. Catal.*, 2005, **230**, 237–248.

6 M. Dhakad, T. Mitshuhashi, S. Rayalu, P. Doggali, S. Bakardjiva, J. Subrt, D. Fino, H. Haneda and N. Labhsetwar, *Catal. Today*, 2008, **132**, 188–193.

7 M. Machida, Y. Murata, K. Kishikawa, D. J. Zhang and K. Ikeue, *Chem. Mater.*, 2008, **20**, 4489–4494.

8 E. Aneggi, J. Llorca, C. de Leitenburg, G. Dolcetti, A. Trovarelli, C. De Leitenburg and O. Ag, *Appl. Catal. B-Environmental*, 2009, **91**, 489–498.

9 V. G. Milt, C. A. Querini and E. E. Miro, *Thermochim. Acta*, 2003, **404**, 177–186.

10 G. Neri, L. Bonaccorsi, A. Donato, C. Milone, M. G. Musolino, A. M. Visco, M. Grazia and A. Maria, *Appl. Catal. B-Environmental*, 1997, **11**, 217–231.

11 J. L. Hu, W. P. Cai, C. C. Li, Y. J. Gan and L. Chen, *Appl. Phys. Lett.*, 2005, **86**, 1–4.

Contents

Chapter 6. Transition Metal Oxide Supported Catalysts

6.1 Introduction

Many transition metal oxides have been used in conjunction with Ag as soot combustion catalysts[1–4]. Guilhaume *et al.* reported the change in oxidation state of Mn promoted the soot combustion reaction by reducing from +3 to +2. Ag was observed to be in the form of Ag_2O, and reducing to Ag at 260 ^{o}C, oxidising C to form CO_2 in the process. The use of $^{18}O_2$ in isotope labelled studies also showed the existence of $C^{16}O_2$ and $C^{16}O^{18}O$, suggesting that the metal oxide was indeed a source of oxygen for soot combustion. On the other hand, Neri *et al.* suggested an oxygen spillover mechanism, where the metal oxide was a mere oxygen transporter, with no oxygen provided by the oxide itself[5]. It was proposed that the melting point of the metal oxide support, which correlated to the oxygen mobility and transport ability, played a role in the soot combustion reaction.

6.2 Transition Metal Oxide Supported Catalysts

Ag/Transition Metal Oxides (TMO) were synthesised using the method described in Chapter 2.2, and a series of different transition metal oxides were used as a background screening test.

Table 6-1 Electronic configuration of various transition metal oxides, and the T_m of the correlating 10% Ag/MO with ex-CRT soot in tight contact.

Metal Oxide	Electronic Configuration	T_m (°C)
TiO_2	d^0	601 ± 1
V_2O_5	d^0	478 ± 2
Cr_2O_3	d^3	554 ± 3
Fe_3O_4	d^5, d^6	610 ± 2
Fe_2O_3	d^5	601 ± 3
Co_3O_4	d^6, d^7	537 ± 2
CuO	d^9	478 ± 2
ZnO	d^{10}	392 ± 2

Table 6-1 shows the electronic configuration of various transition metal oxides, and the T_m of the correlating 10% Ag/MO with ex-CRT soot in tight contact. It could be seen that apart from ZnO, the other transition metal oxides were not very active soot combustion catalysts. A trend could be spotted that T_m increased to the highest with Fe_3O_4, and the later transition metal oxides were steadily better soot combustion catalysts. The trend could be seen clearly in Figure 6-1**Error! Reference source not found.** below.

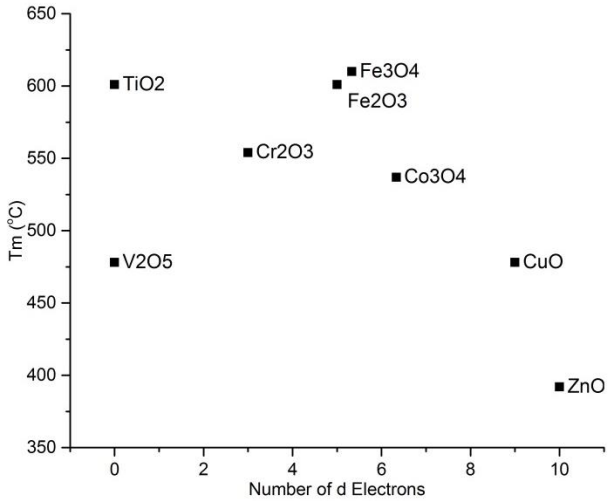

Figure 6-1 T_m against number of valence d-electrons of transition metal oxide.

With the exception of TiO_2, the other transition metals follow a volcano shape correlation between T_m and the number of valence d-electrons. A reason why TiO_2 might not conform to the trend could be due to its complex structure. Instead of a simple phase like the other oxides, TiO_2 had a mixed phase of anatase and rutile, as shown in Figure 6-2.

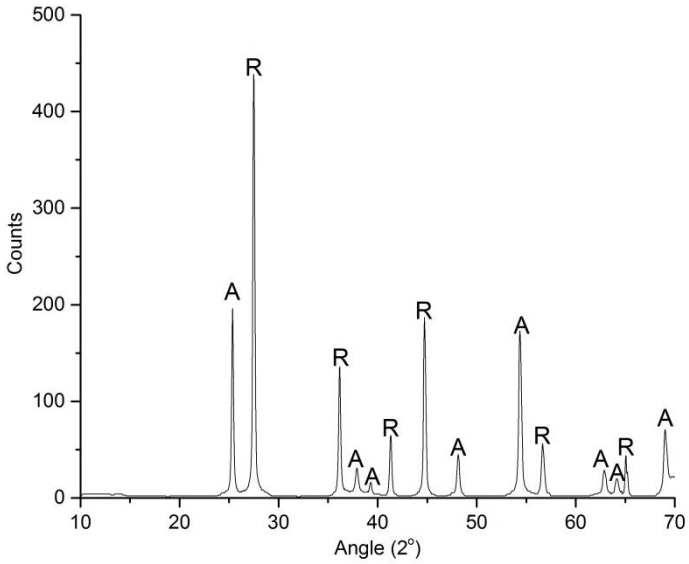

Figure 6-2 XRD Profile of TiO_2, where A represents Anatase, and R represents Rutile.

This mixed phase led to phase changes during the soot combustion reaction, and thus resulting in a higher T_m. When pure rutile was used in place of the mixed TiO_2, the T_m dropped to 497 ^{o}C, clearly indicated that the phase of the metal oxide was as important as the number of valence d-electrons.

The increase in T_m in the early transition metal series could be due to the increasing occupancy of the d-band, with a maximum in exchange energy at d^5 and d^{10}, making them the most stable, and thus inactive, catalysts. As the d-band continues to be filled, the band began to drop in energy, giving a better energy match with the Ag 4d Fermi Level (E_f). This facilitated a more facile electron transfer between the conduction band (E_c) and Ag E_f, and so a more active soot combustion catalyst.

6.3 Oxygen Mobility

In order for Ag/TMO to be as active as Ag/Ln_2O_3, then mobile oxygen species must be present for the low temperature combustion soot like their lanthanide oxide analogues.

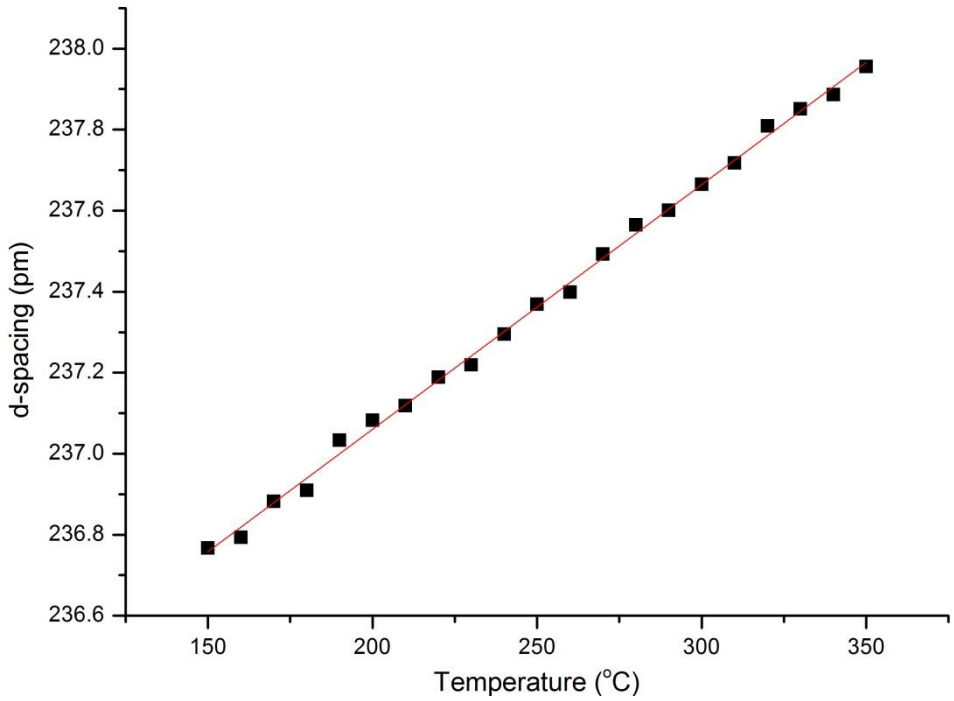

Figure 6-3 Ag (111) lattice parameter of Ag/ZnO in air as measured by *in situ* XRD.

Figure 6-3 shows Ag (111) lattice parameter of Ag/ZnO when heated in air. At the temperature range where "steps" indicating the formation of Ag_2O in Ag/Nd_2O_3, no such artefacts were present for Ag/ZnO. Instead, linear thermal expansion of Ag was observed, analogous to late Ag/Ln_2O_3. However, the rate of expansion was measured to be 7 fm K^{-1}, which was slightly higher than that measured for late Ag/Ln_2O_3 (ca. 5.5 – 5.7 fm K^{-1}). This suggested that the extent of oxygen adsorption was greater for Ag/ZnO than late Ag/Ln_2O_3, though not as strong as early Ag/Ln_2O_3 for a formal charge transfer to form Ag_2O.

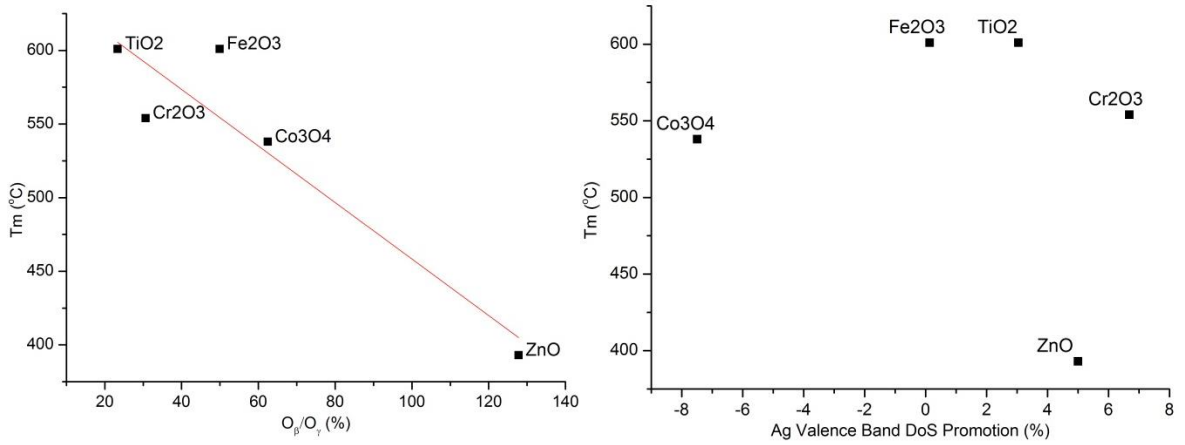

Figure 6-4 ex-CRT soot T_m versus O_β/O_γ ratio (left), and valence band DoS promotion by Ag (right).

Figure 6-4 show the XPS results obtained for Ag/TMO, where the O_β/O_γ ratio and the VB DoS promotion were correlated to ex-CRT soot T_m. It could be seen that the ratio of O_β increased across the transition metal series, though it was still a much small proportion than that of the early Ln_2O_3 (*cf.* Ag/La_2O_3 = 835%). The activated O_β promoted the soot combustion reaction, albeit at a much lesser extent than Ag/Ln_2O_3.

There appeared to be no obvious trend between the amount of Ag electronic promotion into the metal oxide valence band and the soot combustion temperature. The percentage of promotion was also much smaller for Ag/TMO than Ag/Ln_2O_3, which suggested there was a much lower band energy matching between the TMO conduction band and Ag Fermi Level.

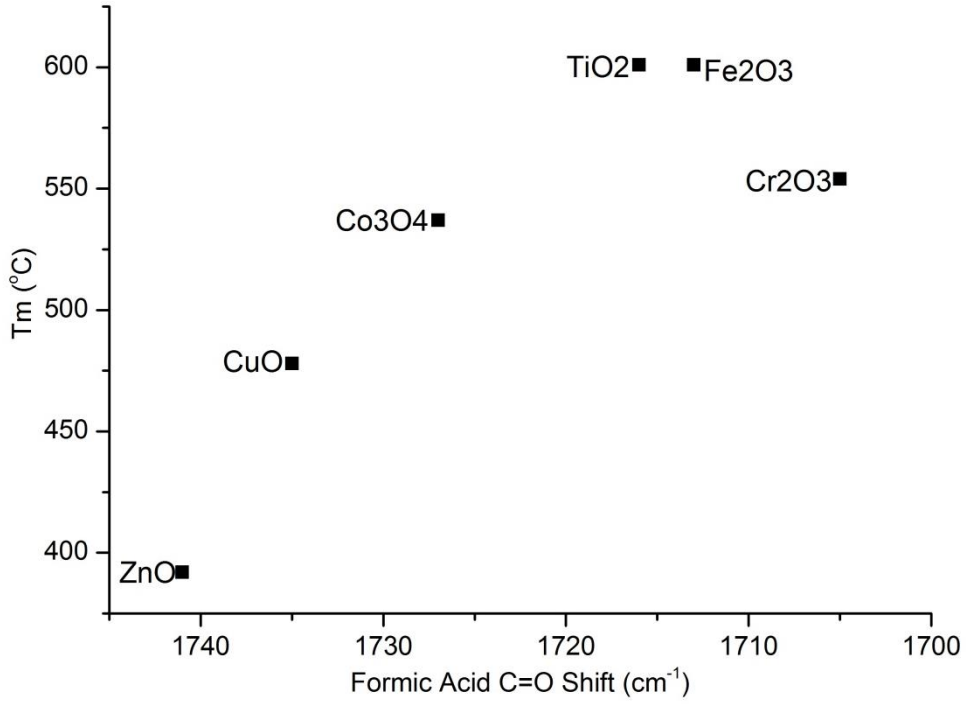

Figure 6-5 ex-CRT Soot T_m versus v_s(C=O). Pure formic acid has v_s(C=O) at 1694 cm^{-1}.

All TMO appeared to be electron withdrawing, with v_s(C=O) all higher than 1694 cm^{-1}. Comparing to Ag/Ln_2O_3, most TMO had a formic acid shift at a higher wavenumber (cf. Ag/Nd_2O_3 = 1706 cm^{-1}), which suggested that TMO were in fact more electron withdrawing than Ln_2O_3. This could be due to the ability for direct interactions between the Ag 4d orbital with the empty 3d orbitals of the TMO for better orbital overlap compared to 4d/4f interaction with Ln_2O_3.

The same trend could be observed where the more electron withdrawing TMO could polarise Ag more positively, thus polarising soot more and resulting in a lower soot combustion temperature.

However, it was evident that as the metal – support interaction between Ag and TMO was much poorer than Ag/Ln_2O_3, with little oxygen activation or valence band electron promotion, the activity of Ag/TMO catalysts were going to be much poorer than Ag/Ln_2O_3.

6.4 Modification of Synthetic Method

A major problem with the Ag/TMO catalysts was that there was not a strong enough metal – support interaction for Ag to effectively induce the activation of oxygen. Therefore catalysts with a stronger metal – support interaction should be able to overcome this problem. By modifying the synthetic method, more intimate contact between Ag and TMO would hopefully be achieved, and thus a stronger metal – support interaction.

Ag/ZnO was synthesised using the sol –gel method, as described in Chapter 2.4. Sol – gel relied on the fact that two possible reaction pathways could occur when reacting a metal precursor with base, condensation and hydrolysis.

$$M\text{-}OH + H\text{-}OM \longrightarrow M\text{-}O\text{-}M + H_20 \qquad \text{Equation 6-1}$$

$$M\text{-}OR + H_20 \longrightarrow M\text{-}OH + HOR \qquad \text{Equation 6-2}$$

The relative rate of these two reactions is thought to affect the physicochemical properties of the sol – gel product significantly. A schematic diagram can be used to summarise this effect, shown in Figure 6-6.

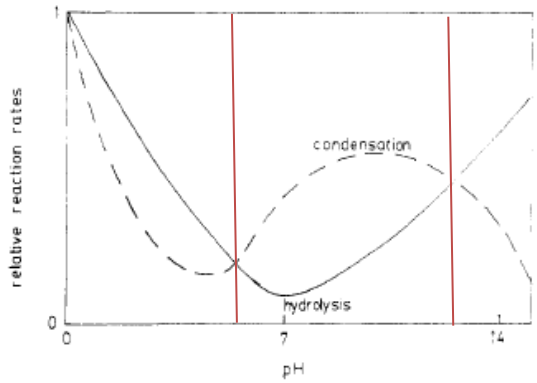

Figure 6-6 Schematic diagram of the effects of pH on the relative rates of condensation and hydrolysis[6].

At the pH range where the rate of condensation is greater than hydrolysis (between two red lines), metal oxide could be formed instead of metal hydroxides.

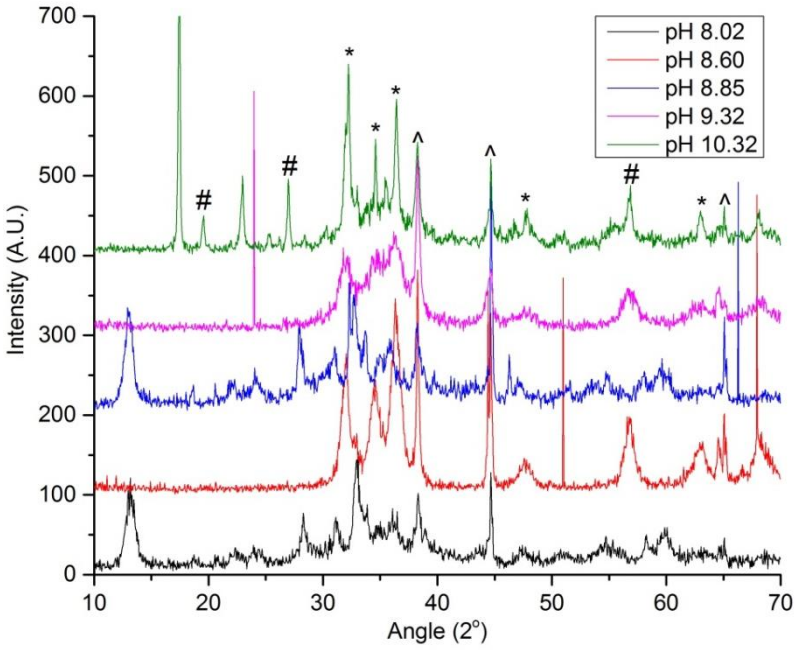

Figure 6-7 XRD Profiles of Ag/ZnO synthesised using the sol – gel method at different pH's. (#) = $Zn(OH)_2$, (*) = ZnO, (^) = Ag.

Figure 6-7 shows the XRD profiles of Ag/ZnO synthesised using the sol – gel method at different pH values. It could be seen that at pH 10.32, Zn $(OH)_2$ was beginning to form as a major crystalline phase, suggesting the rate of hydrolysis was comparable to the rate of condensation. The different ZnO phases appeared to be getting more crystalline at higher pH up to pH 8.85, then became more amorphous again at even higher pH due to the decreasing rate of condensation.

On the other hand, as pH increased, the Ag particle size increased accordingly. Figure 6-8 shows the correlation between the pH of catalyst synthesis, Ag particle size, and ex-CRT T_m.

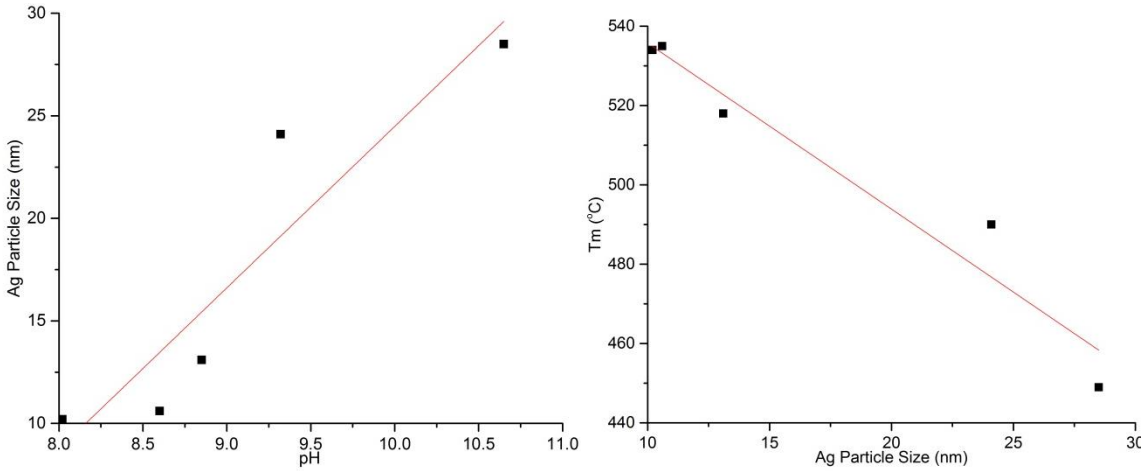

Figure 6-8 Ag particle size at different synthesis pH (left), and ex-CRT soot T_m with different Ag particle sizes (right).

As the Ag particle size increased, ex-CRT soot T_m decreased in a linear relationship, as previously found with Ag/Al_2O_3 catalysts. This again confirmed the hypothesis that there was an inverse size effect between Ag and its soot combustion ability.

However, even though a more intimate metal – support interaction had been achieved, the soot combustion temperature was still high due to the small Ag particle sizes caused by the sol – gel method. Therefore, a balance between size effect and metal – support interaction must be achieved in order to produce the optimal soot combustion catalyst.

6.5 Summary

Ag/TMO was synthesised, and used as soot combustion catalysts. However, with the exception of Ag/ZnO, with a T_m of 392 ^oC, none of the other catalysts burnt soot at below 450 ^oC. This was comparatively much worse than the activity of Ag/Ln_2O_3.

It was found that although oxygen adsorption was possible on the Ag surface, little dissociation and activation of atmospheric oxygen took place to form O_β. *In situ* XRD results also indicated that there was no Ag_2O formation with Ag/TMO, unlike early Ag/Ln_2O_3.

The sol – gel method was used as an alternate synthetic method for making Ag/ZnO, in the hope of forming a catalyst with more intimate metal – support interaction. However, the small size of Ag proved to be detrimental to the soot combustion activity.

6.6 References

1 B. Bialobok, J. Trawczynski, T. Rzadki, W. Mista and M. Zawadzki, *Catal. Today*, 2007, **119**, 278–285.

2 P. Ciambelli, V. Palma, P. Russo and S. Vaccaro, *J. Mol. Catal. a-Chemical*, 2003, **204**, 673–681.

3 P. Ciambelli, P. Corbo, P. Parrella, M. Scialo and S. Vaccaro, *Thermochim. Acta*, 1990, **162**, 83–89.

4 N. Guilhaume, B. Bassou, G. Bergeret, D. Bianchi, F. Bosselet, B. Jouguet, C. Mirodatos and A. Desmartin-Chomel, *Appl. Catal. B Environ.*, 2012, **119-120**, 287–296.

5 G. Neri, L. Bonaccorsi, A. Donato, C. Milone, M. G. Musolino, A. M. Visco, M. Grazia and A. Maria, *Appl. Catal. B-Environmental*, 1997, **11**, 217–231.

6 H. D. Gesser and P. C. Goswami, *Chem. Rev.*, 1989, **89**, 765–788.

Contents

Chapter 7. Size Control *vs.* Metal – Support Interaction

7.1 Introduction

In Chapter 4.4, it has been established that there was an inverse relationship between Ag particle size and its soot combustion activity. However, Ag supported on Al_2O_3 behaved like free particles with little metal – support interaction. It has then been discovered that with an interacting support, such as Nd_2O_3, excessive Ag aggregation would hinder soot combustion instead of promoting it. Therefore, contradicting effects between size and metal–support interaction would occur when the size of Ag particles increased.

In order to explore the two opposing effects, and understand how each effect could affect the soot combustion performance, different sizes of Ag supported on interacting oxides were made. Their size and extent of metal–support interaction were measured using various techniques in an attempt to qualify the extent of influence on soot combustion, and how these two factors influenced each other.

ZnO and Nd_2O_3 were chosen to be studied more extensively as they showed the lowest T_m in the transition metal oxide series and lanthanide oxide series respectively. This suggested they had the strongest meta–support interactions with Ag nanoparticles, which would make them good subjects to study on the role of Ag particle size and metal – support interaction.

7.2 Size Control of Ag/MO

7.2.1 Ag/ZnO

Different sizes of Ag supported on ZnO were achieved by altering the reaction time and temperature. Table 7-1 shows a summary of the reaction conditions used.

Table 7-1 Summary of Ag Size and T_m with different reaction conditions.

Reaction Time (hr)	Reaction Temp. (°C)	Ag Size (nm)	Ag Size Standard Deviation (nm)	T_m (°C)
1	100	18.6	3.7	380
1	120	16.5	3.1	393
1	140	25.7	4.2	366
1	160	26.7	4.6	362
1	180	25.2	5.2	364
2	120	22.4	3.4	367
4	120	27.4	4.3	358

As the reaction temperature increased, the rate of Ag particle growth increased, and therefore Ag particle size increased accordingly. A longer reaction time also yielded larger particles as they were given more time to grow.

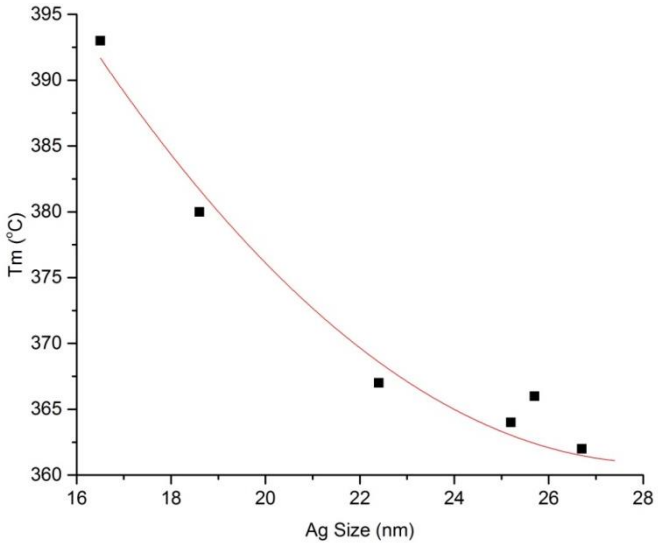

Figure 7-1 ex-CRT Soot T_m vs. mean Ag particle size.

Whereas Ag/Al_2O_3 had a linear relationship between Ag particle size and ex-CRT soot T_m in Chapter 4, the soot T_m actually decreased in a much smaller extent as T_m increased for Ag/ZnO. This could be explained by the diminishing influence of metal – support interaction, where a larger Ag nanoparticle formed would not be able to form an as intimate contact as a smaller particle.

Even though the size of Ag nanoparticles could be controlled by altering reaction conditions, the size difference was quite small. Therefore a different approach had to be taken in order to achieve a much larger Ag particle size range.

7.2.2 Ag/Nd_2O_3

Instead of changing reaction conditions, different reducing agents were used for the size control of Ag/Nd_2O_3. Instead of ethylene glycol, which was used in a typical synthesis, other polyols were used, such as diethylene glycol and triethylene glycol.

Table 7-2 Summary of Ag Size and T_m with different reducing agents.

Reducing Agent	**Ag Size (nm)**	**Ag Size Standard Deviation (nm)**	**T_m (^oC)**
Ethanol (EtOH)	27.2	6.7	401
Ethylene Glycol (EG)	76.7	26.8	284
Diethylene Glycol (DEG)	27.6	6.7	375
Triethylene Glycol (TEG)	30.6	6.9	335

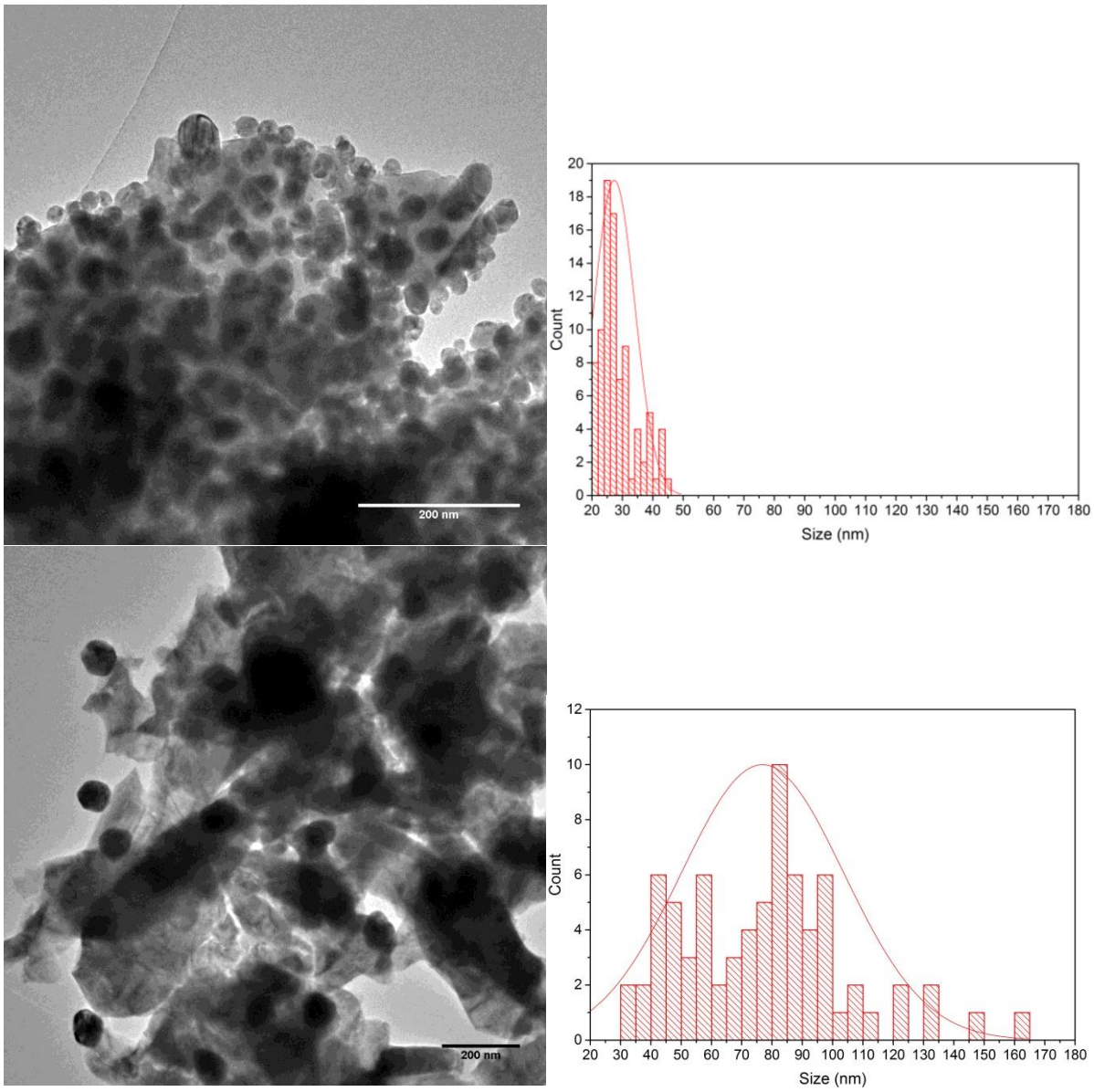

Figure 7-2 TEM images of Ag/Nd2O3 made by reduction with EtOH (top left), its Ag size distribution histogram (top right) , and EG (bottom left), its Ag size distribution histogram (bottom right).

With the exception of EG, the other three reducing agents appeared to have little effect on the Ag particle size, as they all had a mean Ag particle size of around 27 nm, as measured by TEM. EG, on the other hand, resulted in much larger Ag particles. This could be due to the higher reduction potential of EG compared to the other reducing agents. This was particularly obvious during the synthesis process, where the Ag precursor and Nd_2O_3

mixture dispersed in EG was seen to reduce (colour change from blue to brown) at a much lower temperature than the other reducing agents.

EG was also found to produce Ag nanoparticles in a much wider size range than the other reducing agents, as summarised in Table 7-3.

Table 7-3 Summary of Mean and Standard Deviation (SD) of Ag particle sizes.

Reducing Agent	Mean (nm)	Standard deviation (nm)	SD/Mean
EtOH	27.2	6.72	0.247
EG	76.7	26.80	0.349
DEG	27.6	6.74	0.244
TEG	30.6	6.90	0.225

The SD/mean ratio for EG as the reducing agent was much higher than the other reducing agents, which suggested that the resulting Ag particles were polydispersed. This was evidence that Ostwald Ripening was taking place, where a particle was "absorbed" by another particle to give two particles with a large size difference, shown in Figure 7-3.

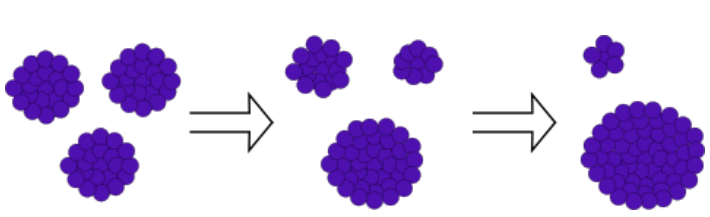

Figure 7-3 Schematic diagram of Ostwald Ripening[1].

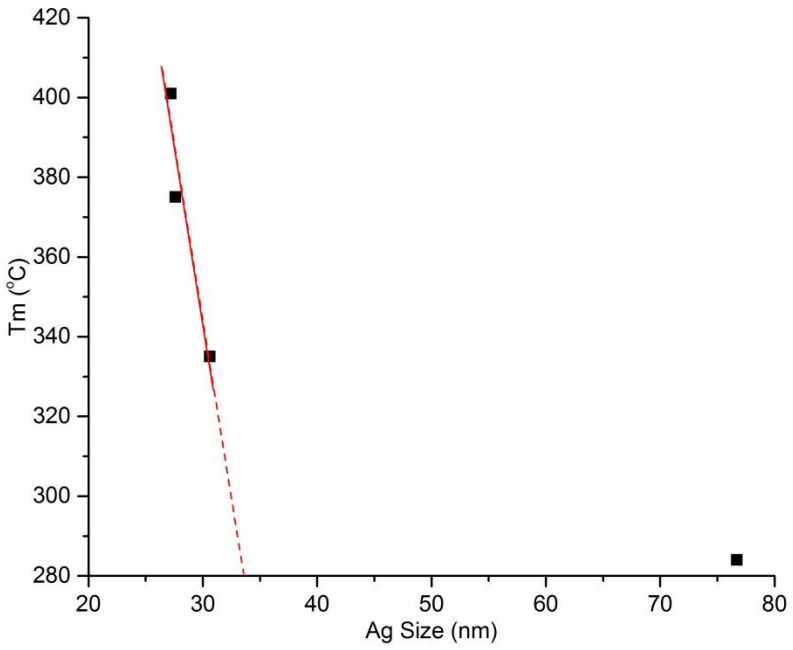

Figure 7-4 ex-CRT Soot T_m vs. mean Ag particle size. Linear trend line for the inverse size effect of first three points (solid red line) with extrapolation (dashed red line).

Figure 7-4 shows the relationship between Ag particle size and its corresponding ex-CRT T_m. Like Ag/ZnO, the relationship over a large range of particle sizes was not linear. If the linear relationship of the first 3 points were to be extrapolated, an Ag particle size of over 70 nm would have had a much lower T_m than observed. This was again evident that a metal–support interaction also played a vital role in soot combustion alongside Ag size effect.

7.3 Metal–Support Interaction

7.3.1 Ag/Ln_2O_3 Synthesised Using Sol–Gel Method

Like Ag/ZnO, Ag/Ln_2O_3 was synthesised using the sol–gel method in order to investigate the effects of strong metal support interactions. They were not expected to be good soot combustion catalysts, though it would be interesting to see the metal–support interaction across the lanthanide series.

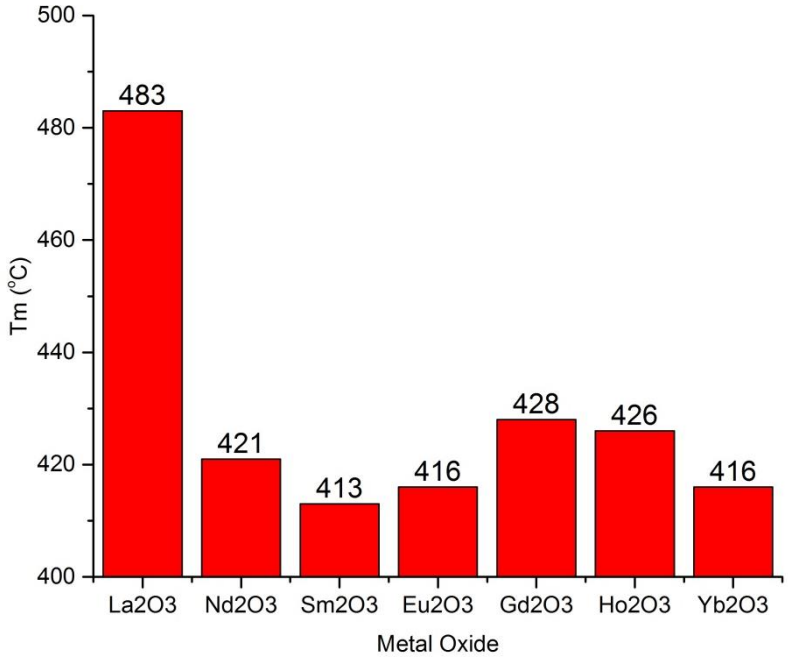

Figure 7-5 ex-CRT soot T_m with Ag/Ln2O3 made using the sol–gel method.

As expected, the ex-CRT soot T_m with Ag/Ln_2O_3 made using the sol–gel method were much higher than their analogues prepared by wet impregnation method. In particular Ag/La_2O_3 had an increase in T_m from 315 ^oC to just under 485 ^oC. However, no clear trend could be observed across the lanthanide series, except the early Ag/Ln_2O_3, established to have a stronger metal–support interaction compared to the late Ag/Ln_2O_3, appeared to have a lower T_m, though not by a huge extent.

A better understanding of the phases of these catalysts could be established from the *in situ* XRD profiles.

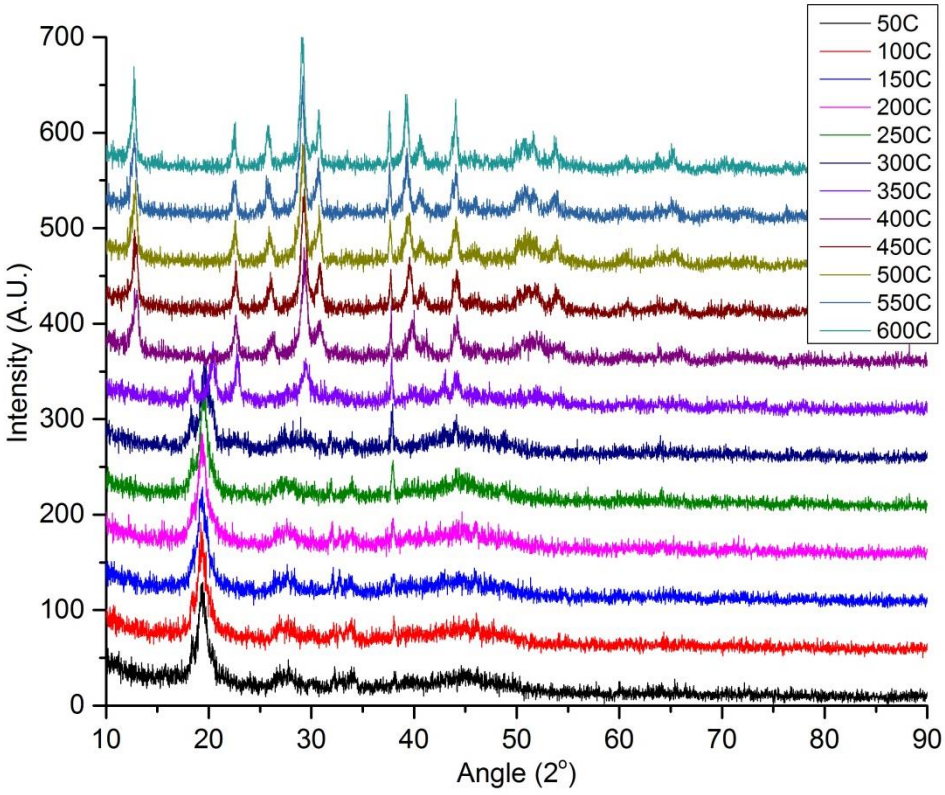

Figure 7-6 *In situ* XRD profiles of Ag/La_2O_3 synthesised using the sol – gel method.

At temperatures up to 300 ^{o}C, La_2O_3 appeared to be amorphous, with a small Ag (111) phase at 38^{o}, and a strong $La(OH)_3$ (100) peak at 19^{o}. At 350 ^{o}C, there appeared to be a phase change, where a pure La_2O_3 phase was formed. Unlike La_2O_3 bought from Sigma – Aldrich, no La_2O_3 aggregation was observed, nor was there any CO_2 adsorption to form $La_2O_2CO_3$ at high temperature.

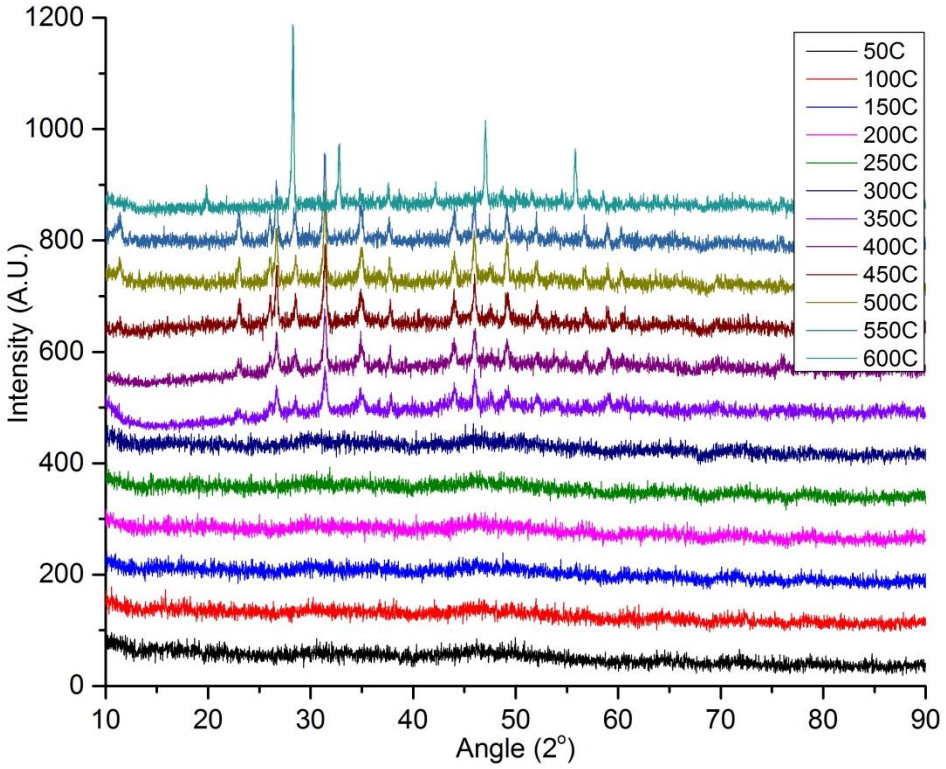

Figure 7-7 *In situ* XRD profiles of Ag/Eu_2O_3 synthesised using the sol–gel method.

A very similar pattern was observed for Ag/Eu_2O_3, where the catalyst remained amorphous until 300 °C, then it underwent a phase change to give a pure Eu_2O_3 phase. However, at 600 °C, all the Eu_2O_3 peaks seemed to have disappeared, and only the Ag peaks were observed. This phenomenon was not seen in any of the other lanthanide oxide supports, and appeared to be unique only to Eu_2O_3. It suggested that Eu_2O_3 could break down at high temperature, though the exact mechanism by which this process happened is not understood.

The above results suggested that with little Ag size promotion effects, the metal–support interaction alone was not influential towards the soot combustion catalytic performance.

7.3.2 Surface Plasmon Resonance

In Chapter 4.4, a redshifting of the quadrupolar surface plasmon resonance of Ag was observed when supported on Al_2O_3, conforming to the trends observed in open literature[2]. However, different trends were observed for ZnO and Nd_2O_3.

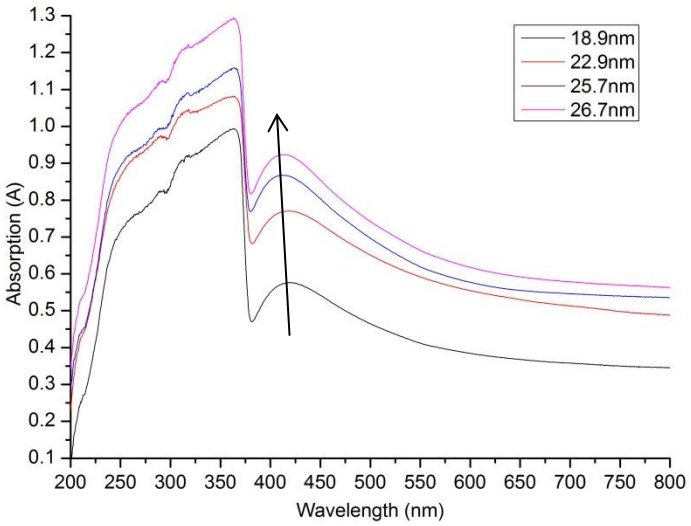

Figure 7-8 UV-Vis spectra of Ag/ZnO at different Ag particle sizes.

For both ZnO and Nd_2O_3, a blueshifting of the Ag quadrupolar SPR peak was observed, which was completely opposite to what was observed with the Al_2O_3 supported Ag particles. This was due to the metal–support interaction between Ag and the metal oxide, where the s^1 electron was able to resonate into the metal oxide valence band.

By imagining the s^1 electron movement like a particle in a box, this increased perturbation would mean a larger area in which the electron could move, resulting in a "larger" particle in

a box. As the Ag particle size increased, the metal–support interaction was weaker, leading to a “decrease” in box size.

As surface plasmon resonance (SPR) takes into account both size effect and metal–support interaction, it can be powerful technique to describe qualitatively the Ag nanoparticle interaction with the metal oxide support at different sizes.

A range of different Ag/Ln_2O_3 were synthesised by changing the reducing agent, and their UV-Vis spectra and TGA profiles were used for a correlation between surface plasmon resonance and soot combustion performance.

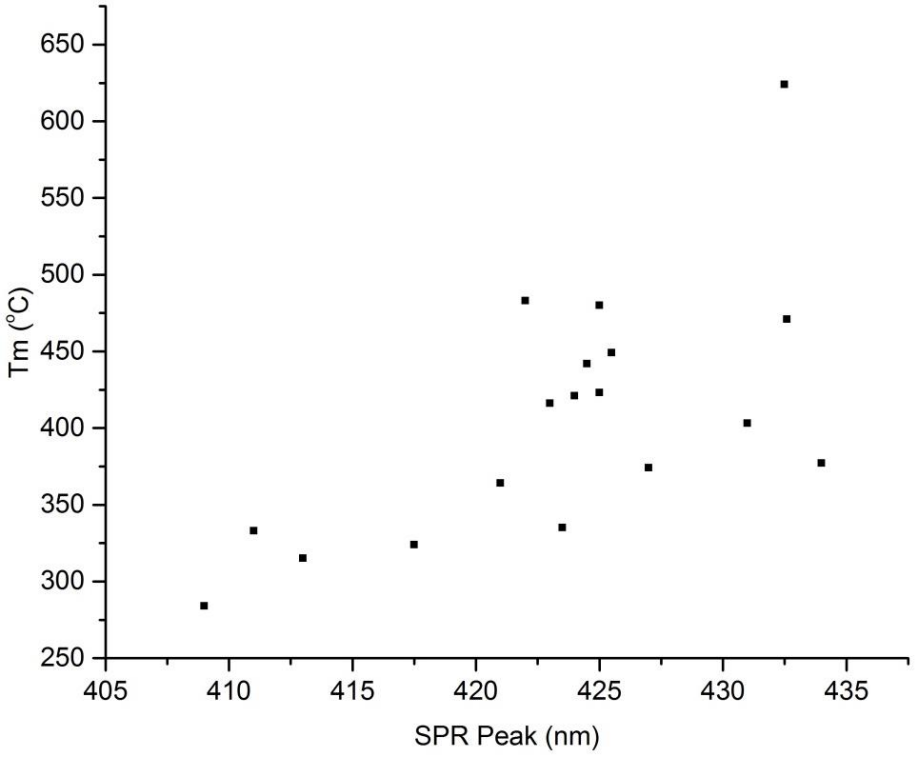

Figure 7-9 ex-CRT Soot T_m versus quadrupolar SPR peak of Ag/MO.

Figure 7-9 shows the correlation between the position of the quadrupolar Ag SPR peak, and the T_m of the corresponding Ag/MO. It shows a general relationship where a higher SPR wavelength resulted in a higher soot combustion temperature. No information was obtained for either the size or the nature of the metal oxide support, nor was it required for this characterisation technique, as the SPR has taken into account both the size effect and metal–support interaction.

However, this was an opposite trend to what was expected, where a higher wavelength would mean either a larger particle size, or a stronger metal–support interaction, either of which should be a favourable factor for soot combustion. A possible explanation for this observation was that it had already been demonstrated that neither factors on its own, but

a combination of both, was favourable for soot combustion. This would result in a blueshifted SPR peak as the optimal catalyst would have a large particle size with a good metal–support interaction. This blueshifting, or "reduction" in size of the "box", would result in a higher energy transition from the Ag Fermi level to the localised surface plasmon state. This higher energy transition could then facilitate a more facile electron spillover into the metal oxide conduction band for a reduction in T_m.

7.3.3 TPR

In chapter 5.4.4, TPR was used to investigate the oxygen mobility of O_β on Ag/Ln_2O_3. It was found that across the lanthanide series, a higher temperature activation of O_β would lead to a higher soot combustion temperature. This effect was solely attributed to metal–support interaction, with no emphasis placed on the Ag particle size at all. Therefore, the size effect on oxygen activation should be investigated as well.

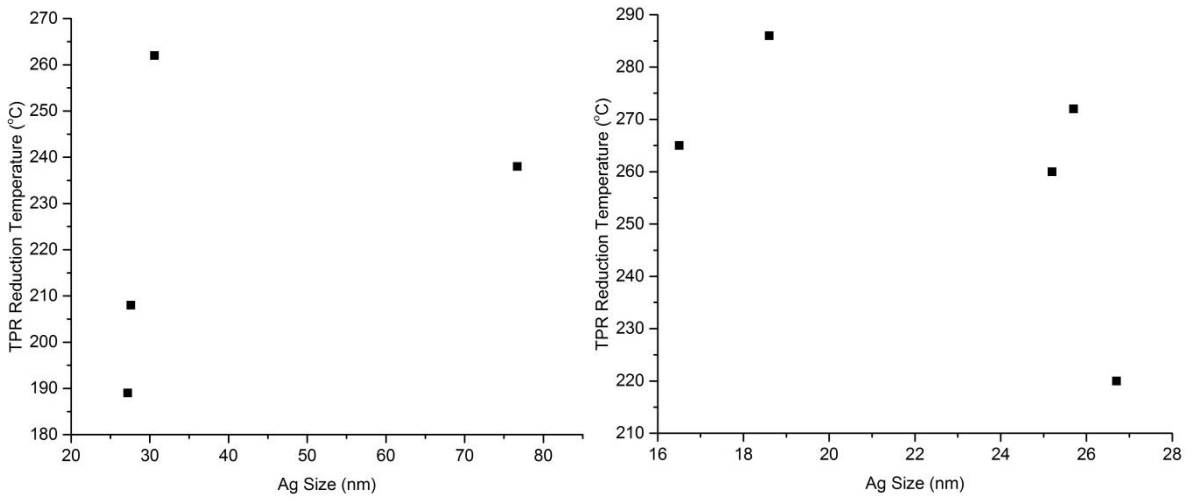

Figure 7-10 TPR reduction temperature of different size Ag nanoparticles supported on Nd_2O_3 (left), and ZnO (right).

As with other characterisation techniques, it was impossible to separate size effect from metal–support interaction for any interacting metal oxide supports. However, by using the same support, it was possible to keep the changes to the metal–support interaction to a minimum. Figure 7-10 shows the relationship between the size of Ag supported on Nd_2O_3 and ZnO, and the reduction temperature of O_β measured by TPR. A volcano trend could be seen, where an increase in particle size would initially increase the reduction temperature, then subsequently reduce it.

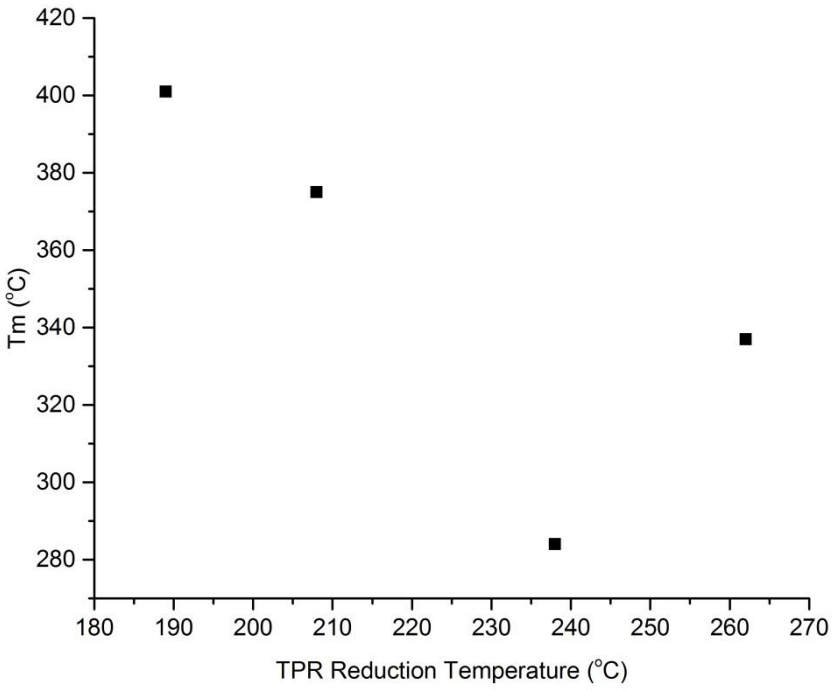

Figure 7-11 ex-CRT soot T_m versus TPR reduction temperature of different Ag/Nd_2O_3 catalysts.

In stark contrast to the observation made in Chapter 5, it was found that there was a reverse volcano trend between the TPR reduction temperature and ex-CRT soot T_m. However, as there are only 4 points in this plot, no meaningful conclusion could be drawn

from it. Like SPR, TPR has also taken into account both size effect, and metal–support interaction, so reduction temperatures from multiple supports could be plotted together without the need to know the size of the Ag nanoparticles, or the nature of the support.

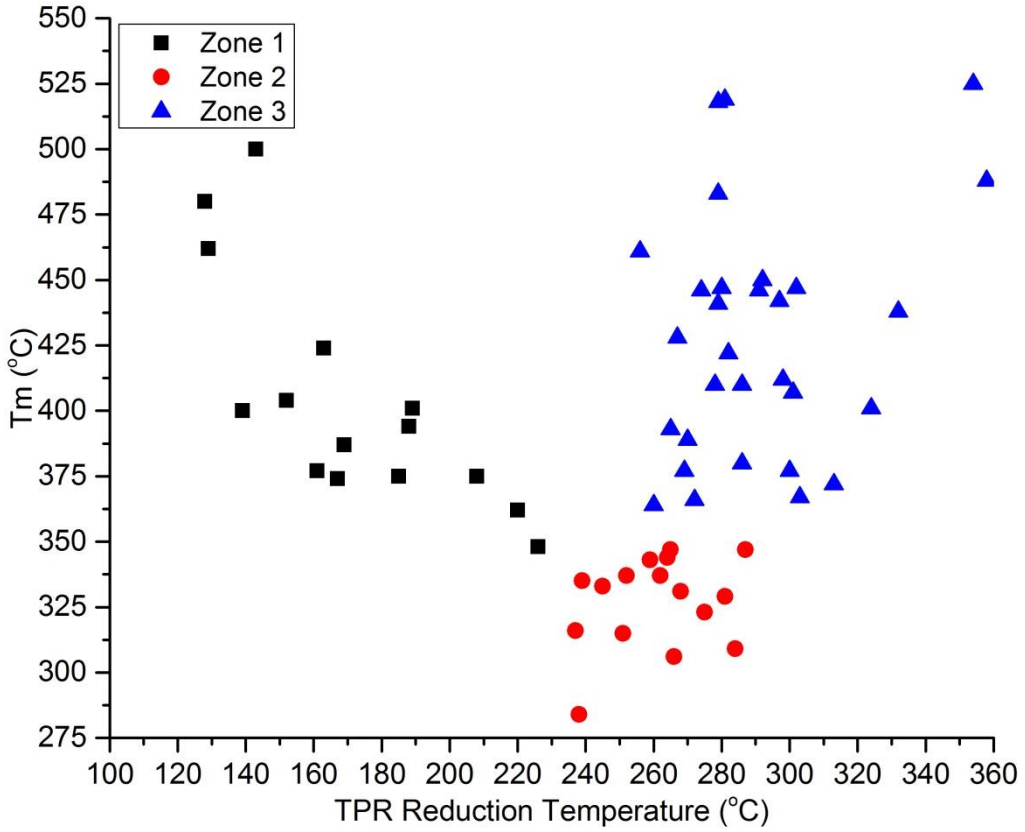

Figure 7-12 ex-CRT Soot T_m versus TPR reduction temperatures of Ag/MO. Three zones have been designated: Zone 1 (black), Zone 2 (red), and Zone 3 (blue).

Figure 7-12 shows the relationship between TPR reduction temperature and ex-CRT soot T_m, where a clear inverse volcano trend was observed, where the linear relationship observed in previous studies was in fact part of the overall inverse volcano trend.

For a better understanding, the overall general inverse volcano was split into three zones. Zone 1 was the low temperature oxygen activation; Zone 2 medium temperature oxygen activation; and Zone 3 high temperature oxygen activation. Catalysts in Zone 1 have extremely low temperature oxygen activation of below 220 ^{o}C, where the O_{β} was activated at such a low temperature that they were unable to get over the energy barrier for effective soot combustion. At the temperature range of soot combustion, the O_{β} would have desorbed from the subsurface of the Ag nanoparticles. The opposite was true for Zone 3, where O_{β} activation began at such a high temperature that soot combustion was only possible at an even higher temperature. Zone 2 was the optimum temperature range of oxygen activation, where the oxygen was activated at a relatively high temperature to have the right energy to react with soot, yet relatively low to activate the reaction.

In summary, TPR proved to be a very powerful technique for estimating the catalytic activity of Ag/MO. It took into account both size effect and metal–support interaction, and the two counteracting effects on Ag. Therefore, no knowledge of Ag size, nor the nature of the support was required when using TPR as a characterisation technique. By knowing which zone a particular catalyst lied within the plot, a general idea of its catalytic performance would be evaluated without any further information.

7.3.4 XPS

XPS was also employed to see which of the changes observed in previous characterisations were due to size effect, and which were due to metal–support interaction. Different sizes of Ag/ZnO were characterised using XPS, which should hopefully eliminate any Ag promotions due to metal–support interaction.

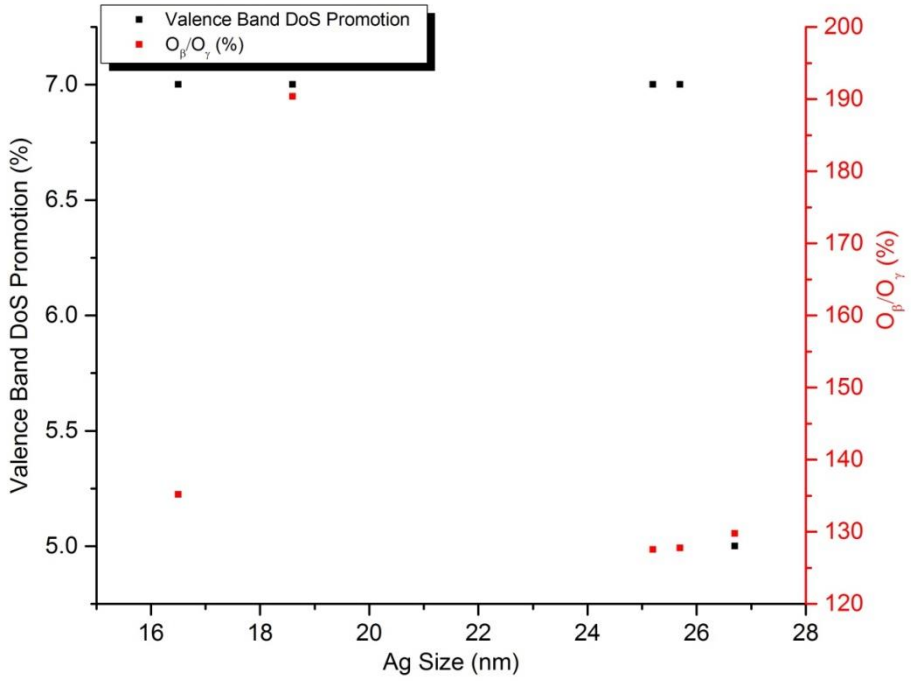

Figure 7-13 Ag Valence Band DoS promotion (black); and O_β/O_γ ratio (red) at different Ag sizes.

From Figure 7-13 it could be clearly seen that altering the Ag particle size had little difference on it valence band DoS promotion on the metal oxide, nor did the O_β/O_γ ratio change. This was strong evidence that any changes observed in previous tests were due to the nature of the metal oxide support, and not due to Ag particle size.

7.4 Summary

Size effect and metal–support interaction were the two main factors that determine the catalytic activity of the Ag/MO catalyst. Unlike conventional catalysts, an increase in Ag particle size resulted in a lower soot combustion temperature. However, a further increase in size saw a diminishing reduction in T_m, as the level of metal–support interaction reduced.

This made the understanding of the interactions between Ag and the support rather complicated as there were now two contradicting effects at play. An increase in Ag size would result in a decrease in metal–support interaction, and *vice versa*.

It was found that SPR characterisation and TPR reduction temperature appeared to give a general indication of how the catalyst was affected by the two effects. No size or support information was required, which made them ideal techniques for establishing a general estimation of the catalytic activity of an unknown new catalyst.

However, not all factors were affected by Ag particle size. For example, the extent of Valence Band DoS promotion by Ag, and the extent of O_β activation appeared to be size independent. Therefore, these measurements could give a better indication of the extent of metal–support interaction without considering size effect.

7.5 References

1 *http://www.scienceminusdetails.com/2013/02/why-does-old-ice-cream-get-crunchy.html*.

2 K. Qian, B. C. Sweeny, A. C. Johnston-Peck, W. X. Niu, J. O. Graham, J. S. DuChene, J. J. Qiu, Y. C. Wang, M. H. Engelhard, D. Su, E. A. Stach and W. D. Wei, *J. Am. Chem. Soc.*, 2014, **136**, 9842–9845.

Contents

Chapter 8. Morphology Controlled Supports

8.1 Introduction

Previous studies have shown that different facets on a material would provide different exposed faces, and therefore giving different interactions with adsorbed particles. Kliewer *et al.* have demonstrated that furan adsorbed differently on Pt (100) and (111) surfaces, leading to a difference in hydrogenation reaction[1]. Mclaren *et al.* have shown the (001) polar surface of ZnO was more active for photocatalysis than the non-polar (100) surface[2]. Therefore having a control on the selective growth of metal oxide particles would result in the preferential growth of specific face, and thus optimising the proportions of the exposed active surfaces.

Polar ZnO and Nd_2O_3 nanorods were synthesised, then Ag was supported onto the metal oxide using the wet impregnation method. The component peaks of the TGA profile during soot combustion reactions gave an insight into the composition and activity of the respective nanorods.

8.2 Zinc Oxide Nanorods

ZnO nanorods were synthesised using the method as described by Mclaren *et al.*[2], as described in Chapter 2.5 in more detail.

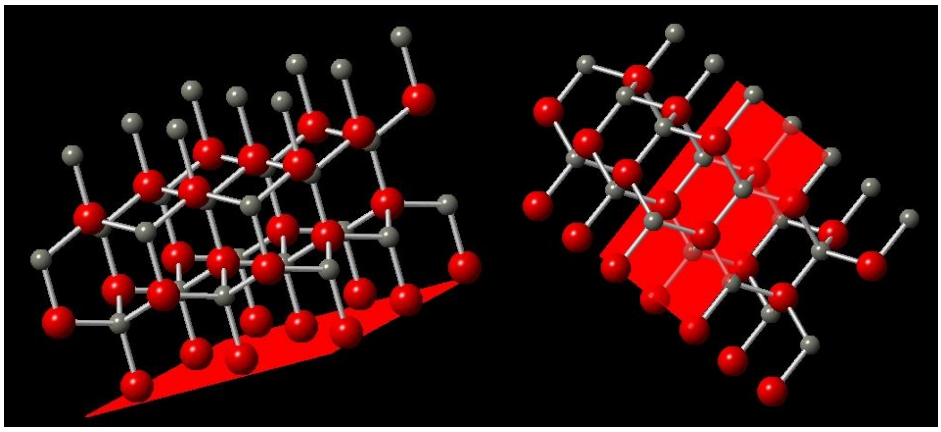

Figure 8-1 Structure of ZnO, showing the (001) face (left), and (100) face (right). Red atoms represent oxygen, and grey atoms represent zinc.

For wurtzite ZnO, the Zn terminated (001) face, with an O terminated (00-1) face could be considered as a polar surface; whereas the (100) with its equal distribution of Zn and O was non-polar. By adjusting the amount of capping agent used in the synthesis process, selective binding to one face to give the greatest change in free energy. In the case of oleic acid and trioctylamine, preferential growth of the [001] direction was achieved to give nanorods.

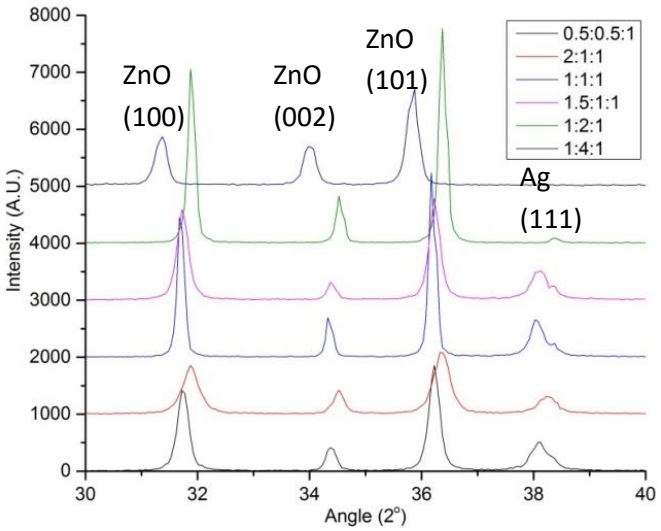

Figure 8-2 XRD profiles of Ag/ZnO synthesised at different $Zn(OAc)_2$: OA: TOA mass ratios, showing the ZnO (100), (002), (101) peaks, and the Ag (111) peak.

Table 8-1 (100)/(002) Ratio at different Zn: OA: TOA Ratios.

Zn: OA: TOA Mass Ratio	(100)/(002) Ratio
0.5: 0.5: 1	3.038
2: 1: 1	2.025
1.5: 1: 1	5.582
1: 1: 1	3.549
1: 2: 1	4.453
1: 4: 1	1.459

The increase in (002) peak intensity with respect to the (100) peak showed a preferential growth along the c axis to yield rod like structures. Therefore, by increasing the ratio of capping agent, a more plate like (less rod like) structure was achieved.

At a Zn: OA ratio of 1:4, the (100)/(002) ratio dramatically decreased, which suggested the formation of nanorods with predominant non-polar surfaces. From the TEM images of Figure 8-3, it was found not to be the case. Whereas by increasing the Zn:OA ratios from 1:1

to 1:2 made the ZnO into a more plate like structure, increasing the ratio further to 1:4 actually made a nanoprism. As the proportion of the polar (001) increased, the nanoplate became increasingly unstable with a higher surface energy. This led to the collapse of the nanoplate to form a nanoprism to reduce its surface energy in order to achieve increased stability of the highly energetic polar surface.

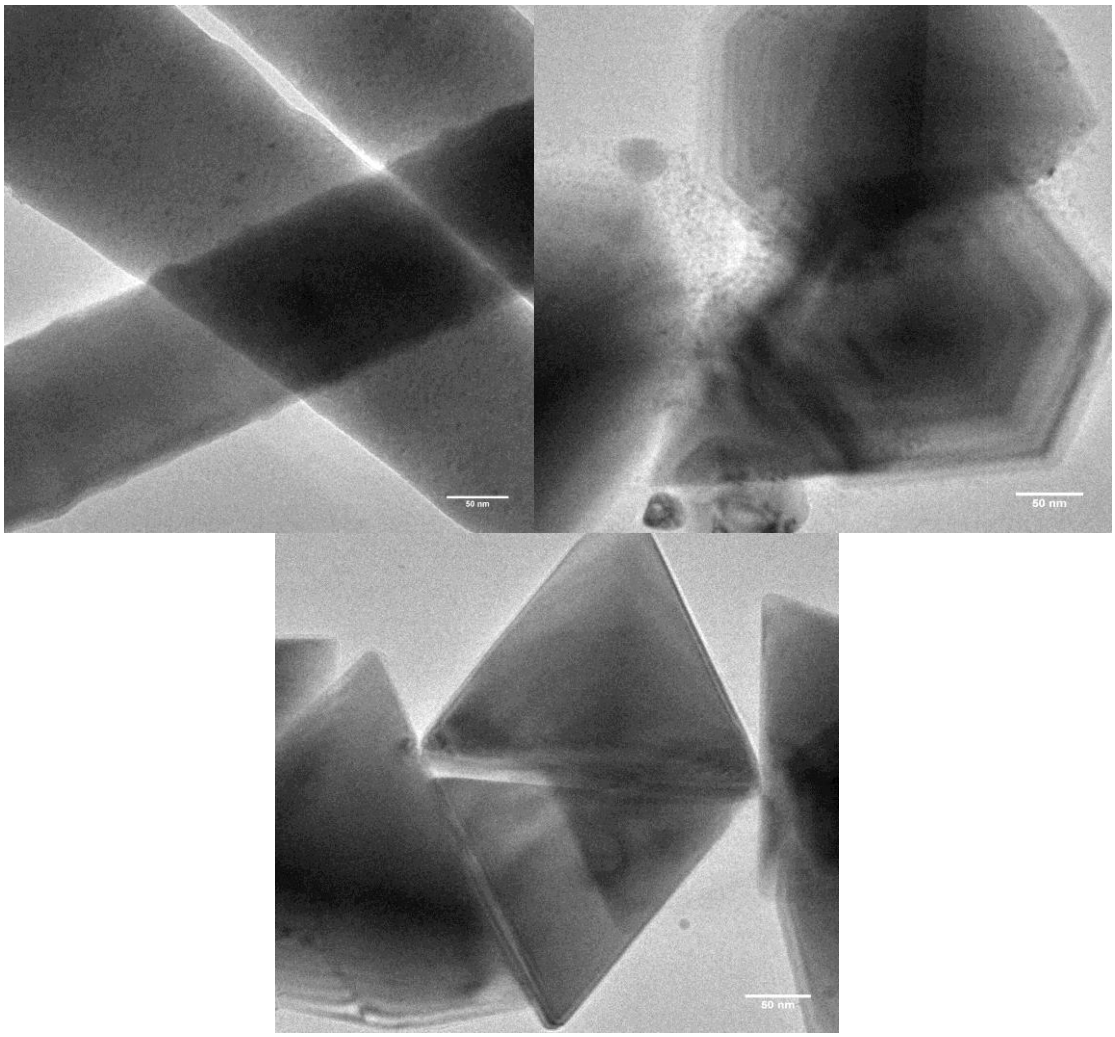

Figure 8-3 TEM images of ZnO at Zn: OA ratios of 1:1 (top left), 1:2 (top right), and 1:4 (bottom). All scale bars are 50 nm.

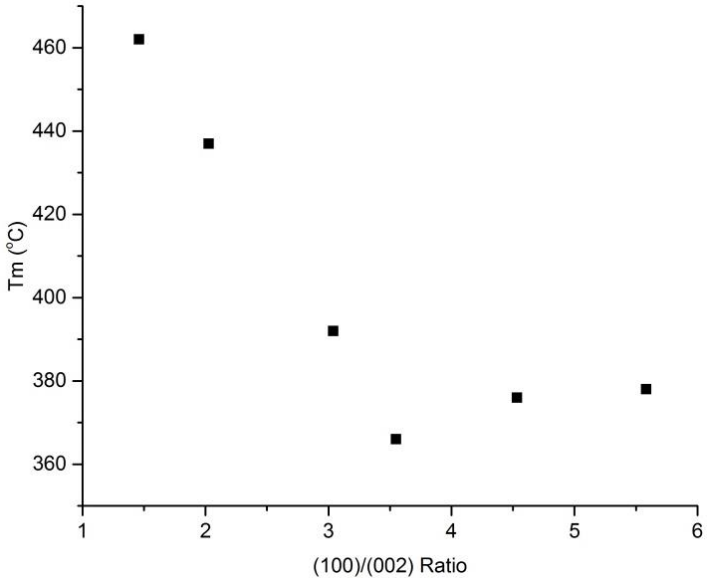

Figure 8-4 ex-CRT soot T_m versus ZnO (100)/(002) peak intensity ratios.

As the ZnO became more plate like, the ex-CRT soot T_m decreased. This suggested that the oxygen terminated (00-1) face of the ZnO was favourable for soot combustion over the non-polar (100) face. This was in good agreement with previous studies where energetic oxygen with a low activation temperature favoured soot combustion.

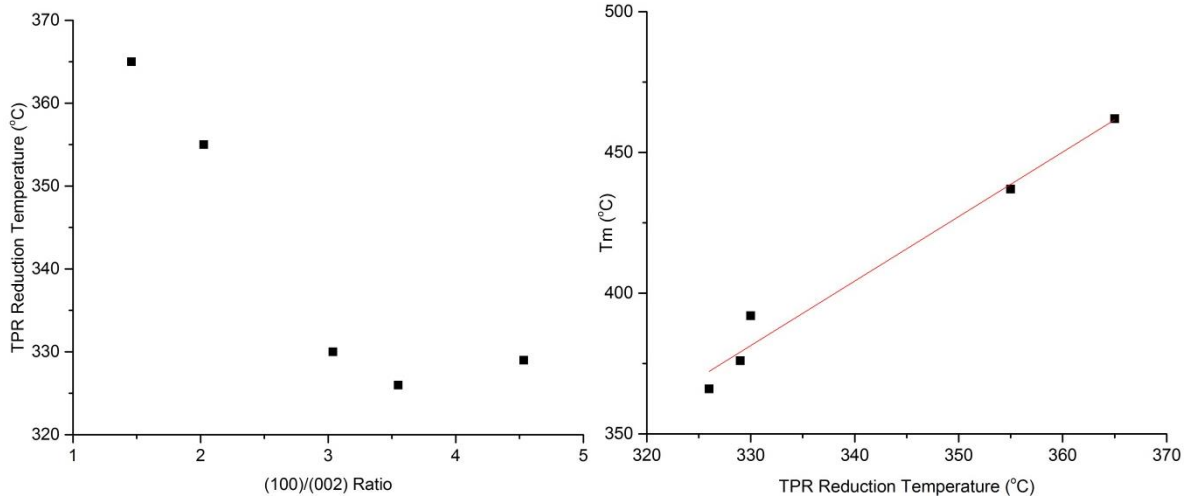

Figure 8-5 TPR reduction temperature of Ag/ZnO versus (100)/(002) ratio (left); and ex-CRT soot T_m versus TPR reduction temperature of Ag/ZnO (right).

Figure 8-5 shows that as ZnO became increasingly polar with more exposed (001) oxygen termination, the TPR reduction temperature of the Ag/ZnO decreased accordingly as the proportion of energetic oxygen increased. This then resulted in a linear relationship between the TPR reduction temperature and ex-CRT soot T_m. These Ag/ZnO catalysts could be classified in Zone 3 (*c.f.* Chapter 7.3.3), where oxygen activation was relatively difficult and it was reflected by the high TPR reduction temperature, in spite of having polar oxygen terminations.

8.3 Neodymium Hydroxide/Neodymium Oxide Nanorods

Apart from ZnO nanorods, Nd_2O_3 nanorods were also made to investigate the effects of polar surfaces. Unlike ZnO, which was synthesised using a high temperature hydrothermal method, Nd_2O_3 nanorods made by this method was impossible to isolate, as they were found to be clumped into a large aggregate. Therefore an alternative method, based on Zhang *et al.*[3], was used. A detailed synthetic procedure was described in Chapter 2.6.

Different amounts of NaOH were added to the $Nd(NO_3)_3$ solution to achieve nanorods with different lengths. This was due to the increasing preferential stacking of OH^- along the c-axis of the nanorod. The $Nd(OH)_3$ nanorod would then be calcined to give Nd_2O_3 nanorods.

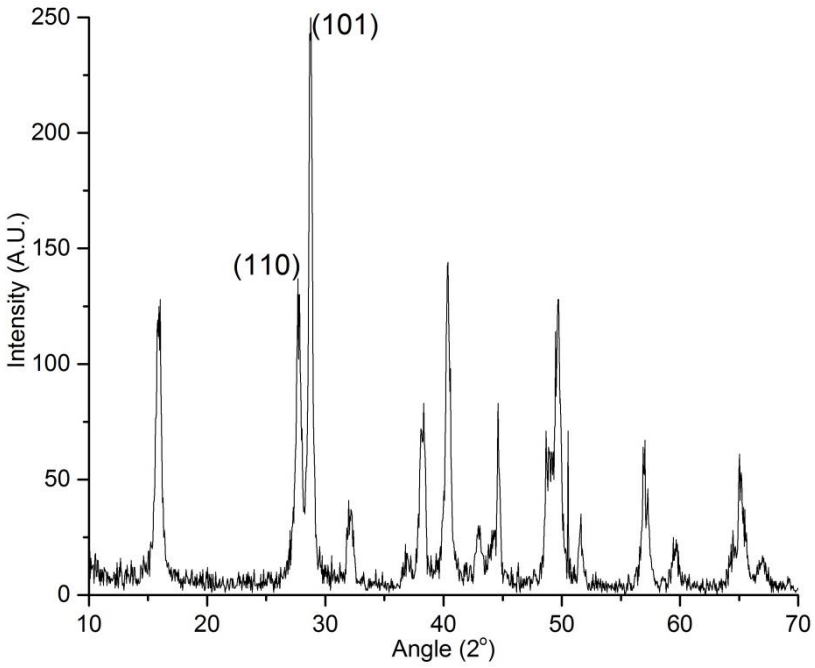

Figure 8-6 XRD profile of typical $Nd(OH)_3$ nanorod.

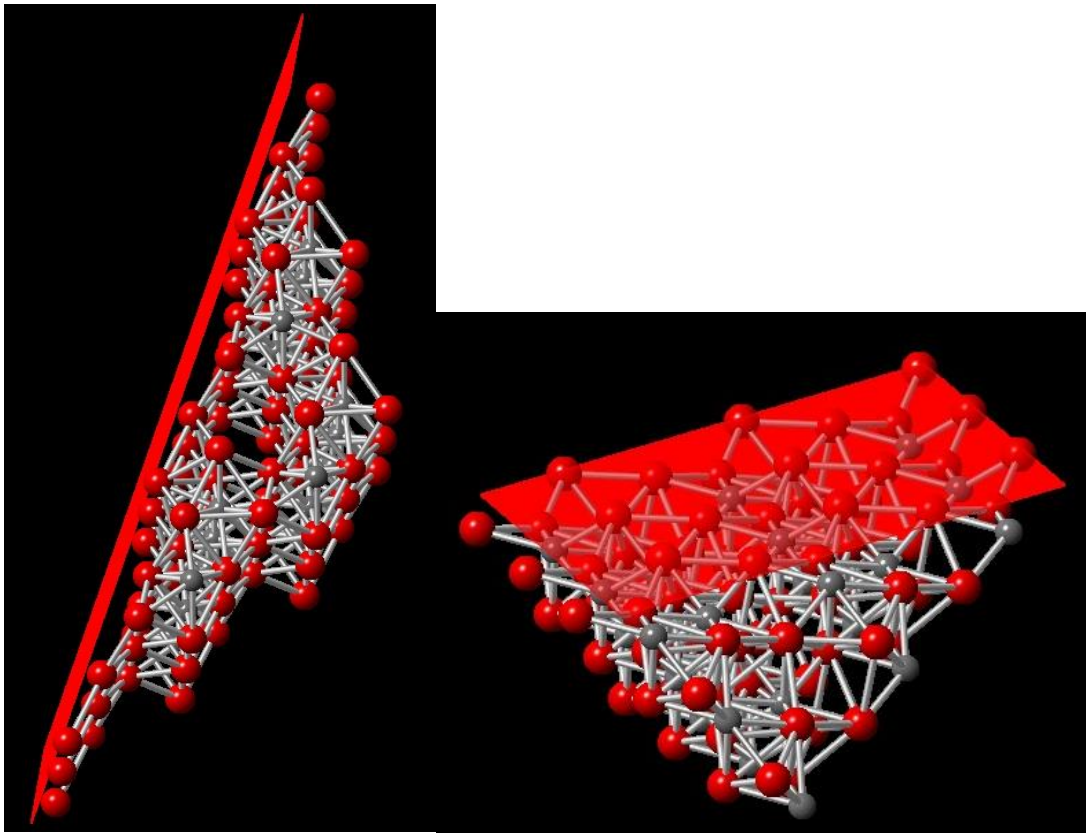

Figure 8-7 Structure of $Nd(OH)_3$ nanorod showing the (101) face (left), and (110) face (right). Red atoms represent oxygen, and grey atoms represent neodymium. Hydrogen has been left out for simplicity.

Like the ZnO (001) face, the $Nd(OH)_3$ (101) face has an oxygen termination, which makes it a polar surface. By controlling the amount of NaOH added in the synthesis process, a control of the preferential growth in the [110] direction could be achieved to yield polar nanorods.

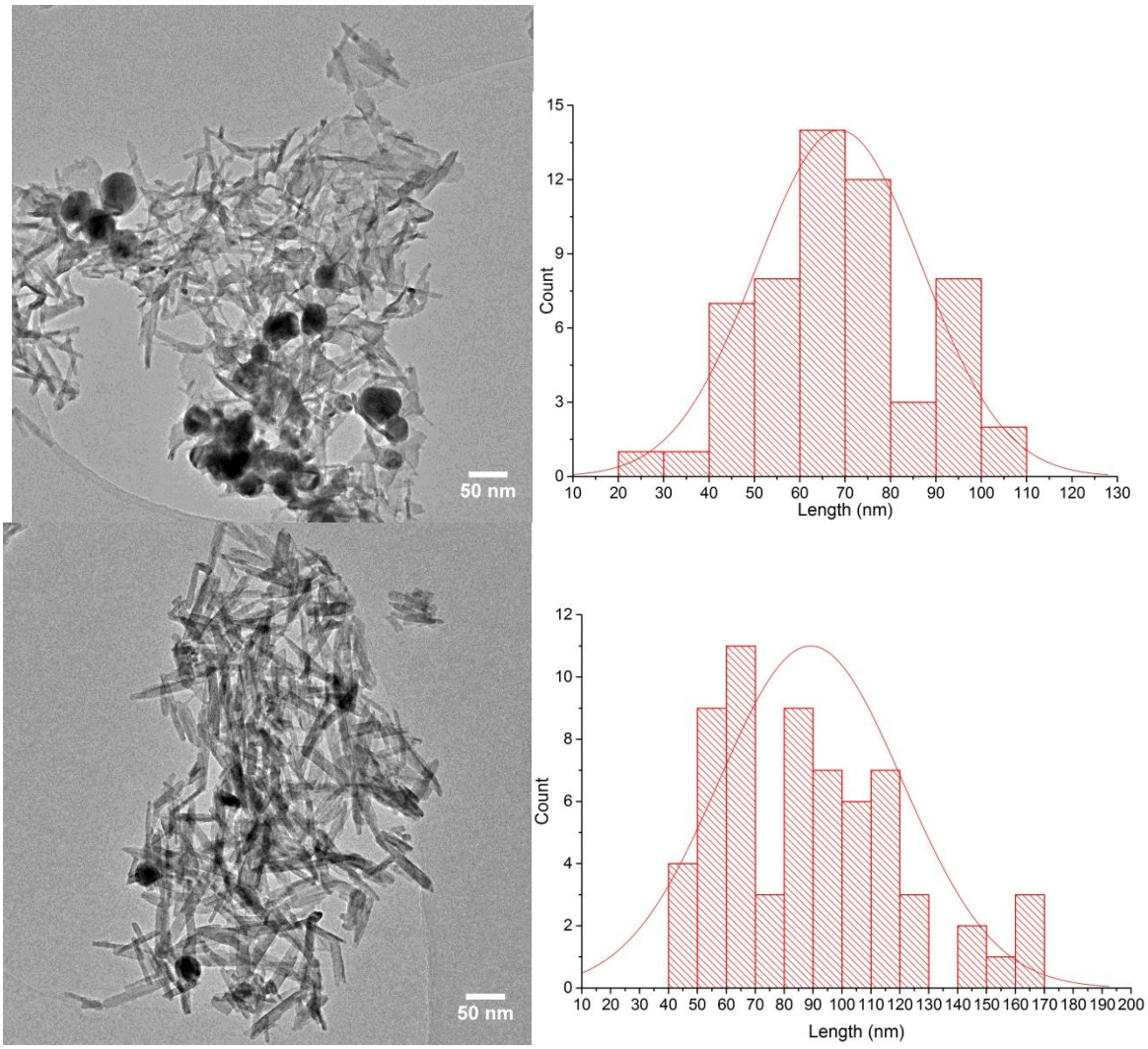

Figure 8-8 TEM image of Ag/Nd_2O_3 nanorod with 4g of NaOH added (top left); its histogram of length distribution (top right); TEM image of Ag/Nd_2O_3 nanorod with 8g of NaOH added (bottom left); its histogram of length distribution (bottom right).

Table 8-2 Summary of mean lengths and standard deviation of Nd_2O_3 nanorods.

NaOH Added (g)	Mean Length (nm)	Standard Deviation (nm)	Mean/SD
4	68	18	3.78
8	89	31	2.87

As the amount of NaOH added in the synthesis increased, the amount of OH^- stacking increased, giving longer rods. The control of the stacking was also better with increasing amount of NaOH, which resulted in more homogeneous nanorods. This increase in nanorod length was reflected in the XRD profiles, where the (110) and (101) peak intensities changed according to the length of the rod. The width of all the nanorods were found to be around 6 nm, which suggested the width was independent of the rate of OH^- stacking.

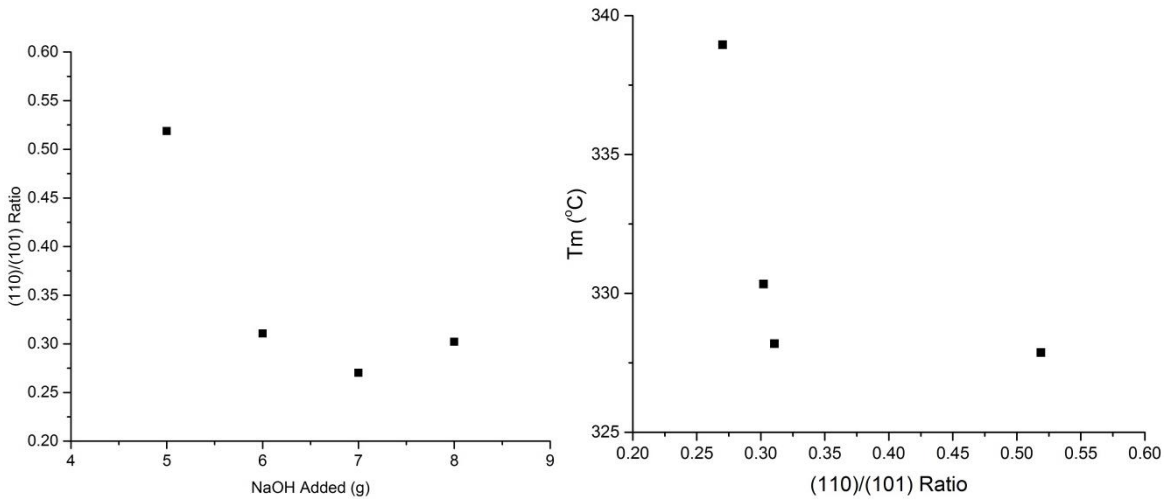

Figure 8-9 (110)/(101) peak intensity ratios versus amount of NaOH added (left); and ex-ECT soot T_m versus (110)/(101) peak intensity ratios (right).

A similar trend was observed with Nd_2O_3 nanorods as ZnO nanorods. As the proportion of polar surface increased, the amount of energetic oxygen on the polar surface also increased, which facilitated the low temperature combustion of soot.

Moreover, an interesting feature was present in the TGA profile of the Ag/Nd_2O_3 nanorods with ex-CRT soot. They were found to possess a double peak, which could be correlated to Ag supported on the polar (101) surface, and the non-polar (110) surface.

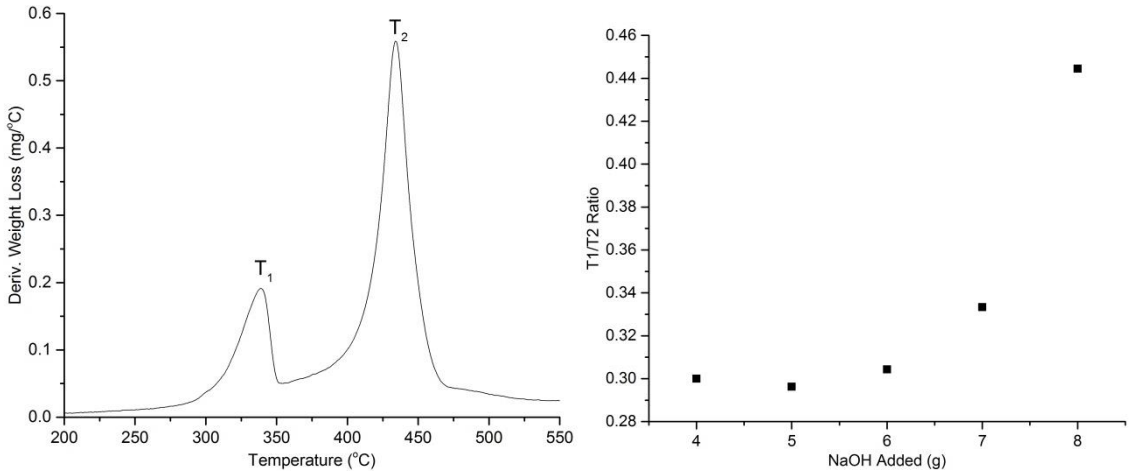

Figure 8-10 DTG profile of ex-CRT soot combustion with Ag/Nd_2O_3 nanorod. T_1 and T_2 are two combustion peaks (left); T_1/T_2 ratio with different amount of NaOH added (right).

As the amount of NaOH added increased, the amount of polar surface increased, and the T_1/T_2 ratio also increased. As the low temperature combustion peak, T_1, could be attributed to soot combustion on a polar surface, this meant that this result agreed with the finding that the proportion of polar surfaces increased with more base added. As the amount of polar surfaces increased with respect to the non-polar surface, the amount of soot would

increase correspondingly. Therefore, the T_1 peak intensity would rise with respect to T_2, as observed in Figure 8-9.

8.4 Summary

ZnO and Nd_2O_3 nanorods were synthesised, and used as a soot combustion catalyst. Both species have shown to form structures with polar surfaces with oxygen termination. This energetic polar surface could provide active oxygen for low temperature soot combustion.

By controlling the morphology of the nanostructure, the catalyst system could be selectively tuned to specific requirements by altering the reaction conditions. This will no doubt give a much greater control into catalyst design in furture work.

8.5 References

1 C. J. Kliewer, C. Aliaga, M. Bieri, W. Y. Huang, C. K. Tsung, J. B. Wood, K. Komvopoulos and G. A. Somorjai, *J. Am. Chem. Soc.*, 2010, **132**, 13088–13095.

2 A. Mclaren, T. Valdes-solis, G. Q. Li and S. C. Tsang, *J. Am. Chem. Soc.*, 2009, **131**, 12540–1541.

3 N. Zhang, R. Yi, L. B. Zhou, G. H. Gao, R. R. Shi, G. Z. Qiu and X. H. Liu, *Mater. Chem. Phys.*, 2009, **114**, 160–167.

Contents

Chapter 9. Modified Supported Ag Catalysts

9.1 Introduction

In previous chapters, early Ag/Ln_2O_3, particularly Ag/Nd_2O_3, and Ag/ZnO have been found to be effective soot combustion catalysts. Many factors have been identified that were vital to lower the soot combustion temperature.

Mul *et al.* proposed the employment of metal oxychloride as an additive for soot combustion[1], whereas Querini *et al.* showed further promotion of soot combustion by co-doping Co and K on a MgO support[2]. NO_x and SO_x has also been added into the feed stream to promote, or hinder, soot combustion[3–5]. Many more have reported promotional effects of other reactions by catalyst modification[6–9].

Therefore it is important in understanding catalyst modification and optimisation in order for the design of the catalyst that best suits the needs of a specific reaction. Other additive effects also need to be understood as they give a better understanding into the reaction mechanism of soot combustion.

Different mixed oxides were synthesised and tested in order to have a better understanding in their catalytic behaviour, Nd_2O_3 and other Ln_2O_3 nanorods were also co-supported onto industrial catalysts to reduce the amount of expensive rare earth material used in the catalyst.

9.2 Additive Effects

It has been known that adding NO_2 in the gas feed would promote soot combustion, and NO hinders it[3,10]. However, in a commercial exhaust system, it is not practical to stream NO_2 for soot combustion as it causes more pollution. A viable alternative is to dope the catalyst with additives in order to enhance its soot combustion performance. A series of alkali metal halides was used as additives, and their promotion (or hindrance) effects were investigated.

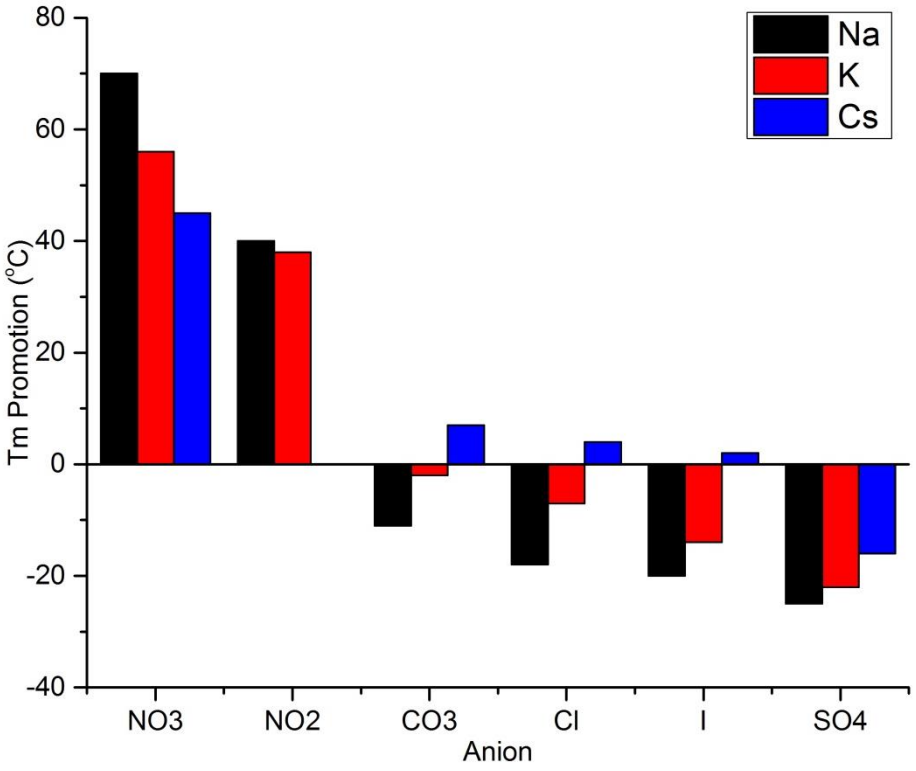

Figure 9-1 ex-CRT soot T_m promotion of alkali metal salt doped Ag/Nd_2O_3. N.B. $CsNO_2$ not available for testing.

A few trends could be observed from the different dopants. Firstly, with the exception of nitrates and nitrites, it was found that Cs salts were the most promoting amongst the three alkali metals tested. This was in good agreement with the findings of Aneggi *et al.*[11], where

it was found the promotional effect order was Cs > Rb > K > Na, *i.e.* greater promotion effect down the group. Secondly, a trend with the different anions could be established, where NO_3^- > NO_2^- > CO_3^{2-} > Cl^- > I^- > SO_4^{2-}. No previous studies have been done on the effects of the anion, and this effect would be well explained in this section. Finally, a very clear reverse trend was observed for NO_3^-, where $NaNO_3$ was found to be the most active dopant, and $CsNO_3$ least active. In order to have a better understanding of the effects of these dopants, their thermal behaviour should first be understood.

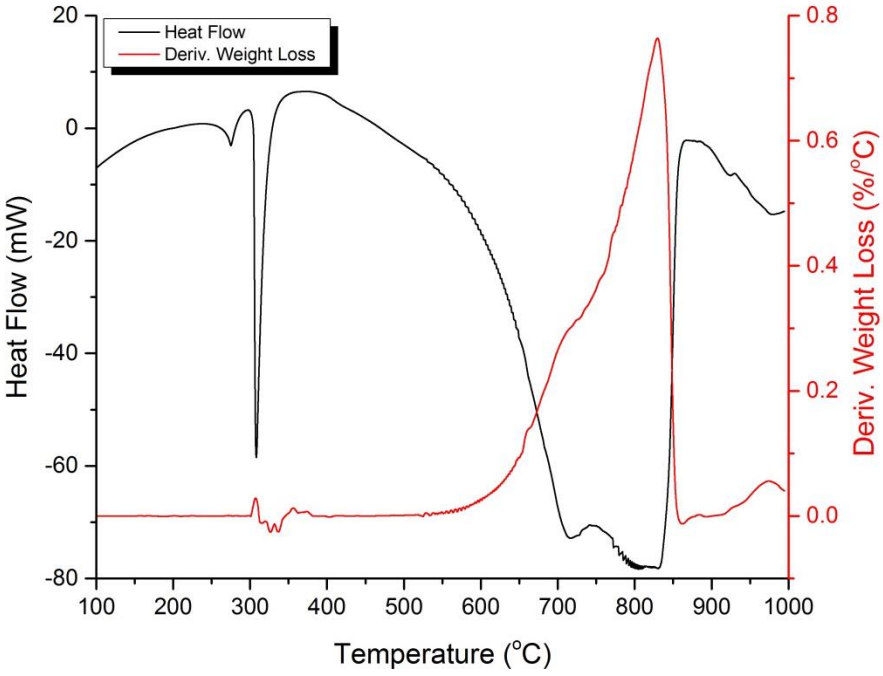

Figure 9-2 DSC profile (black) and DTG profile (red) as obtained by SDT of $NaNO_3$.

Figure 9-2 shows the SDT profile of $NaNO_3$, of which the DSC and DTG profiles were shown. It could be seen that at 300 °C, there was a sharp endothermic peak with no weight loss. The enthalpy of phase change was found to be 16.96 kJ mol^{-1}, which was in good agreement

with the enthalpy of fusion of $NaNO_3$ in literature[12]. The second endothermic peak with weight loss could be attributed to the boiling point of $NaNO_3$ at 700 ^oC. This profile was typical of the alkali metal salts, except the carbonates. The carbonates were found to decompose at temperatures below 200 ^oC to give oxides.

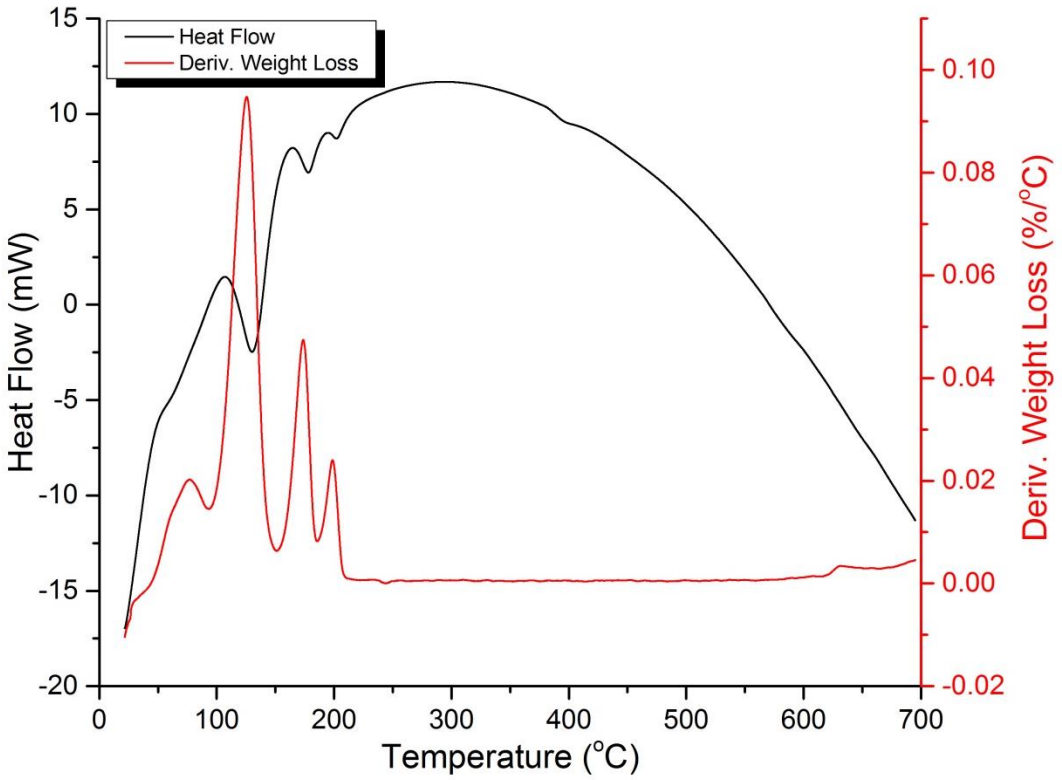

Figure 9-3 DSC profile (black) and DTG profile (red) as obtained by SDT of Cs_2CO_3.

Table 9-1 Table of melting points of Group 1 salts.

	Na	K	Cs
NO_3	308	312	407
NO_2	283	430	N/A
Cl	801	770	477
I	661	680	620
SO4	884	1069	1019

Some clear parallels could be drawn from Figure 9-1 and Table 9-1. Firstly, the melting points of the metal anion followed the opposite trend with its promotion effects. So a lower melting point anion, for example NO_3^-, had a greater promotion effect than a higher melting point anion, like SO_4^{2-}. Secondly, the melting point of the metal salts generally decreased down the group except for the nitrates and nitrites, with Cs salts having the lowest melting point. This general agreement between the trends of the melting point of the metal salts and their promotion effects therefore suggested that the melting point of these salts was important for the promotion of soot combustion.

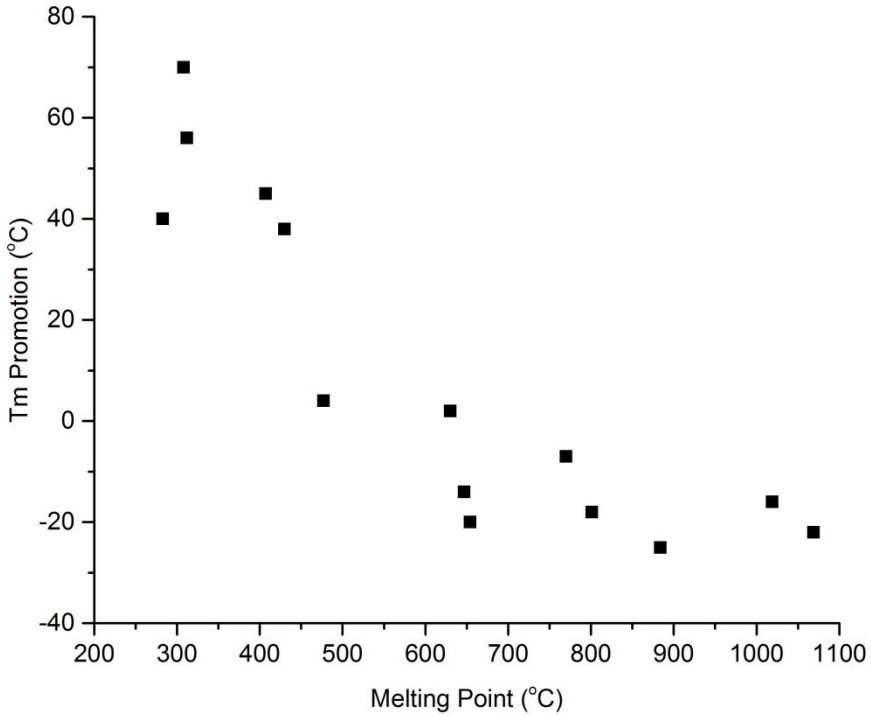

Figure 9-4 ex-CRT soot T_m Promotion versus melting point of metal salts.

This could be due to the increased mobility at a low temperature for the low melting point metal salts, which could be involved with the soot combustion. The higher melting point salts would become mobile at a much higher temperature, thus hindering soot combustion by hindering the mobility of surface oxygen species.

As the nature of the anion appeared to give a greater range in promotion effect, it would appear that the electronic withdrawing anion played a more important role in promoting soot combustion.

As to the cation, it could work in parallel with Ag to activate atmospheric oxygen to form chemisorbed oxygen species. The observed trend (Cs > K > Na) was due to the larger size and less electronegative, therefore softer, Cs cation which could be more readily polarised compared to the other cations.

Therefore, melting point (ion mobility), anionic electron withdrawing effect, and cation polarizability were the three main factors that determined the promotion ability of a certain metal salt.

9.3 Zinc Based Mixed Oxide Supports

Early Ln_2O_3 have been shown to be effective soot combustion catalysts, and ZnO has shown its potential with its diversity and tenability. In order to lower the cost of the catalyst, the amount of expensive rare earth materials must be reduced. Therefore, Zn based Ln doped oxides were synthesised in an attempt to produce a catalyst that could be tuned to the desired reactivity. No previous reports on zinc lanthanide oxides have been reported before, however, lanthanide doped metal oxides have been reported to show a great promotion in catalytic activity[13]. The zinc lanthanide oxides were made using the sol – gel method, then calcined at 600 ^{o}C overnight, before Ag was supported onto the support using the wet impregnation method. The atomic ratio of zinc oxide and lanthanide oxide was 1: 1.

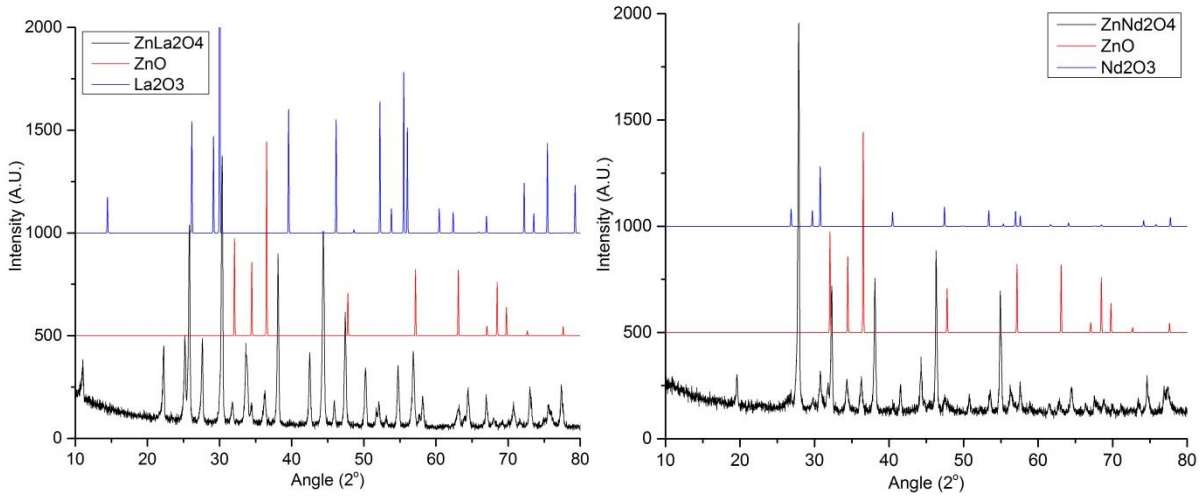

Figure 9-5 XRD Profile of $ZnLa_2O_4$ (left), and $ZnNd_2O_4$ (right). Simulated XRD profiles of ZnO (red) and Ln_2O_3 (blue) are shown together with $ZnLn_2O_4$ (black).

Figure 9-5 shows the XRD profiles of $ZnLa_2O_4$ and $ZnNd_2O_4$. When compared to the profiles of ZnO, and their respective Ln_2O_3, it was found that few of the peaks matched either of the pure oxides, which suggested that no pure ZnO or Ln_2O_3 were synthesised. Instead, a new material with unknown peaks has been made, as no XRD profiles of these $ZnLn_2O_4$ materials have been published before in open literature.

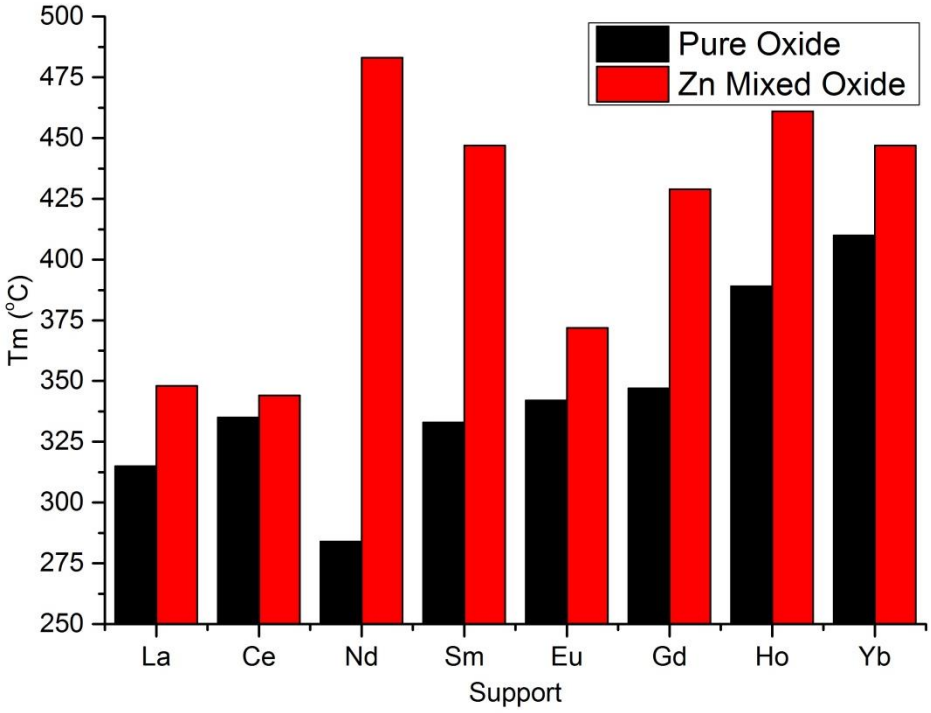

Figure 9-6 ex-CRT soot T_m of Ag/Ln2O3 (black) and Ag/ZnLa2O4 (red).

Figure 9-6 shows the ex-CRT T_m of $Ag/ZnLn_2O_4$, and compared to the corresponding Ag/Ln_2O_3. It could be seen that all the Zn mixed oxides had a much higher T_m, especially Nd, whose T_m rose from 284 ^oC to over 475 ^oC.

This $ZnLn_2O_4$ system could be thought as a Ln doped ZnO, which made this catalyst system an p-type semiconductor, with the Ln^{3+} acting as holes. In order to understand the high activities of $ZnCe_2O_3$, and $ZnEu_2O_3$, a better understanding of the electronic environment of the native lanthanides should be established.

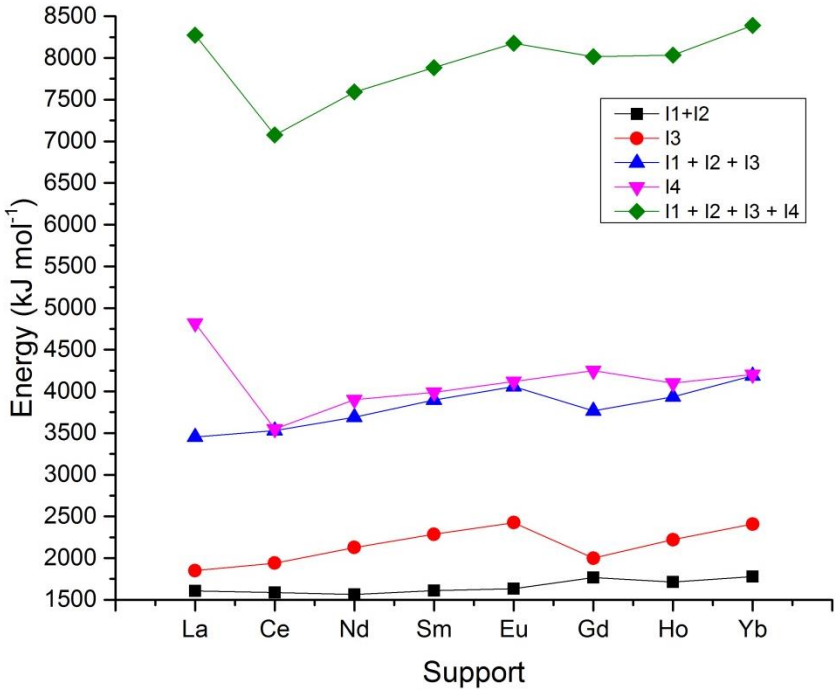

Figure 9-7 nth ionisation energy of the lanthanides, and the sum of the first nth ionisation energies[14].

For Ce, it has a very low 4th ionisation energy, which makes the formation of Ce^{4+} very favourable compared to other lanthanides; whereas the 3rd ionisation energy of the Eu is much higher than other rare earth metals, making the formation of Eu^{3+} particularly unfavourable.

It was possible that there was a facile $Ce^{3+/4+}$ and $Eu^{2+/3+}$ redox couple established in the catalyst system, which facilitated lower energy electronic transfer from Zn^{2+} to the Ln^{n+}. TPR was used to investigate the oxygen activation temperature, which would give an overall picture of metal–support interaction of the system.

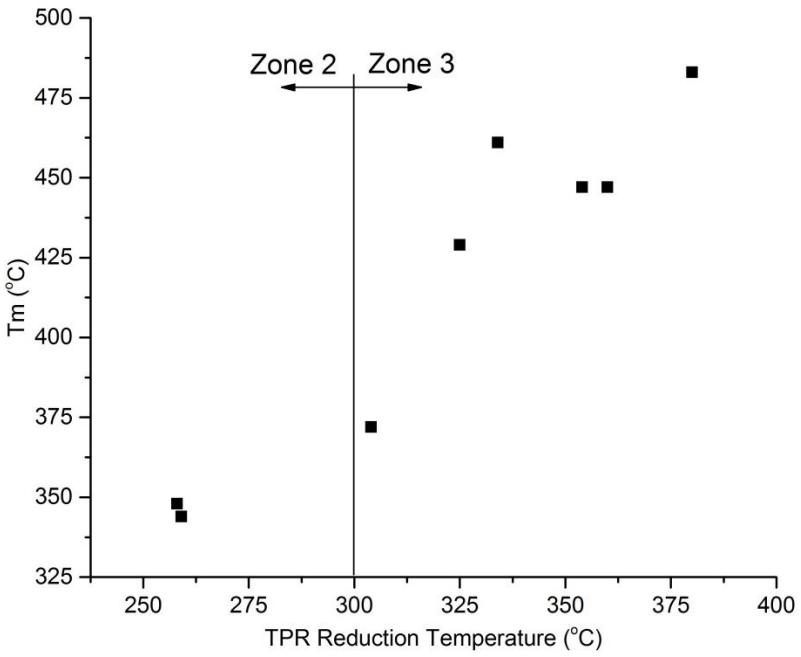

Figure 9-8 ex-CRT soot T_m versus TPR reduction temperature of $Ag/ZnLn_2O_4$.

Using the classification system laid out in Chapter 7, $ZnLa_2O_4$ and $ZnCe_2O_4$ would have been in Zone 2, whilst the other $ZnLn_2O_4$ compounds were in Zone 3. This was in good agreement with what was previously found, and so it could be concluded that $ZnLa_2O_4$ and $ZnCe_2O_4$ were able to activate oxygen to O_β at lower temperatures than the other mixed oxides. $ZnEu_2O_4$ had a TPR reduction temperature of 304 °C, which was the borderline between Zones 2 and 3. This meant that $ZnEu_2O_4$ could also activate O_β at a relatively low temperature.

9.4 Industrial Catalyst Modification

In Chapter 4, industrial 8% Ag/Al_2O_3 was used as screening tests for preliminary studies. This catalyst was synthesised using flame spray pyrolysis, which gave a narrow size distribution with monodispersed Ag. This maximised the potential for any metal–support interaction it

may have with a dopant onto the catalyst. Therefore, various Ln_2O_3 were doped onto the industrial catalyst to investigate the electronic interactions between Ag and Ln_2O_3 on a common support. The Ln_2O_3 was loaded using the sol–gel method.

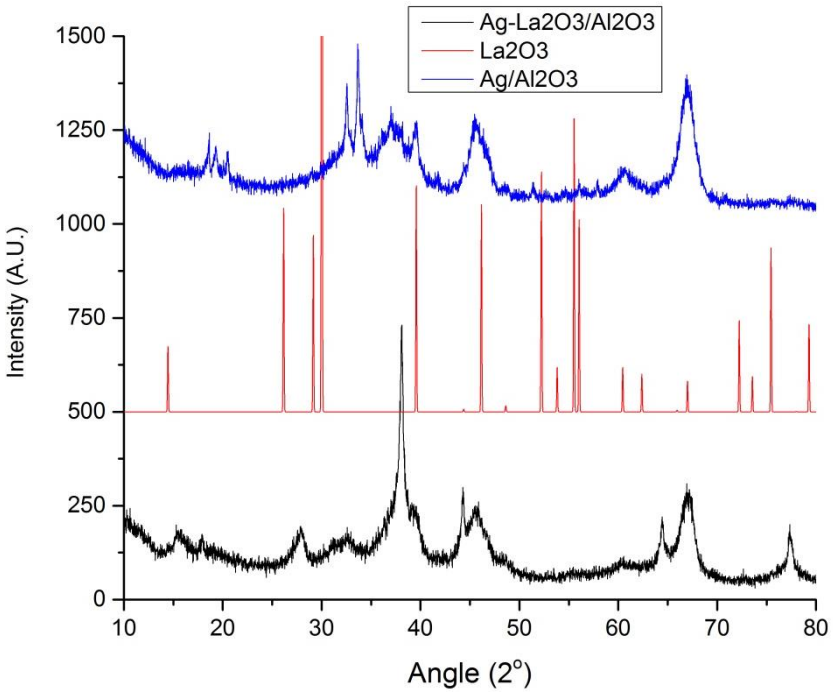

Figure 9-9 XRD profile of Ag-La_2O_3/Al2O3 (black); with Ag/Al_2O_3 (blue) and simulated La_2O_3 (red) as reference.

Unlike the Zn mixed oxides, clear La_2O_3 peaks could be seen in the XRD profile, which suggested that there was clear phase separation between Ag/Al_2O_3 and La_2O_3. The same was observed across the lanthanide series, where crystalline Ln_2O_3 could clearly be observed in the XRD profiles.

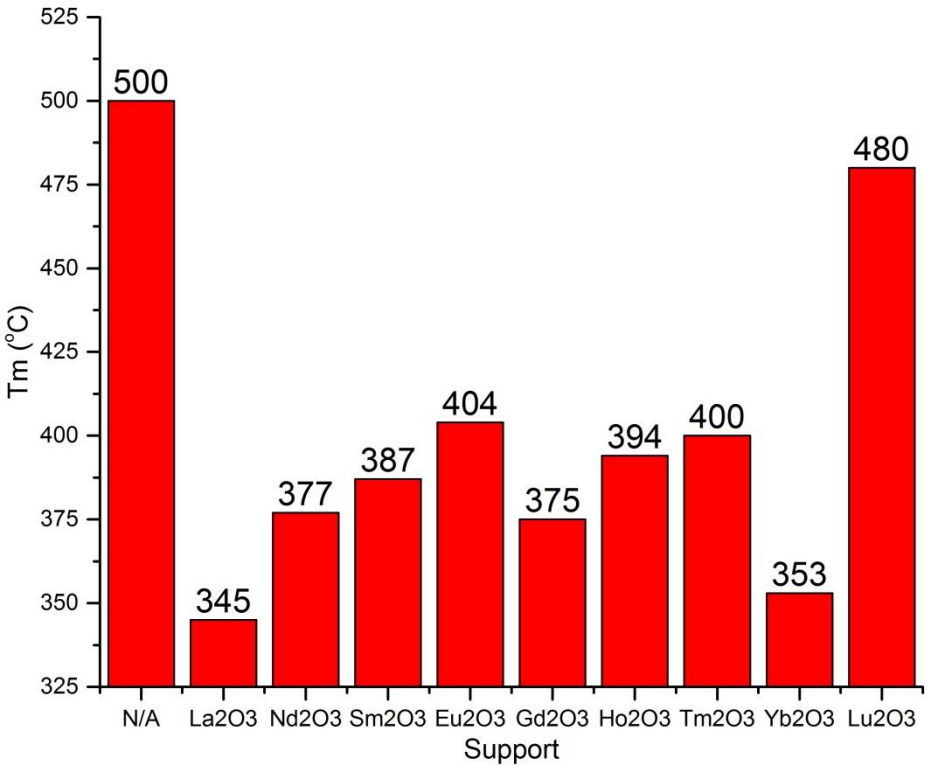

Figure 9-10 ex-CRT soot T_m of Ag-Ln_2O_3/Al_2O_3, N/A represents no co-support.

All the co-supported catalysts had a lower T_m than the unmodified JM catalyst, which showed clearly the promotional effects of metal – support interaction. The extent of the promotion due to the co-support was quite different to what was observed in previous tests. However, as no standardised measure of metal – support interaction was devised for quantification of this important parameter, the TPR characterisation test could give a qualitative indication of metal – support interaction *via* the measure of O_β activation.

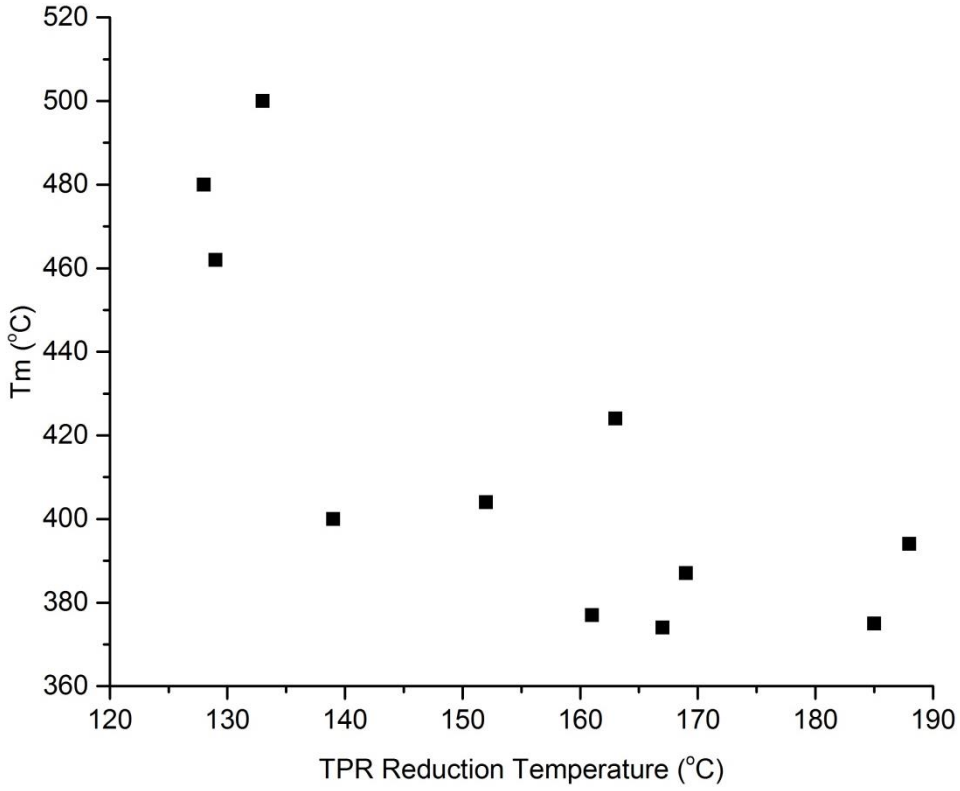

Figure 9-11 ex-CRT soot T_m versus TPR reduction temperature of Ag-Ln_2O_3/Al_2O_3.

All the co-supported catalysts were in Zone 1, where the TPR reduction temperature was below 230 °C. This meant that O_β activation occurred at very low temperatures, resulting in the inability of these active oxygen species in taking part in the soot combustion reaction. As a consequence, as the TPR reduction temperature of O_β increased, the corresponding soot combustion T_m decreased.

9.5 Summary

Various catalyst modification methods have been used in an attempt to promote the soot combustion reaction. A series of alkali metal salts were doped with Ag/Nd_2O_3, and it was found that $NaNO_3$ was the most effective dopant with a promotion of 70 °C. The reason for the metal salt promotion was due to an increase in ionic mobility with its low melting point.

The polarizability of the softer Cs cation was also found to be more effective in promoting soot combustion than the more ionic K and Na cations.

Ln doped Zn mixed oxides were made to create n-type semiconductor. Despite all the mixed oxides had a higher soot combustion temperature than the pure Ln_2O_3 support, an understanding in the electronic interaction between Ln and Zn was established. Ag-Ln_2O_3/Al_2O_3 was also made based on the industrial catalyst, which demonstrated the effects of metal – support interaction and its promotional effects. The TPR technique developed in previous chapters was used to successfully classify these catalysts into the respective zones, which showed again the possibility to estimate the soot combustion activity of a certain catalyst without any further information on either size or nature of the support.

9.6 References

1 G. Mu, F. Kapteijn, J. A. Moulijn and G. Mul, *Appl. Catal. B-Environmental*, 1997, **12**, 33–47.

2 C. A. Querini, L. M. Cornaglia, M. A. Ulla and E. E. Miro, *Appl. Catal. B-Environmental*, 1999, **20**, 165–177.

3 I. Atribak, I. Such-Basaniez, A. Bueno-Lopez and A. Garcia-Garcia, *J. Catal.*, 2007, **250**, 75–84.

4 I. Atribak, A. Bueno-Lopez and A. Garcia-Garcia, *J. Catal.*, 2008, **259**, 123–132.

5 V. G. Milt, C. A. Querini, E. E. Miro and M. A. Ulla, *J. Catal.*, 2003, **220**, 424–432.

6 S. N. Goncharova, E. A. Paukshtis and B. S. Bal'zhinimaev, *Appl. Catal. A-General*, 1995, 67–84.

7 W. Yao, Y. L. Guo, X. H. Liu, Y. Guo, Y. Q. Wang, Y. S. Wang, Z. G. Zhang and G. Z. Lu, *Catal. Letters*, 2007, **119**, 185–190.

8 C. Koenigsmann, A. C. Santulli, K. P. Gong, M. B. Vukmirovic, W. P. Zhou, E. Sutter, S. S. Wong and R. R. Adzic, *J. Am. Chem. Soc.*, 2011, **133**, 9783–9795.

9 S. Satokawa, J. Shibata, K. Shimizu, S. Atsushi and T. Hattori, *Appl. Catal. B-Environmental*, 2003, **42**, 179–186.

10 D. Uner, M. K. Demirkol and B. Dernaika, *Appl. Catal. B-Environmental*, 2005, **61**, 334–345.

11 E. Aneggi, C. de Leitenburg, G. Dolcetti and A. Trovarelli, *Catal. Today*, 2008, **136**, 3–10.

12 J. G. Cordaro, A. M. Kruizenga, R. Altmaier, M. Sampson and A. Nissen, *Proc. SolarPACES Conf. Granada, Spain*, 2011.

13 A. Bueno-Lopez, K. Krishna, M. Makkee and J. A. Moulijn, *J. Catal.*, 2005, **230**, 237–248.

14 S. Cotton, *Lanthanide and Actinide Chemistry*, 1995.

Contents

Chapter 10. Other Oxidative Reactions

10.1 Introduction

Ag is a versatile oxidation catalyst, and it has been previously used in a range of other reactions other than the soot combustion reaction. Mills *et. al.* have demonstrated the possibility of photocatalytic decomposition of soot over a period of 45 days[1]. Ag has also been used for methane oxidation and methane coupling reactions[2–5]. More significantly, selectively epoxidation of ethylene and propylene using an Ag catalyst have attributed this selectivity to the existence of subsurface electrophilic oxygen species[6–11]. However, no studies on the promotion effects of Ln_2O_3 as a series have been carried out before.

This chapter concentrates on the possibility of the employment of Ag/Ln_2O_3 as a photothermal catalyst for the decomposition, and to investigate the possibility and reaction mechanism of facile photocatalytic decomposition of soot. Furthermore, Ag/Ln_2O_3 was used as a catalyst for the selective epoxidation of propylene to propylene oxide (PO). Its activity and selectivity compared to conventional Al_2O_3 supported catalysts, and the role of mobile interstitial oxygen investigated.

10.2 Photocatalytic Decomposition of Soot

10.2.1 Preliminary Feasibility Tests

"Conventional" photocatalysts, such as P25 TiO_2 and ZnO, were used as supports in preliminary experiments to give a benchmark on the activity of the photocatalytic of soot. Different reaction parameters were also explored in order to optimise the conditions used for the reaction.

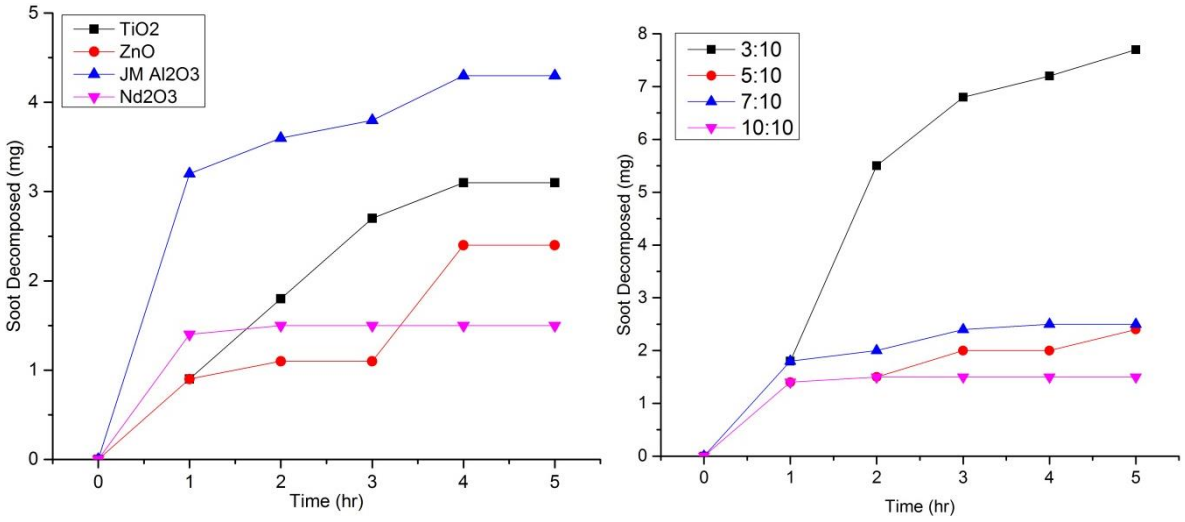

Figure 10-1 Rate of photocatalytic decomposition activity of soot with Ag/MO, catalyst: soot ratio = 1:1 (left); Rate of photocatalytic decomposition activity of soot with Ag/Nd_2O_3 with different Catalyst: Soot ratio (right).

Ag/Nd_2O_3 was found to be not very effective photocatalyst, with 15% conversion of soot after 5 hours, with quick deactivation after 1 hour. Compared to P25 or ZnO, which were thought to be "conventional" photocatalyst, Nd_2O_3 was comparatively inactive. However, rather surprisingly, the JM 8% Ag/Al_2O_3 catalyst was found to be the most active photocatalyst, with 43% conversion after 5 hr.

The above tests were done with a catalyst: soot ratio of 1:1, where 10 mg of catalyst was mixed with 10 mg of soot. The catalyst: soot ratio was then reduced, which found to give a massive increase in photoactivity. In the case of Ag/Nd_2O_3, conversion after 5 hr increased from 15% to 78% as the catalyst loading decreased from 10 mg to 3 mg. This was probably due to the increase rate of quenching at higher catalyst loading, which made the catalyst self-deactivating.

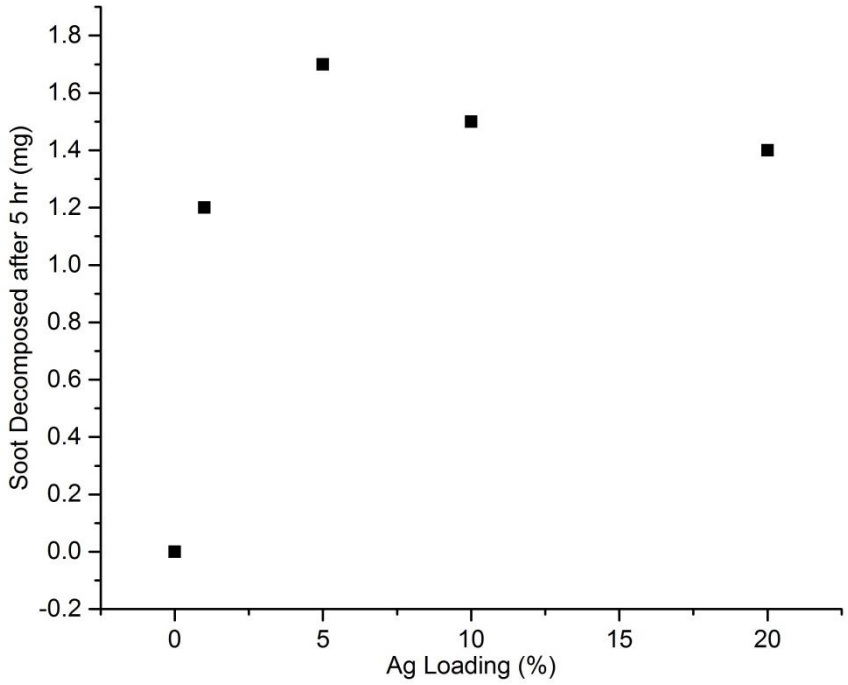

Figure 10-2 Soot decomposed after 5 hr at different Ag loading of Ag/Nd2O3. Catalyst: soot ratio = 1:1.

5% Ag/Nd_2O_3 was found to be the most active photocatalyst, with an increase in Ag loading reducing its photoactivity. This supported the theory that Ag was self-quenching, and a higher loading of Ag would be auto-deactivating for the photocatalytic reaction with soot.

10.2.2 Modification of JM Catalyst for Photoreaction

It was interesting to find in the preliminary tests that the JM catalyst was the most active photocatalyst, with a conversion rate higher than both P25 or ZnO. Ln_2O_3 was co-supported onto the JM catalyst to investigate the metal–support interaction and its effects with the photodecomposition of soot.

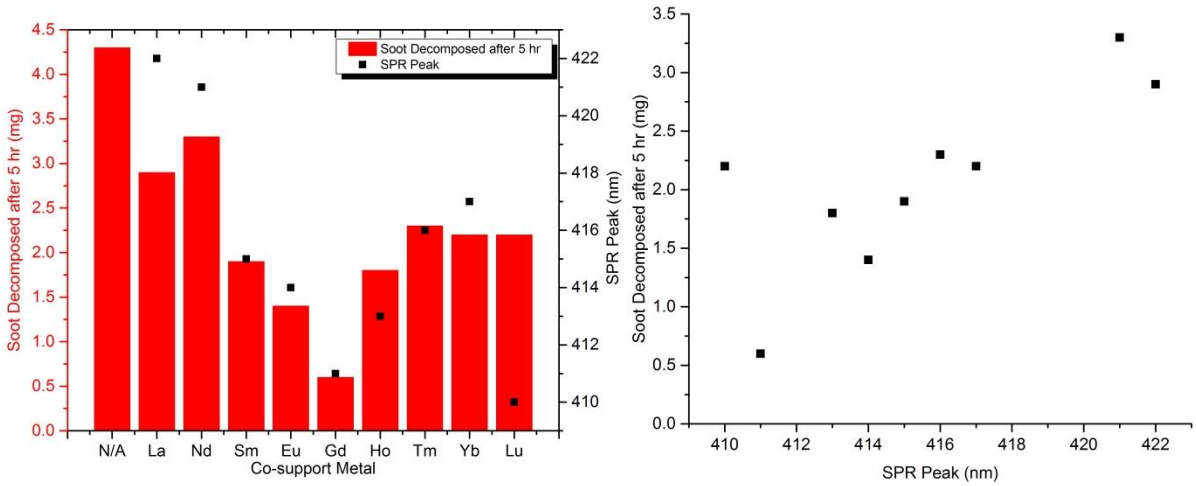

Figure 10-3 Soot decomposed after 5 hours using Ag-Ln_2O_3/Al_2O_3 after 3 hours and their corresponding SPR peak (left); and soot decomposed versus SPR peak (right).

Unlike thermal decomposition of soot, photocatalytic decomposition of soot did not depend on the metal–support interaction. Adding a Ln_2O_3 co-support hindered the photoreaction as a whole, though the extent was different depending on which oxide it was. It appeared that the photocatalytic activity of the catalyst depended on the SPR peak position of the Ag nanoparticles. No quadrupolar SPR peak was detected for Ag/Al_2O_3 with no co-support, which was probably due to the small Ag particle size resulting in no quadrupolar excitation, only dipolar excitation.

10.2.3 Surface Plasmon Resonance

The trend appeared to be a linear relationship between the SPR peak position and its photocatalytic activity. Taking other catalysts into account, a more complete picture could be drawn.

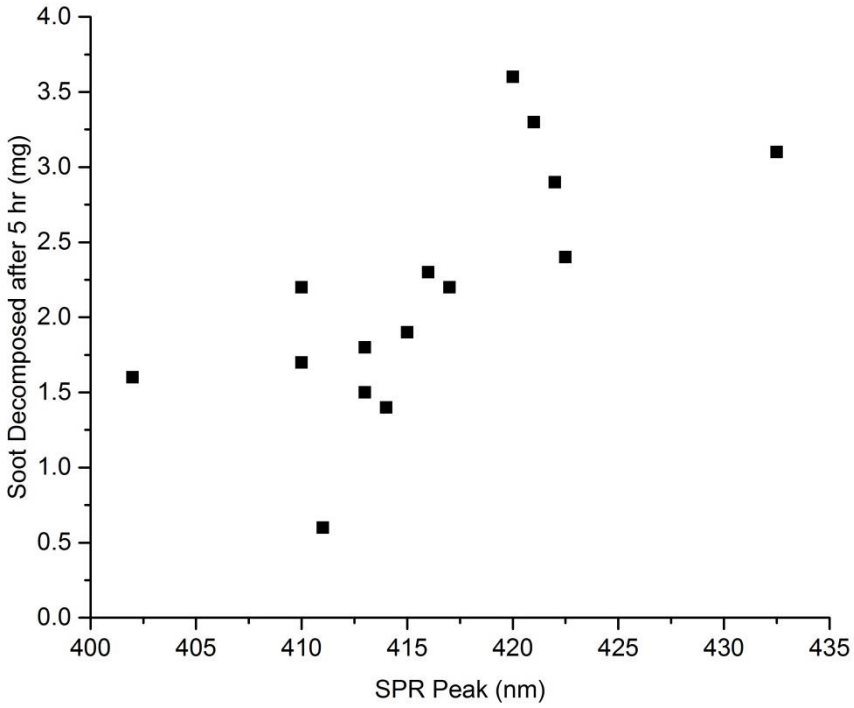

Figure 10-4 Soot decomposed after 5 hours versus SPR quadrupolar peaks of the Ag nanoparticles.

It appeared that the general trend observed was that a higher SPR peak shift wavelength resulted in a higher rate of soot decomposition. SPR could be seen as a "virtual excited state" where the electron was excited into a localised surface plasmon "virtual energy level". As the SPR peak wavelength increased, it meant the energy of excitation decreased. This provided a better energy overlap with the conduction band of the metal oxide, thus providing better electron transfer.

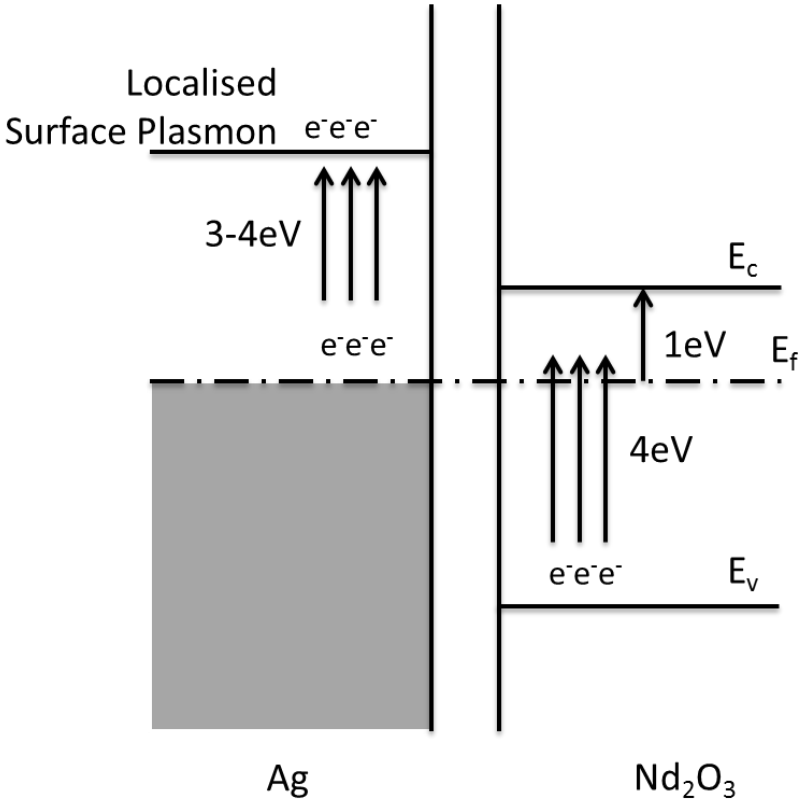

Figure 10-5 Schematic diagram of the band structure of Ag/Nd2O3 with surface plasmon resonance. E_v, E_f, and E_c represents valence band, Fermi level, and conduction band, respectively.

The localised surface plasmon (LSP) first excited the electrons into a "virtual state", which could then relax into the conduction band of the metal oxide through surface plasmon resonance. A better energy overlap was achieved as the LSP excitation energy and the conduction band with lower energy "virtual states", which would result in a more facile electron transfer.

10.3 Partial Oxidation of Propylene

10.3.1 Introduction

Ethylene epoxidation using Ag as catalyst has been widely studied, with selectivity as high as 80%[12]. On the other hand, the selectivity of propylene epoxidation was much lower at around 10%[13].

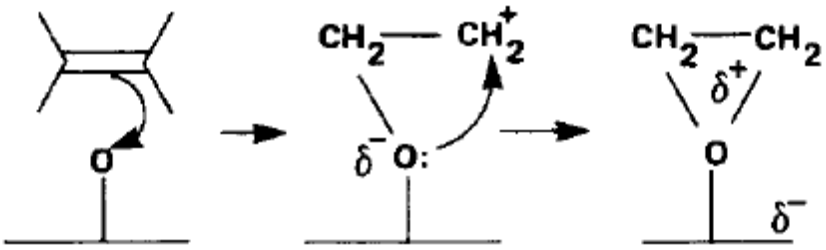

Figure 10-6 Schematic diagram of the reaction mechanism of ethylene epoxidation.

In order for epoxidation to occur, ethylene must be adsorbed in a bidentate mode on the surface of the catalyst for oxygen attack on either side of the double bond. The methyl group on the propylene caused steric hindrance to the double bond adsorption, which significantly lowered the selectively of propylene epoxidation to PO. Therefore, in order to increase the selectivity of PO, the oxygen species must not be too active to indiscriminantly react with monodentate binding propylene to give CO_2 or other oxidative products, such as acrolein or acetone.

Previous research has shown that the production of PO depended greatly on the adsorption of propylene onto the catalyst surface, and the ability for oxygen to attack the double bond in a concerted fashion.

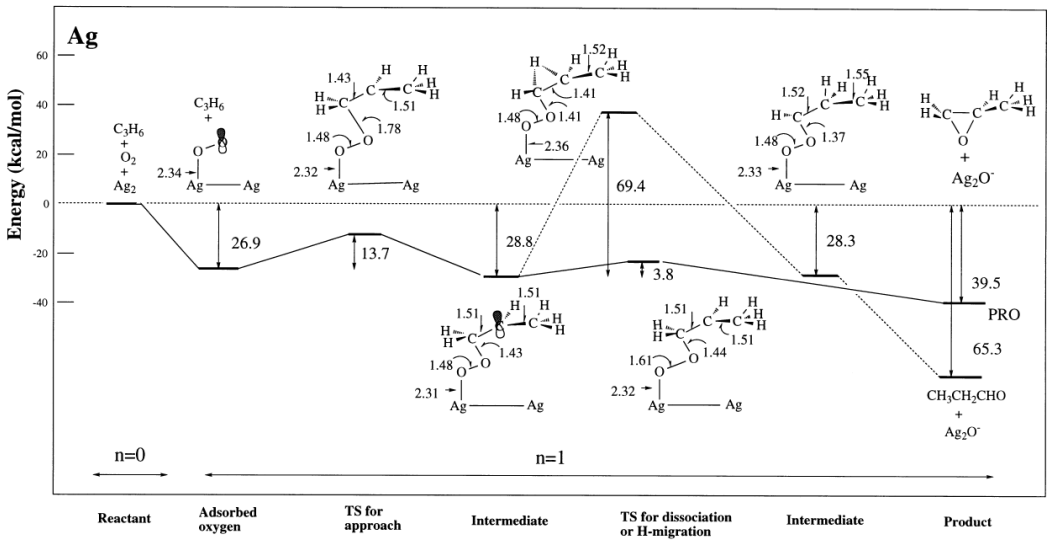

Figure 10-7 Energy diagram for the reaction between terminal carbon atom and molecularly adsorbed oxygen. Solid line: PO product; aldehyde product[14].

Many reaction mechanisms have been proposed, where Figure 10-7 depicts a proposed mechanism that does not have a concerted attack mechanism. It shows the terminal carbon is initially attacked by the adsorbed oxygen molecule, then the resultant complex can either be attacked by the central carbon to yield PO, or by the terminal carbon again to yield propanal. The pathway to form propanal involves hydrogen migration, which results in a much higher energy in the transition state. However, the lack of strain of the three-membered ring makes propanal a more stable product. Therefore, PO can be seen as the kinetic product, whereas propanal or other products as the thermodynamic product.

The partial oxidation of propylene was performed in collaboration with Bin Yu, a member of the Tsang Group. The reaction was performed under stoichiometric ratio of propylene and oxygen, *i.e.* 2:1. The reactant mixture was diluted with Ar at 0.5%, and the flow of the reactant stream was controlled using a mass flow controller at 100 mL min^{-1}.

10.3.2 Preliminary Screening Tests

Ag/Al_2O_3 and Ag/SiO_2 were used as catalysts for the initial screening tests for the partial oxidation reaction of propylene. Three major products were observed across the temperature range tested, namely CO_2, CO and propylene oxide (PO). CO_2 and CO were the result of complete oxidation of propylene, whereas PO was the desired product from the partial oxidation of propylene.

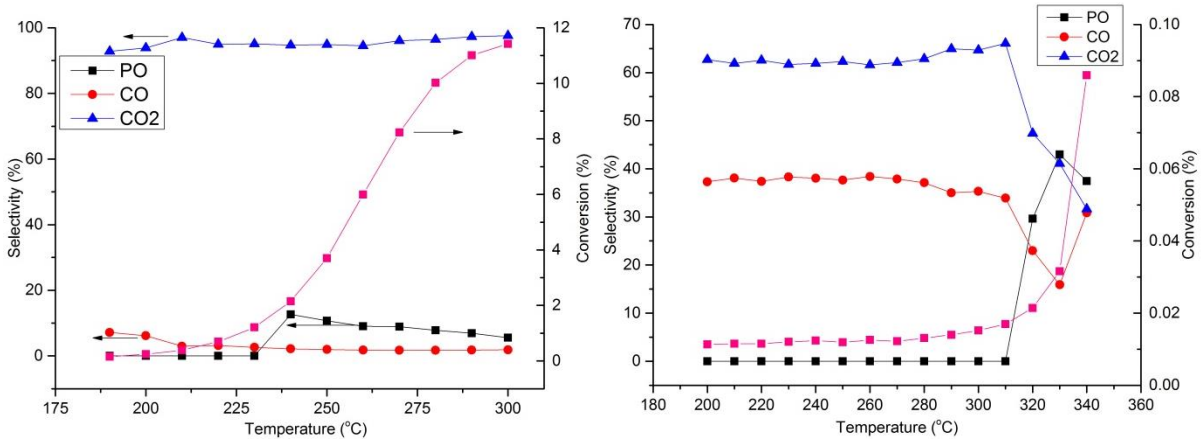

Figure 10-8 Conversion and selectivity of propylene oxidation using Ag/Al_2O_3 (left) and Ag/SiO_2 (right) catalyst. Pink line: Conversion; Black line: PO Selectivity; Red line: CO Selectivity; Blue line: CO_2 Selectivity.

PO was not produced at lower temperatures, where the only products observed were the complete oxidation products. In the case of Ag/Al_2O_3, PO was beginning to be produced at 240 ^oC, whereas no PO was produced with the Ag/SiO_2 catalyst until 310 ^oC. This suggested that Ag/Al_2O_3 was much more reactive towards the propylene oxidation than Ag/SiO_2. The conversion of the two catalysts was also clear indication of their activities, where Ag/Al_2O_3 achieved a conversion rate of 11.4% at 300 ^oC, and Ag/SiO_2 <0.1% at the same temperature. Thus it could be concluded that SiO_2 was an inactive support for the oxidation reaction of propylene. A reason for this inactivity could be due to the covalent nature of SiO_2, resulting in a lack of mobile energetic oxygen species which could be involved with the reaction.

Nonetheless, although Ag/SiO_2 had a much lower conversion rate than Ag/Al_2O_3, its PO selectivity was over twice as high as that of Ag/Al_2O_3. A possible explanation could be due to the lack of mobile O_β species in SiO_2, therefore the only oxygen source would be from molecular oxygen from the reactant stream. This adsorbed oxygen could result in selective partial oxidation of propylene, which would increase PO selectivity.

At a higher propylene concentration of 4:1, less oxygen was present in the reaction gas stream, which should increase selectivity towards partial oxidation of propylene.

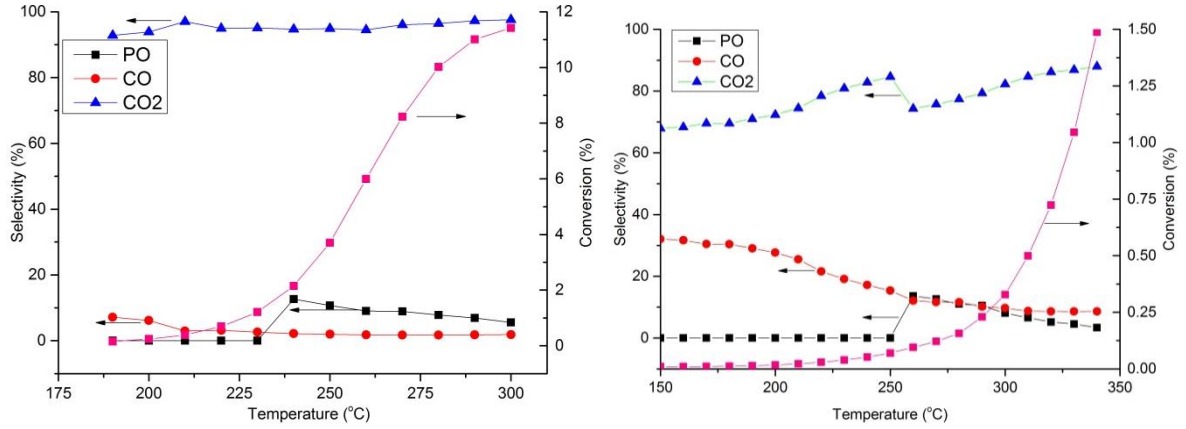

Figure 10-9 Conversion and selectivity of propylene oxidation with Ag/Al_2O_3 at Propylene:Oxygen ratio = 2:1 (left), and 4:1 (right).

By halving the concentration of oxygen in the reaction stream, the selectivity of PO increased from 12.6% to 13.6%. However, the onset of PO production increased from 240 ^{o}C to 260 ^{o}C, and the conversion rate decreased from 11.4% to 0.25% at 300 ^{o}C. Therefore, by reducing the oxygen content in the reaction stream, the yield of PO had reduced from 0.64% to 0.03%. This suggested the reaction was consistent with the Eley – Rideal mechanism, where molecular oxygen would react with adsorbed propylene species to form PO.

The marginal increase in PO selectivity and the detrimental effects of decreasing oxygen concentration on both conversion and yield of PO suggested that the optimal reaction condition was a stoichiometric ratio between propylene and oxygen.

10.3.3 Partial Oxidation of Propylene Using Ag/Ln_2O_3

Ag/Ln_2O_3 was thus used in order to verify the theory of the involvement of O_β in the partial oxidation reaction of propylene. Figure 10-10 shows the conversion rate of propylene using different Ag/Ln_2O_3 catalysts up to 340 ^oC.

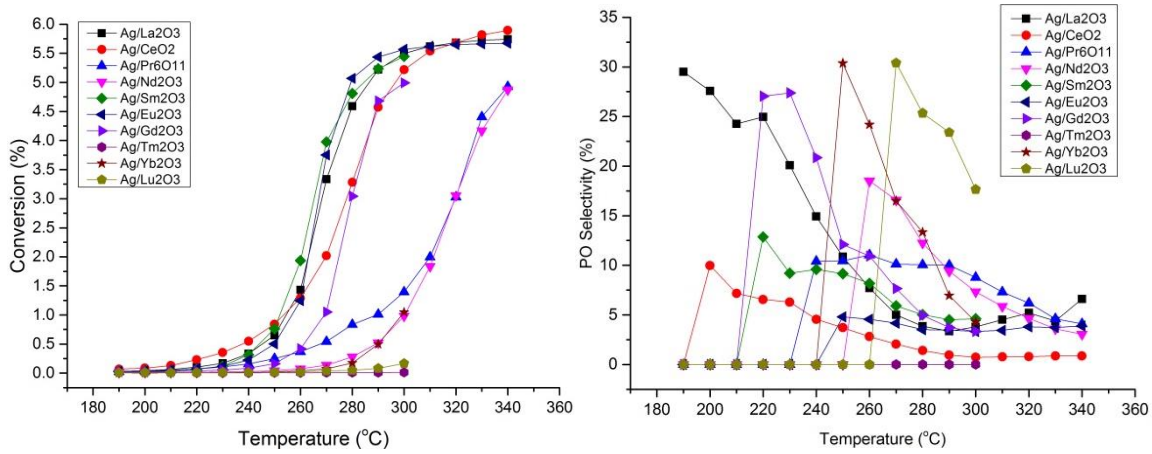

Figure 10-10 Conversion rates (left), and PO selectivity (right) of propylene using Ag/Ln_2O_3 catalysts.

Several general features could be observed from Figure 10-10 above. The conversion rate for all the Ag/Ln_2O_3 catalysts, with the exception of Ag/Tm_2O_3, increased as temperature increased. However, PO selectivity decreased as temperature increased, which meant at higher temperature the rate of complete oxidation was significantly greater than that of partial oxidation. The onset temperature of PO production also varied across the lanthanide series, with Ag/La_2O_3 producing PO at temperatures below 190 ^oC; whereas Ag/Tm_2O_3 was not active towards oxidation of propylene, either complete or partial, at temperatures up to 340 ^oC. As selectivity for PO decreased at higher temperatures, it was general true that the highest PO selectivity for each individual catalyst was at the temperature of PO production

onset. Table 10-1 below gives a summary of the maximum PO selectivity for each catalyst across the lanthanide series, and the temperature of maximum PO selectivity.

Table 10-1 Maximum PO Selectivity of Ag/Ln2O3. The number shown in brackets corresponds to the temperature of maximum PO selectivity. TPR reduction temperatures shown as reference.

Catalyst	Maximum PO Selectivity (%)	TPR Reduction Temperature (^{o}C)
Ag/La_2O_3	29.5 (190 ^{o}C)	230
Ag/CeO_2	10.0 (200 ^{o}C)	239
Ag/Pr_6O_{11}	10.4 (240 ^{o}C)	332
Ag/Nd_2O_3	18.5 (260 ^{o}C)	238
Ag/Sm_2O_3	12.9 (220 ^{o}C)	245
Ag/Eu_2O_3	4.8 (250 ^{o}C)	252
Ag/Gd_2O_3	27.1 (220 ^{o}C)	265
Ag/Tm_2O_3	0 (N/A)	297
Ag/Yb_2O_3	30.4 (250 ^{o}C)	286
Ag/Lu_2O_3	30.4 (270 ^{o}C)	278

With the exception of Ag/Nd_2O_3, the onset temperature of PO production increased across the lanthanide series, which correlated to the increase in TPR reduction temperature. The selectivity was found to be the highest with the late Ag/Ln_2O_3 of Yb_2O_3 and Lu_2O_3, and the lowest for Eu_2O_3 (discounting Tm2O3, which did not produce any PO at all). This was in stark contrast to the soot combustion behaviour, where the early lanthanide oxides were found to be much more active supports than the late lanthanide oxides.

10.3.4 Oxygen Activation

It has been established in previous chapters the role of mobile oxygen played in the activation of soot, and the subsequent promotion of the soot combustion reaction. However, as soot combustion was a complete oxidation reaction, the nature of the oxygen was not important as long as it was energetic enough for soot activation. With the partial

oxidation of propylene, the oxygen species involved in the reaction should be selective towards PO production, and not complete oxidation to form CO and CO_2.

A major obstacle in comparing the selectivity of PO and the role of O_β was that the onset temperature for PO production was different for each catalyst, and so it was impossible to quantify the amount, or reactivity, or O_β on the selectivity of PO.

As propylene conversion and PO selectivity were dramatically affected by temperature, several temperatures were chosen in an attempt to understand the effects of O_β on the selectivity of the partial oxidation of propylene.

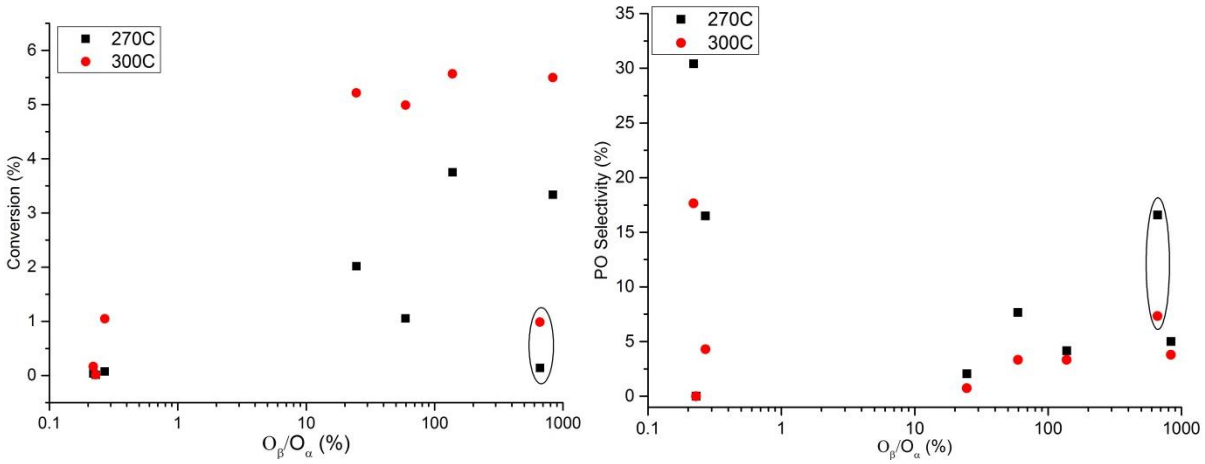

Figure 10-11 Propylene conversion (left), and PO selectivity (right) with Ag/Ln2O3 against O_β/O_γ ratio. Black points: 270 °C; red points: 300 °C.

Figure 10-11 shows the propylene conversion rates and PO selectivities with Ag/Ln_2O_3 catalysts at 270 °C and 300 °C. These two temperatures were chosen as they were the

lowest and highest temperatures that had PO production across the entire lanthanide series. Some general trends could be observed from the graphs. Firstly, there was a general decrease in conversion and a decrease in PO selectivity as temperature increased. This was due to the increased activity of the oxygen species at higher temperature which could get over the energy barrier for reaction, and its increase indiscrimination in reacting with propylene.

Propylene conversion rate appeared to increase with higher O_β/O_γ ratio, and PO selectivity decreased with increasing O_β/O_γ ratio. The two highlighted points in either graphs were from the Ag/Nd_2O_3 catalyst, where it had an anomalously low conversion and high PO selectivity. Nonetheless, it was generally true that a catalyst with a high conversion would result in a low PO selectivity, and *vice versa*.

By increasing the reaction temperature from 270 ^oC to 300 ^oC, conversion increased and PO selectivity decreased. However, the extent of change appeared to be dependent on the O_β/O_γ ratio. A higher O_β/O_γ ratio resulted in a greater increase in conversion, whereas a lower O_β/O_γ ratio had a greater decrease in PO selectivity on increasing temperature. This could be explained by the increased activation of O_β relative to O_γ at higher temperature, which were more favourable towards complete oxidation than partial oxidation, resulting in a more significant drop in PO selectivity. However, as the XPS measurements were performed at room temperature, additional information had to be provided in form of *in situ* XPS at the temperature range where the reaction occurred in order to investigate the

O_β/O_γ ratio at these temperatures. The anomalous behaviour of Ag/Nd_2O_3 suggested that the O_β/O_γ ratio was in fact lower than measured.

The relationship observed between O_β proportion and propylene conversion and PO selectivity suggested that O_β played a role in the reaction mechanism. Therefore, the Eley – Rideal mechanism were unable to fully describe the reaction mechanism, as it assumed the sole source of oxygen was from molecular oxygen. The difference in the promotion of conversion, and the reduction in PO selectivity, suggested that there was a difference in the extent in the ability of O_γ to O_β promotion across the lanthanide series.

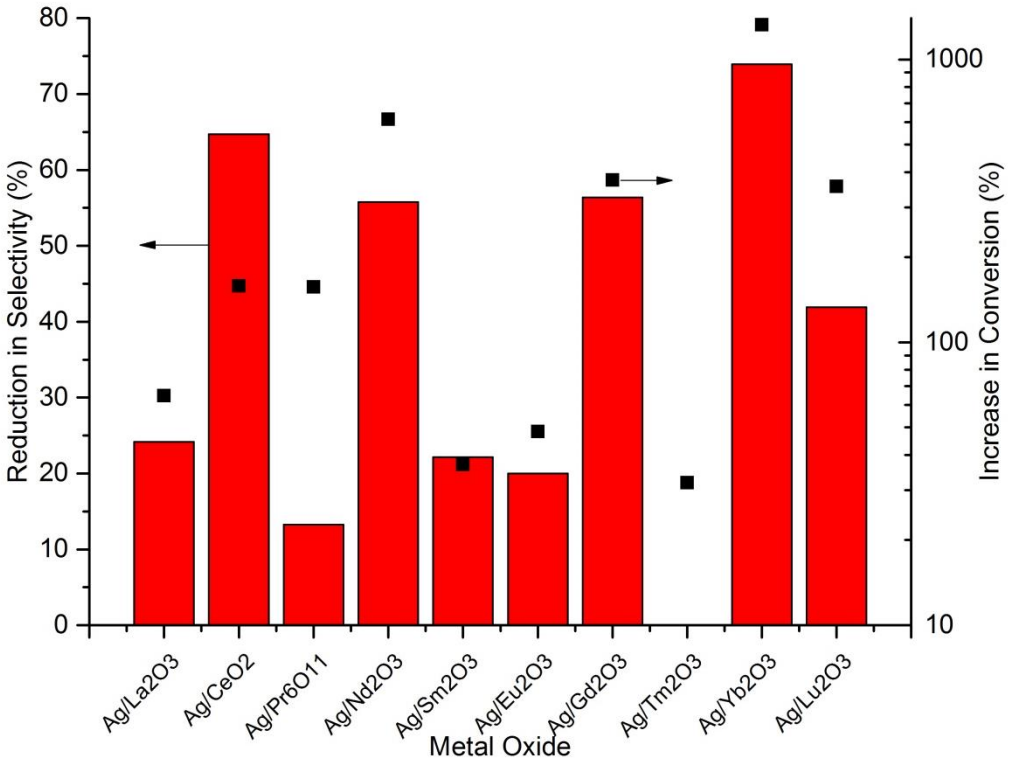

Figure 10-12 Reduction in PO selectivity (red bar), and increase in conversion (black scatter) using different Ag/Ln_2O_3 from 270 °C to 300 °C.

Figure 10-12 shows the decrease in PO selectivity, and the increase in propylene conversion as temperature increased from 270 °C to 300 °C. As previously discussed, the late lanthanide oxides tended to have a greater decrease in PO selectivity, and a higher propylene conversion at higher temperature. However, since the increase in propylene conversion for the late lanthanide oxides were over an order of magnitude greater than that of the early lanthanide oxides, and the decrease in PO selectivity was comparable across the series, it would suggest the over yield increase for the later lanthanide oxides were much greater than the early lanthanide series, as shown in Figure 10-13 below.

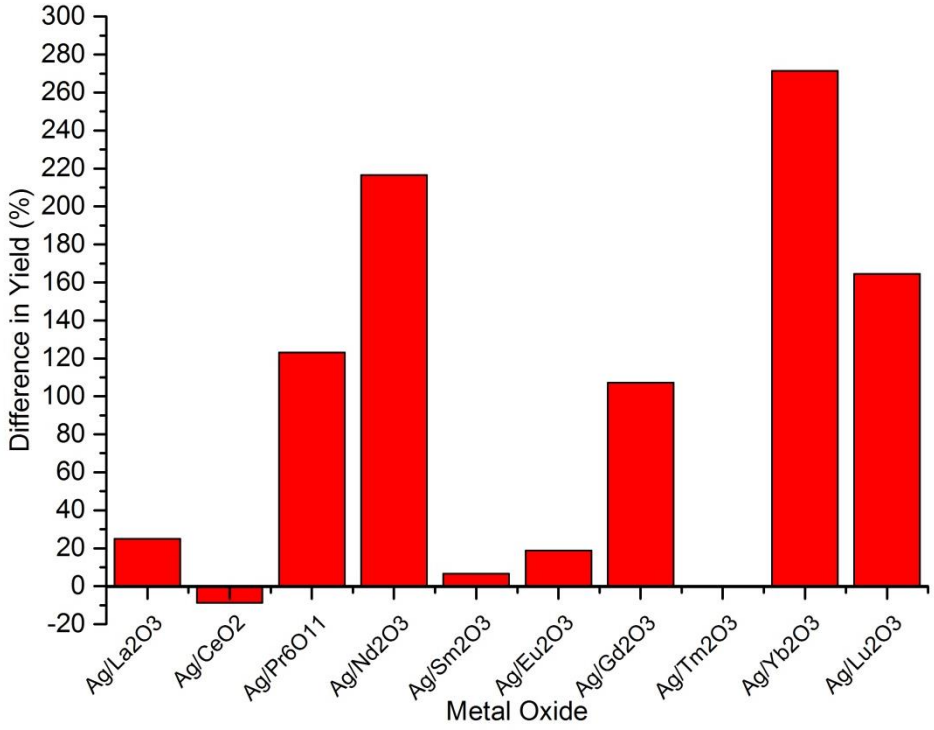

Figure 10-13 Difference in PO yield between 270 °C and 300 °C with different Ag/Ln_2O_3.

With the exception of Ag/CeO_2, which had a decrease in yield, and Ag/Tm_2O_3, which had a 0% yield up to 300 °C, PO yield increased as temperature increased. This was due to the

overwhelming exponential increase in the rate of propylene conversion compared to the linear rate of decrease of PO selectivity. The later lanthanide oxides generally had a greater increase in PO yield compared to the early lanthanide oxides, as the increase in propylene conversion was significantly greater than the early lanthanide oxides.

In general, the early lanthanide oxides had a high proportion of O_β, which resulted in a high rate of complete oxidation of propylene. These reactive oxygen species offered little selectivity towards the partial oxidation of propylene to form PO. On the other hand, the late lanthanide oxides had a much lower proportion of reactive O_β, which meant the reaction relied on molecular oxygen adsorption on the catalyst surface for reaction. This resulted in a much lower conversion rate, but higher PO selectivity.

The unusual activity of Ag/Nd_2O_3 might be explained by an increased ability for molecular oxygen to adsorb onto the catalyst surface, causing a dramatically decreased activity, but a much higher PO selectivity. However, more work will have to be done in the future in order to fully understand the oxygen adsorption properties on these catalyst surfaces at high temperatures.

10.4 Summary

Other oxidation reactions were tested using Ag/Ln_2O_3 catalysts, most notably the photodecomposition of soot, and the partial oxidation reaction of propylene. It was found that a lower energy SPR excitation resulted in a higher photoactivity in soot decomposition.

This was due to the better energy overlap between the Ag LSP virtual state and the metal oxide conduction band, thus facilitating a more favourable electronic transition from the Ag Fermi Level to the metal oxide conduction band.

The nature of oxygen species was found to be highly influential on the reaction mechanism of the oxidation reaction of propylene. O_β generated from the catalyst was found to favour complete oxidation to form CO and CO_2, whereas molecular oxygen was found to favour partial oxidation to form PO. O_β was also found to be much more reactive than molecular oxygen, and giving a much higher rate of conversion as a consequence, though at the detriment of PO selectivity. Both PO selectivity and propylene conversion rate appeared to be highly dependent on temperature, where selectivity decreased linearly and conversion rate increased exponentially. Furthermore, the onset temperature of PO production appeared to be somewhat dependent on the O_β activation temperature as observed by TPR.

These results have provided a platform to demonstrate the versatility of Ag/Ln_2O_3 as a series of catalyst, being able to perform a range of different reactions other than the thermal decomposition of soot. However, more work will have to be done in order to fully understand the interactions of the catalyst with propylene in a true heterogeneous reaction.

10.5 References

1 A. Mills, J. S. Wang and M. Crow, *Chemosphere*, 2006, **64**, 1032–1035.

2 X. Bao, M. Muhler, R. Schlogl and G. Ertl, *Catal. Letters*, 1995, **32**, 185–194.

3 P. Gelin, M. Primet and P. Gélin, *Appl. Catal. B-Environmental*, 2002, **39**, 1–37.

4 L. Kundakovic and M. Flytzani-Stephanopoulos, *J. Catal.*, 1998, **179**, 203–221.

5 L. Kundakovic and M. Flytzani-Stephanopoulos, *Appl. Catal. a-General*, 1999, **183**, 35–51.

6 M. A. Barteauf, R. J. Madix and M. A. Barteau, *J. Am. Chem. Soc.*, 1983, **105**, 344–349.

7 E. L. Force and A. T. Bell, *J. Catal.*, 1975, **371**, 356–371.

8 S. Ghosh, S. S. Acharyya, R. Tiwari, B. Sarkar, R. K. Singha, C. Pendem, T. Sasaki and R. Bal, *ACS Catal.*, 2014, **4**, 2169–2174.

9 M. F. Luo, J. Q. Lu and C. Li, *Catal. Letters*, 2003, **86**, 43–49.

10 Y. Lei, F. Mehmood, S. Lee, J. Greeley, B. Lee, S. Seifert, R. E. Winans, J. W. Elam, R. J. Meyer, P. C. Redfern, D. Teschner, R. Schlögl, M. J. Pellin, L. a Curtiss, S. Vajda and R. Schlogl, *Science (80-.).*, 2010, **328**, 224–228.

11 X. E. Verykios, F. P. Stein and R. W. Coughlin, *Catal. Rev.*, 2006, **22**, 197–234.

12 R. E. Kenson and M. Lapkin, *J. Phys. Chem. B*, 1970, **74**, 1493–1502.

13 J. Q. Lu, J. J. Bravo-Suarez, A. Takahashi, M. Haruta and S. T. Oyama, *J. Catal.*, 2005, **232**, 85–95.

14 H. Nakatsuji and H. Nakai, *Surf. Sci.*, 1998, **401**, 371–391.

Contents

Chapter 11. Conclusions and Future Perspectives

11.1 Conclusions

Within this thesis, a range of different metal oxides has been employed as a support for Ag for the soot combustion reaction. The main aim of the support was to stabilise the high surface energy Ag nanoparticles, and to promote soot combustion with a strong metal – support interaction. These metal oxides have had a varying degrees of success in promoting soot combustion, but most notably, Ag/Nd_2O_3 was able to burn soot at a temperature of 284 ^{o}C, the lowest temperature in any open literature.

It was found that there was an inverse size effect on the soot combustion temperature of a given catalyst system. A larger Ag particle was found to have a lower T_m than a smaller Ag particle on the same metal oxide support. However, this effect was not linear, but instead it was found to be of diminishing effect as the Ag particle size increased. This was due to the metal – support interaction becoming smaller, and thus had a smaller promotional effect on soot combustion.

A few trends were also found to be present in terms of metal – support interaction. Firstly, early lanthanide oxides were found to have a much stronger metal – support interaction than late lanthanide oxides, which could enable Ag activation of atmospheric oxygen to form energetic subsurface oxygen species for soot combustion.

O_β activation from O_γ showed to be a crucial step for oxygen activation, and the correct temperature range activation of O_β resulted in the lowering of soot combustion temperature. Neither O_β activation at low or high temperature gave any promotional effects to soot combustion. At low enough oxygen content, atmospheric oxygen activation on the catalyst interface became diffusion limited, thus hindering soot combustion.

In addition, the synthesis and testing of ZnO and Nd_2O_3 nanorods showed the preferential combustion of soot on the oxygen terminated polar surfaces. This also confirmed the hypothesis that lattice oxygen activation of mobile oxygen played a key role in the low temperature initial combustion of soot.

The formation of Ag_2O species further activated oxygen to become fully ionic species, which were then released upon heating with soot as a high energy source. Only early lanthanide oxide supported Ag catalysts had the ability for such Ag_2O formation.

An energy diagram and reaction mechanism were devised from the information obtained in the characterisations of the soot combustion technique, and it was discovered that early lanthanide oxides were not pure ionic species like previously imagined, but had an intimate metal – support interaction, both SMSI and EMSI, with Ag

to give soot combustion temperatures of below 350 ^{o}C. The extent of metal – support interaction of Ag and transition metal oxides was much weaker, resulting in a much higher soot combustion temperature.

11.2 Future Perspectives

Having successfully found potential candidates as soot combustion catalysts, scaling up synthesis and deployment in a commercial system is going to be a major challenge. Although initial testing has shown the catalysts to be thermally stable in laboratory conditions, more rigorous testing in real life catalytic converters and diesel traps will give a better understanding their thermal survivability.

Additives have been shown to reduce the soot combustion temperature by up to 70 ^{o}C, so the doping technique shall be further developed for further improvement in the promotional effects.

The subsurface oxygen has been found to be the major source of oxygen for soot combustion at low temperature. This energetic oxygen can be exploited for use in other industrial reactions, such as propylene epoxidation and methane combustion. The demonstrated effects of oxygen promotion by Ag may provide techniques for further catalyst development.

However, current techniques were ineffective in quantifying the amount of subsurface oxygen in the catalyst system. Currently, only the presence of subsurface oxygen was confirmed, and their activity was qualified using TPR. Hydrogen titration can be performed in the future at isothermal conditions to quantify the amount of mobile oxygens, though certain problems will first have to be overcome, such as the problem of hydrogen multisorption on Ag surface.

In situ measurements of oxygen adsorption behaviour at reaction temperatures would be a useful indication of the reactivity of the catalysts under reaction conditions. This measurement would also provide valuable information on the reaction mechanism of gas phase reactions, such as the partial oxidation of propylene. The relative reactivity of O_β and molecular oxygen can also be quantified in order to give a better understand towards the reasoning behind the activity an selectivity of propylene oxidation.